Studies of Valence Electron Densities Using Electron Momentum Spectroscopy and Computational Quantum Chemistry

by

John J. Neville

B.Sc., The University of New Brunswick, 1991

A THESIS SUBMITTED IN PARTIAL FULFILLMENT OF

THE REQUIREMENTS FOR THE DEGREE OF

DOCTOR OF PHILOSOPHY

in

THE FACULTY OF GRADUATE STUDIES

DEPARTMENT OF CHEMISTRY

We accept this thesis as conforming
to the required standard

THE UNIVERSITY OF BRITISH COLUMBIA

February 1997

In presenting this thesis in partial fulfilment of the requirements for an advanced degree at the University of British Columbia, I agree that the Library shall make it freely available for reference and study. I further agree that permission for extensive copying of this thesis for scholarly purposes may be granted by the head of my department or by his or her representatives. It is understood that copying or publication of this thesis for financial gain shall not be allowed without my written permission.

Department of CHEMISTRY

The University of British Columbia
Vancouver, Canada

Date 17 april 1997

DE-6 (2/88)

Abstract

The valence shell binding energy spectra and momentum profiles of acetone, dimethoxymethane and glycine have been studied by electron momentum spectroscopy at a total energy of 1200 eV. These experimental measurements present several challenges, in both data collection and analysis, that are typically not encountered in electron momentum spectroscopy studies of smaller molecules. A newly constructed energy-dispersive multichannel electron momentum spectrometer yields improvements in both sensitivity and energy resolution as compared with single-channel spectrometers used in previous studies. These instrumental improvements address several of the challenges of performing electron momentum spectroscopy studies of larger molecules and make possible the experimental measurements presented in this thesis.

The studies of acetone and dimethoxymethane each encompass the approximate binding energy range of 5–60 eV, while the study of glycine is limited to the binding energy range of 6–27 eV. The current work provides the first experimental values of the inner-valence $(6a)^{-1}$, $(4b)^{-1}$ and $(5a)^{-1}$ ionization potentials of dimethoxymethane, which are 20.4, 22.6 and 23.9 eV, respectively. For all three molecules, many-body effects are evident in the ionization spectra at binding energies greater than 16 or 17 eV.

The experimental momentum profiles of all three molecules are compared with theoretical profiles obtained from Hartree–Fock (HF) and density functional theory (DFT) calculations using the target Hartree–Fock and target Kohn–Sham approximations, respectively. The

convergence of the theoretical results with basis set is investigated by performing the calculations with a range of basis sets. In the case of the DFT calculations, the sensitivity of the theoretical profiles to the choice of exchange–correlation functional is also investigated. The outermost experimental momentum profiles of acetone (i.e., $5b_2$ and $2b_1$) and dimethoxymethane ($10b + 11a$) are also compared with theoretical profiles calculated by E. R. Davidson from multi-reference single and double excitation configuration interaction (MRSD-CI) calculations of the corresponding neutral molecules and ions.

The theoretical momentum profiles obtained from DFT calculations are generally in good agreement with the experimental profiles. The notable exceptions are the $5b_2$ profile of acetone and the 9b profile of dimethoxymethane, for which none of the theoretical methods considered here reproduce the experimental profiles. Agreement is poorer between the HF profiles and the experimental data. This is particularly so for the outer-valence momentum profiles, where the HF calculations tend to underestimate the intensity at low momentum. There is little difference between the large-basis-set HF calculations and the MRSD-CI calculations of the outermost momentum profiles of acetone and dimethoxymethane. Convergence of the theoretical momentum profiles with respect to basis set occurs with the 6-311++G** basis set for both the HF and DFT calculations; theoretical momentum profiles calculated using smaller basis sets tend to underestimate the intensity at low momentum, particularly for the outer-valence momentum profiles. The DFT profiles are relatively insensitive to changes in the exchange–correlation functional.

Table of Contents

List of Tables

List of Figures

List of Abbreviations

ADC	analogue-to-digital converter
BES	binding energy spectrum
BW	background window
CFD	constant fraction discriminator
CGF	contracted Gaussian function
CI	configuration interaction
CISD	configuration interaction, single and double excitations
CW	coincidence window
DFT	density functional theory
DWIA	distorted-wave impulse approximation
EMS	electron momentum spectroscopy
fwhm	full width at half maximum
GGA	generalized gradient approximation
GW-PG	Gaussian-weighted planar grid
HF	Hartree–Fock
HOMO	highest occupied molecular orbital
IP	ionization potential
KS	Kohn–Sham
LCAO	linear combination of atomic orbitals

LSDA	local spin-density approximation
MO	molecular orbital
MP	Møller–Plesset
MRSD-CI	multi-reference single and double excitation configuration interaction
PES	photoelectron spectroscopy
PSDA	position sensitive detector analyser
PWIA	plane-wave impulse approximation
SCA	single-channel analyser
SCF	self-consistent field
TAC	time-to-amplitude converter
TAP	theoretical angle profile
THFA	target Hartree–Fock approximation
TKSA	target Kohn–Sham approximation
TMP	theoretical momentum profile
XAP	experimental angle profile
XMP	experimental momentum profile

Preface

Some of the work included in this thesis has been published previously.

1. Y. Zheng, J. J. Neville, C. E. Brion, Y. Wang and E. R. Davidson, "An electronic structure study of acetone by electron momentum spectroscopy: a comparison with SCF, MRSD-CI and density functional theory." *Chem. Phys.* **188** (1994) 109–129.

2. Y. Zheng, J. J. Neville and C. E. Brion, "Imaging the electron density in the highest occupied molecular orbital of glycine." *Science* **270** (1995) 786–788.

3. John J. Neville, Y. Zheng and C. E. Brion, "Glycine valence orbital electron densities—comparison of EMS experiments with Hartree–Fock and density functional theories." *J. Am. Chem. Soc.* **118** (1996) 10533–10544.

4. J. J. Neville, Y. Zheng, B. P. Hollebone, N. M. Cann, C. E. Brion, C.-K. Kim and S. Wolfe, "EMS studies of larger molecules of chemical and biochemical interest." *Can. J. Phys.* **74** (1996) 773–781.

Publication 1 presents the results of an EMS study of acetone based upon the same experimental data described in Chapter 4 of this thesis and also includes a description of the spectrometer constructed by research associate Dr. Yenyou Zheng and myself and described in Chapter 3. Dr. Zheng was the principal author of this publication, with the remaining authors, including myself, contributing to the analysis of the data and revision

of the manuscript. The acetone study presented in Chapter 4 includes a reanalysis of the data presented in publication 1 and considerable additional computational work performed subsequent to the writing of publication 1.

Publication 2 is a short communication presenting preliminary EMS results of the HOMO of glycine. All three authors made significant contributions to the writing of this publication, with Dr. Zheng writing the initial draft and myself and then Prof. Brion performing extensive redrafts of the manuscript. A comprehensive report of the EMS study of the valence shell of glycine is given in publication 3, for which I was the principal author. As such, I performed the electronic structure calculations and data analysis and wrote all drafts of the manuscript, incorporating the invaluable suggestions of my co-authors during the data analysis and manuscript editing and revising processes. The work reported in publication 3 is presented in Chapter 6.

Publication 4 is the text of an invited talk I prepared and presented at the International Symposium on (e, 2e), Double Photoionization and Related Topics, a satellite conference of the XIX ICPEAC. This paper describes the experimental and computational techniques used in extending electron momentum spectroscopy to the study of larger molecules and includes preliminary results from the studies of glycine (Chapter 6) and dimethoxymethane (Chapter 5). Elements of this publication have been incorporated into Chapters 1–3.

All of the EMS data presented in the publications listed above and in this thesis was collected by myself with the assistance and guidance of Dr. Zheng and Prof. Brion.

Acknowledgements

While performing the research presented in this thesis, I have benefitted from the contributions of many individuals, whom I gratefully acknowledge. Foremost among them is my research supervisor, Prof. Chris Brion, who introduced me to electron momentum spectroscopy and whose wisdom and guidance has impacted (!) upon all aspects of this work.

A special thanks is owed to Dr. Yenyou Zheng, with whom I worked closely during the construction, testing, debugging and operation of the energy-dispersive spectrometer. His experience and expertise were key to the success of the experimental aspects of this work.

The successful design, construction and operation of the energy-dispersive spectrometer also depended greatly upon the contributions of the staff of the mechanical and electronic engineering services of the Department of Chemistry. In particular, the expertise and technical skills of Brian Snapkauskas, Ed Gomm and Brian Greene are gratefully acknowledged.

I thank Prof. Saul Wolfe of Simon Fraser University for suggesting that dimethoxymethane would be an interesting molecule to study and for posing many thoughtful and challenging questions concerning EMS. Our meetings not only increased my knowledge of organic chemistry but also improved my understanding of electron momentum spectroscopy.

Prof. Ernest Davidson of Indiana University performed the MRSD-CI calculations of argon, acetone and dimethoxymethane and provided many insightful comments and suggestions concerning the interpretation of the results of these studies.

I thank Prof. Dennis Salahub of the Université de Montréal for generously providing a copy of Reference [85] prior to publication and for several helpful comments concerning the study of glycine.

I gratefully acknowledge the assistance of Prof. Delano Chong, who provided many helpful comments and brought to my attention several relevant publications.

Many of my early questions concerning EMS were answered by Bruce Hollebone, who also helped me learn to program in C and clarified many programming and computational issues. I thank Dr. Natalie Cann for her development and refinement of the HEMS and resfold programs, which were used throughout this research, and for many helpful and interesting conversations.

I gratefully acknowledge the many others with whom I have had the pleasure to work, talk and drink numerous cups of coffee during my studies at U.B.C., in particular Jennifer Au, Gord Burton, Dr. Glynn Cooper, Noah Lermer, Terry Olney, Jim Rolke and Dr. Bruce Todd. They have helped to make my graduate studies an enjoyable experience and I have learned much from them.

The financial support of the Natural Sciences and Engineering Research Council is gratefully acknowledged.

Special thanks go to 'the gang' at the Lutheran Campus Centre, for their friendship and support throughout my time at U.B.C., and for helping me to develop an appreciation of fine beer. Thanks also to Vaughan and Janet Roxborough for their support and interest throughout my graduate studies.

I gratefully acknowledge the contributions of my parents, not only during my graduate studies but throughout my education. I would not have reached this point without their support and encouragement.

Finally, I thank Margie for her support, patience and understanding and Alexander for ensuring there was some excitement and play in every day.

JOHN J. NEVILLE

The University of British Columbia
February 1997

To my mother and father.

Chapter 1

Introduction

Knowledge of the electron density distribution of a molecule is important for the understanding and prediction of reactivity and chemical behaviour. It is straightforward to obtain theoretical electron density distributions, either from the square of the electronic wavefunction obtained from, for example, Hartree–Fock (HF) or configuration interaction (CI) calculations or by calculating the density directly using density functional theory (DFT). These theoretical densities, however, are of necessity approximations of the true electron density as a result of the simplifying assumptions associated with each theoretical method. Therefore, experimental measurements of electron distributions are invaluable not only for the information they provide directly concerning the electronic structure of the molecule but also as a means of assessing the quality of calculated electron densities and electronic wavefunctions. Detailed experimental information of total charge distributions is available using x-ray and electron scattering techniques [1,2]. However, as the success of the frontier orbital theory of Fukui [3,4] has demonstrated, chemical reactivity is influenced primarily by the electron density distributions of the outer-valence orbitals and in particular the highest occupied molecular orbital (HOMO). Experimental measurement of individual valence orbital electron distributions is possible using electron momentum spectroscopy (EMS) [5–9].

The electron distributions obtained using EMS are in momentum space (i.e., they are electron momentum distributions) rather than in position space (electron position or charge distributions). In a series of theoretical papers entitled "Momentum distributions in molecular systems," published in the 1940's, Coulson and Duncanson explored this alternative momentum space representation of the electron density for molecular hydrogen and a number of simple hydrocarbons [10–12]. Their work illustrates the correspondence between momentum and position space and demonstrates how chemical concepts such as molecular bonding are reflected in the momentum space electron density. More recently, the usefulness of working in momentum space when considering chemical reactivity and physical properties has been demonstrated in theoretical work by Allan, Cooper and co-workers [13–15]. They have found that molecular similarity and dissimilarity indices calculated using momentum space electron densities are capable of rationalizing physical and chemical properties and biological activity in cases where there is no obvious relationship between the bonding structure of the molecule and the property of interest. For example, such theoretical momentum space studies have been able to predict satisfactorily the relative effectiveness of anti-HIV phospholipids observed in clinical testing [13–15]. In Reference [14], Allan and Cooper summarize the effectiveness of working with the momentum space density as follows:

> "In marked contrast to the position space density, the momentum density highlights some of the most chemically interesting parts of the electron distribution, without over-emphasizing the bonding topology."

The above quote could have been written just as readily concerning the effectiveness of EMS for studying molecular electron density, as demonstrated by the many experimental studies performed in the quarter-century since the first successful implementation of the EMS technique.[1] The majority of these EMS studies have been of atoms and simple polyatomic

[1] Brief outlines of the history and applications of EMS are given in Sections 1.1.1 and 1.1.2, respectively.

molecules such as the hydrides of the elements of the second row of the periodic table (i.e., CH_4, NH_3, H_2O and HF). The purpose of the present work is to extend EMS to the study of larger and more complicated molecules than have been studied previously, specifically acetone ($(CH_3)_2CO$), dimethoxymethane ($(CH_3O)_2CH_2$) and glycine (NH_2CH_2COOH). To address some of the challenges posed by the study of these molecules (discussed in Section 1.2 below), an energy-dispersive multichannel electron momentum spectrometer has been constructed. This spectrometer, similar in design to one constructed previously at the Flinders University of South Australia [16–18], has a sensitivity approximately one order of magnitude better than that of the single-channel spectrometers used previously in this group [19] and elsewhere to perform EMS measurements. In addition to the experimental measurements, the recently formulated application of Kohn–Sham density functional theory to EMS [20,21] is evaluated for the molecules studied and compared with the results of Hartree–Fock and configuration interaction calculations.

1.1 Electron momentum spectroscopy

Electron momentum spectroscopy involves the ionization of a (usually gas phase) atom or molecule by impact with a high-energy electron and the coincident detection of the two outgoing electrons (the scattered electron and the ionized electron). This ionization process is referred to as the (e, 2e) reaction, the name reflecting the origins of EMS in nuclear physics. The kinematics of the ionization are fully determined—i.e., the energies and trajectories of the incident electron and the two detected outgoing electrons are known. If the energies of the incident and outgoing electrons are sufficiently high and an appropriate experimental geometry is employed, electronic structure information of the neutral atom or molecule, independent of kinematic factors, can be obtained.

From conservation of energy, the electron binding energies (also called ionization potentials or IPs) of the target atom or molecule can be determined. By varying the energy of the incident electron beam and/or using a multichannel spectrometer capable of recording simultaneously data at a range of binding energies, a binding energy spectrum (BES) can be obtained. This contains information similar to that provided by photoelectron spectroscopy (PES, where ionization occurs as the result of the absorption of a photon rather than by electron impact), albeit with poorer energy resolution than is possible using PES. What makes EMS unique is the additional ability to determine, to a good approximation, the spherically-averaged distribution of electron momenta corresponding to the single-particle orbital from which the electron has been ionized, i.e., $\int |\psi_j(\mathbf{p})|^2 \, d\Omega$. This is done by recording the variation in the (e, 2e) differential cross-section at a particular binding energy as a function of the trajectories of the two outgoing electrons. This momentum distribution—or experimental momentum profile (XMP), as it is more commonly termed in the field of EMS—is the momentum-space analogue to the position-space orbital electron density $\int |\psi_j(\mathbf{r})|^2 \, d\Omega$. The momentum-space and position-space orbitals themselves ($\psi(\mathbf{p})$ and $\psi(\mathbf{r})$) are related by a Fourier transform (Equation (1.1) below). Note that the momentum distributions provided by other experimental techniques such as Compton scattering and positron annihilation are considerably more limited than those from EMS as they are of the total molecular electron density (the sum of all orbital densities) rather than of the electron density of individual orbitals [5].

1.1.1 Development of EMS

It was first suggested that the (e, 2e) reaction might be used to obtain the momentum distributions of electrons in binding energy-selected states by Baker, McCarthy and Porter in 1960 by analogy with the (p, 2p) reaction used to obtain momentum distributions of protons

in nuclei [22]. Further theoretical exploration of the possibilities of (e, 2e) experiments was performed by Neudatchin and co-workers [23, 24] and Glassgold and Ialongo [25] in the late 1960's.

The first experimental work involving the (e, 2e) reaction in which the scattering kinematics were fully determined was reported by Ehrhardt et al. in 1969 and involved the scattering of low energy electrons ($\approx$ 100 eV) off helium using an asymmetric coplanar geometry [26]. The terms used to describe the (e, 2e) experimental kinematics indicate if the energies and polar angles of the detected electrons are equal (symmetric or asymmetric) and whether or not the trajectories of the two detected electrons are in the same plane (coplanar or non-coplanar). The reaction kinematics are discussed in more detail in Chapter 2. The purpose of Ehrhardt's work was to test theories of electron impact ionization at low impact energies rather than to obtain electronic structure information of the helium target. That same year, Amaldi et al. reported the results of high energy (14.6 keV) coplanar symmetric electron impact experiments measuring the binding energy spectrum of the carbon K and L (i.e., core and valence) shells using a thin carbon film target [27]. Although no momentum profile data were obtained, this very low energy resolution study helped to demonstrate the feasibility of obtaining electronic structure information using the (e, 2e) reaction.

The first momentum profiles determined experimentally by EMS were reported in 1972 by Camilloni et al. [28]. Momentum profiles of the K and L shells of carbon were obtained using a thin carbon foil target but the energy resolution was not sufficient to resolve the individual C 2s and 2p orbitals of the L (valence) shell. The following year, Weigold and co-workers reported the first atomic and molecular valence orbital momentum profiles, of gas phase argon [29] and methane [30], respectively. These measurements were obtained using symmetric non-coplanar kinematics, which, for reasons discussed in Chapter 2, have been found to be particularly well-suited to studies of electronic structure [6]. In the case of the

argon measurements, clear evidence of the breakdown of the independent particle model of ionization was observed in the form of BES peaks at binding energies greater than those for ionization from the single-particle 3p and 3s orbitals. The XMPs of these argon "satellite peaks" indicated that they correspond to ionization of a 3s electron of neutral argon and the simultaneous excitation of a second electron. These results confirmed the prediction of Levin made one year previously that (e, 2e) experiments would be capable of detecting such electron correlation effects [31].

Following the success of these initial gas-phase experiments, electron momentum spectroscopy (originally known as binary (e, 2e) spectroscopy) has been used by several research groups [32–34] to study the electronic structure of a large number of gaseous atoms and molecules. Much of this research has been summarized in review articles[2] and bibliographies of all studies reported up until 1990 have been published [36, 38]. Several studies are discussed in the following section to demonstrate some of the applications of EMS. Additional EMS studies that serve to validate the theoretical interpretation of the EMS differential cross-section are discussed in Chapter 2.

1.1.2 Applications of EMS

As mentioned above, EMS provides both binding energy spectra and binding energy-selected momentum profiles. With currently available instrumentation, the EMS energy resolution is approximately two orders of magnitude worse than that of photoelectron spectroscopy. Consequently, EMS is not the best choice of experimental technique if accurate ionization potentials are desired. However, EMS does have one important advantage over PES for the study of ionization—namely that the BES are obtained as a function of electron momentum. This provides symmetry as well as energy information and aids greatly in the assignment

[2]Recent reviews of EMS include References [7–9, 35–37].

of the ionization peaks. For example, EMS measurements have resolved the question of the energetic ordering of the $(5a_1)^{-1}$ and $(1b_2)^{-1}$ valence ionizations of formaldehyde (H_2CO) [32, 39].

This symmetry information is also very useful when studying inner-valence ionization (typically, binding energies in the range 20–60 eV). In this energy region, the single-particle model of ionization tends to break down (see for example Reference [40]). Ionization from an inner-valence orbital ψ_j may occur at several ionization energies, each leading to a different final ion state. This results in "satellite peaks" in the BES, as mentioned in the previous section for argon. If initial-state correlation effects are small, as is typically the case for inner-valence ionization, the intensities of all ionization peaks resulting from the removal of an electron from orbital ψ_j will exhibit the same electron-momentum dependence, thus facilitating the determination of the "parentage" of these satellite peaks, i.e., the orbital from which the electron has been ionized. In addition, in contrast to PES, the intensities of the EMS binding energy peaks are directly proportional to the spectroscopic factors (discussed in Chapter 2) of the ionization processes [5, 41], which can be calculated using CI [39] or many-body Green's function theory [40]. The EMS studies of hydrogen sulphide [42], carbon monoxide [43] and molecular fluorine [44] include particularly detailed analyses of inner-valence ionization.

The ability of EMS to "image" the momentum space electron density of individual molecular orbitals (within the approximations discussed in Chapter 2) has been the principal motivation for most EMS studies. Comparisons of momentum profiles from EMS experiments with the corresponding theoretical profiles from *ab initio* calculations have resulted in new insights into what constitutes an "accurate" electronic wavefunction [9,45,46]. In particular, the accurate theoretical modeling of EMS momentum profiles has proven sensitive to basis set and electron correlation effects.

Much of the utility of EMS studies is a consequence of the experimental electron density profiles being in momentum space rather than position space, the perspective from which chemists typically view electronic structure. The momentum space molecular orbital $\psi(\mathbf{p})$, the spherically-averaged square of which generally provides a good description of the EMS XMP, is related to the position space molecular orbital $\psi(\mathbf{r})$ by the Fourier transform relationship

$$\psi(\mathbf{p}) = (2\pi)^{-3/2} \int \mathrm{e}^{-i\mathbf{p}\cdot\mathbf{r}} \psi(\mathbf{r}) d\mathbf{r}. \tag{1.1}$$

This relationship results in an approximately inverse weighting of position (r) and momentum (p) space.

EMS is most sensitive to regions of low momentum (small p) and, consequently, strongly emphasizes the chemically sensitive outermost spatial regions of electron density. Although the outermost (large r) region of electron density plays a significant role in chemical reactivity, this area is often represented poorly by variationally determined wavefunctions as a result of its small contribution to the total energy, a property dominated by the core (small r) electron density. This has been demonstrated clearly in EMS studies of H_2O and NH_3, where theoretical momentum profiles (TMPs) generated from Hartree–Fock wavefunctions considered at the time to be of high quality underestimated the intensity at low momentum of the outermost valence orbital XMPs [9, 45, 47]. Several factors were found to contribute to this disagreement, one being that the basis sets used for the calculations did not describe adequately the large r regions of electron density. The addition of further extremely diffuse functions and polarization functions to the basis sets resulted in a significant improvement in the theoretical description of the low momentum regions of the momentum profiles while having very little impact on the calculated total energies.

EMS measurements of many small molecules [9] have confirmed the importance of using sufficiently diffuse basis sets in order to calculate accurate momentum profiles. This has

been found to be of particular significance for outermost (highest energy) valence orbitals, which should be of the most significance to chemical reactivity. In addition, there has been a growing appreciation of the potential pitfalls of over-emphasising the total energy when assessing the "goodness" of a wavefunction, especially when the properties of interest are primarily dependent upon the large r (or small p) regions of electron density. To ensure that a wavefunction accurately models all regions of electron density, it is important to consider a range of properties that each emphasizes a different region of space. The total energy (small r), dipole or quadrupole moment (medium r) and EMS momentum profiles (large r) have proven to be effective choices to guide the development of "universal" wavefunctions [9,45,46]. In situations where a universal wavefunction is not necessary, care must be taken to choose a basis set well-suited to the regions of electron density emphasized by the particular properties of interest.

In the case of the H_2O and NH_3 studies mentioned above, an additional factor contributing to the disagreement between theory and experiment for the HOMO momentum profiles was found to be the absence of a treatment of electron correlation effects in the theoretical calculations.[3] When electron correlation effects were accounted for (using multi-reference single and double excitation configuration interaction, or MRSD-CI) and the GW-PG resolution-folding method was used to account for the instrumental angular resolution (see footnote), excellent agreement between theory and experiment was obtained [9]. In general, it has been found that electron correlation effects are important in the momentum-space outer-valence orbital electron densities of the polar hydrides of the elements of the second-row of the periodic table (i.e., NH_3, H_2O and HF), but not of the corresponding hydrides of the third-row elements or small hydrocarbons [9].

[3]The final factor responsible for the disagreement was an inadequate treatment of the instrumental angular resolution [9]. This has been corrected with the development by Duffy et al. of the Gaussian-weighted planar grid method (GW-PG) [48], discussed in Chapter 2.

In addition to the study of individual atoms or molecules, the study by EMS of series of chemically related molecules has provided some interesting insights into aspects of molecular electronic structure. A prime example is the series of increasingly methylated amines $NH_x(CH_3)_{3-x}, x = 0, \ldots, 3$ [49,50]. An examination of the HOMO XMPs of these molecules indicated that the methyl group is electron withdrawing with respect to hydrogen in the HOMOs of the methyl amines. Similar findings have been obtained for the series water [45], methanol [51], dimethyl ether [52,53] and formaldehyde, acetaldehyde, acetone [54].

1.1.3 Recent advances in EMS

The coincidence nature of the EMS experiment and the necessary kinematics result in a small experimental differential cross-section and long data collection times. This was so particularly for the first generation of EMS spectrometers [6,19]. These single-channel spectrometers were only capable of collecting data at a single binding energy and electron momentum at a time, thereby disregarding the majority of the (e, 2e) events. Consequently, several weeks were required to collect either one momentum profile or a valence shell BES at a single momentum value. Comprehensive studies of the entire valence shells of even small molecules routinely required several months of data collection.

The advent of multichannel electron momentum spectrometers has significantly increased the sensitivity of the technique and made possible many interesting new experiments. Multichannel spectrometers improve data collection efficiency by collecting data simultaneously over a range of binding energies [16, 17], electron momenta [55] or a combination of the two [56]. Improvements in sensitivity of one to two orders of magnitude over that of single-channel spectrometers are obtained. The development of an energy-dispersive electron momentum spectrometer has facilitated the first EMS study of an excited and oriented target, sodium atoms pumped by a polarized laser to the $3^2P_{3/2}, m_l = +1$ state [57]. In addition, a

detailed study of the experimental momentum profiles arising from ionization to excited ion states of helium ($n = 2$ and $n = 3$ ion states) and H_2 and D_2 ($2p\sigma_u, 2s\sigma_g$) has been performed recently using a momentum dispersive EMS spectrometer [58–60]. Measurements of these momentum profiles had been reported previously [18,61–65] but were limited because of the very small cross-sections for ionization to the excited ion states of He^+ and H_2^+. Finally, Storer et al. have reported a spectrometer for the study of thin solid films that is multichannel in both energy and momentum [56]. Valence measurements of amorphous and graphitic carbon using this new spectrometer demonstrate the relationship between electronic and physical structure and the use of EMS for the characterization of condensed matter [56].

In addition to these experimental advances, there are recent theoretical developments of considerable significance to EMS. As discussed above, EMS studies of many small molecules have demonstrated the importance of using relatively large basis sets containing diffuse and polarization functions and in some cases correlated methods to calculate accurate theoretical momentum profiles. Although for small molecules it is generally possible to perform calculations of the necessary complexity, this becomes increasingly challenging as the size of the molecules being studied increases, to the point where only very approximate theoretical results are available for comparison with experiment. This is, of course, a general problem in computational chemistry rather than one specific to EMS. Consequently, the application of density functional theory (DFT) to chemical problems [66, 67] has been of great interest to chemists and this has been an area of considerable research activity in recent years. Reference [68] describes the current range of chemical applications of DFT. DFT is computationally less demanding than Hartree–Fock theory and has been shown, in at least some applications, to provide results as good as or better than HF and some post-HF methods. In recent work by Duffy et al. [20, 21], DFT has been applied to EMS and used to calculate theoretical momentum profiles (TMPs). Comparisons of DFT TMPs of several small

molecules with experimental data and TMPs obtained using HF and CI methods indicate that the DFT results are at least as good as those from the HF calculations and are in better agreement with experiment than the HF results in those cases where an accounting of electron correlation effects was found to be important, such as was described above for the HOMO of water [20, 21].

1.2 EMS of larger molecules

As has been discussed in Section 1.1 above, over the past two decades electron momentum spectroscopy has been used extensively for the study of atoms and small molecules typically having only a few heavy (i.e., non-hydrogen) atoms. Although a few studies of larger systems have been performed, they have been limited principally to molecules of high symmetry, such as sulphur hexafluoride [16] and transition-metal hexacarbonyls [69]. Given the demonstrated success of EMS for the investigation of molecular electronic structure and also as an experimental tool to aid in the evaluation and design of electronic wavefunctions for molecules such as water [9, 45] and ammonia [9], it is natural to consider applying EMS to the study of more complicated molecules.

The extension of EMS measurements and the complementary quantum mechanical calculations to larger molecules poses a number of challenging problems both experimentally and theoretically. The EMS signal-to-noise ratio decreases as the number of electrons increases, thereby necessitating greater data collection times to obtain data of reasonable precision. Experimental measurements are more complicated in many cases due to the low volatility of the target molecule. This may necessitate the use of a heated sample system which must provide sufficient target density for gas phase studies over long measuring times and concurrently avoid thermal decomposition of the sample. One of the primary reasons that EMS studies

have been limited principally to simple systems is the rather poor energy resolution that has been typical of EMS experiments. The number of closely-spaced (in energy) valence orbitals tends to increase with increasing molecular size and complexity. Difficulties in resolving ionization processes corresponding to the removal of electrons from orbitals of similar energy result in increased challenges in data analysis and interpretation. Furthermore, in studies of many larger molecules the target will be present in more than one stable conformation at the experimental temperature, thus considerably complicating the data analysis.

The increased coincidence count rates of recently developed multichannel electron momentum spectrometers, discussed in Section 1.1.3 above, makes it possible to address and significantly overcome many of these challenges posed by the study of larger molecules. Increased sensitivity allows measurements to be made using a lower target density than was previously practical, which is of benefit when studying compounds which have a low vapour pressure or which are prone to thermal decomposition. Additionally, some of the increase in coincidence count rate can be sacrificed to obtain improved energy resolution and thus enable EMS measurements of a wider range of molecules.

Even if further improvements in energy resolution (i.e., beyond those realized using the multichannel spectrometers described above) were possible however, they would not fully solve the problem of isolating peaks arising from ionizations from closely spaced orbitals in many molecules because of the natural (vibronic) widths of the ionization peaks. This is clear from an examination of the photoelectron spectra of, for example, many of the larger molecules reported in Reference [70]. Despite an energy resolution approximately two orders of magnitude better than that of EMS experiments, it is not possible to resolve fully the majority of the valence shell ionization peaks of many of these molecules. Consequently, an equally important result of the considerably increased coincidence count rates of multichannel spectrometers is the increased feasibility of recording extensive BES over a range

of azimuthal angles. Using these BES in conjunction with data from high resolution photoelectron spectroscopy (PES), it is possible in many cases to obtain experimental momentum profiles for ionization processes closely spaced in energy. This can be done by fitting the BES using Gaussian peaks located at the known PES IPs and with widths based upon the PES Franck–Condon widths and the experimental energy resolution of the EMS instrument. When the energy spacing is such that this analysis is not possible, an experimental angle profile may still be obtained by summing data over a range of binding energies corresponding to ionizations from several closely spaced orbitals, or by representing several closely spaced ionization processes by a single fitted peak. Although this reduces the amount of available information, these studies may still be useful for the evaluation of theoretical methods and the design and evaluation of wavefunctions.

From a theoretical standpoint, computational complexity rapidly increases with number of electrons even at the Hartree–Fock level and high-level correlated treatments such as CI quickly become infeasible for larger molecules. The conformational mobility of many larger molecules further increases the computational difficulties since separate theoretical momentum profile calculations are required for each stable conformer (conformational potential energy minimum) present at the experimental conditions. The individual conformer calculations must then be Boltzmann weighted at the experimental temperature and summed together prior to comparison with the EMS experimental data. For these reasons, the less computationally intensive approach to quantum mechanical calculations provided by DFT is of particular interest. As previously mentioned, initial applications of DFT to EMS [20,21,71] have been encouraging. However, comparisons have thus far only been performed in a limited number of cases, all of them small molecules. Further evaluation of DFT as applied to EMS, involving comparisons with the results of HF and post-HF (e.g., CI) calculations and experimental data, is necessary to determine whether it will provide a viable approach to

the calculation of valence electron densities and other properties of larger molecules.

1.3 Overview of the thesis

The work presented in this thesis involves the extension of EMS to the study of molecules of greater complexity than have previously been investigated using this technique. Several experimental and theoretical considerations—many of them outlined above—arising from such studies are explored. This is done in the context of experimental EMS and theoretical studies of the valence shells of acetone, dimethoxymethane and glycine. The remainder of the thesis is organized as outlined below.

Chapter 2 presents the theoretical background necessary for the interpretation of the experimental EMS differential cross-section and the calculation of theoretical momentum profiles for comparison with the experimental results. In addition, the computational methods used in performing the studies presented in Chapters 4–6 are described.

The multichannel electron momentum spectrometer constructed in the course of this work is described in Chapter 3, along with the calibration and operating procedures used in the collection of the experimental data presented in subsequent chapters. This energy-dispersive instrument is similar to one developed previously by Weigold et al. [7, 16] and is capable of collecting data simultaneously over a binding energy range of $\approx$ 16 eV. Procedures for sample handling and the processing of the experimental data are also discussed.

EMS measurements of the valence shell of acetone over the binding energy range 6–60 eV are presented in Chapter 4. These measurements serve as a "bridging" study between previous EMS experiments and the studies presented in Chapters 5 and 6. Experimental results for the $5b_2$ HOMO of acetone have been reported previously by Hollebone et al. [54] in a paper comparing the HOMO momentum profiles of acetone, acetaldehyde and

formaldehyde. These single-channel EMS results for acetone had rather poor statistical precision, making the comparison with theoretical momentum profiles, including the results of large basis set HF and MRSD-CI calculations, somewhat inconclusive. Nevertheless, there appeared to be a discrepancy between the $5b_2$ XMP and all of the reported TMPs at electron momenta > 0.8 au. The previous single-channel study was limited to the HOMO as a consequence of the low experimental count rates of the single-channel spectrometer and the experimental energy resolution of 1.7 eV full width at half maximum (fwhm). The improved energy resolution (1.4 eV fwhm) of the multichannel results presented in the current work has enabled a comprehensive study of the valence shell of acetone, including the collection of individual XMPs for six of the valence orbitals. The experimental results are compared with TMPs calculated using the HF and MRSD-CI wavefunctions reported in Reference [54] as well as the results of additional HF calculations and DFT calculations using a range of basis sets and several exchange–correlation functionals. Furthermore, the effect of the orientation of the acetone methyl groups on the calculated momentum profiles is investigated.

The EMS studies of dimethoxymethane and glycine, reported in Chapters 5 and 6 respectively, represent the first EMS studies of these molecules. Both of these molecules are of biochemical interest, glycine as the simplest amino acid and dimethoxymethane both as a model compound for the glycosidic linkage in polysaccharides and for the study of the anomeric effect [72], a conformational effect observed in carbohydrates and related molecules. These molecules are both important for use as prototypes for the evaluation of theoretical methods that are being considered for use with much larger molecules—proteins in the case of glycine and polysaccharides in the case of dimethoxymethane. To be feasible, theoretical studies of these much larger molecules will require that the calculations be performed at as efficient a level as is possible and will necessitate compromises between computational expense and accuracy of the results. Prior to performing such calculations, it is necessary to

have an understanding of the potential impact on calculated properties of, for example, the neglect of electron correlation effects or the use of small basis sets. Benchmark calculations on molecules such as dimethoxymethane and glycine, for which a broad range of theoretical methods are still practical and for which experimental data are available for comparison, are therefore of considerable importance. Experimental momentum profiles obtained via EMS should be particularly useful experimental "checks" of theoretical results for these molecules as a result of the sensitivity of EMS to the outer regions of electron density that may be expected to play significant roles in conformation (through interactions such as intramolecular hydrogen bonding), reactivity and molecular recognition.

The EMS study of dimethoxymethane reported in Chapter 5 covers the valence shell from 5–59 eV. XMPs are compared with TMPs obtained from HF and DFT calculations spanning a considerable range of basis set size and complexity. In addition, the results of MRSD-CI calculations for the two lowest energy ionizations (outermost orbitals), performed by Ernest R. Davidson of Indiana University, are compared with the experimental and other theoretical results. The sensitivity of the calculated momentum profiles to changes in molecular geometry and conformation are also investigated.

The study of glycine is of the outer-valence orbitals, covering the binding energy range of 6–27 eV, and is reported in Chapter 6. The roles of basis set size and composition and also electron correlation effects in modeling the outer-valence orbitals of this molecule are studied by comparing the experimental measurements to HF and DFT calculations using a range of basis sets. A number of experimental [73–78] and theoretical [79–85] studies indicate that several stable conformers of glycine will be present at the experimental conditions used for the EMS measurements. Consequently, a thorough study of the outer-valence TMPs of all conformers likely to contribute to the observed experimental signal is performed.

General observations and conclusions arising from this work are presented in Chapter 7,

along with a summary of the major findings and some suggestions for possible areas of future research.

Chapter 2

Theoretical Background and Computational Methods

Two of the principal applications of EMS experiments are the evaluation of theoretical models used to describe molecular electronic structure, in particular valence electron densities, and the investigation of the relationships between molecular geometry and composition, electronic structure as described by EMS momentum profiles, and other molecular properties. For such applications of EMS to be possible, a thorough understanding of the EMS differential cross-section and how it may be related to or predicted from electronic structure calculations is necessary. Considerable work has been published describing the EMS differential cross-section and deriving tractable forms for the calculation of theoretical momentum profiles (TMPs) for comparison with and to aid in the interpretation of their experimental counterparts (XMPs). See for example the reviews of McCarthy and Weigold [5–7] and work referenced therein. A brief overview of the theoretical representations of the EMS differential cross-section used in this work is given in the following sections, following a description of the (e, 2e) reaction that is the basis of EMS. The latter half of this chapter consists of an overview of the methods used to calculate theoretical representations of the experimental EMS data reported in subsequent chapters of this thesis.

2.1 The (e, 2e) reaction

The (e, 2e) reaction, upon which EMS experiments are based, is shown in Equation (2.1) and is illustrated in Figure 2.1.

$$e_0 + M \rightarrow M_f^+ + e_1 + e_2 \tag{2.1}$$

As discussed briefly in Chapter 1, the reaction consists of the ionization of a target atom or molecule M, assumed to be at rest and in its ground electronic state, by an inelastic collision with an incident electron e_0 having a kinetic energy E_0 and a momentum $\mathbf{p}_0$. The collision results in an ion M^+ in state f, with recoil energy and momentum E_{recoil} and $\mathbf{q}$, respectively, and two outgoing electrons e_1 and e_2, with respective kinetic energies and momenta of $E_1, \mathbf{p}_1$, and $E_2, \mathbf{p}_2$.

The sum of the kinetic energies of the two outgoing electrons is the *total energy* (E) of the reaction ($E = E_1 + E_2$). The electron binding energy ϵ_f for ionization to the ion state f can be determined from conservation of energy:

$$\epsilon_f = E_0 - E_1 - E_2. \tag{2.2}$$

The ion recoil energy E_{recoil} is very small and can be neglected. In contrast, the ion recoil momentum $\mathbf{q}$ is not negligible. It can be determined using conservation of momentum:

$$\mathbf{q} = \mathbf{p}_0 - \mathbf{p}_1 - \mathbf{p}_2. \tag{2.3}$$

If the kinetic energies of the incident electron and the two outgoing electrons are sufficiently high and the momentum transfer $\mathbf{K}$ of the reaction is high ($\mathbf{K} = \mathbf{p}_0 - \mathbf{p}_1$), then the (e, 2e) reaction can be regarded as an electron-electron collision with the ion acting only as a spectator [7]. This simplification of the ionization reaction involves the binary encounter approximation and the impulse approximation, which are discussed below in more detail.

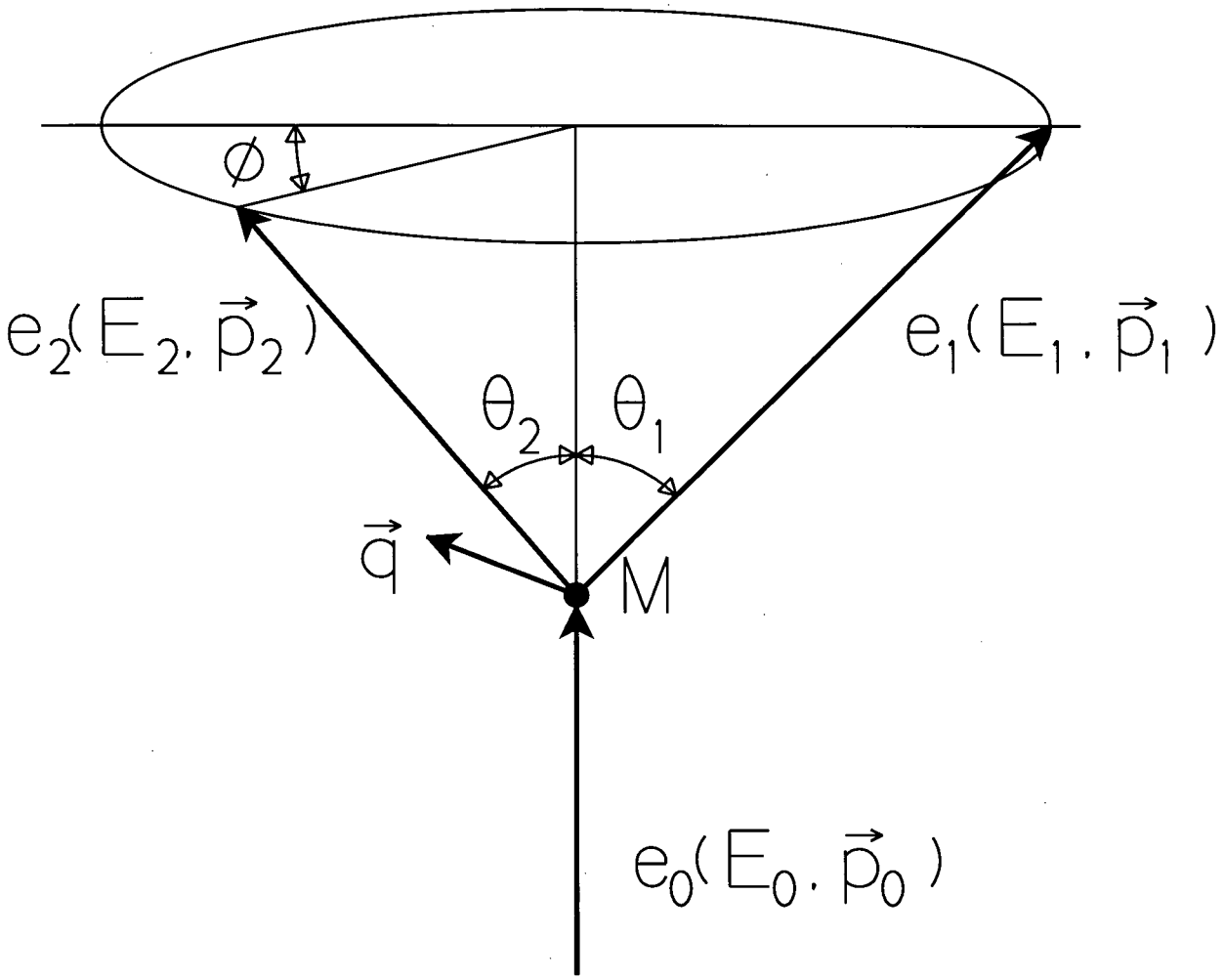

Figure 2.1: EMS scattering kinematics. The figure depicts the symmetric non-coplanar (e, 2e) kinematics used in the current work, where $\theta_1 = \theta_2 = \theta = 45°$, $E_1 = E_2 = 600$ eV and ϕ is variable over the range $\pm 30°$.

Under these conditions, the ion recoil momentum is equal in magnitude and opposite in sign to the momentum **p** of the ionized electron prior to ionization (i.e., while still part of the target molecule M):

$$\mathbf{p} = -\mathbf{q}. \tag{2.4}$$

The binary encounter and impulse approximations are almost always invoked in the interpretation of EMS experiments and the work presented in this thesis is no exception.

The scattering kinematics of the (e, 2e) reaction are illustrated in Figure 2.1. The arrangement shown represents symmetric non-coplanar kinematics. The polar angles θ_1 and θ_2 between the two outgoing electron trajectories and the direction of the forward-scattered electron beam are equal and fixed ($\theta_1 = \theta_2 = \theta$), as are their kinetic energies. The out-of-plane azimuthal angle ϕ is variable to allow access to a range of recoil momentum values **q** and hence electron momenta **p**. With symmetric non-coplanar kinematics, the magnitude of **p** is

$$p = [(2p_1 \cos\theta - p_0)^2 + (2p_1 \sin\theta \sin(\phi/2))^2]^{1/2}. \tag{2.5}$$

If the electron energies are high in comparison to the binding energy and $\theta = 45°$, the first term of Equation (2.5) will be near zero and p will be approximately proportional to ϕ for small values of ϕ.

Using symmetric non-coplanar kinematics, the experimental differential cross-section is essentially independent of kinematic factors (i.e, variation of E_0 and ϕ) and is thus a probe only of electronic structure. This kinematic arrangement also results in a large momentum transfer **K** and high kinetic energies for both outgoing electrons, conditions necessary for the validity of the binary encounter and impulse approximations. Consequently, the majority of EMS experiments, including those reported in this thesis, have been performed using this kinematic arrangement. A second kinematic arrangement that is also a good probe of electronic structure is asymmetric coplanar kinematics near the Bethe ridge [7]. In this

experimental arrangement, $E_1 >> E_2$, $\phi = 0°$, $\theta_1 \lesssim 20°$ and θ_2 is varied. This arrangement is used in the recently reported spectrometer of Storer et al. [56] for the EMS study of thin solid films.

2.2 The EMS differential cross-section

The differential cross-section, in atomic units, for the (e, 2e) reaction is [7]

$$\frac{d^5\sigma}{d\mathbf{p}_1 d\mathbf{p}_2 dE_1} = (2\pi)^4 \frac{p_1 p_2}{p_0} \frac{1}{4\pi} \sum_{\text{av}} \int |T_f(\epsilon_f; \mathbf{p}_0, \mathbf{p}_1, \mathbf{p}_2)|^2 \, d\Omega \tag{2.6}$$

where $\sum_{\text{av}}$ represents a sum over final state degeneracies and an average over initial state degeneracies and the spherical averaging ($\frac{1}{4\pi} \int d\Omega$) accounts for the random orientations of the gas-phase target molecules. $T_f(\epsilon_f; \mathbf{p}_0, \mathbf{p}_1, \mathbf{p}_2)$ is the reaction amplitude for ionization leading to the final ion state f. It can be written as

$$T_f = \left\langle \chi^{(-)}(\mathbf{p}_1) \chi^{(-)}(\mathbf{p}_2) \Psi_f \right| \tau \left| \Psi_i \chi^{(+)}(\mathbf{p}_0) \right\rangle . \tag{2.7}$$

The electrons have been represented by incoming (+) and outgoing (−) distorted waves ($\chi^{\pm}$), Ψ_f and Ψ_i are the wavefunctions of the final ion in state f and the initial neutral target in its ground electronic state and τ is the operator describing the ionization reaction.

The initial approximation upon which the interpretation of the EMS cross-section is based is the binary encounter approximation, which assumes that τ depends upon the coordinates of the two electrons but not on those of the particles constituting the ion [7]. This allows Equation (2.7) to be factored into a probe part, dependent upon the reaction kinematics, and a structure part, dependent upon the electronic structure of the target and ion.

2.2.1 The distorted-wave impulse approximation

A further level of approximation is required to obtain a representation of the cross-section that is amenable to calculation. In the distorted-wave impulse approximation (DWIA), the electrons are represented by distorted waves, as in Equation (2.7), and τ is the free two-electron amplitude, i.e., the amplitude for inelastic collisions between two free electrons. In essence, the assumption is that the collision occurs so fast that the presence of the ion does not affect the collision process. The experimental cross-section then becomes [7]

$$\frac{d^5\sigma}{d\mathbf{p}_1 d\mathbf{p}_2 dE_1} = 4\pi^3 \frac{p_1 p_2}{p_0} f_{\mathrm{ee}} \sum_{\mathrm{av}} \int \left| \left\langle \chi^{(-)}(\mathbf{p}_1)\chi^{(-)}(\mathbf{p}_2)\Psi_f \right| \Psi_i \chi^{(+)}(\mathbf{p}_0) \right\rangle \right|^2 d\Omega \qquad (2.8)$$

where f_{ee} is the Mott scattering cross-section for electron-electron collisions. An explicit form of f_{ee} in the symmetric non-coplanar geometry is given in Reference [7]. It depends only upon known kinematic factors and has been shown [19] in symmetric non-coplanar kinematics at $E = 1200$ eV to be essentially independent of the out-of-plane azimuthal angle ϕ over the range of $\pm 30°$ typically used in EMS experiments. The Mott scattering cross-section does have a small dependence on the energy of the incident electron. For the symmetric non-coplanar kinematics used in this work ($E = 1200$ eV, $\theta = 45°$) the variation in f_{ee} is small over an electron binding energy range corresponding to the outer-valence orbitals of atoms or molecules. Consequently, the EMS cross-section can be considered to be proportional to the final, electronic structure, factor of Equation (2.8) for most purposes. However, over a binding energy range of 50 eV, f_{ee} has been shown to vary by approximately 13% [59,86]. Thus, when the precise relative intensities of ionization processes well separated in binding energy are of prime concern, the impact-energy dependence of the Mott scattering cross-section should be taken into account. For the purposes of the present work, this impact-energy dependence has been neglected.

The representation of the electrons using distorted waves accounts for perturbations of

the electron trajectories by the target both prior to and following ionization. The validity of the DWIA and the underlying binary encounter approximation has been tested extensively for atoms [5–7]. The DWIA has been found to give an excellent description of the EMS experimental cross-section for electron momenta up to at least $p \sim 3$ au when symmetric non-coplanar kinematics are used with a total energy $E \geq 1000$ eV [5–7]. In the case of molecules, the multiple nuclei prevent the use of a centrally symmetric potential for calculation of the distorted waves and DWIA calculations are not, at present, feasible [6]. Consequently, a different approximation is necessary when considering the EMS cross-section of molecules.

2.2.2 The plane-wave impulse approximation

If the energies of the electrons are sufficiently high, perturbations of their trajectories by the target and by each other will be small and the electrons can be represented as plane waves. If this is done and the impulse approximation is also invoked (i.e., τ is taken to be the free two-electron amplitude), the EMS differential cross-section can be written as [7]

$$\frac{d^5\sigma}{d\mathbf{p}_1 d\mathbf{p}_2 dE_1} = 4\pi^3 \frac{p_1 p_2}{p_0} f_{\mathrm{ee}} \sum_{\mathrm{av}} \int |\langle \mathbf{p}\Psi_f | \Psi_i \rangle|^2 \, d\Omega \tag{2.9}$$

where $\mathbf{p}$ here represents a plane-wave electron having a momentum determined using Equations (2.3) and (2.4). This is the plane-wave impulse approximation (PWIA).

The EMS experimental energy resolution is such that rotational and vibrational states of molecules are not resolved, thus necessitating the sum over unresolved final states and average over unresolved initial states indicated by $\sum_{\mathrm{av}}$ in Equation (2.9) and previous equations. Using the Born–Oppenheimer approximation, the molecular and ion wavefunctions Ψ_i and Ψ_f can be expressed as the products of electronic, vibrational and rotational wavefunctions. The sums over final vibrational and rotational states can be eliminated from Equation (2.9) by closure [7]. Rotation of the molecular target is accounted for by the spher-

ical averaging $\int d\Omega$ that is required because of the random orientations of the gas-phase target molecules. Initial-state vibrations are typically accounted for in EMS studies by calculating the electronic wavefunctions at the equilibrium molecular geometry. The validity of these approximations has been clearly demonstrated by EMS studies of H_2 and D_2 [87] and of H_2O and D_2O [45]. In both cases, isotopic substitution had no effect on the experimental momentum profiles.

Taking into account the considerations outlined in the previous paragraph and the near-invariance under EMS conditions of the kinematic factors in Equation (2.9), the EMS differential cross-section for closed-shell molecules is essentially proportional to the spherically averaged square of the overlap of the neutral and ion electronic wavefunctions:

$$\frac{d^5\sigma}{d\mathbf{p}_1 d\mathbf{p}_2 dE_1} = \text{constant} \int |\langle \mathbf{p}\Psi_f | \Psi_i \rangle|^2 \, d\Omega \tag{2.10}$$

where Ψ_i and Ψ_f now represent the electronic wavefunctions of the target and ion. It is this representation of the EMS cross-section that will be referred to as the PWIA in the remainder of this thesis. It is straightforward to calculate the cross-section as given by Equation (2.10) using the many-body wavefunctions of the neutral molecule in its ground electronic state and the ion in electronic state f. Such descriptions of the EMS cross-section are sometimes referred to as ion-neutral overlap distributions. Procedures for calculating electronic wavefunctions are described in Section 2.3.

An examination of the body of EMS studies that have been conducted in the past twenty years [7] indicates that the plane-wave impulse approximation is generally adequate for describing the shapes of orbital momentum profiles for $p \leq 1.5$ au. For higher values of electron momentum, distortion effects tend to result in greater observed intensity than is predicted using the PWIA. The PWIA has been found to predict inaccurately the relative ionization cross-sections of atoms (e.g., it overestimates the $(3s)^{-1} : (3p)^{-1}$ ratio of argon) but typically gives good predictions of the relative ionization amplitudes of molecules [7].

2.2.3 The target Hartree–Fock approximation

The evaluation of Equation (2.10) for all valence ionization processes of a molecule can be a considerable task, since separate many-body electronic wavefunctions must be calculated for the neutral molecule and the ion in each accessed electronic state. (Each peak in the binding energy spectrum corresponds to ionization to a different electronic state of the ion.) Often, electron correlation effects in the neutral molecule are not significant when describing the (e, 2e) ionization process. If this is the case, the electronic wavefunction of the neutral molecule (Ψ_i) can be replaced in Equation (2.10) by the Hartree–Fock wavefunction Ψ_0 (HF theory is discussed in Section 2.3.1). This is the target Hartree–Fock approximation (THFA). If, in addition, the ion is represented as a linear combination of electron configurations (Slater determinants) obtained by various occupations of the target HF orbitals, the EMS differential cross-section then becomes [7, 8]

$$\frac{d^5\sigma}{d\mathbf{p}_1 d\mathbf{p}_2 dE_1} \propto S_f^j \int |\psi_j(\mathbf{p})|^2 \, d\Omega \tag{2.11}$$

where $\psi_j(\mathbf{p})$ is the momentum-space target orbital j from which the electron is ionized and S_f^j is the probability of the final ion state f having a contribution from the electron configuration formed by annihilating an electron in orbital j of the target configuration Ψ_0. S_f^j is known as the spectroscopic factor or pole strength of the ionization. It can be calculated by taking the square of the overlap between the ion wavefunction Ψ_f and the target wavefunction with a hole in orbital j ($\Psi_0^{(j)}$):

$$S_f^j = \left| \left\langle \Psi_f | \Psi_0^{(j)} \right\rangle \right|^2 . \tag{2.12}$$

Equation (2.11) indicates that, within the THFA, the momentum dependence of the EMS differential cross-section (i.e., the experimental momentum profile) is an initial-state property, described by the spherically-averaged square of the target orbital from which the

electron is removed, and is independent of the final state of the ion.[1] This greatly simplifies theoretical predictions of the EMS differential cross-section since only a single electronic structure calculation, of the neutral molecule, is necessary. Within the THFA, all ionizations from the same target orbital j (i.e., ionization manifold j), regardless of the final ion state f, will give rise to momentum profiles of the same shape, greatly facilitating the assignment of "many-body" or "satellite" ionization peaks. The relative intensities of the ionization peaks within a manifold are given by the spectroscopic factors S_f^j. The spectroscopic sum rule [5] states that the sum of all spectroscopic factors for a given ionization manifold is unity:

$$\sum_f S_f^j = 1. \tag{2.13}$$

Equation (2.13) indicates that if EMS measurements are performed for a binding energy range encompassing all ionization peaks in a particular manifold j, the absolute spectroscopic factors S_f^j for ionization from target orbital ψ_j can be determined experimentally. Previous EMS studies (see for example References [44,71,88]) and many-body Green's function calculations [40] indicate that the spectroscopic factors for ionizations from outer-valence orbitals are usually near unity; i.e., each outer-valence orbital typically gives rise to a single ionization peak. In contrast, ionizations from inner-valence orbitals often give rise to multiple ionization peaks corresponding to different final electronic states of the ion. These are the so-called "many-body" or "satellite" peaks. Their presence is a consequence of electron correlation effects (many-body effects) in the ion. Breakdown of the THFA is evidenced by shape discrepancies between experimentally measured momentum profiles and the corresponding theoretical momentum profiles calculated using Equation (2.11) and by variations in the shapes of momentum profiles belonging to the same ionization manifold.

[1] This is also suggested by the description of the (e, 2e) reaction kinematics within the binary encounter and impulse approximations, in which the experimentally determined ion recoil momentum ($\mathbf{q}$) is of equal magnitude to that of the struck electron ($\mathbf{p}$) just prior to ionization (see Section 2.1 and Reference [7]).

2.2.4 The target Kohn–Sham approximation

Use of the THFA considerably reduces the computational effort necessary to obtain theoretical momentum profiles. It has proven adequate to describe the EMS experiment for many atoms and small molecules. However, the neglect of target correlation and electronic relaxation of the ion implicit in the THFA has proven significant in some cases, particularly for the outermost valence orbitals of polar hydrides such as HF, H_2O and NH_3 [9]. In the case of these molecules, calculation via Equation (2.10) of the overlap of the ion and neutral CI wavefunctions (obtained using saturated basis sets) was found to be necessary in order to obtain quantitative agreement [9, 48, 89] between experiment and theory. As increasingly larger molecules are studied by EMS, the feasibility of performing CI calculations (and, to a lesser extent, HF calculations) to obtain theoretical momentum profiles becomes increasingly limited, particularly in light of the need to employ extended basis sets in order to obtain theoretical results that agree with experiment. One computational alternative is Kohn–Sham (KS) density functional theory. The comparatively low computational demands of DFT, particularly in comparison with other methods that include electron correlation effects, make DFT an attractive method for use in theoretical studies of chemical problems. Recent work by Casida [90] and Duffy et al. [20, 21] has provided the theoretical basis necessary to apply DFT to EMS. The key results of their work, as it pertains to this thesis, are presented below. A general overview of Kohn–Sham DFT is given in Section 2.3.3.

The target Kohn–Sham approximation (TKSA), introduced by Duffy et al. [20], approximates the ion-neutral overlap of Equation (2.10) by a momentum-space Kohn–Sham orbital $\psi_j^{\mathrm{KS}}(\mathbf{p})$:

$$\frac{d^5\sigma}{d\mathbf{p}_1 d\mathbf{p}_2 dE_1} \propto \int \left|\psi_j^{\mathrm{KS}}(\mathbf{p})\right|^2 d\Omega. \tag{2.14}$$

Although the form of the EMS differential cross-section in the TKSA is similar to that in

the THFA (Equation (2.11)), the basis for the approximation is different from that discussed above for the THFA. The overlap of the ion and neutral wavefunctions in Equation (2.10) is a Dyson orbital. Instead of calculating the Dyson orbital by taking the overlap of the two wavefunctions, as discussed above, it can be determined [20] by solving Dyson's quasiparticle equation, which describes both ionization and electron attachment. Solving Dyson's quasiparticle equation or calculating the overlap of the ion and neutral wavefunctions yields identical results in the limit of a full treatment of electron correlation. The TKSA is based upon the work of Casida [90] which showed that the Kohn–Sham equation is the variationally best local approximation to Dyson's quasiparticle equation. Consequently, the Kohn–Sham orbitals may be viewed as approximations to Dyson orbitals.[2] There are an infinite number of Dyson orbitals but, for an N electron molecule, only N occupied Kohn–Sham orbitals. The TKSA implies that the shape of each Dyson orbital will correspond to that of a Kohn–Sham orbital. This is equivalent to the consequence of the THFA that all momentum profiles from the same ionization manifold have an identical shape which is determined by the target orbital from which the electron has been removed. Despite the similarities between the target Hartree–Fock and target Kohn–Sham approximations, they differ in the significant respect that the TKSA allows for the inclusion of target electron correlation effects and the THFA does not.

There are, in practice, two levels of approximation involved in the TKSA. Firstly, Kohn–Sham orbitals are approximations of Dyson orbitals. This is true even in the case of exact DFT, i.e., even if the exact exchange–correlation functional could be used in the DFT calculations, thereby yielding Kohn–Sham orbitals whose densities summed to the true total density. Secondly, DFT calculations of molecules use approximate functionals and limited basis sets and consequently do not produce "exact" Kohn–Sham orbitals. The TKSA says

[2]The THFA may be regarded in a similar manner; the HF equation is the exchange-only case of Dyson's quasiparticle equation and HF orbitals are thus equivalent to Dyson orbitals in the exchange-only limit.

nothing of the accuracy of these approximations. The approximation therefore must be evaluated by comparing momentum profiles calculated using the TKSA (Equation (2.14)) with those obtained using the PWIA only (Equation (2.10)) and/or momentum profiles obtained experimentally. In their paper introducing the TKSA [20], Duffy et al. performed such comparisons for the valence orbital momentum profiles of six atoms and small molecules for which the results of high-quality CI calculations and EMS experiments were available. For all of the molecules considered, the TMPs derived from the CI calculations were in excellent agreement with the experimental momentum profiles. Consequently, comparisons were made with the CI TMPs and not with the XMPs. They concluded that the TKSA performed about as well as the THFA, but with the differences from the CI results (i.e., making only the PWIA) tending to be in the opposite direction than was found for the THFA. Whereas the THFA TMPs tended to underestimate the intensity at low momentum, the reverse was most often the case for the TKSA TMPs. With the exception of the valence TMPs of H_2O, all of the DFT calculations reported by Duffy et al. [20] were performed using the local spin-density approximation (LSDA). The calculations of H_2O performed using a gradient-corrected functional resulted in improved agreement between the TKSA and PWIA (i.e., CI) TMPs. This suggests that some of the differences observed for the other molecules may be attributable to the approximate functional used for the DFT calculations rather than limitations inherent in the TKSA. Subsequent EMS studies of ethylene [71], PH_3 and derivatives [91] and the open-shell molecules O_2, NO and NO_2 [92] have included comparisons with TMPs obtained using the TKSA. The results suggest that the TKSA yields TMPs in as good or better agreement with the experimental data than is the case for the THFA. Further evaluation of the TKSA, as applied to larger molecules, will be performed in subsequent chapters of this thesis by comparing TKSA TMPs with experimental data and with the results of HF and CI calculations for acetone, dimethoxymethane and glycine. Results obtained using several

exchange–correlation functionals and basis sets of varying complexity will be compared in an attempt to separate to some extent inaccuracies resulting from the TKSA itself from those resulting from the choice of functional and basis set.

2.2.5 Angular resolution effects

The theoretical descriptions of the EMS differential cross-section discussed above, whether they are obtained using Equation (2.10), (2.11) or (2.14), correspond to a hypothetical EMS experiment performed using a spectrometer having perfect resolution. In practice, of course, the instrumental energy and angular resolutions (in both the polar (θ) and azimuthal (ϕ) angles) are finite and are reflected in the experimental binding energy spectra and momentum profiles, respectively. In order to make a rigorous comparison between theoretical and experimental momentum profiles, it is necessary to account for the effects of the finite experimental angular resolution. The Gaussian-weighted planar grid (GW-PG) method of Duffy et al. [48] has proven to be an effective choice to account for these angular resolution effects, resulting in excellent agreement between experiment and high-quality theoretical calculations for a wide range of atoms and molecules [9, 48]. All theoretical momentum profiles presented in this thesis (unless otherwise noted) have been corrected for angular resolution effects using the GW-PG method prior to comparison with the experimental data.

2.3 Electronic structure calculations

To make use of the expressions for the EMS differential cross-section discussed above requires knowledge of the molecular and ionic electronic wavefunctions in the case of the PWIA (Equation (2.10)) or either the HF or KS molecular orbitals (MOs) in the case of the THFA or TKSA (Equations (2.11) and (2.14)). In the work discussed in this thesis, these quanti-

ties have been obtained using standard theoretical models of molecular electronic structure, namely the Hartree–Fock and configuration interaction *ab initio* methods and Kohn–Sham density functional theory. These methods are used widely throughout chemistry and many detailed references are available. For example, both the theoretical and computational aspects of the *ab initio* methods are discussed in References [93] and [94]. Details of the application of density functional theory to molecules can be found in Reference [66]. A summary of the basic concepts of DFT and a review of current chemical applications are given in Reference [68]. Consequently, only a general overview of these methods is presented here. In addition to those methods mentioned above, Møller–Plesset (MP) perturbation theory, used in some of the studies presented in this thesis, is also discussed.

The HF, CI and MP methods are all based upon finding solutions of the time-independent Schrödinger equation,

$$\hat{H}\Psi = E\Psi \tag{2.15}$$

where E is the energy of the stationary state of the system described by the wavefunction Ψ and $\hat{H}$ is the total-energy operator or Hamiltonian of the system. Equation (2.15) has an infinite number of solutions Ψ. The ground state of the system is described by the solution having the lowest energy E.

The non-relativistic Hamiltonian for a molecule contains terms describing the kinetic energies of all of the constituent particles (i.e., the electrons and nuclei) and the potential energy of the system resulting from the Coulombic forces between particles. The number of moving particles present in all but the simplest atomic systems makes impossible the exact solution of the Schrödinger equation for most systems of chemical interest. The HF, MP and CI approaches yield approximate solutions of the Schrödinger equation by making simplifying assumptions of varying severity. Although approximate, these three approaches are all *ab initio* methods—they find solutions of (2.15) without the use of experimental data,

other than the values of some fundamental physical constants.

An approximation common to all of the methods discussed here is that the electrons, being much lighter than the nuclei, move so much faster than the nuclei that the electronic motion is dependent only upon the instantaneous positions of the nuclei and not upon their velocities. Consequently, the problems of electronic and nuclear motion can be separated and the electronic problem solved in the static field of the fixed nuclei. This is known as the Born–Oppenheimer approximation. It is the solutions to the electronic problem—i.e., electronic wavefunctions—that are of interest in EMS.

The non-relativistic electronic Hamiltonian for an n electron molecule with m nuclei, in the absence of an external field and written in atomic units, is

$$\hat{H} = -\frac{1}{2}\sum_{i=1}^{n}\nabla_i^2 - \sum_{i=1}^{n}\sum_{A=1}^{m}\frac{Z_A}{r_{iA}} + \sum_{i=1}^{n}\sum_{j>i}^{n}\frac{1}{r_{ij}} + \sum_{A=1}^{m}\sum_{B>A}^{m}\frac{Z_A Z_B}{r_{AB}} \tag{2.16}$$

where the indices i and j refer to electrons and A and B to nuclei. The atomic numbers of the nuclei are denoted by Z_A and r_{iA} is the distance between particles i and A. The first term of Equation (2.16) represents the kinetic energies of the electrons and the remaining terms represent the potential energy. The final term, describing the Coulombic repulsion between nuclei, is constant for a given nuclear arrangement and does not affect the electronic wavefunction of the system. Despite the simplification resulting from the Born–Oppenheimer approximation, determination of the electronic wavefunction for a many-electron system remains a formidable problem because of the interdependence of the electrons arising from the $1/r_{ij}$ terms of the Hamiltonian. The most common means of addressing this is using Hartree–Fock theory.

2.3.1 Hartree–Fock theory

Hartree–Fock theory assumes that the electrons in a molecule are independent of one another so that their behaviour can be described by a series of one-electron functions or *orbitals*. The HF electronic wavefunction Ψ^{HF} has the form of a single determinant of one-electron spin orbitals, with each spin orbital being the product of a spatial orbital ψ_i (a function of the position of the electron) and a spin function α or β. The determinant is a sum of products of spin orbitals formed such that the wavefunction is antisymmetric with respect to the exchange of any two electrons. The HF energy E_{HF} (i.e, the expectation value of the energy corresponding to Ψ^{HF}) is given by

$$E_{\mathrm{HF}} = \left\langle \Psi^{\mathrm{HF}} \right| \hat{H} \left| \Psi^{\mathrm{HF}} \right\rangle . \tag{2.17}$$

Substituting for $\hat{H}$ using Equation (2.16) and expanding Ψ^{HF} in terms of the constituent orbitals, the Hartree–Fock energy of a closed-shell molecule is

$$E_{\mathrm{HF}} = 2\sum_{i=1}^{n/2} h_i + \sum_{i=1}^{n/2}\sum_{j=1}^{n/2}(2J_{ij} - K_{ij}) + V_{\mathrm{NN}} \tag{2.18}$$

where

$$h_i = \left\langle \psi_i(1) \left| -\frac{1}{2}\nabla_1^2 - \sum_A \frac{Z_A}{r_{iA}} \right| \psi_i(1) \right\rangle \tag{2.19}$$

$$J_{ij} = \left\langle \psi_i(1)\psi_j(2) \left| \frac{1}{r_{12}} \right| \psi_i(1)\psi_j(2) \right\rangle \tag{2.20}$$

$$K_{ij} = \left\langle \psi_i(1)\psi_j(2) \left| \frac{1}{r_{12}} \right| \psi_j(1)\psi_i(2) \right\rangle \tag{2.21}$$

V_{NN} is the internuclear repulsion energy given by the final term of Equation (2.16) and J_{ij} and K_{ij} are called respectively the Coulomb and exchange integrals. (1) and (2) refer to different electrons. In a closed-shell molecule, the n occupied spin orbitals consist of electrons of α and β spin in $n/2$ different spatial orbitals ψ_i, hence the sums over $n/2$ occupied spatial

orbitals and the factors of 2 in the above equations. Two identical spatial orbitals containing equal-energy electrons of opposite spin are often referred to collectively as a *molecular orbital.*

The variational principle states that any normalized trial wavefunction will yield an expectation value for the energy which is greater than or equal to the energy of the true lowest-energy solution of the Schrödinger equation for the system. For a molecule, the lowest-energy solution of the electronic Schrödinger equation is the ground-state electronic wavefunction Ψ_0 and the corresponding energy is the ground-state electronic energy E_0. Since any single determinant wavefunction will always be an approximation of the true wavefunction, therefore $E_{\mathrm{HF}} > E_0$. The HF wavefunction of a molecule is defined as the single determinant wavefunction yielding the lowest value of E_{HF} (and hence the energy closest to E_0). It is obtained by finding the set of orthonormal molecular orbitals ψ_i that minimizes E_{HF}. These are the HF orbitals. Minimization of E_{HF} with respect to ψ_i results in a set of $n/2$ coupled one-electron differential equations [93]

$$\hat{F}\psi_i = \epsilon_i \psi_i \tag{2.22}$$

where ϵ_i is the energy of orbital ψ_i and $\hat{F}$ is the Fock operator:

$$\hat{F}(1) = -\frac{1}{2}\nabla_1^2 - \sum_A \frac{Z_A}{r_{1A}} + \sum_{j=1}^{n/2}[2\hat{J}_j - \hat{K}_j] \tag{2.23}$$

The Coulomb and exchange operators $\hat{J}_j$ and $\hat{K}_j$ can be defined by their operation on an arbitrary function $f(1)$:

$$\hat{J}_j f(1) = f(1)\int \psi_j(2)^*\psi_j(2)\frac{1}{r_{12}}dv_2 \tag{2.24}$$

$$\hat{K}_j f(1) = \psi_j(1)\int \psi_j(2)^* f(2)\frac{1}{r_{12}}dv_2 \tag{2.25}$$

$\hat{J}_j$ and $\hat{K}_j$ are one-electron operators; they depend upon the coordinates of one electron only and describe the interaction between that electron and the average electric field of the

remaining electrons. This approximation neglects the instantaneous interactions between electrons but is necessary to allow separation of the total electronic wavefunction into products of one-electron wavefunctions. The one-electron operator $\hat{F}$ depends upon the solutions ψ_i to (2.22) through the Coulomb and exchange operators. Therefore, the equations must be solved iteratively until self-consistency is achieved, i.e., until no change in the solutions occurs upon further iteration. This is referred to as the self-consistent field or SCF method because the molecular orbitals are determined using their own effective electric field.

To allow for the practical implementation of HF theory, the problem of finding the $n/2$ molecular orbitals ψ_i that provide the minimum HF energy is simplified by expressing the molecular orbitals as linear combinations of known functions ϕ_i, called *basis functions.* The set of all basis functions used for the expansion is the *basis set.* If a basis set consisting of N functions is used for the expansion, each molecular orbital can then be expressed as

$$\psi_i = \sum_{\mu=1}^{N} \phi_\mu c_{\mu i} \tag{2.26}$$

Rather than having to determine the functional form of the molecular orbitals, the problem has been reduced to determining the expansion coefficients $c_{\mu i}$.

If the basis set constitutes a complete set, then by definition it will be possible using a basis set expansion to express exactly any well-behaved function. The wavefunction resulting from the SCF procedure will be the best possible single-determinant wavefunction for the system, yielding the lowest possible HF energy. These are referred to as the *HF-limit* wavefunction and energy. To be complete, a basis set must generally consist of an infinite number of basis functions (i.e., $N = \infty$). In practice, a basis set consisting of a limited number of basis functions is used, resulting in an energy greater than the HF-limit energy. By performing calculations using successively more complete basis sets and monitoring the decrease in energy, it is possible to get a sense of the proximity of the calculated energy

to the HF-limit energy. Unfortunately, this does not necessarily indicate how similar the calculated wavefunction is to the HF-limit wavefunction.

For molecular calculations, the basis set consists most commonly of functions resembling atomic orbitals centred on each of the nuclei of the molecule. This is called the linear combination of atomic orbitals or LCAO approximation. If one basis function is used for each core and valence-shell atomic orbital of each atom, then the basis set is a minimal basis set. Use of a minimal basis set generally results in calculated molecular properties of poor accuracy as a result of the lack of flexibility inherent in such a basis set. Further discussion of basis sets, including descriptions of those used for the calculations reported in this thesis, is given in Section 2.3.4 below.

2.3.2 Post-Hartree–Fock methods: electron correlation

HF theory neglects the instantaneous interactions between electrons and consequently does not yield the exact wavefunction and energy of the molecule. The difference between the exact non-relativistic energy of a molecule and the corresponding HF-limit energy is defined as the correlation energy:

$$E_{\text{corr}} = E_{\text{exact}} - E_{\text{HF}}. \tag{2.27}$$

Although the HF energy generally differs from the exact energy by only $\sim 1\%$, the accurate description of electron correlation is of key importance for calculating many chemical properties. In a recently published review article [95], Raghavachari and Anderson survey the techniques commonly used for the treatment of electron correlation in molecules and discuss the applicability and limitations of the various methods. Many of these techniques use the HF wavefunction as their starting point and thus are often called post-HF methods. Computational results of two post-HF methods, configuration interaction (CI) and Møller Plesset (MP) perturbation theory, are discussed in the latter chapters of this thesis and are

used to aid in the interpretation of the EMS experimental data.

Configuration interaction

A HF calculation of a closed-shell molecule using N basis functions will result in N molecular orbitals. If the molecule has $2n$ electrons, n of these orbitals will be occupied and $N-n$ will be vacant or *virtual orbitals*. The HF wavefunction will be a determinant composed of the spin orbitals formed from the occupied MOs. This is referred to as the ground-state electron configuration. Other electron configurations can be created by forming determinants with some of the occupied orbitals replaced with virtual orbitals. This corresponds to the excitation of one or more electrons to virtual orbitals. A configuration interaction wavefunction Ψ^{CI} is formed by taking a linear combination of electron configurations. This can be written as

$$\Psi^{\mathrm{CI}} = \sum_{x \geq 0} a_x \Psi_x \tag{2.28}$$

where Ψ_0 is the HF configuration and $\Psi_{x>0}$ are excited electron configurations. The CI expansion coefficients a_x are determined variationally so as to minimize the total energy. Typically, the coefficient of the HF configuration is much larger than that of any of the excited configurations.

If all possible electron configurations for a given basis set are included in the CI expansion (2.28), the calculation is described as full CI. Full CI calculations using basis sets large enough to provide chemically useful results are only practical for very small molecules. Consequently, some subset of all possible electron configurations is normally chosen. The most common choice, known as configuration interaction, single and double excitations or CISD, includes only those excited configurations formed by exciting one or two electrons. The configurations formed by double excitations account for the largest fraction of the correlation energy. Although making a much smaller contribution to the total energy, inclusion of the

single excitation configurations has been found to be important for the accurate computation of some molecular properties [95].

A second common method of limiting the size of CI calculations is to make the frozen-core approximation. This approximation limits excitations to those involving the valence electrons. In other words, configurations involving excitation of core electrons are neglected. This assumes that the contribution of inner-shell electrons to the total correlation energy is reasonably independent of molecular geometry and environment.

The CI calculations compared with the experimental data in this thesis were performed by Ernest Davidson and co-workers at Indiana University and use a somewhat more complicated technique than that described above. Instead of using a single reference configuration (i.e., the HF configuration) to form the remaining electron configurations, multiple reference configurations are employed. These reference configurations are chosen by performing an initial CISD calculation and identifying those configurations that have significant expansion coefficients. A second CI calculation is then performed in which all single and double excitations from the reference configurations are included. As a result, the calculation includes some configurations involving triple and quadruple excitations from the HF configuration. This is called a multi-reference single and double excitations CI (MRSD-CI) calculation.

Møller–Plesset perturbation theory

An alternative method of treating electron correlation is that introduced by Møller and Plesset [96], in which electron correlation is treated as a perturbation of the Hartree–Fock problem. The electronic Hamiltonian for the system is expressed as the sum of two operators

$$\hat{H}_\lambda = \hat{H}_0 + \lambda\hat{V} \tag{2.29}$$

where $\hat{H}_0$ is the sum of the one-electron Fock operators given by Equation (2.23), $\hat{V}$ is the difference between the correct electronic Hamiltonian $\hat{H}$ (Equation (2.16)) and $\hat{H}_0$, and λ is

a dimensionless parameter indicating the magnitude of the perturbation. The wavefunction and energy of the system are then expressed as power series in λ, that is

$$\Psi_\lambda = \sum_{i=0}^{\infty} \lambda^i \Psi_{(i)} \tag{2.30}$$

$$E_\lambda = \sum_{i=0}^{\infty} \lambda^i E_{(i)}. \tag{2.31}$$

Setting λ equal to 1, the Equations (2.30) and (2.31) give the exact wavefunction and energy of the system (in the limit of a complete basis set). This is equivalent to a full CI treatment. In Møller–Plesset perturbation theory, the two series above are truncated and the level of the theory is referred to by the highest-order energy term retained in expansion (2.31), i.e., MP2, MP3, etc.

$\Psi_{(0)}$ of Equation (2.30) is the HF wavefunction; $E_{(0)}$ is the sum of the individual HF orbital energies (ϵ_i of Equation (2.22)) and $E_{(0)}+E_{(1)}$ is the HF energy. First-order and higher terms of Equation (2.30) consist of electron configurations formed by excitations from the HF configuration, as also appeared in the CI expansion of the electronic wavefunction discussed in the previous section. The MP calculations performed for this thesis are second order (i.e., MP2), the lowest order that accounts for some electron correlation. At the MP2 level, only configurations involving double excitations from the HF configuration contribute to the MP expansion of the wavefunction. Configurations involving other excitations (e.g., singles and triples) do not appear until the MP4 level. The MP2 method is an efficient means of partially accounting for electron correlation effects, requiring only a single step following the iterative determination of the HF wavefunction. However, it has the disadvantage of being non-variational, so that the resulting energy is not an upper bound on the true energy of the system. Also, perturbation theory tends to converge slowly and oscillate with order [95], so results calculated to different orders can differ significantly.

2.3.3 Density functional theory

An alternative approach to problems of molecular electronic structure is provided by density functional theory. In contrast to the wavefunction-based electronic structure theories discussed in the preceding sections, DFT is based upon the electron density distribution $\rho(\mathbf{r})$. Although DFT has been used by physicists for several decades to describe the electronic structure of solids, the developments necessary for the routine application of DFT to chemical problems have only occurred in the past decade or so. Despite this, the computational advantages of DFT over the more traditional methods of quantum chemistry discussed above have resulted in a rapid growth in research concerning chemical applications of DFT.

The foundation of DFT was laid by Hohenberg and Kohn [97], who showed that the total energy of a system of n interacting electrons (e.g., the electronic energy of an n-electron molecule) can be expressed (as can many other properties) as a functional of the electron density. Furthermore, analogous to the variational theorem discussed in Section 2.3.1, Hohenberg and Kohn showed that for any arbitrary electron density chosen for a system, the corresponding total energy is an upper bound of the ground-state energy of the system.

Subsequent work by Kohn and Sham [98] provided the framework necessary to make DFT a computationally practical technique. They considered a model system of n non-interacting electrons having a total density equal to the true electron density of the system (of interacting electrons) of interest. As in HF theory, in Kohn–Sham DFT the motions of the independent electrons are described by one-electron functions, in this case the Kohn–Sham orbitals ψ^{KS}. Thus, the total density can be written as

$$\rho(\mathbf{r}) = \sum_{i=1}^{n} \left|\psi_i^{\mathrm{KS}}(\mathbf{r})\right|^2 . \tag{2.32}$$

Integration of $\rho(\mathbf{r})$ over all space gives n, the total number of electrons in the system. Although Kohn and Sham introduced the orbitals ψ^{KS} purely as a computational convenience,

recent work by Casida [90] and Duffy et al. [20] discussed in Section 2.2.4 above indicates that they are of considerable significance to EMS. The total energy in Kohn–Sham DFT is [68]

$$E[\rho(\mathbf{r})] = T_{\mathrm{s}}[\rho(\mathbf{r})] + \int v(\mathbf{r})\rho(\mathbf{r})d\mathbf{r} + J[\rho(\mathbf{r})] + E_{\mathrm{xc}}[\rho(\mathbf{r})] \tag{2.33}$$

where the four terms contributing to the total energy of the non-interacting system with density $\rho(\mathbf{r})$ are respectively the kinetic energy of the system, the potential energy resulting from the interactions between the external field $v(\mathbf{r})$ and the density, the classical Coulomb repulsion and the exchange–correlation energy. For a free molecule in the absence of any external fields, $v(\mathbf{r})$ is the field of the nuclei, given by the second term of Equation (2.16). The exchange–correlation functional $E_{\mathrm{xc}}[\rho(\mathbf{r})]$ is defined to be the functional necessary for E of (2.33) to be the true ground-state energy of the system. The first three terms of Equation (2.33) have equivalent terms in the expression for the HF energy (Equation (2.18)) and if $E_{\mathrm{xc}}[\rho(\mathbf{r})]$ is replaced by the HF exchange energy defined by Equations (2.18) and (2.21) then Equation (2.33) is simply a different formulation of the HF electronic energy expression. Minimization of $E[\rho(\mathbf{r})]$ with respect to the Kohn–Sham orbitals yields the Kohn–Sham equations

$$\hat{F}^{\mathrm{KS}}\psi_i^{\mathrm{KS}} = \epsilon_i\psi_i^{\mathrm{KS}} \tag{2.34}$$

where the operator $\hat{F}^{\mathrm{KS}}$ is [68]

$$\hat{F}^{\mathrm{KS}} = -\frac{1}{2}\nabla^2 + v(\mathbf{r}) + \int \frac{\rho(\mathbf{r}')}{\mathbf{r}-\mathbf{r}'}d\mathbf{r}' + v_{\mathrm{xc}}(\mathbf{r}) \tag{2.35}$$

and the exchange–correlation potential $v_{\mathrm{xc}}(\mathbf{r})$ is defined by

$$v_{\mathrm{xc}}(\mathbf{r}) = \frac{\delta E_{\mathrm{xc}}[\rho(\mathbf{r})]}{\delta\rho(\mathbf{r})}. \tag{2.36}$$

The similarity of the Kohn–Sham equations to the Hartree–Fock equations (2.22) and (2.23) is evident, the only difference being the presence of the exchange–correlation potential in the

KS equations in place of the exchange operator in the HF equations. As is the case in HF theory, the Kohn–Sham equations are solved iteratively for ψ_i^{KS} and ϵ_i until self-consistency is achieved. The Kohn–Sham orbitals are typically expressed as linear combinations of atomic orbitals in a manner analogous to that described in Section 2.3.1 for the HF orbitals, so determination of the Kohn–Sham orbitals consists of choosing a basis set and determining the corresponding set of orbital coefficients.

Despite the obvious similarities between the Kohn–Sham and the Hartree–Fock equations, they differ in a significant manner: the Kohn–Sham equations are in principle exact while the HF equations are not. In order to realize this "exactness", the exact exchange–correlation functional $E_{\mathrm{xc}}[\rho(\mathbf{r})]$ must be used. The form of this functional is not known so approximations for $E_{\mathrm{xc}}[\rho(\mathbf{r})]$ are used, thereby introducing errors into the theory. Much of the research activity concerning DFT has involved the derivation and assessment of exchange–correlation functionals. Several commonly used functionals, employed for the work presented in this thesis, are described below.

Exchange–correlation functionals

The simplest exchange–correlation functionals make use of the local spin-density approximation (LSDA), in which $E_{\mathrm{xc}}[\rho(\mathbf{r})]$ is taken to be equal to the exchange–correlation energy of a homogeneous electron gas of density ρ. This may seem a drastic approximation for molecules, where the electron density can vary considerably, and indeed calculations using the LSDA seriously overestimate the binding of atoms in molecules. However, the LSDA does provide reasonably accurate structural properties and consequently has been applied to many chemical problems. The formulation of the LSDA exchange–correlation functional used in this thesis is that recommended by Vosko, Wilk and Nusair [99].[3] They use the an-

[3]This is the functional selected using the keyword LOCAL in the *deMon* [100, 101] density functional program and SVWN5 in the GAUSSIAN92 [102] and GAUSSIAN94 [103] programs.

alytic expression derived by Dirac [104] for the exchange energy of a homogeneous electron gas and a function obtained by a least-squares fit to the results of Monte Carlo calculations of homogeneous electron gases of various densities for the correlation energy. This separation of the exchange–correlation energy into separate exchange and correlation terms is common to all of the functionals discussed here.

Several exchange and correlation functionals have been developed that improve upon the LSDA by introducing a dependence on the gradient of the density in addition to that on the density itself. This is known as the generalized gradient approximation (GGA) [68]. A key feature addressed in the development of these functionals is the overestimation of atomic binding energies mentioned above. This overbinding is a consequence of the incorrect asymptotic form of the LSDA exchange potential. The potential v_{x} (obtained from E_{x} via Equation (2.36)) falls off too rapidly with r, so that electrons at large r experience a greater Coulomb repulsion than they should, causing the outer-most regions of the electron density distribution to be too diffuse. The gradient-corrected exchange functional proposed by Becke in 1988 [105] has been constructed such that E_{x} has the correct asymptotic form and results in much-improved calculated thermochemical properties. It should be noted, however, that having the correct asymptotic form for the exchange energy E_{x} does not ensure that the same is true for the exchange potential v_{x}. Also, this functional contains one semiempirical parameter, set by performing a fit to exact atomic HF data [105]. The Becke '88 functional is the gradient-corrected exchange functional that has been used in this thesis. Two gradient-corrected correlation functionals have been used in this thesis: Perdew's 1986 functional [106] and that of Lee, Yang and Parr [107]. In general, gradient corrections to the correlation energy have been found to be of lesser significance than those to the exchange energy [68].

A third class of functional has recently been proposed which is a hybrid of the GGA functionals and the HF exchange energy and which is generally of greater accuracy than the

GGA functionals alone. The most widely used hybrid functional is Becke's three-parameter functional [108], in which the relative contribution of the HF exchange energy to the total exchange energy was determined by a fit to experimental thermochemical data. For the work in this thesis, a popular variant of Becke's three-parameter functional has been used in which the gradient-corrected correlation functional of Perdew and Wang [109] has been replaced by that of Lee, Yang and Parr [107].

2.3.4 Basis sets

All of the electronic structure methods discussed in the preceding sections make use of a basis set expansion to express the molecular wavefunction (in the case of the HF and post-HF methods) or the electron density (in the case of DFT). The use of a finite basis set for this expansion, although necessary for practical reasons, introduces an additional level of approximation (and therefore source of error) into the calculations. The magnitude of this error can be minimized by choosing the basis functions carefully. A large number of basis sets of widely varying size and accuracy have been described in the literature. The choice of basis set for a particular calculation is influenced by the size of the system being studied, the available computational resources, the theoretical method employed, the properties to be calculated and the level of accuracy required. This choice becomes increasingly limited as the size of the molecule increases, thereby necessitating trade-offs between accuracy and tractability.

One of the goals of this thesis is to assess the sensitivity of calculated momentum-space electron density profiles to computational method and basis set. It is hoped that this may provide additional information to aid in the choice of basis set for the calculation of other chemical properties of similar molecules. Consequently, theoretical momentum profiles for comparison with the experimental data have been obtained from electronic structure calcu-

lations using a range of basis sets.

All of the basis sets considered here are composed of functions centred on each nucleus, with the specific functions used dependent upon the respective atomic number (i.e., nuclear charge). The functions are chosen such that they have the same symmetry properties as atomic orbitals and are classified as s, p, d,... according to these properties. Basis sets typically consist of either Slater or Gaussian functions. Slater functions have an exponential dependence $\exp(-\zeta r)$ on the radial distance r. The exponent ζ determines the size (spatial extent) of the orbital. Gaussian functions have an exponential dependence on the *square* of the radial distance: $\exp(-\zeta r^2)$. Slater functions are better choices to represent atomic orbitals because they have the correct form at the nucleus (a cusp). For this reason, they are commonly used for electronic structure calculations of atoms. However, Gaussian functions are commonly used for calculations of molecules because all of the multi-centre integrals can be evaluated analytically; this is not possible using Slater functions. To minimize errors resulting from the incorrect shape of Gaussian functions, a linear combination of Gaussian functions with different exponents ζ is often used to form one basis function. The individual Gaussian functions are then referred to as primitive Gaussian functions and the resulting basis function as a contracted Gaussian function (CGF). All of the basis sets used in this thesis consist of Gaussian functions. Those common to all of the studies performed are described below. The information is summarized in Table 2.1. Further discussion of Gaussian basis sets can be found in Reference [94].

STO-3G The STO-3G basis set designed by Pople and co-workers [110] is a minimal basis set in which each basis function is a linear combination of three Gaussian functions. The coefficients and exponents of the primitive Gaussians are determined by a least-squares fit to a Slater function. Minimal basis sets are often described as *single-*ζ (single-zeta) basis

Table 2.1: Basis sets utilized for electronic structure calculations. In addition to the basis sets listed, others formed by augmenting the 6-31G and 6-311G basis sets with diffuse (+,++) and polarization (*,**) functions have been used.

Name	Ref.	Primitive functions (C, N and O/H)	Contracted functions [C, N and O/H]
STO-3G	[110]	(6s,3p/3s)	[2s,1p/1s]
4-31G	[111]	(8s,4p/4s)	[3s,2p/2s]
6-31G	[111, 112]	(10s,4p/4s)	[3s,2p/2s]
6-311G	[113]	(11s,5p/5s)	[4s,3p/3s]
aug-cc-pVTZ	[114, 115]	(11s,6p,3d,2f/6s,3p,2d)	[5s,4p,3d,2f/4s,3p,2d]
augmentations[a]			
**	[116]	(1d/1p)	[1d/1p]
++	[117]	(1s,1p/1s)	[1s,1p/1s]

[a]Used with the 6-31G and 6-311G basis sets to form, e.g., the 6-31G** and 6-311++G** basis sets.

sets because they are equivalent to using a single Slater function for each atomic orbital. For example, a minimal basis set for the hydrogen atom consists of a single s-type basis function and for carbon, nitrogen or oxygen consists of two s-type functions and one set of three p-type functions. The lack of flexibility in minimal basis sets typically leads to inaccuracies in describing the electronic structure of molecules.

4-31G This basis set [111] is an example of a *split-valence* basis set, in which the valence atomic orbitals are each represented by multiple basis functions. The basis set label is derived from the number of primitive Gaussians used for each CGF, with the number before the dash referring to core AOs and the numbers following the dash referring to the valence AOs. In the case of the 4-31G basis set, one CGF consisting of three primitive Gaussians and a second consisting of a single (uncontracted) Gaussian are used for each valence atomic orbital, e.g., the 1s orbital in the case of hydrogen and the 2s and three 2p orbitals for carbon, nitrogen and oxygen. This is also referred to as *valence double-zeta.* The use of multiple basis functions with different exponents to describe the valence electrons helps to

account for the perturbation of the electron density that may occur upon the formation of molecular bonds by allowing the electron density about a nucleus to expand or contract. This perturbation is much smaller in the case of the core electrons and consequently the core description has been kept at single-zeta quality in the 4-31G basis set. The use of four primitive functions to describe the core rather than the three used in the STO-3G basis set allows for a more accurate representation of the shape of these orbitals near the nucleus, resulting in lower SCF energies.

6-31G The 6-31G basis set [111, 112] is very similar to the 4-31G basis set described above, differing however in the number of primitive functions used to form the core AO basis functions. As a result, total energies obtained with the 6-31G basis set are lower than those obtained using the 4-31G basis set but properties that depend primarily upon the valence electrons differ by a much smaller amount.

6-311G This valence triple-zeta basis set [113] features increased flexibility for the description of the valence orbitals. It forms the basis of the 6-311G** basis set (see polarization functions, below) which, in contrast to the basis sets described above, has been optimized for use in correlated calculations (specifically MP2).

Polarization functions Frequently, basis sets are augmented to include functions of higher angular quantum number than is necessary to describe the atoms in their ground electronic states. For example, p-type basis functions are added to hydrogen and d-type functions to carbon. These augmentations are called polarization functions because they allow for the polarization of electron density. This is particularly important for the accurate description of the electronic structure of highly polar molecules [94]. Augmentations of the above basis sets by the minimal set of polarization functions on all non-hydrogen (*heavy*)

atoms are commonly identified by an asterisk (*) following the "G" in the basis set name. If (p-type) polarization functions are also added to the hydrogen atom basis, two asterisks are used (**). Alternatively, the functions added may be stated more explicitly by their atomic symmetry labels with the heavy-atom polarization functions stated first by convention. For example, the 6-31G** basis set, consisting of the 6-31G basis set augmented by a set of d-type polarization functions on heavy atoms and p-type polarization functions on hydrogens, may also be referred to as 6-31G(d,p). This notation is commonly employed when polarization functions beyond the minimum set are added. In this thesis, * and ** denote the polarization functions recommended by Pople and co-workers [116].

Diffuse functions A second common augmentation is the addition of highly diffuse functions (i.e., having small exponents) to the basis set. Such functions are necessary for the accurate description of the large-r (long-range) electron density and are important for calculations of anions and molecules involving long-range interactions (e.g., hydrogen bonds) as well as for the calculation of properties highly dependent upon the outermost regions of electron density such as electron affinities and outer-valence-orbital momentum profiles. The addition of a single s-type diffuse function and a set of three p-type diffuse functions [117] to the above-described basis sets for heavy atoms is denoted by a single "+" preceding the "G" in the basis set name. The further addition of diffuse s-type functions to the hydrogen atom basis is denoted by a double plus "++".

aug-cc-pVTZ This basis set of Dunning and co-workers [114, 115] is a polarized valence-triple-zeta basis set (cc-pVTZ) augmented with diffuse functions (aug-). It has been developed to give accurate results for calculations including electron correlation effects and includes f-type functions on heavy atoms and d-type functions on hydrogen.

2.4 Molecular conformation

The size and conformational mobility of the molecules studied in this thesis introduces several complications that have generally not been present in the analysis of EMS experiments on smaller molecules. The common practice in EMS studies has been to make use of experimental molecular geometries when calculating theoretical momentum profiles for comparison with the corresponding experimental profiles. Such experimental geometries are readily available in the literature for most small gas-phase molecules. However, this is often not the case for molecules of the size studied in this thesis (10+ atoms). The number of independent geometrical parameters in these larger molecules makes the complete experimental determination of geometries considerably more challenging. In most cases, only partial experimental geometries, in which some parameters have been assumed to equal "standard" values, are available. Furthermore, the conformational mobility of these molecules results in the possibility of multiple stable conformational isomers (conformers) contributing to the observed experimental signal. It then becomes necessary, when calculating TMPs for comparison with the experimental data, to consider all likely conformers. This requires knowledge not only of the geometries of all stable conformers but also of their relative energies, so that the contributions to the total observed signal from individual conformers can be weighted appropriately by their relative abundances in the experimental sample. As a consequence of the incomplete availability in the literature of experimental conformer geometries and relative energies for the molecules studied, theoretical predictions have been used. A brief overview of the standard procedures that have been used for calculating the theoretical geometries and free energies follows.

2.4.1 Geometry optimizations

The *potential energy surface* of a molecule describes the molecule's total energy as a function of the relative nuclear coordinates (i.e., the molecule's geometry). An electronic structure calculation at a fixed geometry yields one point on this surface. The purpose of geometry optimization calculations is to find those sets of relative nuclear coordinates that correspond to minima on the potential energy surface; these are *equilibrium structures.* Simple molecules usually have a single energy minimum; more complicated molecules can have several. The geometry optimization procedure is a multi-step process in which an input geometry is varied so as to minimize the total energy of the molecule. An electronic structure calculation is performed at the initial geometry (using, for example, one of the methods discussed in Section 2.3). This is followed by calculation of the energy gradient, i.e., the first derivative of the energy with respect to displacements of the nuclei. If the gradient is less than a previously chosen threshold, then a *stationary point* has been located on the potential energy surface and the calculation is stopped. Otherwise, the geometry is modified using the forces on the nuclei determined from the gradient calculation and the process is repeated using the new geometry.

The stationary-point geometry determined from a geometry optimization calculation is not necessarily an energy minimum; it may instead correspond to a saddle point on the potential energy surface. A saddle point is an energy minimum with respect to variation of some relative nuclear coordinates and an energy maximum with respect to variation of others. Stationary points can be characterized as energy minima or saddle points by calculating normal-mode vibrational frequencies from the second derivative of the energy at the stationary-point geometry. If the geometry is a true minimum, the calculated vibrational frequencies will all be real. Transition structures (saddle points) are characterized by one or more imaginary vibrational frequencies.

Performance of a geometry optimization calculation and characterization of the stationary point to verify that an energy minimum has been found does not ensure that the *global* minimum on the potential energy surface has been located. For molecules with a large number of geometrical parameters, it may be necessary to perform many geometry optimization calculations using different starting points (initial geometries) in order to maximize the likelihood that all equilibrium structures (conformers) are located. This can require a considerable amount of computational resources, especially if the molecule and basis set are large and the electronic structure method used is a costly one. Rather than sampling all regions of conformational space, the number of initial geometries considered is often limited to those thought likely to be near energy minima on the potential energy surface. Finally, it is important to note that the potential energy surface and the equilibrium structures derived from it depend not only on the molecule but also on the basis set and theoretical method used for the energy calculations. In some cases, a minimum-energy conformation obtained at one level of theory may be a transition structure at a different level of theory.

2.4.2 Relative conformer energies

In an EMS experiment on a conformationally mobile molecule, each stable conformation present in the experimental sample will contribute to the observed EMS signal in proportion to its relative abundance in the sample. Thus, the observed signal will be the sum of the individual signals arising from each conformer, weighted by the respective fractional populations of the conformers. The fractional conformer populations p_i at temperature T are described by a Boltzmann distribution

$$p_i = \frac{g_i e^{-G_{i,T}/RT}}{\sum_j g_j e^{-G_{j,T}/RT}} \tag{2.37}$$

where $G_{i,T}$ is the Gibbs free energy of conformer i at temperature T, g_i is the degeneracy of conformer i and $\sum_j$ is a sum over all conformers.

The energy obtained from an electronic structure calculation is not the free energy of a conformer but rather corresponds to the energy E_0 of an isolated molecule with stationary nuclei at 0 kelvin. The contributions of the zero-point vibrational energy E_{zpv}, the enthalpy change $\Delta H(T)$ from 0 K to T and the entropy S_T at T must be accounted for to determine G_T. Explicitly,

$$G_T = E_0 + E_{\text{zpv}} + \Delta H(T) - T \cdot S_T. \tag{2.38}$$

$E_0 + E_{\text{zpv}}$ is H_0, the enthalpy at 0 K, which when summed with $\Delta H(T)$ gives H_T, the enthalpy at temperature T.

Statistical mechanics provides the techniques necessary to calculate these thermodynamic quantities knowing the normal-mode vibrational frequencies and equilibrium geometry of the conformer[4]. The zero-point vibrational energy per mole is

$$E_{\text{zpv}} = \frac{1}{2} N h \sum_i \nu_i \tag{2.39}$$

where ν_i is the vibrational frequency of normal mode i, N is Avogadro's number, h is Planck's constant and the sum is over all normal modes of the conformer. The thermal enthalpy change $\Delta H(T)$ can be written as the sum of contributions from translational, rotational and vibrational degrees of freedom. The individual terms for non-linear molecules are

$$\Delta H_{\text{trans}}(T) = \frac{5}{2} RT \tag{2.40}$$

$$\Delta H_{\text{rot}}(T) = \frac{3}{2} RT \tag{2.41}$$

$$\Delta H_{\text{vib}}(T) = R\Theta_{\nu_i} \left(e^{\Theta_{\nu_i}/T} - 1 \right)^{-1} \tag{2.42}$$

[4]The relationships used assume ideal-gas behaviour and the validity of the harmonic oscillator and rigid rotor approximations and are derived in many texts. See for example McQuarrie [118] or Mayer [119].

where R is the gas constant and Θ_{ν_i} is the *vibrational temperature* for the normal-mode vibrational frequency ν_i, given by

$$\Theta_{\nu_i} = \frac{h\nu_i}{k} \tag{2.43}$$

where k is Boltzmann's constant. The PV work term has been included in $\Delta H_{\text{trans}}(T)$. The entropy can also be partitioned into translational, rotational and vibrational terms:

$$S_{\text{trans},T} = R \ln \left[\left(\frac{2\pi MkT}{h^2} \right)^{3/2} \frac{Ve^{5/2}}{N} \right] \tag{2.44}$$

$$S_{\text{rot},T} = R \ln \left[\left(\frac{\pi^{1/2} e^{3/2}}{\sigma} \right) \left(\frac{T^3}{\Theta_A \Theta_B \Theta_C} \right)^{1/2} \right] \tag{2.45}$$

$$S_{\text{vib},T} = R \sum_i \left[\frac{\Theta_{\nu_i}}{T} \left(e^{\Theta_{\nu_i}/T} - 1 \right)^{-1} - \ln \left(1 - e^{-\Theta_{\nu_i}/T} \right) \right] \tag{2.46}$$

where M is the mass of the molecule, V/N is the average volume occupied per molecule (an inverse density), Θ_A is a *rotational temperature* derived from the rotational constant $\bar{A}$:

$$\Theta_A = \frac{h\bar{A}}{k} \tag{2.47}$$

and σ is a *symmetry number* determined by the symmetry of the conformer. There is an additional contribution to S_T if the ground electronic state is degenerate. This is not the case for any of the molecules considered in this thesis.

The form of Equation (2.37) is such that it is not necessary to calculate the *absolute* free energies G_T of the conformers; the *relative* conformer free energies ΔG_T are sufficient to determine the fractional conformer populations. Therefore, all terms contributing to Equation (2.38) that are invariant between conformers can be neglected. These terms are $\Delta H_{\text{trans}}(T)$, $\Delta H_{\text{rot}}(T)$ and $S_{\text{trans},T}$. In the remainder of this thesis, all thermodynamic quantities are reported relative to those of the most stable conformer.

Chapter 3

Experimental Methods

All of the experimental EMS data reported in this thesis were obtained using a multichannel energy-dispersive electron momentum spectrometer constructed as part of this project. The spectrometer design is based upon that of a similar instrument developed at the Flinders University of South Australia [16–18]. The main features of the spectrometer as well as the procedures used for the collection and treatment of the experimental data are described below.

3.1 Multichannel energy-dispersive electron momentum spectrometer

The multichannel energy-dispersive electron momentum spectrometer constructed in the course of the present work is shown schematically in Figure 3.1. The spectrometer is housed within a 60 cm diameter cylindrical aluminum vacuum chamber. Two Seiko-Seiki TMP 450 Maglev turbomolecular pumps are used to maintain vacuum in the main chamber. A TMP 300 Maglev turbomolecur pump (located directly behind the electron gun shown in Figure 3.1) differentially pumps the electron gun, reducing the amount of sample that reaches

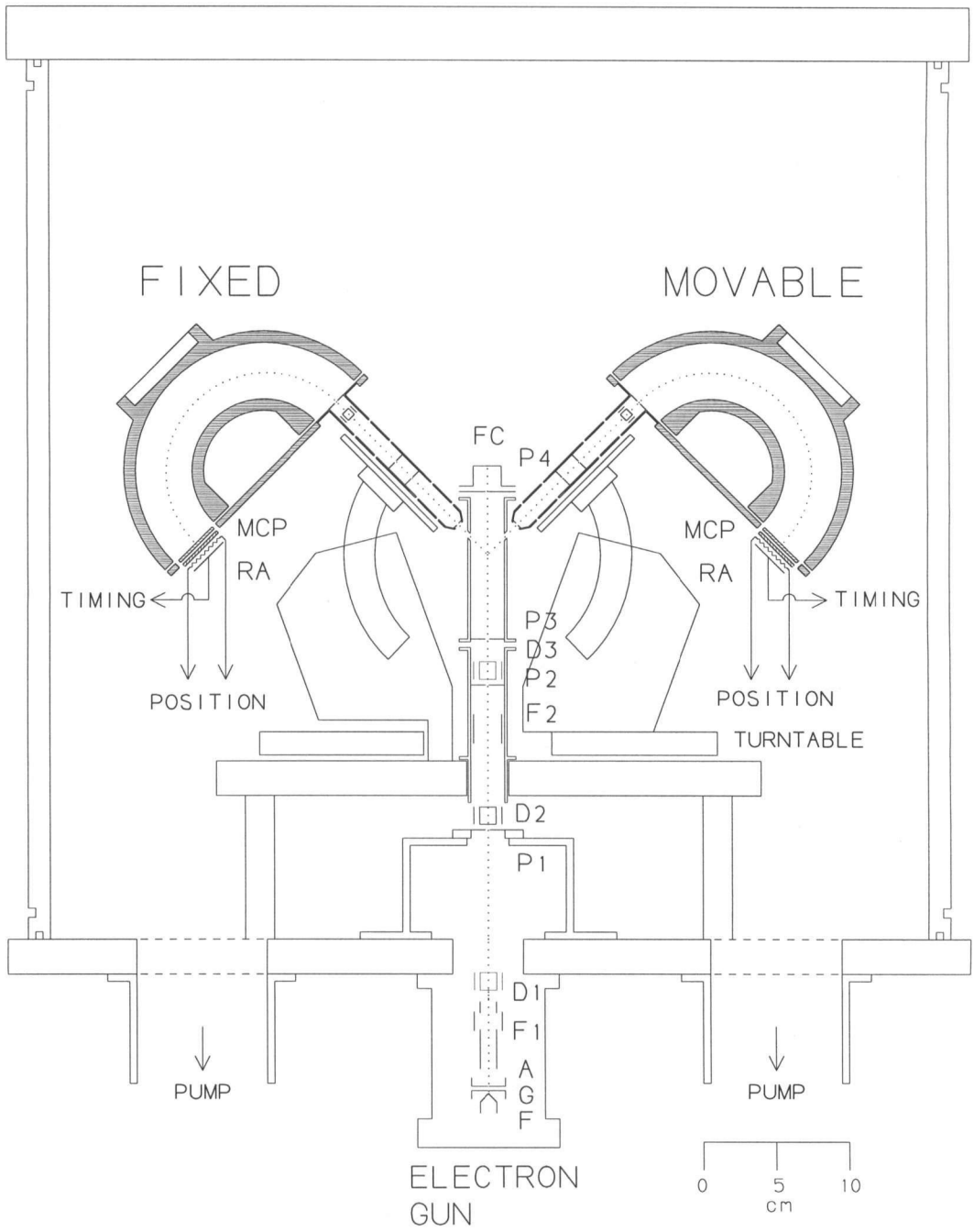

Figure 3.1: Schematic diagram of the energy-dispersive multichannel electron momentum spectrometer constructed and used in the present work. The polar angles θ of the two analysers are kept fixed at 45° and the out-of-plane azimuthal angle ϕ of the movable analyser is varied. The labels used are: F, filament; G, grid; A, anode; F1 and F2, electron lenses; D1–D3, parallel plate quadrupole deflectors; P1–P4, spray plate apertures; FC, Faraday cup; MCP, microchannel plates; RA, resistive anode.

the electron gun filament and thereby prolonging the lifetime of the filament. The output ports of the three turbomolecular pumps are connected to a common backing line that is maintained at a pressure of $\approx 10^{-2}$ torr using a rotary pump. Base pressures of 10^{-7} torr in both the main chamber and the electron gun region are achieved. The vacuum chamber is lined with hydrogen annealed mumetal shielding to reduce the magnetic field in the centre of the spectrometer (horizontal field $\approx$ 30 mGauss after shielding) and hence minimize perturbation of the electron trajectories.

Electron momentum spectroscopy experiments require a source of energetically and directionally well defined electrons. In the case of the spectrometer constructed and utilized in the current work, the electron beam originates from an electron gun mounted underneath the base plate of the spectrometer and is directed upwards through the interaction region in the centre of the instrument. The electrons are produced by a dirrect-current-heated thoriated tungsten wire (diameter 0.05 mm) filament (F in Figure 3.1) and are accelerated and focussed using a commercial electron gun body[1], consisting of a grid (G), anode (A) and electron lens (F1). The interaction region of the spectrometer is at ground potential and the electron gun filament is floated at the negative potential corresponding to the desired electron energy, which under typical operating conditions is 1200 eV greater than the electron binding energy being monitored. A second electron lens (F2) located approximately midway between the electron gun and the interaction region is used to further focus the incident electron beam. Three sets of parallel plate quadrupole deflectors (D1–D3) are used to align the electron beam, which is monitored via four spray plate apertures (P1–P4) and a Faraday cup (FC).

All gaseous samples and most that are liquid at room temperature are introduced into the spectrometer using a gas line connected to the side of the interaction region. The sample

[1] Cliftronics CE5AH

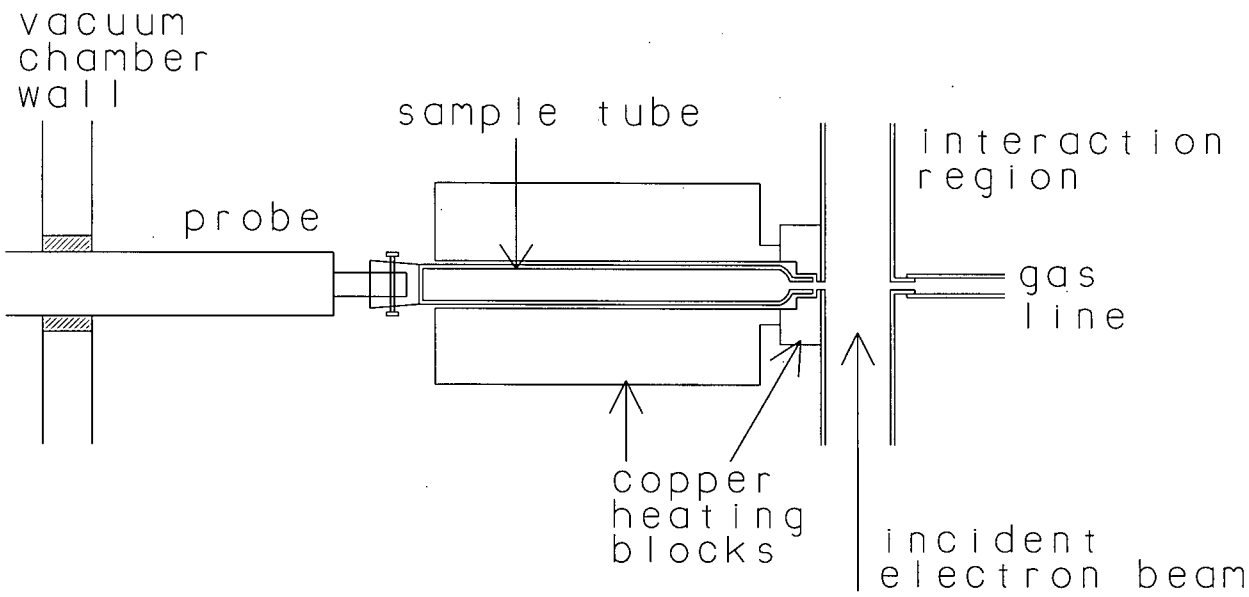

Figure 3.2: Direct probe heated sample system for use in performing EMS measurements on low vapour pressure liquids and solids. The line used for the introduction of gaseous samples to the spectrometer is also shown. (Not to scale.)

vessels are connected to a sample vacuum manifold evacuated by a dedicated rotary pump. A variable leak valve is used to control the sample pressure in the spectrometer. To allow for the study of substances that exist as solids or low vapour pressure liquids at room temperature, a heated sample probe has also been constructed. A schematic diagram of the sample probe and gas line is shown in Figure 3.2. The view shown is perpendicular to that of Figure 3.1. The solid sample is placed in a Pyrex tube which is attached to the end of a metal probe and inserted through a vacuum lock in the wall of the spectrometer vacuum chamber. This allows sample replacement without removing the vacuum chamber and while maintaining a partial vacuum, thus considerably decreasing the delay between data collection periods. The Pyrex tube rests in the spectrometer in a non-inductively wound electrically heated copper block adjacent to the experimental interaction region. A second heating block surrounds the tip of the sample tube, allowing separate temperature control of this area. The temperatures are monitored by thermocouples attached to the copper blocks. In this way, a solid sample

can be vapourized directly into the interaction region, providing a stable gas target density over a period of several days. In the case of some high vapour pressure solids, the proximity of the sample tube to the interaction region results in sufficient target density for EMS measurements without heating of the sample [69].

The two outgoing electrons produced by the electron impact ionization of a target atom or molecule (i.e., one scattered electron and one ejected electron) are each angle and energy selected and detected using hemispherical analysers [120] of mean radius 70 mm. The polar angles of the two analysers (θ in Figure 2.1) can be varied over the range $45 \pm 5°$. Variation of θ is necessary for the study of the lower momentum regions ($p < 1.0$ au) of the momentum profiles of core (IP $>$ 250 eV) electrons (see Equation (2.5)). For valence orbital studies, including all work reported in this thesis, the polar angles of the two analysers are fixed at 45°. The azimuthal position of one of the analysers is also fixed. The second analyser is mounted on a rotatable turntable driven by a computer-controlled stepper motor, allowing the out-of-plane azimuthal angle of the two analysers (ϕ in Figure 2.1) to be varied over a range of $\pm 50°$ and thereby varying the electron momentum that is monitored.

To be detected, electrons must first pass through one of the five-element electron lenses at the entrance of each analyser. These lenses act as two zoom lenses [121], the first defining the acceptance angle and thus the angular resolution of the spectrometer and the second decelerating the electrons. By decelerating the electrons prior to energy analysis, a lower pass energy (typically 50 eV) can be used for the hemispherical analysers, resulting in improved energy resolution. The hemispherical analysers (inner radius 50 mm, outer radius 89 mm) linearly disperse the electrons according to their input energies along the radial direction of the exit plane. One dimensional position sensitive detectors located at the exit plane of each analyser allow the determination of the radial position, and thus the energy, of each detected

electron. Each detector consists of a pair of 25 mm diameter microchannel plates[2] in the double chevron configuration [122] and a Gear type resistive anode [123]. The microchannel plates are operated in the pulse saturated counting mode.

3.2 Instrument electronics

The electronics used for processing the signals from each detector and for controlling the spectrometer are shown schematically in Figure 3.3. The signal processing electronics perform two tasks: screening of the data on the basis of the time correlation between signals received at the two detectors, and determination of the positions at which the electrons strike the detectors, and hence their kinetic energies. In Figure 3.3, the position electronics are shown in the upper portion of the figure and the timing electronics in the lower portion. The time correlation between the two signals is used to determine if the two electrons were detected in coincidence, a necessary condition if they are the result of the same EMS scattering event (i.e., an ionization with both outgoing electrons having approximately equal energies). Accidental coincidences are also detected (see Section 3.2.2 below).

3.2.1 Position electronics

A single electron reaching one of the detectors is amplified on the order of 10^6 times by the cascade effect of the microchannel plates, causing a charge pulse to strike the resistive anode. Output pulses are taken from both ends of each resistive anode (labelled in Figure 3.3 as A_M and B_M and A_F and B_F, referring to pulses originating from the movable and fixed analyser detectors, respectively) and are amplified by preamplifiers (PRE) and amplifiers (AMP).[3] The amplitudes of the A and B pulses from each detector are indicative of where on the resis-

[2]Electro Optical Sensors, VUW8946ZS
[3]Ortec 1421H and 855, respectively.

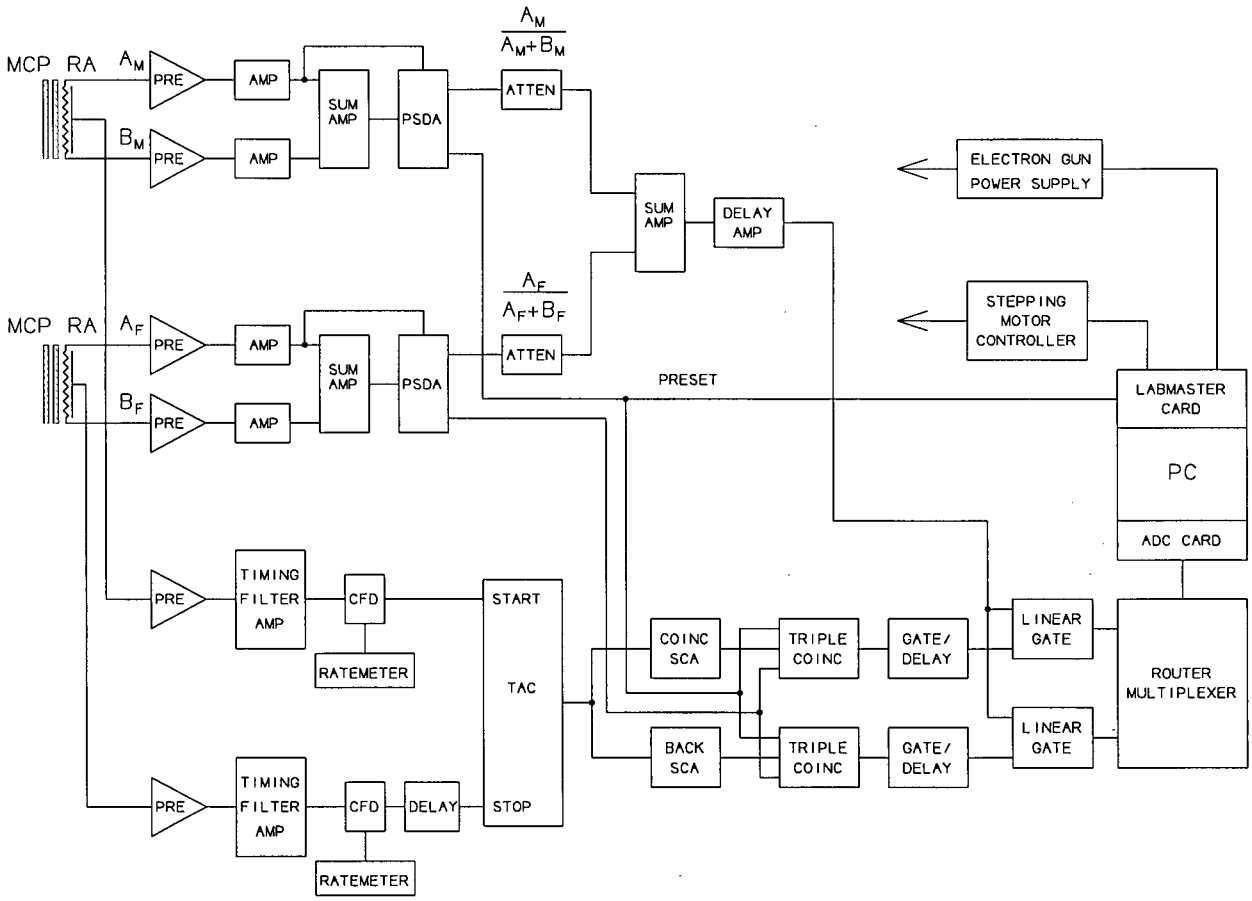

Figure 3.3: Schematic diagram of the position sensitive detectors and signal processing electronics. The detectors each consist of a pair of microchannel plates (MCP) and a resistive anode (RA). Other components illustrated are: PSDA, position sensitive detector analyser; CFD, constant fraction discriminator; TAC, time-to-amplitude converter; SCA, single channel analyser; ADC, analogue-to-digital converter computer card; PC, personal computer.

tive anode the charge pulse struck, since this will determine how much resistance (provided by the resistive anode) the pulse must pass through before reaching the position processing electronics. The A pulse and the sum of the two pulses (A+B, obtained using a summing amplifier (SUM AMP)[4]) are input to a position sensitive detector analyser (PSDA)[5], producing a voltage pulse (0–10 V) with amplitude $\frac{\mathrm{A}}{\mathrm{A+B}}$, proportional to the position on the detector where the electron struck. This pulse will have maximum amplitude if an electron strikes the end of the detector from which the A pulse is taken (B=0, $\frac{\mathrm{A}}{\mathrm{A+B}} = 1$) and minimum amplitude if an electron strikes the opposite end of the detector (A=0, $\frac{\mathrm{A}}{\mathrm{A+B}} = 0$). The A pulses are taken from the outer ends of the detectors (corresponding to greater electron energy) and the B pulses are taken from the inner ends (lesser electron energy). Consequently, the amplitude of the position pulse ($\frac{\mathrm{A}}{\mathrm{A+B}}$) is proportional to the energy of the detected electron (E) less the minimum detectable electron energy of the analyser/detector (E_{min}). That is: $\frac{\mathrm{A}}{\mathrm{A+B}} \propto E - E_{\mathrm{min}}$. The position pulses originating from each detector are then passed through an attenuator[6] and summed using a third summing amplifier, producing a pulse proportional in amplitude to the summed energy of the two detected electrons less the minimum detectable summed energy.

3.2.2 Timing electronics

Timing signals from each detector are taken directly from gold plated copper strip plates at the back of a ceramic plate behind each resistive anode and passed through a preamplifier and timing filter amplifier,[7] followed by a constant fraction discriminator (CFD)[8]. The CFD

[4]Two sum and invert amplifiers (Ortec 533) are used in succession to obtain a summed but not inverted output pulse.

[5]Ortec 464.

[6]Constructed by the UBC Chemistry Department Electronics Shop.

[7]Ortec 474

[8]Ortec 935.

only produces an output pulse when the amplitude of the input pulse is greater than a set threshold. This processing helps to eliminate spurious signals (i.e., "noise"). Ratemeters are used at this point to monitor the individual count rates of the two detectors (the "singles" rates). After delaying the timing signal from one of the detectors by a fixed amount ($\approx$ 30 ns), the two timing signals are passed to a time-to-amplitude converter (TAC)[9] to determine their time correlation. The TAC functions as a "stop-watch," producing an output pulse with amplitude proportional to the time between detection of the start and stop pulses. If two electrons arrive at the detectors in coincidence, the amplitude of the TAC output pulse will correspond to the fixed delay of the timing signal input to the TAC stop channel. A typical time spectrum, obtained from the output of the TAC, is shown in Figure 3.4. A constant amplitude background is obtained in the time spectrum as a result of the detection of uncorrelated electron pairs. To determine the amplitude of this background and thus make possible the correction for random coincidences in the coincidence peak (i.e., determine the number of true coincident events) single channel analysers (SCA)[10] are used to separate coincident and non-coincident events by setting coincidence and background windows (CW and BW, respectively, as illustrated in Figure 3.4). Further details of the background correction procedure are discussed in Section 3.4.3 below.

The SCA output and pulses from each of the PSDAs are entered into a triple coincidence unit (constructed by the UBC Chemistry Department Electronics Shop) to further reduce spurious signals. If a triple coincidence is detected, a linear gate[11] is opened and the summed position pulse enters a router/multiplexer[12]. Delay units[13] are used to ensure the timing and position pulses arrive at the linear gates concurrently. The router/multiplexer adds an offset

[9] Ortec 467.
[10] Ortec 550A and one SCA located on the TAC.
[11] Tennelec TC 310.
[12] Tennelec TC 306.
[13] Ortec 416A for the timing pulses and Ortec 427A for the position pulse.

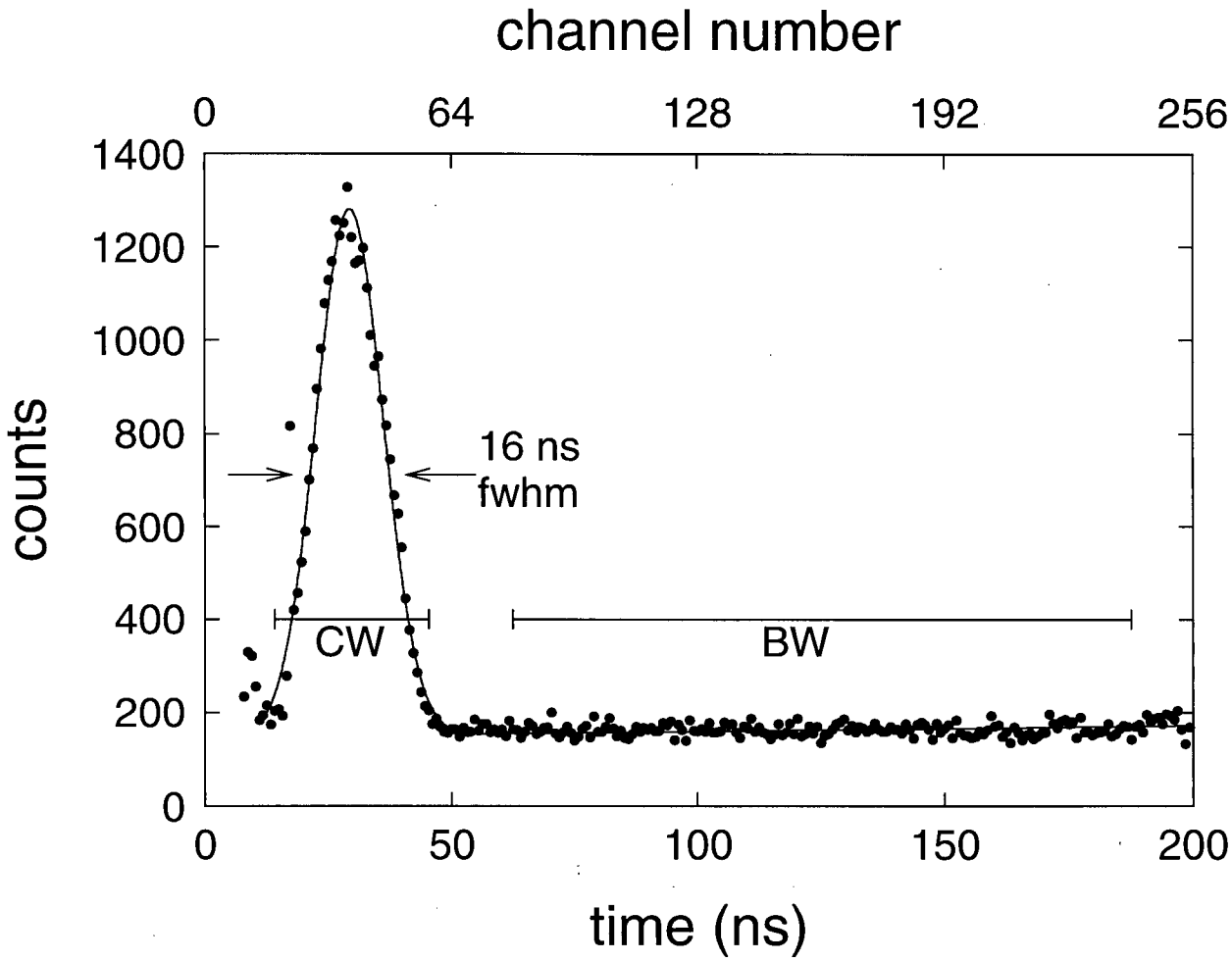

Figure 3.4: Sample time spectrum, collected by the ADC computer card from the output of the TAC. The coincidence (true + random coincidence events) and background (random events) windows, set using single channel analysers, are indicated (CW and BW, respectively). The data are from non-binning mode measurements (see Section 3.4) of the Ar $(3p)^{-1}$ ionization and were collected in 45 minutes.

to pulses coming through the "background" gate and produces an output pulse appropriately scaled for processing by a personal computer card analogue-to-digital converter (ADC)[14]. The ADC card divides the input voltage range into 512 equal-width channels, counts the number of pulses received in each channel and stores the data in memory on the card. As a consequence of the offset added by the router/multiplexer to pulses coming through the background gate, the first 256 ADC channels contain the coincident window pulses and the second 256 the background window pulses. Each of the ADC channels corresponds directly to a narrow range of total energy of the detected electron pair. The subsequent computer processing of the experimental data is described in Section 3.4 below.

A second computer card[15] is used to control the energy of the incident electron beam (via the electron gun power supply) and the azimuthal (ϕ) position of the movable analyser (via a stepping motor controller) and to count the number of processed position pulses originating from the movable analyser (PRESET in Figure 3.3). The PRESET is used to determine the amount of time spent collecting data at each angle ϕ and incident electron beam energy, so as to minimize the effects of small fluctuations in the electron beam intensity and the sample density.

3.3 Spectrometer calibration and operating conditions

The spectrometer is operated with a nominal total energy of 1200 eV. This corresponds to an incident electron energy of (1200 eV + binding energy) and nominal analyser detection energies of 600 eV. The five-element lens systems prior to the entrance of each analyser retard the electrons by 550 eV before entering the hemispherical analysers. The analyser pass energy is 50 eV, meaning that 50 eV electrons (600 eV prior to retardation) take

[14]Series II Personal Computer Analyzer, Nucleus, Inc.
[15]LabMaster DMA, Scientific Solutions, Inc.

the central trajectory through the analysers and strike the centre of the position sensitive detectors. The energy dispersive nature of the analysers allows electrons to be monitored over approximately an eight eV energy range, resulting in a detectable energy range of 600.0 ± 4.0 eV for each analyser. The total energy range monitored is thus 1200.0 ± 8.0 eV. Therefore, for an incident electron energy of 1200 eV + X, a binding energy range of X $\pm$ 8.0 eV is monitored simultaneously. As a consequence of contact potentials, in each EMS experiment there is a constant offset between the energy set by the incident electron beam power supply and the monitored electron binding energy. Energy scale calibration is performed by either introducing a small amount of a calibration gas into the spectrometer during data collection or by assigning the energy of a sharp peak in the BES to the IP determined using high-energy-resolution PES. Note that the relative energy separations of the EMS ionization peaks are not affected by this energy offset.

In the present work, an incident beam current of 25–30 μA (as measured by the Faraday cup) is used. A sample pressure of $\approx 10^{-5}$ torr (measured by an ion gauge on the main vacuum chamber) is used for samples that are gaseous at room temperature. With this combination of beam current and sample pressure, single count rates of $\approx$ 1500 Hz and a coincidence count rate of up to 40 true coincidences per minute are achieved.[16] In the case of the EMS measurements of glycine reported in this thesis, the solid sample was heated to a temperature (165°C) sufficient to produce single and coincident count rates comparable to those typically achieved for gaseous samples.

Prior to performing any EMS studies, a number of testing and calibration procedures must be undertaken to verify the proper operation of the spectrometer. The performance of each analyser is separately calibrated and tested to ensure a uniform response and linear

[16]The true coincidence count rate is dependent upon the target being ionized as well as the incident electron beam energy and out-of-plane azimuthal angle. The stated value was obtained from ionization of argon at a binding energy of 15.8 eV and an out-of-plane azimuthal angle of 8°, i.e., the maximum of the Ar 3p XMP.

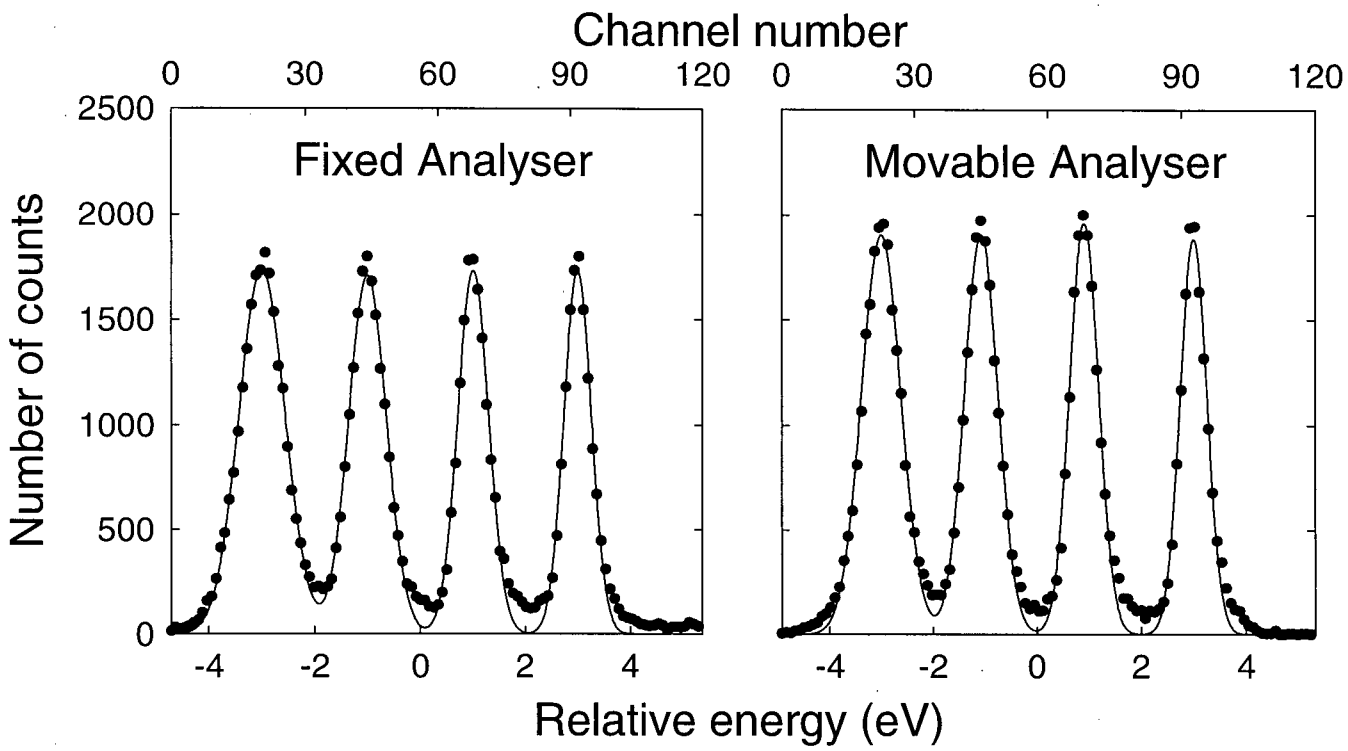

Figure 3.5: A typical test of electron analyser performance using incident electrons elastically scattered off argon. For each analyser test, incident electron energies of 597, 599, 601 and 603 eV were used. In addition to the experimental data (•), a fitted curve (—), obtained from a least-squares fit of Gaussian functions to the experimental data, is shown.

relationship between detected position and electron energy across the entire detected energy range. Also, the relationship between detected position and electron energy must be the same for each detector. The uniformity of the detector response is tested by monitoring the PSDA output ($\frac{A}{A+B}$) for each detector using typical operating conditions. A square response function should be obtained. The linear response and energy resolution of each analyser-detector assembly are tested using elastically scattered electrons produced with an incident electron beam energy of $\approx$ 600 eV. The results of a typical test are shown in Figure 3.5. The linear relationship between electron energy and detected position is evident. The analyser energy resolution is not constant across the tested energy range, with the resolution better

for the higher energy electrons that take an outer trajectory through the analysers. This is thought to be the result of non-uniform electric field lines at the analyser exit. It will not adversely affect spectrometer performance since coincident electron pairs will consist of electrons having all detectable energies with equal probability and the effect will therefore be averaged out. The analyser power supplies are very stable so consequently these tests of individual analyser performance need only be performed infrequently.

Before beginning each EMS experiment, calibration of the monitored total energy range is performed under normal operating conditions. This is done by collecting a BES using the ADC computer card. The He $(1s)^{-1}$ ionization peak is most commonly used for this purpose. The incident electron beam energy is initially set to correspond with the binding energy of the He $(1s)^{-1}$ peak (24.6 eV) and sufficient data is collected to determine accurately the data channel of the ADC card corresponding to the centre of the peak. The incident electron beam energy is then adjusted higher and then lower by a few eV and the resulting shifts in the ionization peak position (in terms of data channels of the ADC card) are noted. This information is then input to the data acquisition software to allow conversion from ADC data channel to electron binding energy.

The overall instrumental energy resolution function is determined by recording the BES of the He $(1s)^{-1}$ ionization peak at 24.6 eV or the Ar $(3p)^{-1}$ ionization peak at 15.8 eV. An energy resolution of 1.4–1.6 eV is typically achieved (see Figure 3.6 in Section 3.4, below). The angular resolution of the spectrometer is determined using the Ar 3p momentum profile. This profile is p-type, with the maximum occurring at 0.65 au. As a consequence of the symmetry of the orbital from which the electron is ionized, the Ar 3p XMP would have no intensity at zero momentum if recorded using a spectrometer having perfect angular resolution. In other words, the observation of any experimental intensity at $p = 0$ au is a consequence of the instrumental angular resolution. Instrumental angular resolution

parameters have been determined by a comparison of the Ar 3p XMP with a high quality CI calculation of the Ar 3p momentum profile [124] resolution-folded using the GW-PG method [48] and a range of values for the angular resolution parameters. The use in the resolution-folding procedure of values of $\Delta\theta = 0.6°$ and $\Delta\phi = 1.2°$ results in excellent agreement between the Ar 3p experimental and theoretical momentum profiles, as shown in the right panel of Figure 3.7 in Section 3.4.4. These angular resolution parameters have been used in the resolution-folding of TMPs performed in all subsequent studies.

Both the energy and angular resolutions of the spectrometer are monitored regularly to ensure that the spectrometer is operating properly and to determine the energy resolution for use in the data analysis. Calibration runs of Ar and He are customarily recorded prior to and following each molecular study and also following any adjustments to the electron beam and analyser settings. The ratio of the observed intensity at the maximum of the Ar 3p profile to that at $p = 0$ provides a convenient test of the angular resolution and is a sensitive indicator of a correctly tuned instrument.

3.4 Data collection and treatment

Data collection is performed under computer control, allowing "hands-off" operation of the spectrometer—a practical necessity when continuous data collection times of several weeks are required to complete one study. Experimental data are collected using one of two data collection modes, termed "non-binning" and "binning". The two data collection algorithms are described below. Argon $(3p)^{-1}$ BES obtained using both the non-binning and binning modes with comparable collection times are shown in Figure 3.6.

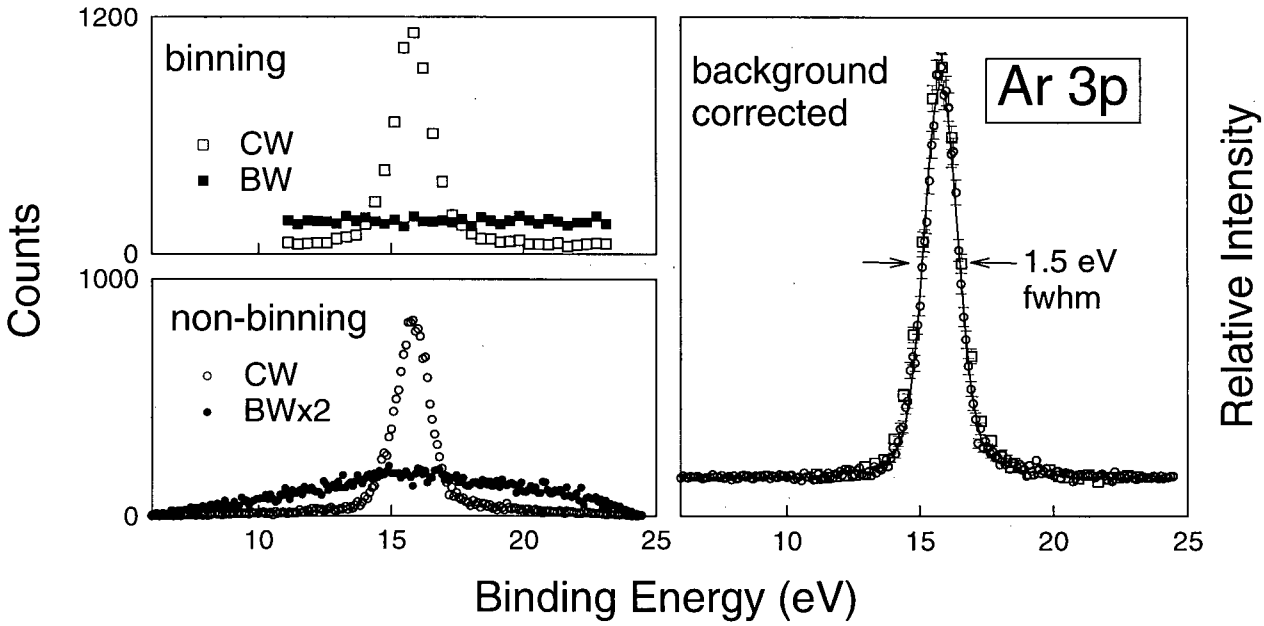

Figure 3.6: Non-binning (squares) and binning (circles) mode argon $(3p)^{-1}$ binding energy spectra. The non-binning data shown are the sum of BES collected in a period of 17 hours at 27 out-of-plane azimuthal angles ranging from $-30°$ to $+30°$. The binning data are the sum of 21 BES collected in 21 hours. The binning and non-binning mode raw data (CW: coincidence window; BW: background window) are shown in the upper-left and lower-left panels, respectively. The BW data are of greater intensity than the CW data because of the greater width of the background window (as shown in Figure 3.4). This is accounted for in the background correction procedure (Section 3.4.3). The binning mode and non-binning mode background corrected BES are shown in the right panel, normalized for height to allow direct shape comparison of the two spectra. The result of a least-squares fit of a pair of Gaussian functions to the ionization peak is indicated by the solid line.

3.4.1 Non-binning data collection mode

In the non-binning mode, the incident electron beam energy is fixed at an appropriate value to allow monitoring of a binding energy range containing the ionization processes of interest. Binding energy spectra are collected sequentially for each of a set of out-of-plane azimuthal angles. Data are collected at each angle by the ADC computer card until a preset number of pulses are detected by the movable analyser detector. These "singles" pulses (as opposed to coincident pairs of pulses, one from each detector) are monitored using a counter on the LabMaster computer card. Prior to stepping to the next angle, the data for the current angle are saved to computer disk and all channels on the ADC card are reset to zero. When the data collection routine has cycled through a full set of angles (constituting one scan), the scan number is incremented and the process repeated. A computer display of the collected data is updated following each angle change and is used by the operator to monitor the data collection procedure and to determine when sufficient data has been collected to allow the experiment to be stopped.

The collected data for each angle consist of the number of coincident and non-coincident events (from the coincidence and background SCA windows, respectively) recorded in each ADC channel. The ADC channel numbers are converted by the acquisition software to electron binding energy using calibration data obtained via the procedure described in Section 3.3. The square response functions of each analyser combine to produce a triangular response function for the coincidence spectrum (evident in the lower left panel of Figure 3.6). As a result of this non-uniform detection efficiency across the monitored binding energy range, the non-binning mode is not well suited to situations where multiple ionization processes at different binding energies are of interest, particularly if the relative intensities of the ionization processes are of interest. However, for the study of a single ionization process that is energetically well separated from neighbouring processes, the non-binning data collection

mode is the most efficient choice. This mode is often used when collecting diagnostic spectra using argon or helium and has been used in the study of acetone, reported in Chapter 4.

3.4.2 Binning data collection mode

The binning data collection mode is designed to circumvent the problem of the triangular response function of the energy dispersive spectrometer and to allow data collection over a binding energy range greater than that simultaneously monitored by the spectrometer [17, 18]. This is done by dividing the energy range monitored by the spectrometer into many narrow energy ranges, or "energy bins." In the experiments reported in this thesis, each energy bin is ≈ 0.36 eV wide and consists of the summed data from four consecutive ADC channels. When collecting the experimental data, once the preset number of singles counts from the movable analyser detector are received by the counter on the LabMaster card, the ADC data are transferred to the appropriate energy bin in computer memory and all ADC channels are reset to zero. The computer display is then updated and the incident electron beam energy is incremented by an energy step equal to the width of the energy bins. By systematically shifting the monitored binding energy range in this manner, data at each binding energy are collected for an equal period of time at all positions of the spectrometer's response function, resulting in equal instrumental sensitivity for all binding energies. Consequently, all experimental data from one study are on the same relative intensity scale and only multiplication by a single normalization factor is necessary to allow direct comparison with theory. After data have been collected at one azimuthal angle at all incident electron beam energies necessary to cover the desired binding energy range, the BES data for that angle are saved to computer disk, the movable analyser is stepped to the next angle, the incident electron beam energy is reset to its initial value and BES data for that angle are collected. As is the case in the non-binning mode, following a complete cycle

through a full set of azimuthal angles (i.e., one scan), the scan number is incremented and the process repeated until the precision of the collected data reaches an acceptable level.

The binning data collection mode is well suited to the study of several ionization processes spread throughout a broad binding energy range, such as ionizations from a molecule's valence orbitals or some subset thereof. The uniform detection efficiency over the entire energy range results in all processes being on a common intensity scale. This is important when investigating the breakdown of the single particle model of ionization and when performing detailed assessments of theoretical models of the EMS momentum profiles. These advantages of the binning mode are tempered by a loss in collection efficiency in comparison to the non-binning mode. Because data for all binding energies are collected at all points in the monitored energy range of the spectrometer, the incident electron beam energy must be varied over a range beginning below and ending above the binding energy range of interest. At these extreme energies, only a fraction of the data collected are within the desired binding energy range. This amounts to only a small proportion of the total data collected when the energy range being studied is large, but is more significant for smaller binding energy ranges with widths comparable to the simultaneously monitored energy range of the spectrometer.

3.4.3 Background correction

The first step in the data analysis process is the correction of the BES for false coincidences. As discussed above in Section 3.2.2, some fraction of the events detected by the spectrometer with a time correlation corresponding to a coincidence (as set with the coincidence (COINC) SCA in Figure 3.3) are the result of a constant background (in the time spectrum) of uncorrelated electron pairs. This background is constant because all time intervals between the detection of two electrons constituting an uncorrelated electron pair are equally likely. The magnitude of this background is determined by the collection of the non-coincident data

gated through the background (BACK) SCA indicated in Figure 3.3. The true coincident signal (N_t) is then obtained from the difference between the coincident (N_c) and background (N_b) data, taking into account the ratio of the widths of the background and coincident windows (r) set by the respective SCAs:

$$N_t = N_c - N_b/r. \tag{3.1}$$

The error in the true coincident signal is

$$\Delta N_t = \sqrt{N_c + \frac{N_b}{r^2}}. \tag{3.2}$$

The width of the background data window is typically set larger than that of the coincident window to minimize ΔN_t.

3.4.4 Experimental angle and momentum profiles

Data collection, using either the binning or non-binning mode and background correction as described above, results in a series of binding energy spectra recorded at different azimuthal angles between the two outgoing electrons (i.e., different positions of the movable analyser). The variation in intensity of an ionization peak in the BES as a function of the out-of-plane azimuthal angles at which the BES are collected is referred to as an experimental angle profile (XAP). Experimental momentum profiles (XMPs) are obtained from the XAPs by conversion of the out-of-plane azimuthal angles ϕ to electron momentum p using Equation (2.5). This is illustrated in Figure 3.7 for the Ar 3p profile. The experimental angle and momentum profiles shown are from the same data sets used to generate the BES shown in Figure 3.6.

XAPs are obtained from the BES data in one of two ways. In cases where the ionization peak of interest is fully resolved from adjacent peaks, it is sufficient to sum the experimental

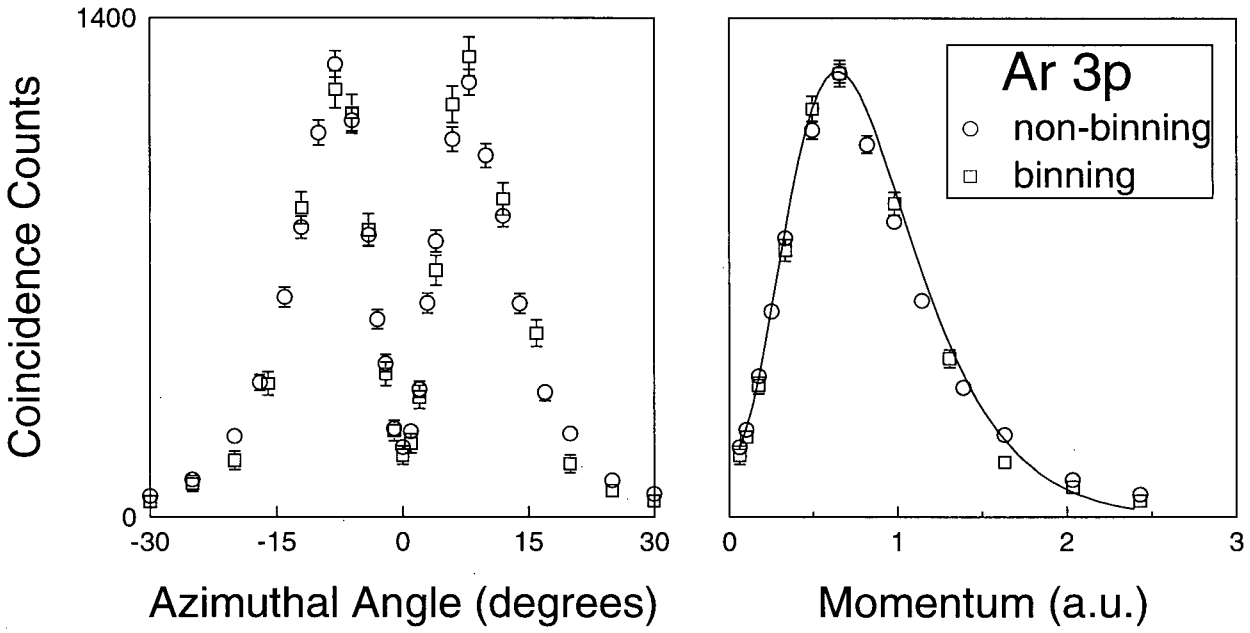

Figure 3.7: Non-binning (○) and binning (□) mode argon 3p angle (left) and momentum (right) profiles. The data sets were collected in 17 and 21 hours, respectively. The binning mode data has been scaled by 1.9 (the factor necessary to normalize the two data sets at their momentum profile maxima) to facilitate comparison of the two data sets. The solid line in the right panel is the Ar 3p theoretical momentum profile from the CI ion-neutral overlap calculation of Davidson [124], with the experimental angular resolution ($\Delta\theta = 0.6°, \Delta\phi = 1.2°$) accounted for using the GW-PG method [48]. The TMP has been normalized to the experimental data at the profile maxima.

BES data over an energy range encompassing the peak in question, as has been done to obtain the profiles shown in Figure 3.7. Such a BES sum will yield one data point of the XAP for each out-of-plane azimuthal angle at which a BES has been collected. This method is also used to obtain angle profiles corresponding to multiple ionization processes by summing BES data over a broader energy range.

In cases where it is not possible to fully resolve all of the ionization processes of interest, a fitting procedure can be used to obtain individual angle and momentum profiles. This method has been used in all of the studies presented in the subsequent chapters of this thesis. Gaussian functions are used to fit the various ionization peaks in the BES. The widths of the fitted functions are fixed at values obtained by convoluting the spectrometer resolution function (determined from measurements of the He $(1s)^{-1}$ ionization) with the Franck-Condon widths of the ionization processes determined, where available, from high resolution photoelectron spectroscopy data. The fitted peak positions are also fixed at values obtained from photoelectron spectroscopy. These positions normally correspond to the vertical IPs, although in cases where the Franck-Condon envelope is highly asymmetric slight adjustments to the peak positions are sometimes necessary. A least-squares fit to the BES is then performed, with only the peak areas allowed to vary. The distribution of fitted peak areas for a particular ionization process as a function of the out-of-plane azimuthal angles at which the BES were collected is the experimental angle profile for that ionization process. In some cases, ionization processes are not sufficiently separated in energy to allow the determination of individual profiles by a fitting procedure. In these instances, single functions can be used to fit a BES peak representing multiple ionization processes. The resulting angle and momentum profiles will correspond to the sum of the profiles for the individual ionization processes.

Experimental angle profiles provide a useful check of correct spectrometer operation.

Positive and negative out-of-plane azimuthal angles ϕ correspond to the same electron momentum p (Equation (2.5)), so BES collected at the same *absolute* out-of-plane azimuthal angles should be the same and XAPs should be symmetric about $\phi = 0°$, as is the case for the Ar 3p profiles shown in Figure 3.7. In particular, mis-alignment of the electron analysers and the incident electron beam will result in asymmetric angle profiles.

Chapter 4

Acetone

4.1 Introduction

Acetone (dimethyl ketone, $(CH_3)_2CO$) has been chosen as the first molecule for study using the multichannel electron momentum spectrometer described in Chapter 3. Several considerations motivated this choice. With 10 atoms and 32 electrons, acetone presents several of the challenges inherent in performing EMS studies of larger molecules, such as a comparatively large number of valence orbitals resulting in a congested binding energy spectrum, some degree of conformational flexibility and increased computational costs. However, the physical properties of acetone (i.e., a liquid having a high vapour pressure at room temperature) make EMS measurements relatively straightforward. Furthermore, theoretical momentum profiles obtained from large-basis-set HF and MRSD-CI calculations [54] have been published for the HOMO of acetone, thus allowing for evaluation of the TKSA using a molecule larger than those considered by Duffy et al. [20, 21] in their initial investigation of the application of DFT to EMS. Such comparisons between the TKSA and more-established EMS theoretical models (i.e., the PWIA and THFA) are necessary to gain some indication of whether or not the TKSA-DFT method can be applied with any confidence to larger molecules for which

high-level HF and CI methods become increasingly impractical.

Previously published single-channel EMS data of the $5b_2$ HOMO of acetone by Hollebone et al. [54] further motivated the current study. The single-channel measurements were performed as part of an investigation of the effects of methyl substitution on the HOMOs of carbonyl compounds, specifically formaldehyde (H_2CO), acetaldehyde (CH_3CHO) and acetone. The low sensitivity of the single-channel spectrometer, in combination with the low cross-section of the acetone $(5b_2)^{-1}$ ionization, resulted in an experimental momentum profile of poor precision [54]. This limited the evaluation that could be performed of the high-level HF and MRSD-CI theoretical calculations mentioned above and presented in Reference [54]. Nevertheless, there appeared to be a discrepancy between the $5b_2$ XMP and all of the reported TMPs at electron momenta > 0.8 au. A remeasurement of this momentum profile with greater precision is desirable to verify this discrepancy between theory and experiment. If this discrepancy is confirmed, the application of DFT via the TKSA to the $5b_2$ XMP of acetone is of particular interest in order to investigate whether this discrepancy between theory and experiment can be eliminated.

The $(5b_2)^{-1}$ ionization is energetically well-separated from the remainder of the outer-valence ionizations of acetone. However, ionizations from the eight remaining outer-valence orbitals occupy a relatively narrow binding energy range, as indicated by a He (II) PES study [125]. The low count rates and 1.7 eV fwhm energy resolution of the single-channel spectrometer thus limited the EMS study of Hollebone et al. [54] to the HOMO XMP. The improved sensitivity and energy resolution of the multichannel spectrometer used in the present work facilitates EMS measurements of the complete valence shell of acetone.

4.2 Experimental details

Valence-shell EMS measurements of acetone have been performed at a total energy of 1200 eV using the energy-dispersive multichannel spectrometer described in Chapter 3. Three data sets were collected. The first consists of 6–60 eV binding energy spectra collected using the binning data collection mode (Section 3.4.2) at out-of-plane azimuthal angles (ϕ) of 0° and 5°. These data are referred to subsequently as the long-range BES data (LR-BES). A set of six shorter energy range binning-mode BES were also recorded (SR-BES), covering the binding energy range 6–40 eV at $\phi = 0°, 2.5°, 7.5°, 10.5°, 14.5°$ and 20°. Finally, in order to allow a precise description of the $5b_2$ (HOMO) momentum profile of acetone, non-binning-mode data (non-bin) were collected at 26 out-of-plane azimuthal angles ranging from 0–30°. The incident electron beam energy during the non-binning data collection was set so as to centre the $5b_2$ ionization peak (IP=9.8 eV from PES [125]) in the monitored binding energy range. The acetone sample was of spectroscopic grade (> 99.9% pure) from BDH chemicals. Repeated freeze-pump-thaw cycles were performed using liquid nitrogen to remove any gaseous impurities dissolved in the sample. The sample pressure was maintained at 1.0×10^{-5} torr during the data collection. Measurements of the Ar $(3p)^{-1}$ ionization were performed both before and after the acetone data collection to ensure proper operation of the spectrometer and to determine the experimental energy resolution, which was found to be 1.4 eV fwhm.

4.3 Computational considerations

4.3.1 Molecular conformation and theoretical momentum profiles

In the single-channel EMS study of the HOMO of acetone [54] and in the publication describing the data discussed in this chapter [126], two different geometries were used in performing electronic structure calculations to obtain TMPs. The majority of the calculations used a zero-point average structure determined from microwave spectroscopy and electron diffraction data [127]. The orientations of the two methyl groups were rather arbitrarily chosen to be "half-staggered," meaning that one methyl group was staggered with respect to the carbonyl group (i.e., with one hydrogen in the plane defined by the carbon and oxygen atoms and anti to the carbonyl group, resulting in an OCCH dihedral angle of 180°) and the other methyl group was eclipsed (i.e., with an OCCH dihedral angle involving the in-plane hydrogen of 0°) [54,126]. In contrast, the MRSD-CI calculations (and therefore the HF calculations used as a basis for the CI calculations) used an MP2/6-31G** optimized geometry [54] in which both methyl groups were eclipsed with respect to the carbonyl group. This conformation, referred to as "eclipsed," was found by Hollebone et al. to be the global minimum structure on the MP2/6-31G** potential energy surface. Two other stationary points were also located, one corresponding to the half-staggered conformation discussed above and a second, referred to as "staggered," in which both methyl groups were staggered with respect to the carbonyl group. These two other conformations were, respectively, 1.2 and 3.6 mhartree higher in energy than the eclipsed conformation [54]. These three conformations of acetone are illustrated in Figure 4.1.

In discussing their choices of geometry, Hollebone et al. noted that an EMS study of dimethyl ether [53] indicated that [54], "methyl group orientation has only a small effect on the resulting TMPs at this level of calculation." A comparison of the 204-CGF basis set

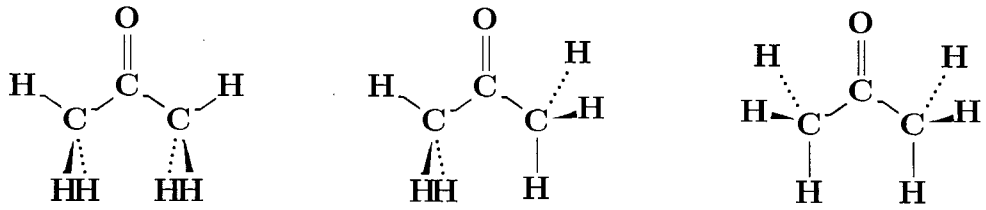

Figure 4.1: Conformers of acetone

[54] HF TMPs calculated using the MP2/6-31G** eclipsed geometry and HF/6-311++G** TMPs calculated using the experimental half-staggered geometry (presented in Fig. 8 of Reference [126]) generally supports this statement. However, the use of more than one geometry for the theoretical calculations makes it impossible to determine to what extent the small observed differences are the result of differences in the basis set employed rather than the geometries used.

In view of the above considerations and the increasing significance of conformational flexibility that may generally be expected in EMS studies of larger molecules, a more thorough investigation of the relationship between acetone conformation and the corresponding theoretical momentum profiles has been performed. Full geometry optimizations have been performed at the MP2(full)/6-31G** level and the three stationary points reported by Hollebone et al. [54] (i.e., the eclipsed, half-staggered and staggered conformations) have been identified. The nature of the stationary points was subsequently determined by performing frequency calculations at each of the stationary points. The computational results (obtained using GAUSSIAN94 [103]) are reported in Table 4.1 along with the zero-point average structural parameters [127] mentioned above and used in Reference [54] and [126].

Examination of the optimized structural parameters reported in Table 4.1 indicates that the bond lengths and angles are relatively invariant with rotation of the methyl groups. The

Table 4.1: Conformers of acetone. MP2(full)/6-31G** optimized bond distances (r), angles (a) and dihedral angles (d), conformer energies and other properties. H_i refers to the hydrogen atom of each methyl group in the plane defined by the heavy atoms; H_o refers to the out-of-plane hydrogens. In the case of the half-staggered conformation, where two numbers are given the first involves the atoms of the eclipsed methyl group and the second involves those of the staggered methyl group. Distances are in angstroms and angles in degrees.

	eclipsed	half-staggered		staggered	experiment[a]
rCO	1.226	1.225		1.226	1.210 ± 0.004
rCC	1.511	1.509	1.516	1.516	1.517 ± 0.003
rCH$_i$	1.085	1.085	1.086	1.085	1.091 ± 0.003
rCH$_o$	1.089	1.090	1.088	1.088	
aOCC	121.8	122.1	120.7	120.3	
aCCC	116.4	117.2		119.4	116.00 ± 0.25
aCCH$_i$	109.6	109.8	112.8	113.2	
aCCH$_o$	110.2	110.0	108.9	108.7	
aH$_i$CH$_o$	109.8	110.0	109.3	109.4	108.5 ± 0.5
aH$_o$CH$_o$	107.2	107.2	107.5	107.3	
dOCCH$_o$	$\pm$120.9	$\pm$121.1	$\pm$58.5	$\pm$58.3	
E(MP2) (au)	-192.589477	-192.588260		-192.585861	
ΔE (kJ/mol)	0.0	3.195		9.494	
symmetry	C_{2v}	C_s		C_{2v}	
# imag. freq.	0	1		2	
dipole mom. (D)	3.345	3.297		3.207	2.90

[a]Experimental structural parameters are zero-point average values reported in Reference [127] and determined from microwave spectroscopy and electron diffraction data. The experimental value of the dipole moment is from Reference [128], a microwave spectroscopy study of acetone.

notable exceptions are the CCC angle and the CCH angle to the in-plane hydrogens, which increase in going from the eclipsed to the staggered conformation. This behaviour may be attributed to steric repulsion between the in-plane hydrogens in the staggered conformation. The optimized parameters are consistent with the experimental parameters of Iijima [127] that are reproduced in Table 4.1. It should be noted that some differences between the optimized and experimental parameters are expected since the former are equilibrium values while the latter are zero-point average values.

Valence theoretical momentum profiles for the three conformations of acetone are shown in Figure 4.2. The TMPs have been obtained using the THFA (Equation (2.11)) from the

HF/6-31G** molecular orbitals of the MP2/6-31G** optimized conformers. Since the TMPs are compared only with each other and not with experimental data, no angular resolution folding (see Section 2.2.5) has been performed. Each panel of Figure 4.2 indicates the MO number of the TMPs shown as well as the orbital symmetry labels, with the C_{2v} labels (corresponding to the eclipsed and staggered conformations) printed above the C_s labels (corresponding to the half-staggered conformation).[1]

For all of the valence orbitals of acetone, the TMPs of the three conformations are qualitatively the same and, in many instances, essentially identical. There are, however, several cases in which differences amongst TMPs of different conformations are evident. Not surprisingly, in those cases where differences are evident, the half-staggered-conformation TMPs are intermediate between the fixed- and staggered-conformation TMPs. Examination of the coefficients of the MOs used to generate the TMPs in Figure 4.2 indicates that those MOs contributing to C–H σ-bonding (MOs 15, 14, 12, 11, 10 and 9) have TMPs that vary with acetone conformation. In contrast, the TMPs for the remainder of the orbitals show very little variation with methyl-group orientation. These results indicate that, at least in the case of acetone, methyl-group orientation does not significantly affect the TMPs of orbitals that make little or no contribution to C–H bonding. However, in the case of those orbitals that do contribute to C–H bonding, methyl-group orientation should not be disregarded.

The frequency calculations indicate that only the eclipsed conformation is an energy minimum. The half-staggered and staggered conformations are saddle points with, respectively, one and two imaginary frequencies corresponding to rotations of the methyl groups. Consequently, the MP2/6-31G** optimized eclipsed conformation of acetone has been used for all further theoretical calculations reported in this chapter. It should be noted that the lowest vibrational frequency of this conformation, corresponding to opposing rotations of the

[1]Note that, in Reference [126], it was stated that acetone has C_s symmetry but the MOs were subsequently referred to by C_{2v} symmetry labels.

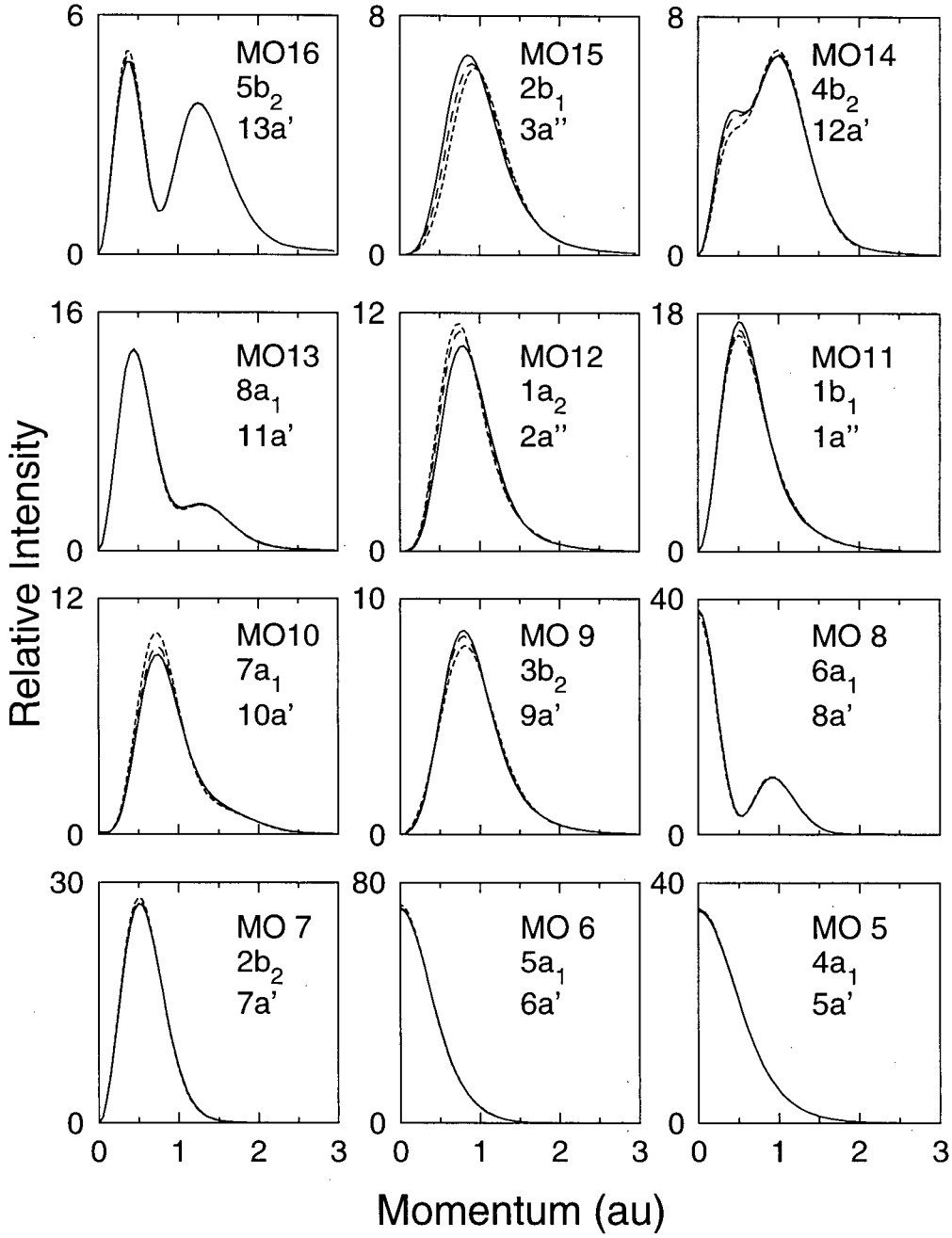

Figure 4.2: Effect of molecular conformation on acetone valence momentum profiles. The TMPs were calculated using the THFA from HF/6-31G**//MP2(full)6-31G** molecular orbitals for the eclipsed (solid lines), half-staggered (long-dashed lines) and staggered (short-dashed lines) conformations. The molecular orbital number and C_{2v} (eclipsed and staggered conformations) and C_s (half-staggered conformation) symmetry labels are indicated in each panel. No angular resolution folding of the TMPs has been performed.

methyl groups, is quite low (58.17 cm^{-1} according to the above calculations). Consequently, appreciable rotation of the methyl groups will occur at room temperature and the use of a single equilibrium geometry for the TMP calculations may result in discrepancies with the experimental momentum profiles of those orbitals contributing significantly to C–H bonding.

4.3.2 Choice of basis set

Theoretical momentum profiles of the valence orbitals of acetone have been calculated using the THFA (Equation (2.11)) and the TKSA (Equation (2.14)) and the results of single-point HF and LSDA-DFT calculations, respectively, performed using GAUSSIAN94 [103]. The exchange–correlation functional proposed by Vosko, Wilk and Nusair [99] has been used for the LSDA calculations. A range of basis sets has been used in order to investigate the sensitivity of the TMPs to basis set quality. All of the basis sets used are described in Section 2.3.4 with the exception of the 204-CGF basis set taken from the single-channel EMS study of the acetone HOMO [54].[2] This basis consists of an (18s13p2d)/[6s7p2d] contraction for carbon and oxygen and a (10s1p)/[5s1p] contraction for hydrogen[3] and is based upon the highly converged basis sets of Partridge [129,130] augmented with polarization functions on all atoms. A summary of the electronic structure calculations is given in Table 4.2. The corresponding $5b_2$ TMPs of the acetone HOMO are shown in Figure 4.3.

Both the HF and LSDA-DFT TMPs show a similar variation with basis set, as is also the case for the other calculated properties shown in Table 4.2. Only the $5b_2$ TMPs are shown here as they exhibit the greatest variation with choice of basis set. Similar but less dramatic variations also occur for the other outer-valence TMPs of acetone. In contrast, the inner-valence TMPs are relatively insensitive to the choice of basis set. In the case of the $5b_2$ TMPs,

[2]This basis set was referred to incorrectly as 196-GTO in Reference [54].
[3]The hydrogen s function contraction was described incorrectly as (10s)/[7s] in Reference [54].

Table 4.2: Hartree–Fock and LSDA density functional theory calculations of acetone. All calculations were performed using the MP2/6-31G** optimized eclipsed conformation described in Table 4.1. The dipole moment of acetone has been determined experimentally to be 2.90 D [128].

Key	Basis set	Hartree–Fock		LSDA-DFT	
		Total energy (hartree)	Dipole moment (D)	Total energy (hartree)	Dipole moment (D)
st	STO-3G	−189.534399	1.945	−189.006897	1.817
4g	4-31G	−191.677185	3.623	−191.244868	3.047
6g	6-311G	−191.918651	3.657	−191.498425	3.158
6p	6-311++G**	−192.014838	3.592	−191.560744	3.213
tz	aug-cc-pVTZ	−192.035127	3.509	−191.581259	3.141
204	204-CGF, Ref. [54]	−192.043241	3.511	−191.593916	3.143

all of the calculations predict a two-peaked momentum profile. However, the minimal-basis-set STO-3G calculations (st on Figure 4.3) differ significantly from the others in predicting that the peak at higher momentum is of appreciably greater intensity than that at lower momentum. As the size and flexibility of the basis set used is increased, the magnitude of the low-momentum peak in the corresponding TMP increases and the positions of both peak maxima shift to lower momentum. This behaviour is typical of that observed in previous EMS studies (see Section 1.1.2 and References [9,35]). Small and medium-sized basis sets, particularly those lacking diffuse functions, tend to underestimate the intensity of valence TMPs at low momentum. This is a consequence of the approximately inverse relationship between position and momentum space and a reflection of the poor representation of the outermost (large-r) regions of the electron density by these basis sets.

Of greater interest for the purposes of the present work is that the acetone TMPs obtained using the three largest basis sets considered here (6-311++G**, aug-cc-pVTZ and 204-CGF) are essentially indistinguishable, indicating that this property has converged and that nothing is gained by calculating acetone HF or DFT TMPs using the 204-CGF or aug-cc-pVTZ (322-CGF) basis sets rather than the considerably smaller 130-CGF 6-311++G** basis set. It

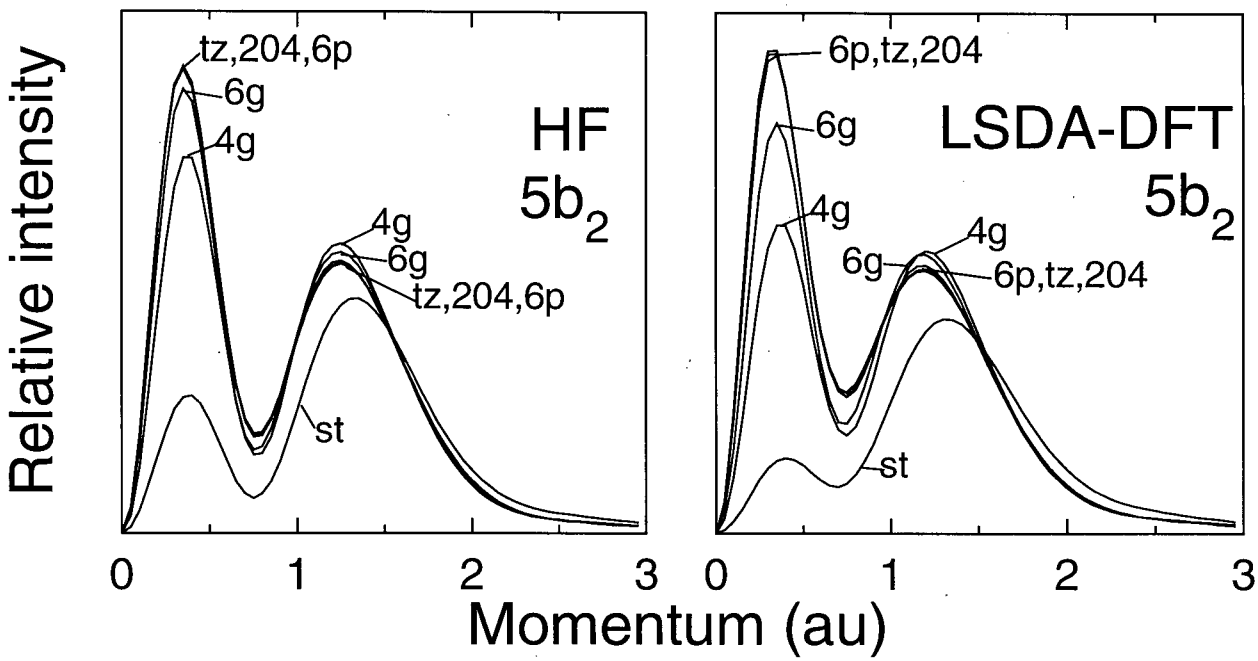

Figure 4.3: Dependence of the $5b_2$ TMP of acetone on basis set. HF TMPs obtained using the THFA are shown in the left panel and LSDA-DFT TMPs obtained using the TKSA are shown in the right panel. The key to the TMP labels is given in Table 4.2. No angular resolution folding of the TMPs has been performed.

should be noted, however, that variations of other calculated properties of acetone do occur amongst these three basis sets, as indicated in Table 4.2. Interestingly, the 204-CGF basis set [54] results in lower HF and LSDA-DFT total energies and very similar dipole moments when compared with the larger aug-cc-pVTZ basis set, suggesting that the former is generally a better choice for HF and DFT calculations of acetone. In view of the agreement amongst the 6-311++G**, aug-cc-pVTZ and 204-CGF valence TMPs of acetone and the respective sizes of the basis sets, the 6-311++G** basis set has been used in calculating TMPs for comparison with the experimental momentum profiles of acetone discussed in Section 4.5.

4.4 Valence binding energy spectra

Acetone has 32 electrons occupying four core orbitals and 12 valence orbitals. The independent particle ground-state electron configuration of the C_{2v} symmetry conformations is

$$\underbrace{(1a_1)^2(2a_1)^2(1b_2)^2(3a_1)^2}_{\text{core}}\underbrace{(4a_1)^2(5a_1)^2(2b_2)^2(6a_1)^2}_{\text{inner-valence}}$$
$$\underbrace{(3b_2)^2(7a_1)^2(1b_1)^2(1a_2)^2(8a_1)^2(4b_2)^2(2b_1)^2(5b_2)^2}_{\text{outer-valence}}$$

The distinction between inner-valence and outer-valence orbitals is somewhat arbitrary. Those MOs which consist primarily of non-bonding carbon or oxygen 2s character have been classified as inner-valence. By analogy with atomic orbitals, momentum profiles having a maximum at zero momentum are conveniently referred to as s-type and those having a minimum at zero momentum and a maximum at some other momentum value are referred to as p-type. In the case of acetone, all ionizations from a_2, b_1 and b_2 symmetry orbitals will result in p-type momentum profiles because of the nodal properties of these orbitals. These momentum profiles should have no intensity at zero momentum except for the small contribution resulting from the finite instrumental momentum resolution [48]. In contrast, ionizations from a_1 symmetry orbitals may give rise to either s-type or p-type momentum profiles, depending upon the nature of the orbital in question.

Binding energy spectra of acetone over the energy range 6–60 eV are shown in Figure 4.4. The spectrum recorded at $\phi = 0°$ is shown in the upper panel and that recorded at $\phi = 5°$ is shown in the lower panel. The close energy spacing of the acetone ionization peaks, in conjunction with their Franck-Condon widths and the EMS energy resolution of 1.4 eV fwhm, results in most of the ionization peaks being only partially resolved. The notable exception is the peak arising from ionization of the $5b_2$ HOMO, a predominantly non-bonding oxygen lone-pair orbital. The p-type nature of the $5b_2$ momentum profile is

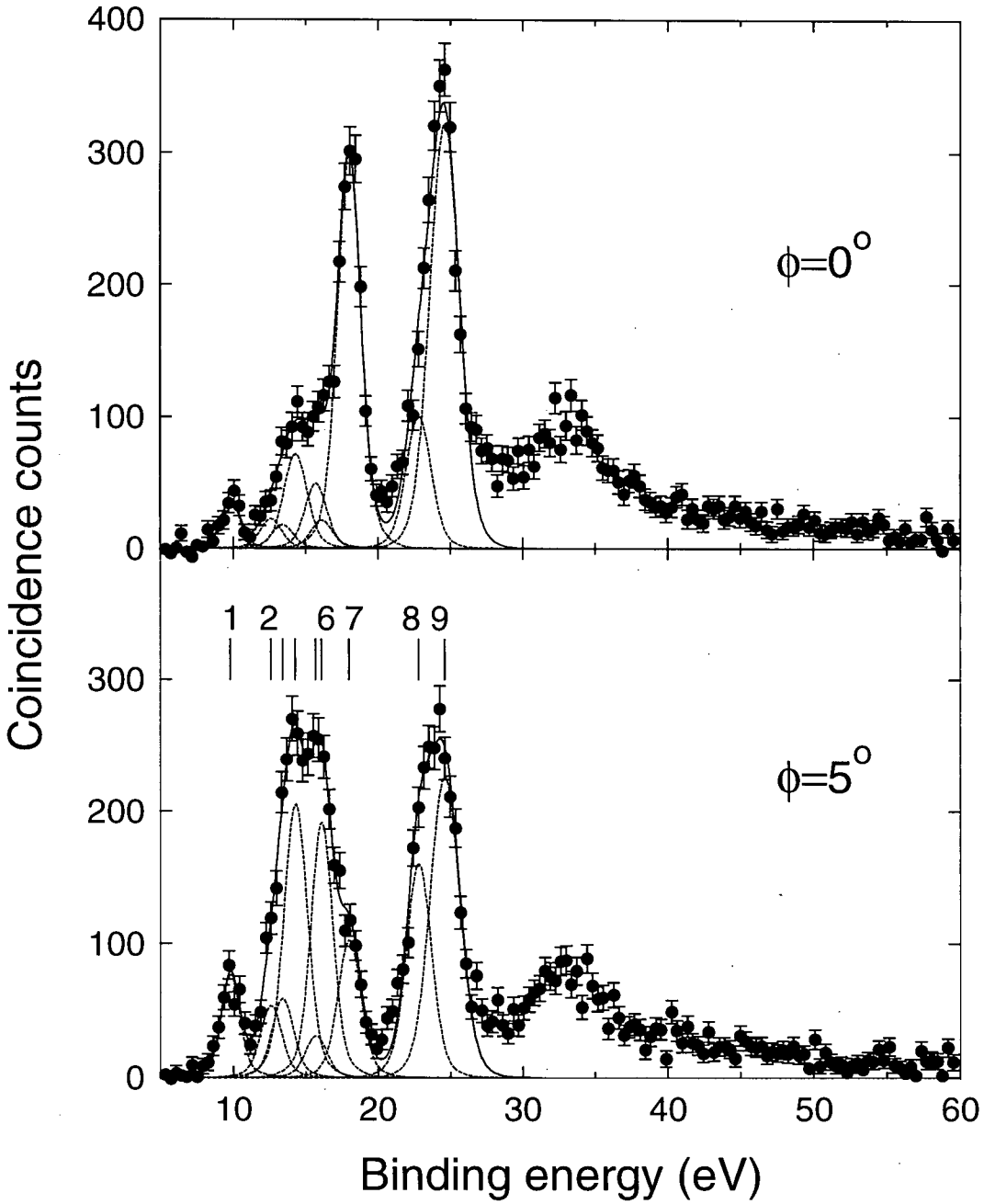

Figure 4.4: Binding energy spectra of acetone from 6–60 eV. The BES (•) at $\phi = 0°$ and 5°, recorded at a total energy of 1200 eV, are shown in the upper and lower panels, respectively. The dashed lines represent the results of a least-squares fit of Gaussian functions to the ionization peaks and the solid curves are the summed fits. The positions of the fitted peaks are indicated by vertical lines. The peaks 1–9 correspond to ionizations from the $5b_2$, $2b_1$, $4b_2$, $8a_1 + 1a_2$, $7a_1$, $3b_2 + 1b_1$, $6a_1$, $2b_2$ and $5a_1$ orbitals, respectively.

Table 4.3: Measured and calculated valence ionization potentials of acetone. Calculated pole strengths are indicated in parentheses. All energies are in eV.

BES peak[a]	Orbital origin	EMS[b]	PES[c]	Green's function[c,d]
1	$5b_2$	9.8	9.8	9.85(0.91)
2	$2b_1$	12.6	12.6	12.65(0.90)
3	$4b_2$	13.4	$\sim$ 13.4	13.45(0.93)
4	$8a_1$	14.3	14.1	14.05(0.92)
	$1a_2$		$\sim$ 14.4	14.40(0.93)
5	$7a_1$	15.7	15.7	15.66(0.91)
6	$3b_2$	16.1		15.93(0.89)
	$1b_1$		$\sim$ 16.0	16.08(0.92)
7	$6a_1$	18.0	18.0	18.21(0.90)
8	$2b_2$	22.8	23.0	23.78(0.45)
				24.76(0.37)
				26.04(0.021)
9	$5a_1$	24.6	24.6	25.42(0.13)
				25.56(0.043)
				25.60(0.13)
				25.89(0.12)
				26.06(0.27)
				26.30(0.096)
	$4a_1$			29.36(0.024)
				33.32(0.032)
				33.51(0.052)
				33.59(0.032)
				33.63(0.044)
				33.73(0.022)
				33.79(0.021)
				34.94(0.022)
				35.30(0.023)
				36.25(0.052)
				36.44(0.036)
				36.60(0.027)
				36.71(0.038)
				36.76(0.060)
				36.94(0.026)
				41.38(0.027)

[a]Peak numbering corresponds to that used in Figure 4.4.

[b]Ionization peak energies used to fit the EMS binding energy spectra. The EMS absolute energy scale was determined by setting the energy of the $(5b_2)^{-1}$ ionization peak to 9.8 eV.

[c]From Reference [125].

[d]The outer-valence Green's function (OVGF) method was used for the outer-valence ionizations and the extended two-particle-hole Tamm–Dancoff approximation was used for the inner-valence ionizations. Basis set [9s5p/4s]/(4s2p/2s).

evident by the increased intensity of this peak (number 1 in Figure 4.4) in the $\phi = 5°$ BES in comparison to that in the $\phi = 0°$ spectrum. The absolute energy scale of the BES has been fixed by setting the position of the $(5b_2)^{-1}$ ionization peak to the PES vertical ionization potential [125] of 9.8 eV. Also evident in Figure 4.4 is the s-type nature of the $(6a_1)^{-1}$ and $(5a_1)^{-1}$ ionization peaks (peaks 7 and 9, respectively), the only two peaks in the valence BES that are of significantly greater intensity at $\phi = 0°$ than at $\phi = 5°$. MO calculations indicate that the $6a_1$ and $5a_1$ orbitals are of primarily non-bonding oxygen 2s and methyl carbon 2s (in-phase) character, respectively.

In order to allow separation of individual ionization processes and generation of experimental momentum profiles, the BES have been fitted with a series of Gaussian functions indicated by the dashed lines in Figure 4.4. The sums of the fitted peaks are indicated by solid lines. The relative positions of the fitted peaks (indicated by vertical lines) have been taken from the He (II) PES study of Bieri et al. [125]. The peak positions used to fit the BES data and the PES IPs are shown in Table 4.3. The widths used for the fitted peaks are a convolution of the Franck-Condon widths estimated from the PES data [125] and the EMS energy resolution function. Only the peak amplitudes were allowed to vary during the least-squares fitting procedure. A single peak at 14.3 eV (peak 4) has been used to fit the closely spaced ionizations from the $8a_1$ and $1a_2$ MOs, which were assigned vertical IPs of 14.1 and 14.4 eV, respectively, by Bieri et al. The close energy spacing and Franck-Condon widths of these ionization peaks makes them nearly unresolvable in the PES, which was obtained with an energy resolution nearly two orders of magnitude better than that of the EMS BES data. A similar situation exists for the ionizations from the $7a_1$, $3b_2$ and $1b_1$ orbitals, which appear in the PES as a single broad asymmetric band located at approximately 16 eV. Despite the paucity of structure on this ionization band, Bieri et al. assigned IPs of 15.7 eV to the $(7a_1)^{-1}$ and $(3b_2)^{-1}$ processes and $\sim$ 16.0 eV to the $(1b_1)^{-1}$ ionization. In the

current work, two peaks (numbers 5 and 6) located at 15.7 and 16.1 eV have been used to fit this region of the BES. It should be noted that the PES IP assignment of Reference [125], which was based primarily on a Green's function calculation (shown in Table 4.3), places the $(1b_1)^{-1}$ ionization at higher energy than the $(7a_1)^{-1}$ and $(3b_2)^{-1}$ ionizations. This differs from the energetic ordering of the acetone HF MOs shown in Figure 4.2 and used to generate the ground-state electron configuration given above and likely represents a breakdown of Koopmans' theorem. The small adjustment of the $(2b_2)^{-1}$ peak (peak 8) to 22.8 eV in the current work from the vertical IP of 23.0 eV reported by Bieri et al. [125] was necessary to obtain a good fit to the band extending from 20 to 27 eV in the BES and appears reasonable from an examination of the PES.

In both the $\phi = 0°$ and $\phi = 5°$ BES of Figure 4.4, there is experimentally observed intensity in the 20–22 eV binding energy range that is not accounted for by the least-squares fit. This could simply be the result of a poor fit to the $(6a_1)^{-1}$ and $(2b_2)^{-1}$ peaks that border this energy range. However, the energies and widths used to fit these peaks appear reasonable upon examination of the PES data of Bieri et al. [125]. There does appear to be a very weak feature at ≈ 20 eV in the PES ionization spectrum [125]. However, no mention of this feature was made in the PES study and it is not clear that it is anything other than noise in the PES data. This "extra" intensity in the BES is examined further in Section 4.5.2 as part of a discussion of the inner-valence momentum profiles.

The binding energy region > 27 eV, containing ionizations from the $4a_1$ MO and possibly satellite peaks resulting from ionizations from other valence orbitals of acetone, has not been fitted because of the comparatively structureless nature of the EMS data in this energy range and the lack of PES data to serve as a guide in the fitting procedure. The considerable ionization intensity evident over this broad energy range (27–60 eV) indicates the presence of significant many-body effects in the inner-valence ionization of acetone. Although most

of this intensity is contained within a broad peak between approximately 30 and 38 eV, the ionization strength is further spread over a large range of binding energies up to the limit of the current data at 60 eV with no apparent peak structure. Comparison of the two BES in Figure 4.4 indicates that the intensity in the 27–60 eV region is greater at $\phi = 0°$ than at $\phi = 5°$, suggesting that the bulk of the intensity in this energy region may be assigned to the s-type $4a_1$, $5a_1$ and/or $6a_1$ ionization manifolds. Further discussion of the assignment of this inner-valence ionization intensity is given in Section 4.5.2 below.

The Green's function calculation of Reference [125], the results of which are reproduced in Table 4.3, is consistent with the BES in that considerable splitting of the ionization intensity of the three inner-most valence orbitals is predicted. A more comprehensive comparison of the Green's function (GF) calculation and the current EMS data is shown in Figure 4.5. The BES data of Figure 4.4 are compared with calculated BES. The calculated spectra have been obtained by convoluting the pole energies and pole strengths from the Green's function calculation with the EMS experimental energy resolution function and the same Franck-Condon widths used for the BES fits shown in Figure 4.4. The momentum (and hence ϕ) dependence of each of the BES has been accounted for by multiplying each of the Green's function pole strengths by the intensity of the corresponding HF/204-CGF theoretical momentum profile [54] at the appropriate ϕ value. The widths of the $4a_1$ poles in the synthesized spectra have been chosen to be the same as that of the $5a_1$ peak since there are no PES data available for this ionization process. The calculated spectra have been scaled by a single factor in order to place them on the same relative intensity scale as the experimental data.

Agreement between experiment and theory is good in the outer-valence region of the spectra shown in Figure 4.5, particularly in terms of the positions of the ionization peaks. The experimentally measured intensity at the lower momentum ($\phi = 0°$) is underestimated

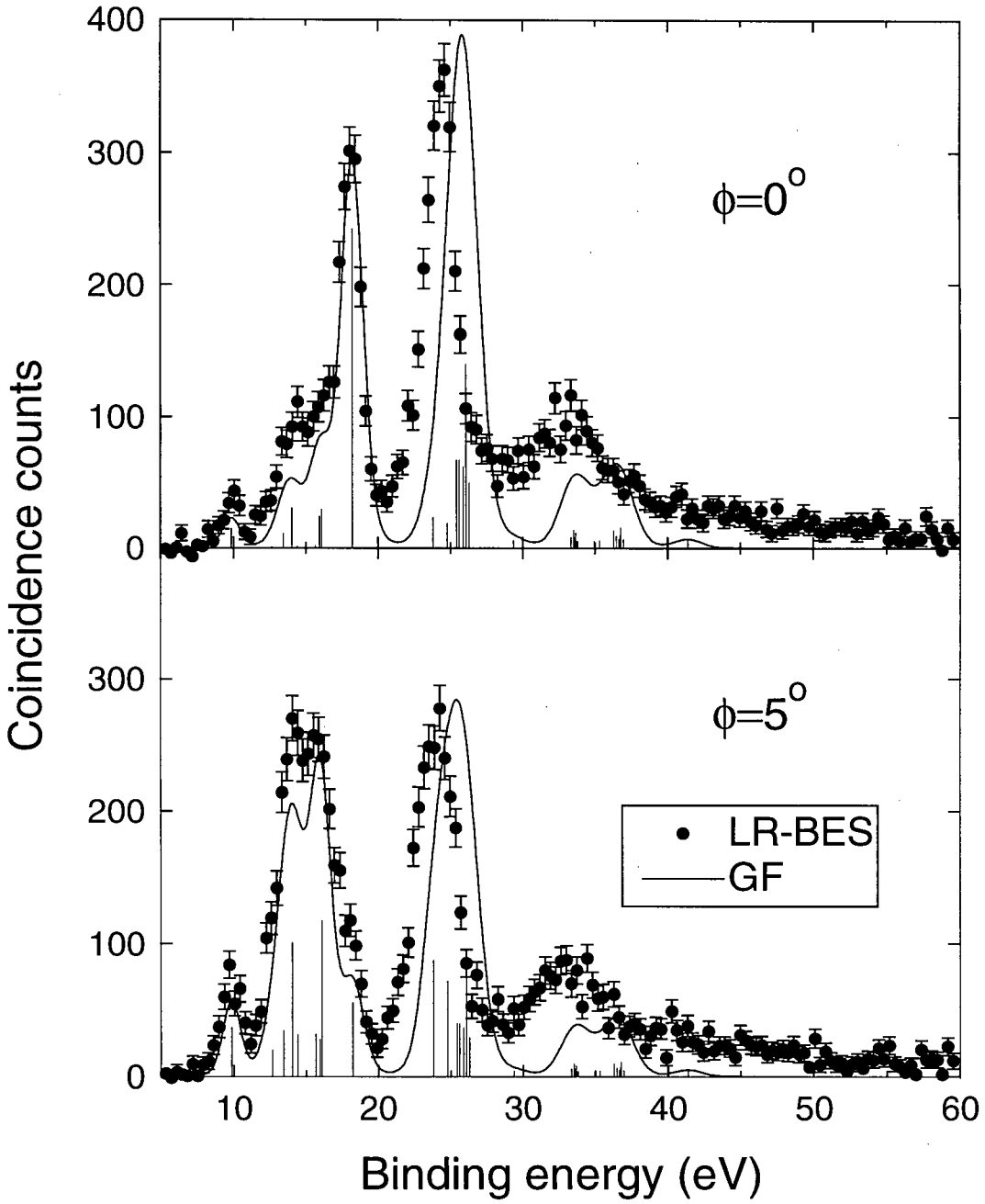

Figure 4.5: Experimental and calculated valence shell binding energy spectra of acetone at $\phi = 0°$ and $\phi = 5°$. The experimental data (•) are the LR-BES data shown in Figure 4.4. The calculated spectra (solid lines) are based upon the ionization energies and intensities (indicated by vertical lines) given by the Green's function (GF) calculation of Reference [125] and reproduced in Table 4.3; the angular dependence has been accounted for using TMPs obtained from a HF/204-CGF calculation [54] of acetone. The same peak widths used to fit the spectra of Figure 4.4 have been incorporated into the calculated spectra.

slightly and this is consistent with the comparison of the experimental and theoretical momentum profiles presented in Section 4.5.1 (i.e., it is attributable to the HF TMPs used to account for the ϕ dependence of the spectra and not to the GF calculation). The relative intensities of the $(2b_2)^{-1}$ and $(5a_1)^{-1}$ main peaks are well described by the calculations. However, the calculated ionization energies of the $(2b_2)^{-1}$, $(5a_1)^{-1}$ and $(4a_1)^{-1}$ main peaks are shifted by 1–2 eV in comparison to the experimental spectra. Furthermore, the experimentally observed intensity in the 30–60 eV energy region is underestimated by the theoretical calculations. This discrepancy is most reasonably attributed to the inadequacy of the Green's function calculation [125] because the HF TMPs give a fair description of the shape of the $2b_2$ and $5a_1$ experimental momentum profiles of acetone, as discussed in Section 4.5.2.

4.5 Valence momentum profiles

Experimental momentum profiles have been obtained for the valence shell of acetone from the results of least-squares fits of the three data sets described in Section 4.2 (i.e., LR-BES, SR-BES and non-bin). The fits to the LR-BES data are shown in Figure 4.4 and discussed in the previous section. The same procedure was used to fit the other binning-mode data set, the SR-BES data extending from 6–40 eV. The positions and widths were fixed at the values used to fit the LR-BES and only the peak amplitudes were allowed to vary. An XMP for each fitted peak was obtained using the procedure described in Section 3.4.4. The ratio of the intensity scales of the SR-BES and LR-BES data was determined by performing a least-squares fit between the two $\phi = 0°$ BES over their common energy range of 6–40 eV. The SR-BES and LR-BES XMPs were then placed on a common intensity scale by scaling the LR-BES XMPs by the ratio determined from this fit. The ionization peaks of binning-

mode binding energy spectra are collected on the same relative intensity scale as a result of the linear background of the binning data collection mode and the fact that the BES data are collected sequentially for many data collection cycles. Consequently, following the above-mentioned scaling of the LR-BES XMPs, all of the acetone binning-mode XMPs are on the same relative intensity scale. In the subsequent figures in this chapter, the LR-BES data are indicated by filled squares (■) and the SR-BES data by filled circles (●).

Obtaining XMPs from the non-binning mode data is a more complicated undertaking because of the non-linear detection efficiency in this data collection mode (refer to Section 3.4.1 for more details). In the case of acetone, the large energy spacing between the $(5b_2)^{-1}$ and $(2b_1)^{-1}$ ionizations allows the HOMO ($5b_2$) XMP to be obtained by summing the non-binning BES data over an appropriate binding energy range, as was done in the original publication [126] of the data discussed in this chapter. The disadvantage to this approach is that it neglects the considerable additional data of the other outer valence ionizations that is collected as a result of the energy-dispersive nature of the spectrometer. An alternative approach has been employed in this thesis which does not suffer from this disadvantage. As was done for the binning-mode data, XMPs have been obtained from the non-binning data by performing a least-squares fit to the 26 non-binning mode BES using the same peak positions and widths, with the exception that the fit only included the outer-valence ionizations because of the shorter binding energy range of the non-binning data. To account for the distortion of the non-binning BES caused by the triangular detection efficiency, prior to performing the least-squares fit the BES were multiplied by the inverse of the detection efficiency function, which was determined by a least-squares fit of two straight lines to the background data (Section 3.4.3). The resulting non-binning XMPs are indicated by inverted triangles (▽) in the subsequent figures in this chapter. Each non-binning XMP has been independently scaled to the corresponding binning-mode XMP using the $\phi = 0°$ and $\phi = 20°$

data points common to both the binning and non-binning data.

Theoretical momentum profiles of the valence shell of acetone have been obtained for comparison with the XMPs from single-point HF/6-311++G** and DFT/6-311++G** calculations using the MP2/6-31G** optimized eclipsed conformation described in Section 4.3.1. Both the HF and DFT calculations were performed using GAUSSIAN94 [103]. In the case of the DFT calculations, a number of exchange–correlation functionals (described in Section 2.3.3) have been used to investigate the sensitivity of the TMPs to the functional used for the electronic structure calculations. The TMPs have been obtained using the THFA and TKSA with the results of the HF and DFT calculations, respectively. In the case of the $5b_2$ and $2b_1$ momentum profiles, the experimental data are also compared with the corresponding TMPs calculated by Y. Wang and E. R. Davidson using Equation (2.10) from the neutral and ion MRSD-CI wavefunctions of acetone. The $5b_2$ TMP was reported originally in the single-channel EMS study of acetone [54]. The CI calculations are based upon the HF/204-CGF wavefunction [54] discussed in Section 4.3.2 above. The effects on the TMPs of the finite spectrometer acceptance angles (i.e., the momentum resolution) have been folded into the calculated profiles using the GW-PG method [48]. The calculations compared to the XMPs are summarized in Table 4.4.

The experimental and theoretical momentum profiles have been placed on a common intensity scale by normalizing the sum of the $2b_1$, $4b_2$ and $8a_1 + 1a_2$ experimental angle profiles (fitted peaks 2–4) to the corresponding BLYP-DFT theoretical angle profile (TAP), as shown in Figure 4.6. This comparison is done using an angle rather than momentum scale because of the binding-energy dependence of the conversion between ϕ and p (Equation (2.5)). These outer-valence momentum profiles were chosen for the normalization because, as is generally the case for outer-valence ionizations, their pole strengths are predicted by the Green's function calculations [125] (see Table 4.3) to be high and approximately equal.

Table 4.4: Calculations used to generate TMPs of acetone. All calculations were performed using the MP2/6-31G** optimized eclipsed conformation described in Table 4.1 and the 6-311++G** basis set, except for the MRSD-CI calculation [54] which uses the 204-CGF basis set described in Section 4.3.2.

Method		Total energy (hartree)	Dipole moment (D)
HF		−192.014838	3.592
DFT	LSDA[a]	−191.560744	3.213
	BLYP[b]	−193.138579	3.114
	BP86[c]	−193.210978	3.110
	B3LYP[d]	−193.217830	3.230
MRSD-CI[e]		−192.629	3.29
experiment			2.90[f]

[a]The Vosko, Wilk and Nusair [99] local exchange–correlation functional was used.
[b]The Becke exchange [105] and Lee, Yang and Parr correlation [107] functionals were used.
[c]The Becke exchange [105] and Perdew correlation [106] functionals were used.
[d] The B3LYP functional is a modification of the hybrid functional proposed by Becke [108] and incorporating the exact exchange energy, with the Lee, Yang and Parr [107] correlation potential replacing that of Perdew and Wang [109].
[e]Reference [54].
[f]Reference [128]. In comparing the experimental and calculated dipole moments, it should be remembered that the calculations ignore the effects of molecular vibrations and rotations.

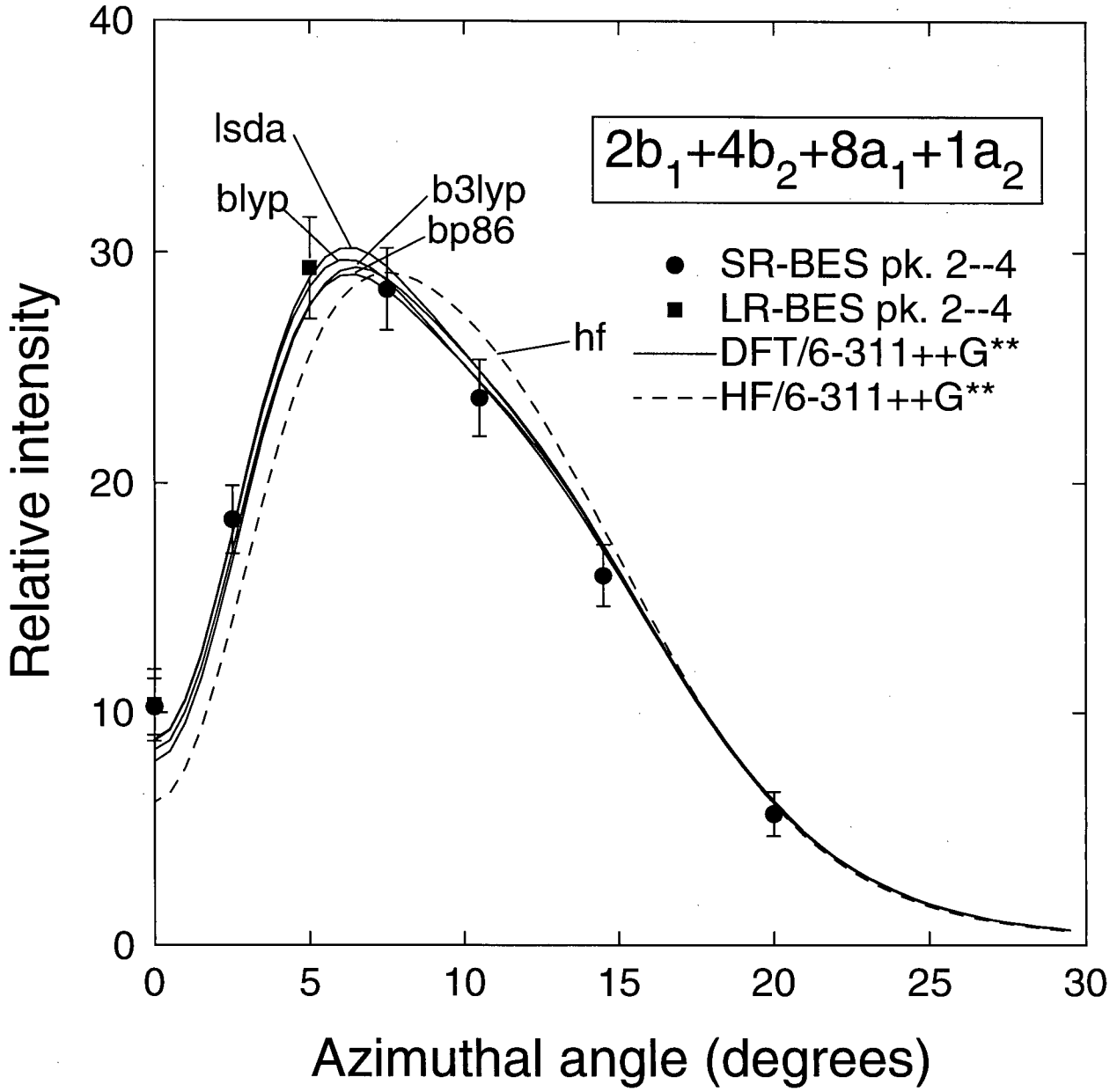

Figure 4.6: Summed $2b_1$, $4b_2$ and $8a_1 + 1a_2$ experimental and theoretical angle profiles of acetone. The experimental profiles are the the sum of the profiles of fitted peaks 2–4 (see Figure 4.4) from the SR-BES (•) and LR-BES (■) data sets and the theoretical profiles are the sums of the corresponding individual profiles. The experimental angular resolution has been accounted for in all theoretical profiles using the GW-PG method [48]. The experimental data have been normalized to the BLYP theoretical profile.

The $5b_2$ profile was not included in this sum because of the disagreement between the theoretical and experimental profiles, as shown in Figure 4.7, below. In performing the normalization, least-squares fits were performed between the experimental profile and each of the theoretical profiles shown in Figure 4.6. The best agreement between experiment and theory was obtained for the fit to the DFT-BLYP profile. Consequently, this normalization factor has been used on the experimental profiles prior to all comparisons of experiment and theory in the remainder of this chapter. Note that the DFT profiles are all of similar shape and intensity; consequently, the normalization factor would differ by less than 2% if either the LSDA or BP86 profiles (the most and least intense, respectively, at the profile maximum) were used instead of the BLYP profile. In contrast, the HF profile, although of similar intensity to the DFT profiles, is quite different in shape from the experimental profile. In particular, the peak maximum of the HF profile is at a greater momentum than is observed experimentally.

4.5.1 Outer-valence momentum profiles

The $5b_2$ experimental and theoretical momentum profiles are shown in Figure 4.7. The $5b_2$ MO is primarily a non-bonding oxygen p orbital. However, there is also significant C–C σ-bonding character and some C–H σ-bonding character, as can be seen from the electron density plot in the inset of Figure 4.7. As discussed by Hollebone et al. [54], this additional orbital density on the carbon and hydrogen atoms and the accompanying nodal surfaces leads to the observed double-lobed form of the $5b_2$ momentum profile. The current experimental data provides a considerable improvement in precision over that of the previous single-channel study [54] and in particular provides a much better characterization of the position and intensity of the high-momentum lobe of the XMP.

All of the theoretical calculations shown in Figure 4.7 predict a similar two-lobed shape

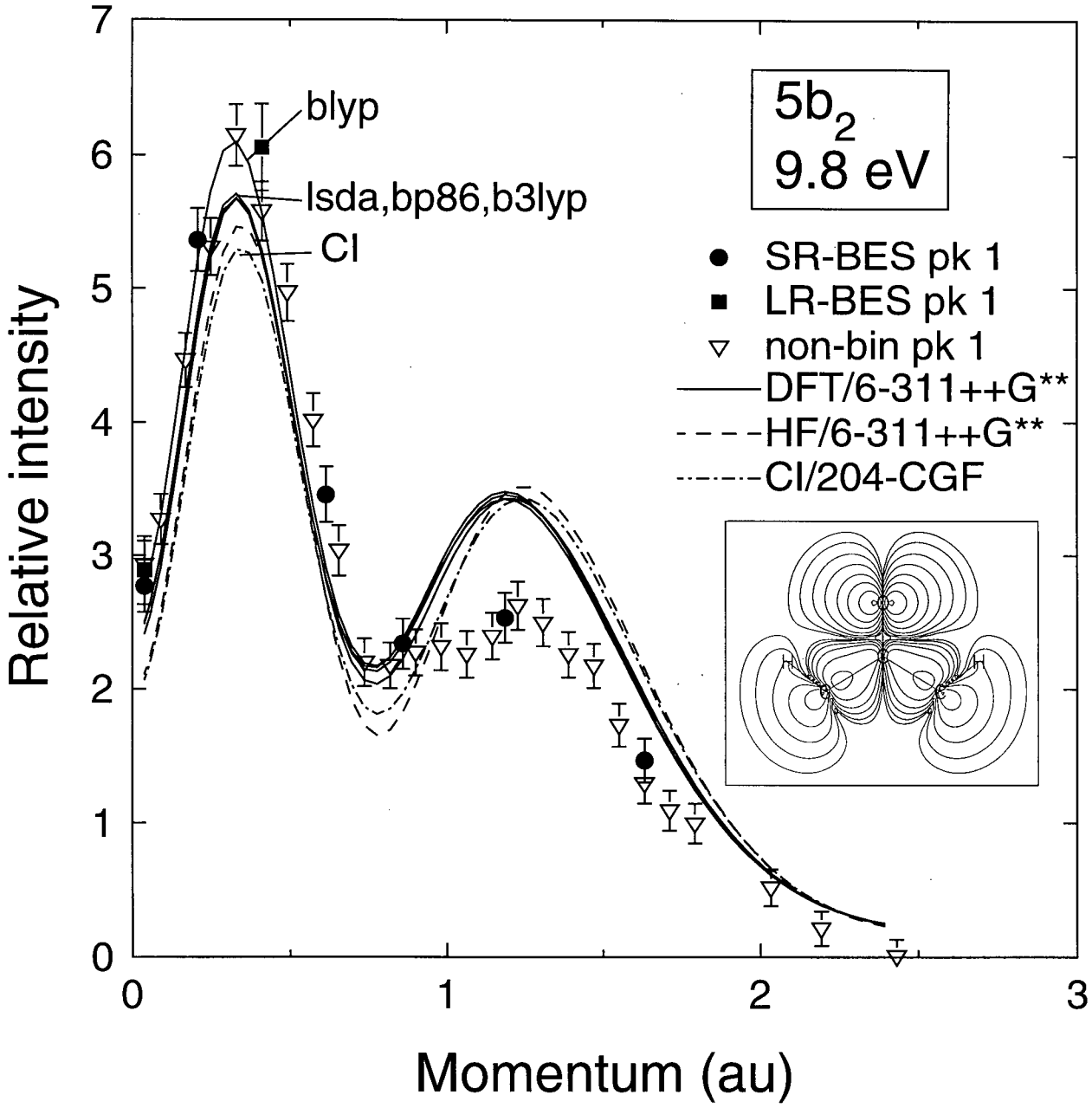

Figure 4.7: Experimental and theoretical $5b_2$ momentum profiles of acetone. The XMPs are of fitted peak 1 (IP=9.8 eV, see Figure 4.4) from the SR-BES (•), LR-BES (■) and non-bin (▽) data sets. The TMPs have been determined from the theoretical calculations listed in Table 4.4. The MRSD-CI TMP is that of Wang and Davidson from Reference [54]. The experimental angular resolution has been accounted for in the theoretical profiles using the GW-PG method [48]. A contour plot of the electron density of the HF/6-311++G** $5b_2$ MO of acetone in the plane containing the heavy atoms is shown in the inset. The contour lines represent densities of 0.0001, 0.0003, 0.001, 0.003, 0.01, 0.03, 0.1 and 0.3 au.

for the TMP but differ in their predictions of the relative intensity of the two lobes and the momentum position of the maximum of the high-momentum lobe. The TMPs are in good agreement with the experimental data in terms of the position and shape of the low-momentum lobe, which peaks at approximately 0.3 au. However, for all calculations considered here, there is considerable disagreement between theory and experiment at momenta greater than 1 au. The TMPs consistently overestimate the intensity of the second lobe of the $5b_2$ profile. This incorrect prediction of the relative intensities of the two lobes is worst for the HF and CI TMPs and slightly improved for the DFT TMPs, particularly the one obtained from the BLYP-DFT calculation. However, it is important to note that the differences between the various TMPs are relatively small when compared with the considerable discrepancy between theory and experiment.

The similarity of the HF, MRSD-CI and DFT TMPs suggests that this discrepancy is not the result of inadequate accounting of electron correlation and relaxation effects, which were the cause of disagreements between theory and experiment in several previous EMS studies of other molecules (see Section 1.1.2). Likewise, the examinations of the basis-set and conformational dependencies of the acetone TMPs, performed in Section 4.3.2 and 4.3.1 above, would appear to rule out both of these as plausible explanations for the observed disagreement between theory and experiment. It should also be noted that the discrepancies at higher momentum are in the contrary direction to that typically observed for distorted wave effects in the experimental data [5, 7]. However, in this regard, recent EMS results [69, 131] suggest that distortion of the incoming and outgoing electrons may impact significantly upon experimental momentum profiles resulting from ionization from MOs resembling atomic d orbitals. In contrast to the generally accepted view [7] that distortion effects are only significant at high momentum, where they typically result in an increase in the observed experimental cross-section, a study of the momentum profiles of the HOMOs

of several transition-metal carbonyls and the corresponding metal atoms [69] indicates appreciable distortion effects at low momentum. Determination of whether this explains the discrepancies observed in the present work for ionization from the $5b_2$ MO of acetone (which bears a qualitative resemblance to an atomic d orbital, see inset of Figure 4.7) must await further investigation. Work is currently underway [131] to investigate the role of distortion in the TMPs of molecules. However, such studies are particularly challenging because (as mentioned in Section 2.2.1) there is at present no tractable computational method for performing distorted-wave calculations on molecules.

The $2b_1$ experimental and theoretical momentum profiles are shown in Figure 4.8. This orbital is responsible primarily for C–O π-bonding, but there is also significant σ-bonding between the methyl carbons and the out-of-plane hydrogens. The decreased precision of this XMP in comparison to that of the HOMO ($5b_2$) reflects the relatively close proximity of the $(2b_1)^{-1}$ ionization peak (IP=12.6 eV) to the $(4b_2)^{-1}$ ionization peak (IP=13.4 eV) in contrast to the larger energetic spacing between the $(5b_2)^{-1}$ and $(2b_1)^{-1}$ ionizations. As expected from symmetry, this momentum profile is p-type. All of the calculations result in very similar $2b_1$ momentum profiles, indicating that the electron correlation and relaxation effects included in the CI wavefunctions are not significant for this momentum profile. The TMPs are in good agreement with the XMP in terms of the position of the profile maximum (p_{MAX}), which occurs at ≈ 0.9 au, but underestimate the experimental intensity below ≈ 1 au. This could be due, in part, to errors in choosing the scale factor used to place theory and experiment on the same intensity scale (Figure 4.6). However, even if the XMP was rescaled to agree with the TMPs at p_{MAX}, the experimental data would still be higher than theory near zero momentum, where the TMPs drop to essentially zero intensity. Although the reason for this discrepancy is not clear, it is worth noting two things: the low momentum region, which corresponds approximately to the outermost spatial regions of the orbital, tends to

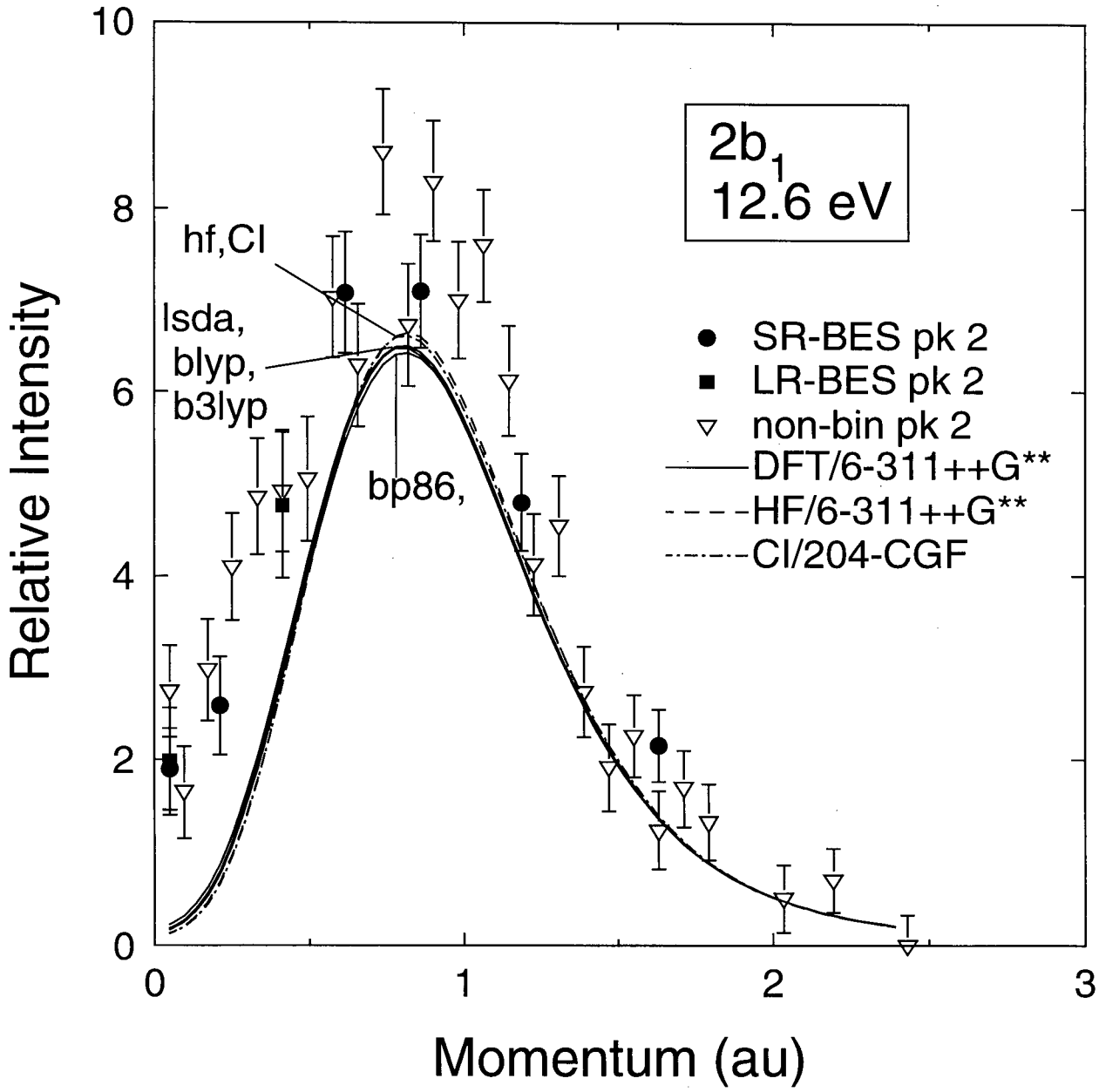

Figure 4.8: Experimental and theoretical $2b_1$ momentum profiles of acetone. The XMPs are of fitted peak 2 (IP=12.6 eV, see Figure 4.4) from the SR-BES (•), LR-BES (■) and non-bin (▽) data sets. The TMPs have been determined from the theoretical calculations listed in Table 4.4. The MRSD-CI TMP is that of Wang and Davidson from Reference [54]. The experimental angular resolution has been accounted for in the theoretical profiles using the GW-PG method [48].

be the region most sensitive to inadequacies in the theoretical calculations (see Section 1.1.2 and References [9, 35]), and the $2b_1$ TMP is amongst those most strongly affected by the orientations of the methyl groups (Figure 4.2)—suggesting that the neglect of vibrational effects when calculating the TMPs may be contributing to the observed discrepancy.

The $4b_2$ XMP, with an IP of 13.4 eV, is compared with the corresponding TMPs in Figure 4.9. This orbital consists primarily of C to in-plane H and C–C σ-bonding. All of the TMPs shown in Figure 4.9 predict a two-lobed momentum profile. The DFT profiles are in close agreement at high momentum (above $\sim$ 0.8 au), with somewhat greater differences at low momentum. The HF TMP differs from the DFT profiles in predicting that the high-momentum lobe is of appreciably greater intensity than the low-momentum lobe. Unfortunately, the scatter in the $4b_2$ XMP precludes comment on the relative quality of the TMPs. If just the binning mode data are considered (• and ■), a significant disagreement with theory is evident for the three high-momentum data points. In contrast, the non-binning mode data (∇) are in good agreement with the TMPs at high momentum (at least above 1.2 au) but disagree considerably at intermediate momenta. This is most likely because of difficulties in fitting the $(4b_2)^{-1}$ ionization peak as a result of the close proximity of the much more intense $(8a_1)^{-1}$ ionization (see Figure 4.10, below), which from PES has an IP of 14.1 eV [125]. This explains the two particularly high data points in the non-bin $4b_2$ XMP near 0.5 au, which correspond to low points in the $8a_1 + 1a_2$ XMP.

The XMP of fitted peak 4 at a binding energy of 14.3 eV is shown in Figure 4.10 and compared with the sum of $8a_1$ and $1a_2$ TMPs. MO calculations indicate that the $8a_1$ orbital is responsible primarily for C–O σ-bonding and the $1a_2$ MO is almost solely involved in bonding between the methyl carbons and out-of-plane hydrogens. The TMPs shown in Figure 4.10 are very similar; the various DFT TMPs differ only in the predicted intensity at p_{MAX} and, in comparison to the DFT TMPs, the HF TMP is shifted slightly to higher

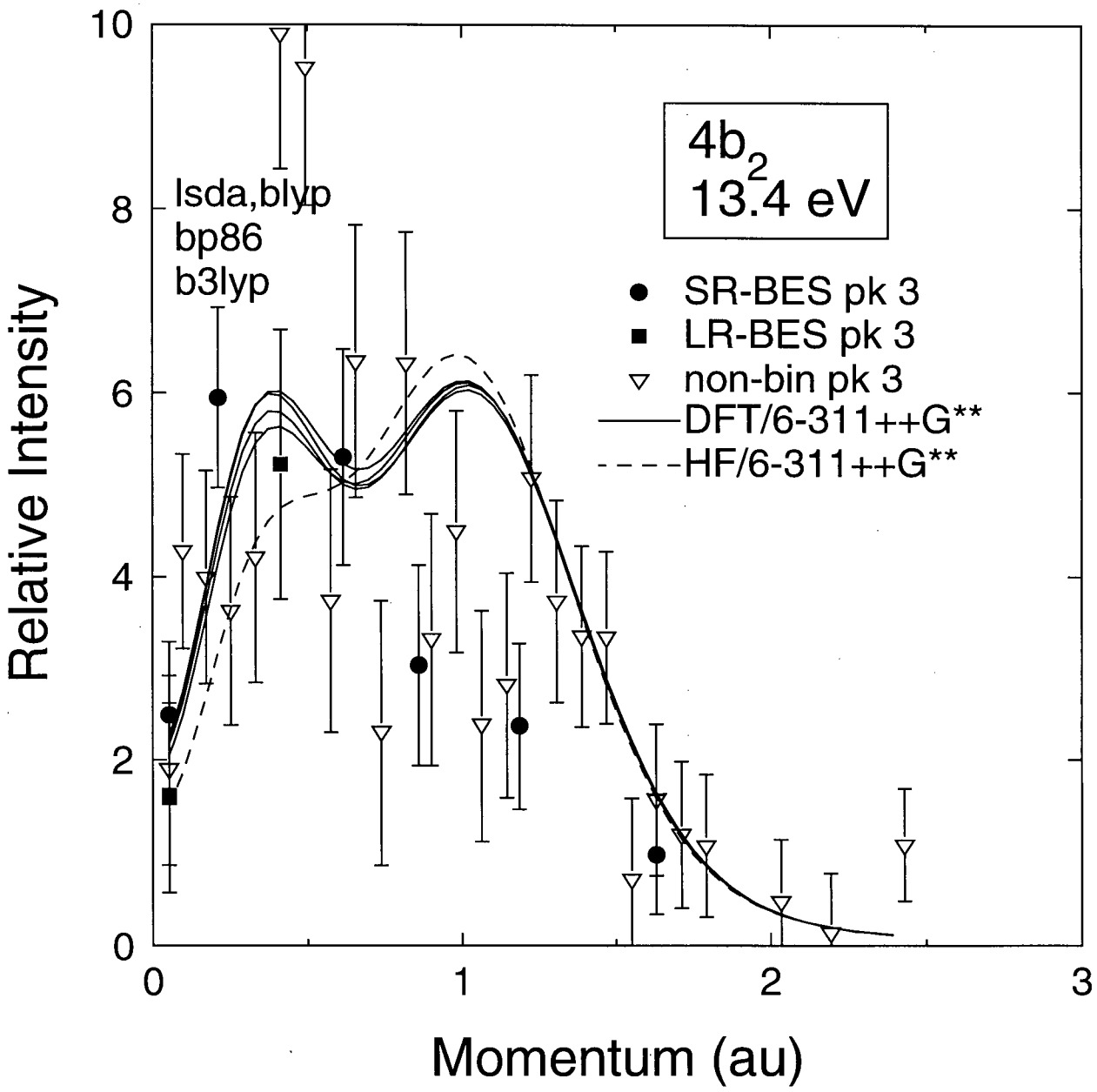

Figure 4.9: Experimental and theoretical $4b_2$ momentum profiles of acetone. The XMPs are of fitted peak 3 (IP=13.4 eV, see Figure 4.4) from the SR-BES (•), LR-BES (■) and non-bin (▽) data sets. The TMPs have been determined from the theoretical calculations listed in Table 4.4. The experimental angular resolution has been accounted for in the theoretical profiles using the GW-PG method [48].

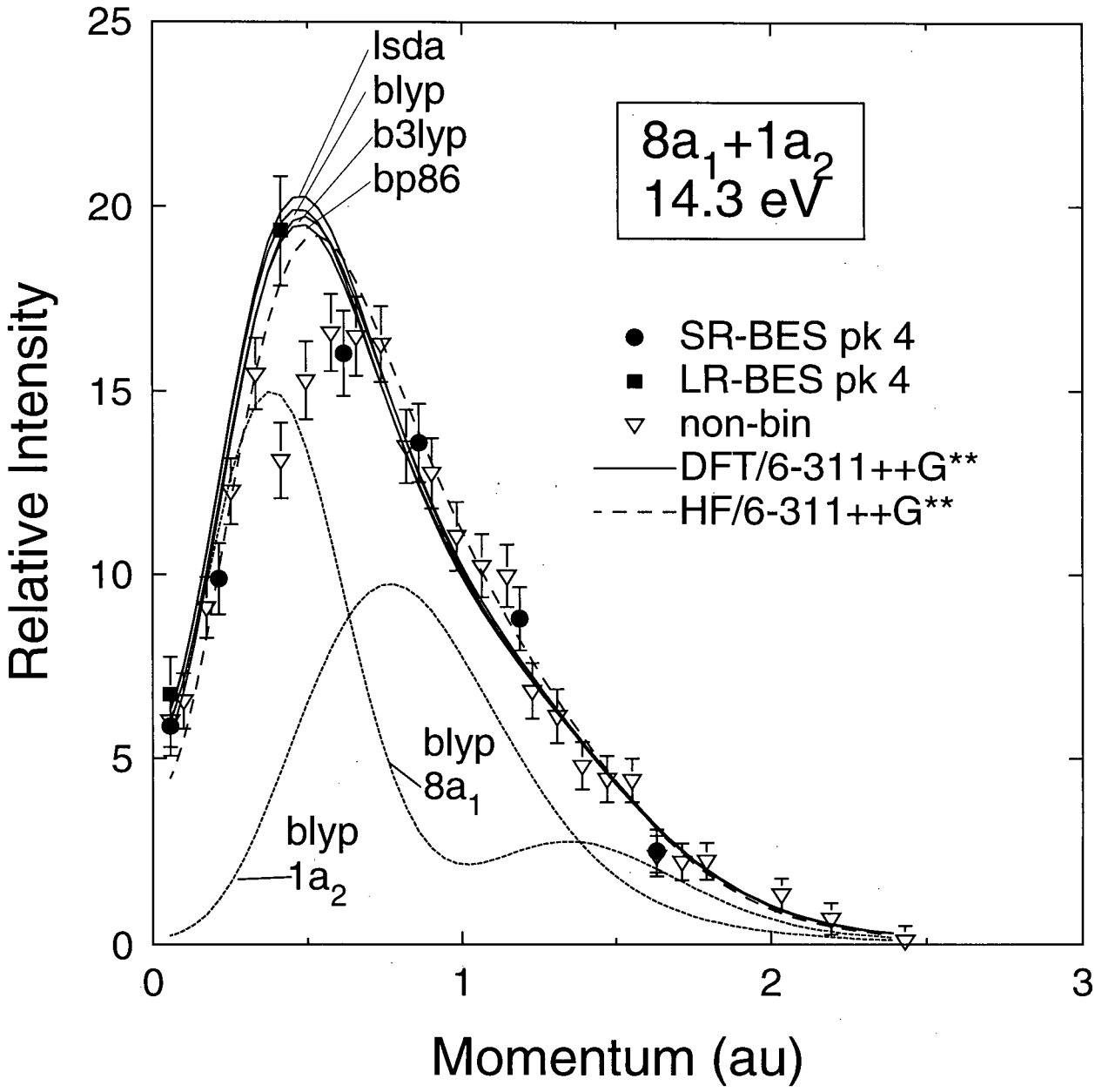

Figure 4.10: Experimental and theoretical $8a_1 + 1a_2$ momentum profiles of acetone. The XMPs are of fitted peak 4 (IP=14.3 eV, see Figure 4.4) from the SR-BES (•), LR-BES (■) and non-bin (▽) data sets. The TMPs are the sum of the $8a_1$ and $1a_2$ TMPs determined from the theoretical calculations listed in Table 4.4. The individual BLYP-DFT $8a_1$ and $1a_2$ TMPs are also shown. The experimental angular resolution has been accounted for in the theoretical profiles using the GW-PG method [48].

momentum. With the exception of two data points near 0.5 au, the agreement between experiment and theory is very good. As discussed in the preceding paragraph, the two low points in the non-bin $8a_1 + 1a_2$ XMP correspond to high points in the $4b_2$ XMP, indicating a failure to fully deconvolute these closely spaced ionization peaks in the fitting procedure.

The experimental and theoretical $7a_1 + 3b_2 + 1b_1$ momentum profiles of acetone are shown in Figure 4.11. As is discussed in Section 4.4 above, two peaks (numbers 5 and 6) have been used to fit the binding energy region corresponding to ionization from the $7a_1$, $3b_2$ and $1b_1$ orbitals. This was found to be necessary to obtain a good fit to the BES data. The very close energy spacing (0.4 eV) of these two fitted peaks makes it unlikely that peaks 5 and 6 will individually correspond to ionizations from different MOs. Consequently, only their sum is considered in Figure 4.11. The individual TMPs of these three orbitals are all p-type and consequently sum to give a p-type profile. The calculations all predict essentially the same profile shape and position of p_{MAX} with only small differences in intensity at p_{MAX}. The XMP is of similar shape to the TMPs, but of considerably less intensity. This represents a breakdown of the single-particle model of ionization and indicates that the spectroscopic factors (see Section 2.2.3) of one or more of these ionization peaks are significantly less than unity (or more correctly, less than those of the outer-valence ionizations used to normalize theory and experiment in Figure 4.6). This differs from the results of the Green's function calculation [125] shown in Table 4.3, which predict that the pole strengths of all of the outer-valence ionizations are approximately equal. A scale factor of 0.67 is necessary to bring the BLYP-DFT TMP into agreement with the XMP in Figure 4.11. It is not possible to comment further regarding the individual spectroscopic factors of the $(7a_1)^{-1}$, $(3b_2)^{-1}$ and $(1b_1)^{-1}$ ionization processes because of their similar ionization potentials and momentum profiles.

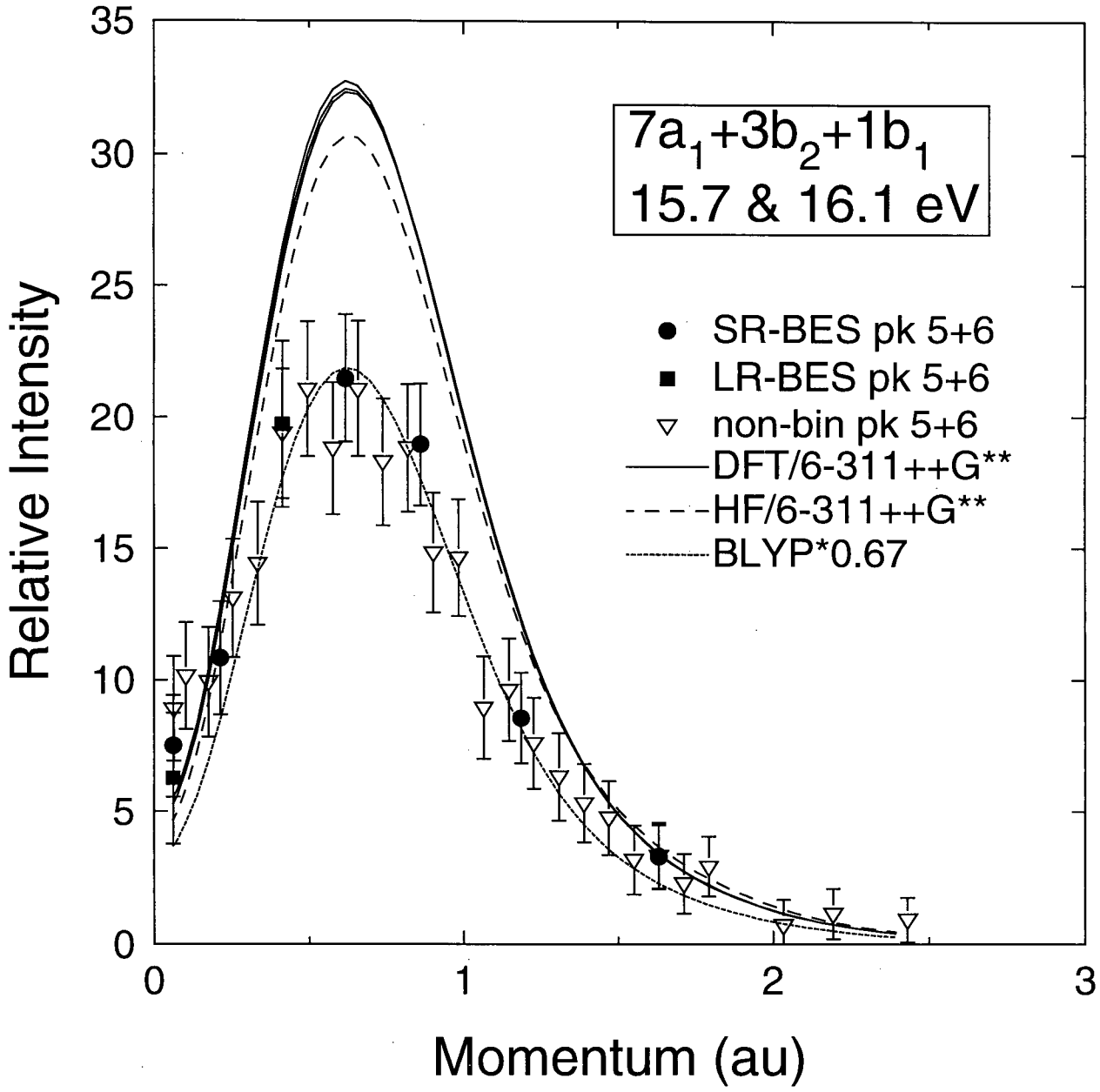

Figure 4.11: Experimental and theoretical $7a_1 + 3b_2 + 1b_1$ momentum profiles of acetone. The XMPs are the sums of fitted peaks 5 and 6 (IPs=15.7 and 16.1 eV, see Figure 4.4) from the SR-BES (•), LR-BES (■) and non-bin (▽) data sets. The TMPs are the sum of the $7a_1$, $3b_2$ and $1b_1$ TMPs determined from the theoretical calculations listed in Table 4.4. The short-dashed line is the BLYP-DFT TMP scaled by 0.67 to better match the experimental data. The experimental angular resolution has been accounted for in the theoretical profiles using the GW-PG method [48].

4.5.2 Inner-valence momentum profiles

The $6a_1$, $2b_2$, $5a_1$ and $4a_1$ inner-valence orbitals of acetone are essentially non-bonding orbitals resembling atomic 2s orbitals of the oxygen and carbon atoms. The experimental and theoretical momentum profiles corresponding to ionization from the $6a_1$ MO at 18.0 eV are shown in Figure 4.12. As was clear from the binding energy spectra in Figure 4.4, this is a strongly s-type momentum profile that drops off quickly in intensity with increasing momentum. The largest contribution to the $6a_1$ MO comes from 2s density on the carbonyl carbon. However, there are also significant contributions, of opposite phase to that from the carbonyl carbon, from 2s density on the methyl carbons and oxygen. The opposite phases of the carbonyl carbon contribution and those from the remaining heavy atoms results in a nodal surface surrounding the carbonyl carbon and produces the minimum in the momentum profile near 0.5 au. All of the $6a_1$ TMPs shown in Figure 4.12 are in good agreement with one another. In contrast, the binning and non-binning XMPs are of somewhat different shape, particularly in the momentum range 0.5–1.0 au. The non-binning XMP has been obtained from the very edge of the binding energy range monitored during the non-binning mode data collection. The detection efficiency at the edge of the monitored binding energy range is very low and consequently the non-binning $6a_1$ XMP is of questionable reliability. Therefore, the comparison between theory and experiment for the $6a_1$ momentum profiles will be performed using the binning-mode experimental data only. The $6a_1$ XMP is of similar shape to the TMPs shown in Figure 4.12, but of lesser intensity. This is particularly evident near zero momentum. The most likely explanation for this is that the spectroscopic factor for this ionization is less than one. If the BLYP-DFT TMP is scaled by 0.86 (determined by a fit of the BLYP-DFT TMP shape to the XMP) reasonable agreement in terms of both shape and intensity is obtained, although the two data points near 0.5 au are somewhat higher than the TMP.

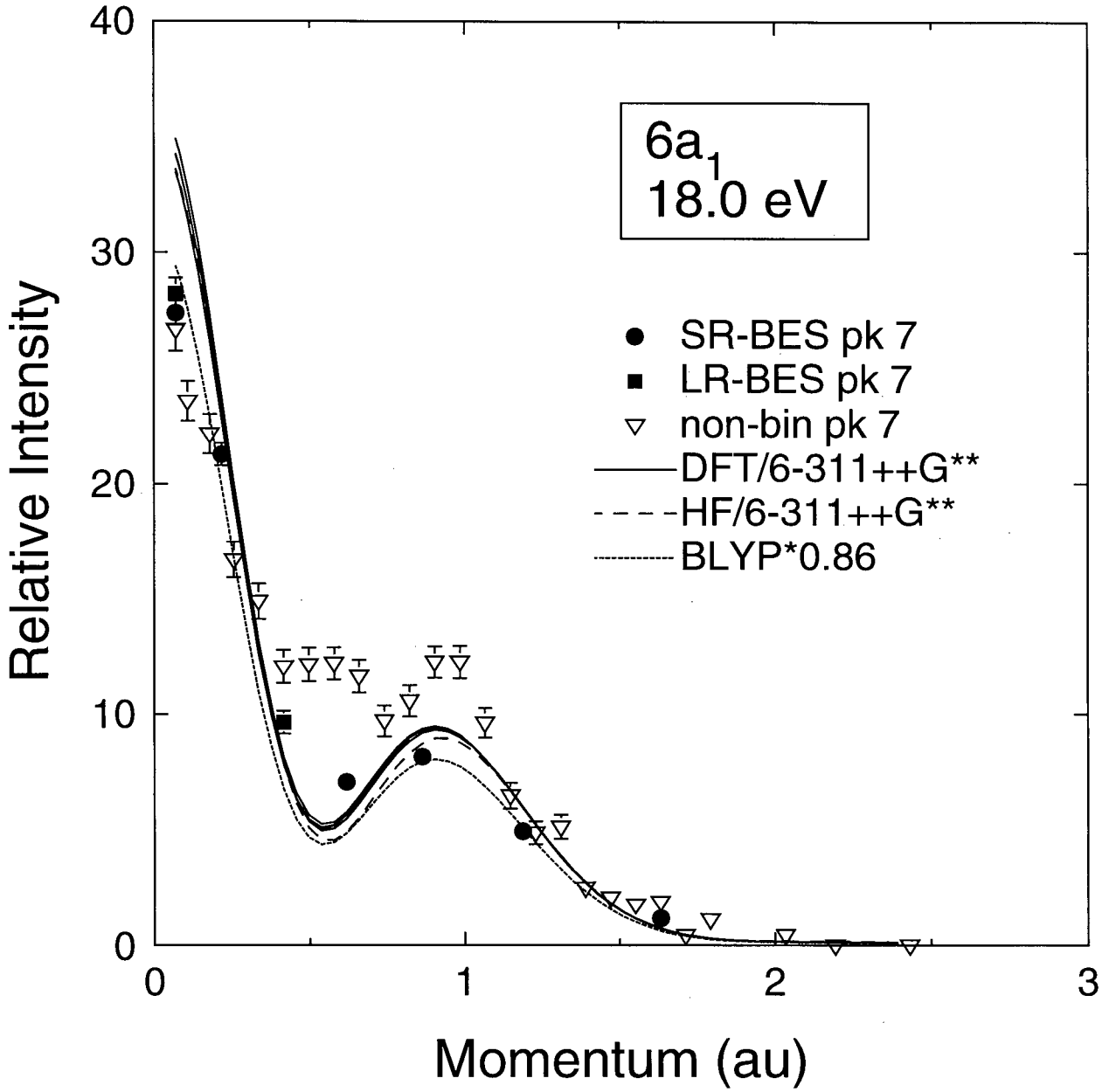

Figure 4.12: Experimental and theoretical $6a_1$ momentum profiles of acetone. The XMPs are of fitted peak 7 (IP=18.0 eV, see Figure 4.4) from the SR-BES (•), LR-BES (■) and non-bin (▽) data sets. The TMPs have been determined from the theoretical calculations listed in Table 4.4. The short-dashed line is the BLYP-DFT TMP scaled by 0.86 to better match the binning-mode (SR-BES and LR-BES) data. The experimental angular resolution has been accounted for in the theoretical profiles using the GW-PG method [48].

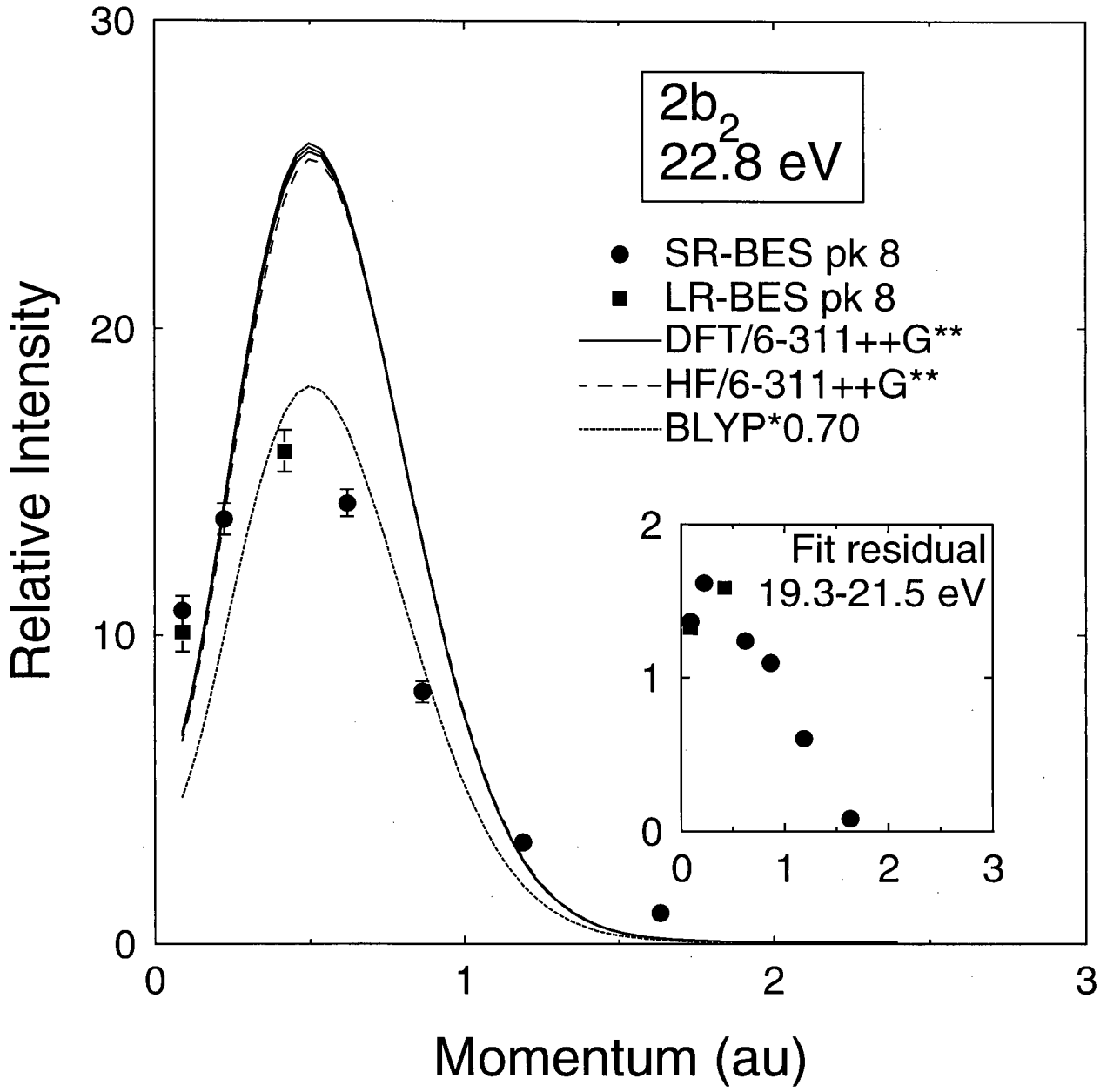

Figure 4.13: Experimental and theoretical $2b_2$ momentum profiles of acetone. The XMPs are of fitted peak 8 (IP=22.8 eV, see Figure 4.4) from the SR-BES (•) and LR-BES (■) data sets. The TMPs have been determined from the theoretical calculations listed in Table 4.4. The short-dashed line is the BLYP-DFT TMP scaled by 0.70 to better match the experimental data. The experimental angular resolution has been accounted for in the theoretical profiles using the GW-PG method [48]. The inset shows the momentum profile of the BES fit residual summed from 19.3–21.5 eV.

The experimental and theoretical $2b_2$ momentum profiles of acetone are shown in Figure 4.13. The 2s intensity of the $2b_2$ orbital is centred on the methyl carbons and is of opposite phase, resulting in the p-type momentum profile seen in Figure 4.13. As was the case for the $6a_1$ profiles, the $2b_2$ TMPs are all essentially the same and of significantly greater intensity than the XMP. A fit of the BLYP-DFT TMP to the XMP results in a scale factor of 0.70 and the rescaled TMP shown in Figure 4.13. The agreement between the rescaled TMP and the XMP is poor. This is most likely at least partly the result of limitations of the fitting procedure resulting in contributions from the neighbouring and strongly s-type $6a_1$ and/or $5a_1$ momentum profiles. If this is the case, it would suggest that the spectroscopic factor for the $2b_2$ ionization at 22.8 eV is even less than 0.7.

There is additional intensity observed in the BES between 20 and 22 eV that is not accounted for by the least-squares fit, as was mentioned in Section 4.4. The momentum profile of the fit residual in this binding energy region is shown in the inset of Figure 4.13. The magnitude of the intensity unaccounted for in the BES fit is clearly small in comparison to that of the adjacent $(6a_1)^{-1}$ and $(2b_2)^{-1}$ peaks. The shape of the resulting XMP may be classified as p-type, but it differs from all of the valence TMPs of acetone. The considerable intensity at low momentum suggests that some of this intensity is from the s-type $(6a_1)^{-1}$ ionization. The remaining p-type intensity could be from the $(2b_2)^{-1}$ ionization at 22.8 eV. However, this seems unlikely considering the 1.4 eV fwhm experimental energy resolution. A more likely explanation is that there is a low-intensity p-type ionization pole near 20 eV. Such a pole could belong to the $7a_1$, $3b_2$, $1b_1$ or $2b_2$ ionization manifolds, all of which have the correct symmetry and are missing some intensity in their main ionization peaks.

The final two inner-valence profiles of acetone are shown in Figures 4.14 and 4.15. An angle rather than momentum scale has been used for the $4a_1$ profiles because the experimental profiles have been obtained by summing data over a wide energy range and the conversion

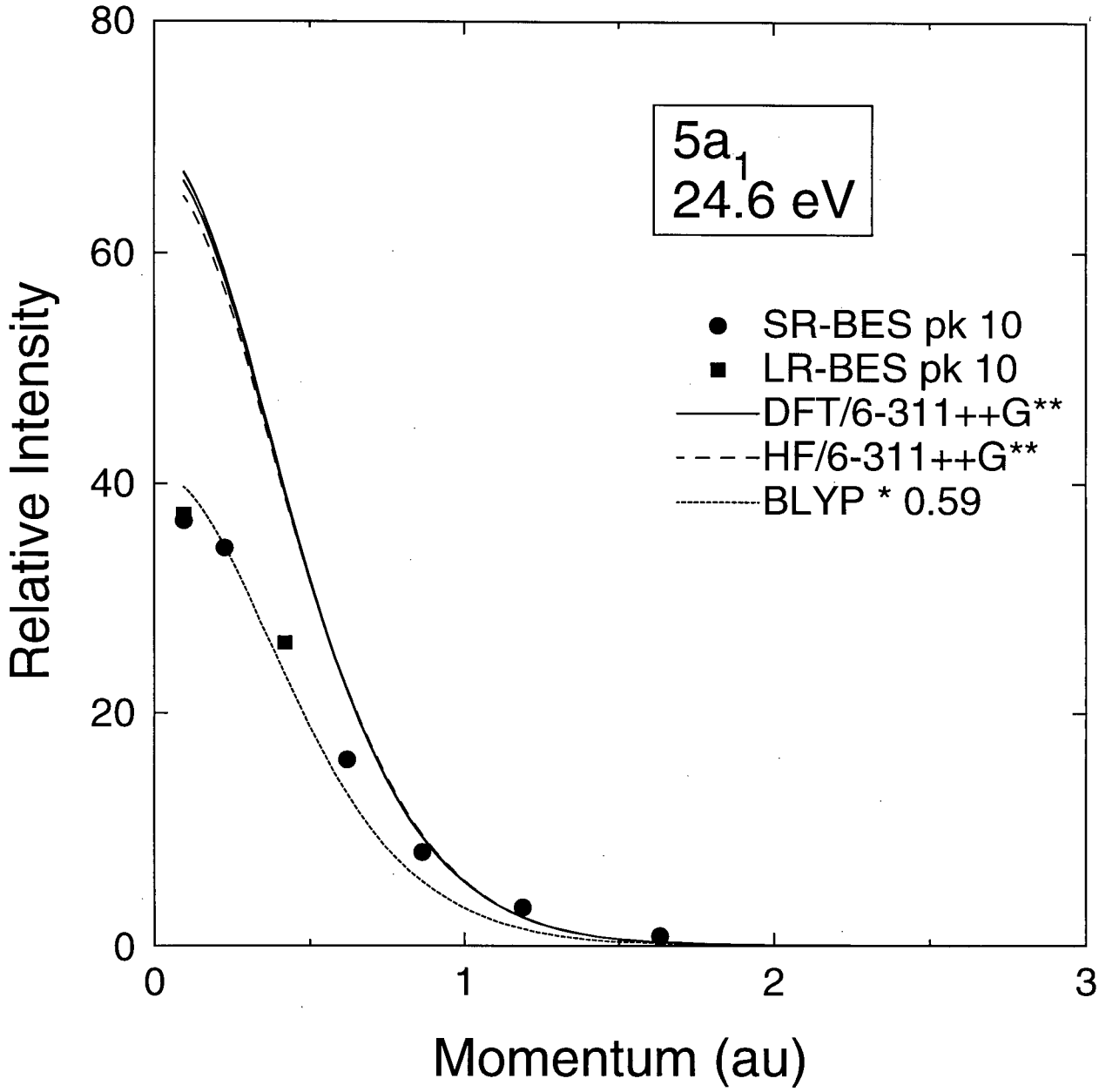

Figure 4.14: Experimental and theoretical $5a_1$ momentum profiles of acetone. The $5a_1$ XMPs are of fitted peak 9 (IP=24.6 eV, see Figure 4.4) from the SR-BES (•) and LR-BES (■) data sets. The TMPs have been determined from the theoretical calculations listed in Table 4.4. The short-dashed line is the BLYP-DFT TMP scaled by 0.59 to better match the experimental data. The experimental angular resolution has been accounted for in the theoretical profiles using the GW-PG method [48].

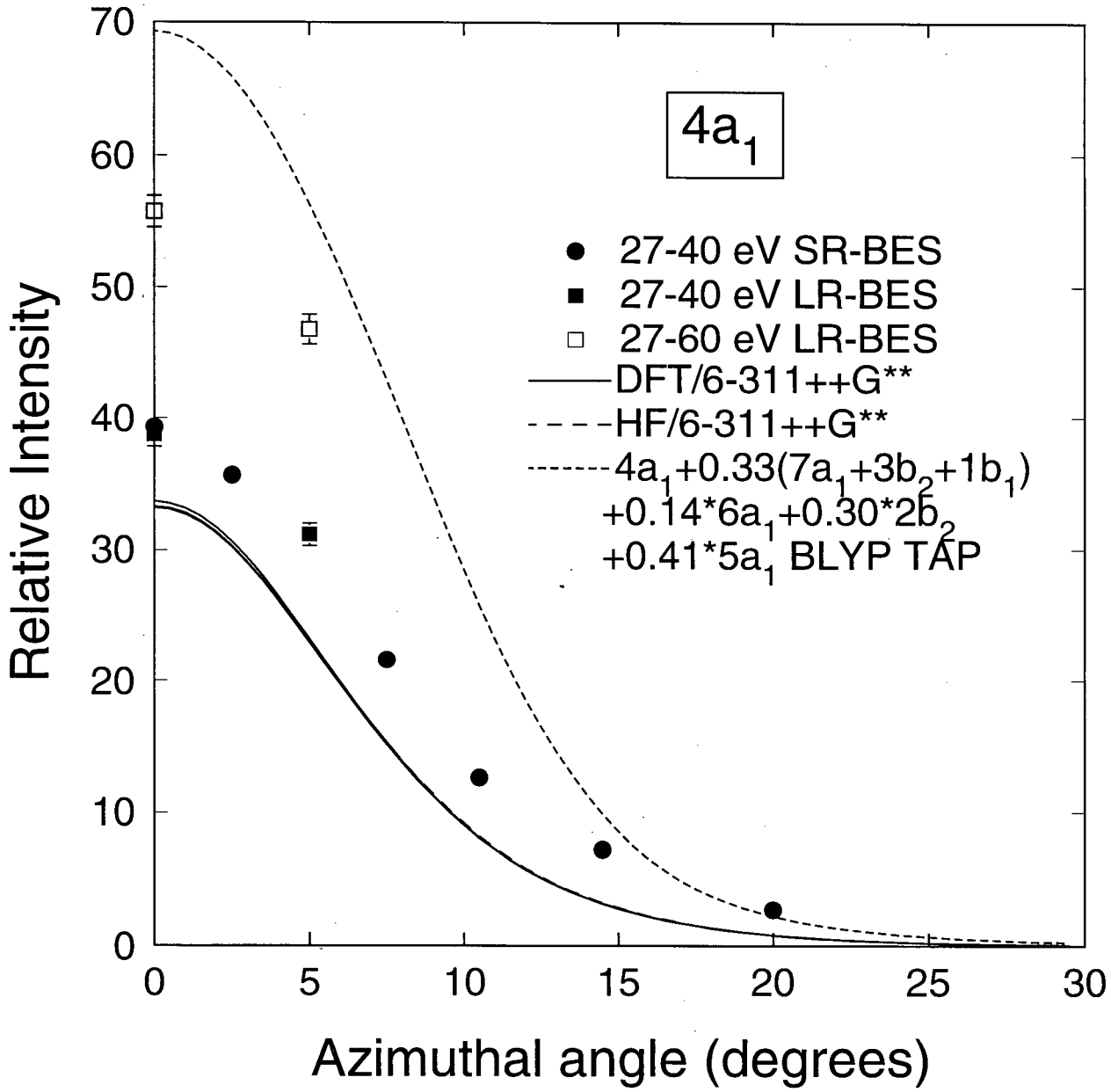

Figure 4.15: Experimental and theoretical $4a_1$ angle profiles of acetone. The $4a_1$ XAPs have been obtained by summing the SR-BES (•) and LR-BES (■) binding energy data from 27–40 eV and by summing the LR-BES data from 27–60 eV (□). The TAPs have been determined from the theoretical calculations listed in Table 4.4. The short-dashed line is the sum of the indicated BLYP-DFT TAPs. The experimental angular resolution has been accounted for in the theoretical profiles using the GW-PG method [48]. A binding energy of 34.0 eV has been use to resolution fold the $4a_1$ TAPs.

between azimuthal angle and momentum is binding energy dependent (see Equation (2.5)). The $5a_1$ MO consists of in-phase 2s character on the three carbon atoms and opposite phase 2s character on the oxygen. In contrast, the $4a_1$ MO consists almost entirely of oxygen 2s character. Ionization from both orbitals results in s-type momentum profiles, with little variation evident between the TMPs from different calculations. In both cases, the experimental profiles differ significantly in intensity from the theoretical profiles. Multiplication of the BLYP-DFT TMP in Figure 4.14 by 0.59 results in reasonably good agreement between experiment and theory for the $5a_1$ momentum profiles.

The $4a_1$ experimental profiles in Figure 4.15 obtained by summing binding energy data from 27–40 eV are of greater intensity than the corresponding TMPs. This result is readily explained by the presence of ionization poles from other valence ionization manifolds in this binding energy range. In view of the considerable intensity present at binding energies greater than 40 eV, it is most likely that some of the $4a_1$ ionization intensity is located in poles occurring outside of the 27–40 eV binding energy range. The shape of the experimental profiles in Figure 4.15 indicates that the majority of the intensity at binding energies greater than 27 eV is the result of ionization from the $5a_1$ and $4a_1$ orbitals. The short-dashed curve in Figure 4.15 represents the sum of the BLYP-DFT $4a_1$ TAP and the $7a_1$, $3b_2$, $1b_1$, $6a_1$, $2b_2$ and $5a_1$ TAPs scaled by the intensity absent from their main ionization peaks. The discrepancy between the dashed line and the 27–60 eV sum XAP (□) suggests that additional valence ionization intensity of acetone is present above 60 eV, which is also suggested by the BES shown in Figure 4.4.

Chapter 5

Dimethoxymethane

5.1 Introduction

An understanding of the electronic structure and electron density distribution of dimethoxymethane ($CH_2(OCH_3)_2$) is of interest in the fields of polymer and carbohydrate chemistry, as it may be viewed as a model compound for both polyoxymethylene ($(CH_2O)_x$) and the acetal linkage in polysaccharides. Dimethoxymethane is of particular interest as a model for studying the anomeric effect. The anomeric effect was originally observed in sugars as the preference of a methoxy substituent at the anomeric carbon to be in the axial rather than the equatorial position, contrary to what would be expected from steric arguments alone. It has since been recognized as a more general effect found in molecules of the type R–X–C–Y where Y is electronegative and X has at least one pair of non-bonding electrons. The preference of electronegative substituents for the axial position in sugars corresponds to a gauche orientation about the X–C bond in R–X–C–Y. The anomeric effect is also characterized by bond lengths that differ from typical values.

Several explanations for the anomeric effect have been proposed. They may be generally grouped into two categories:

1. Electrostatic interactions between the dipoles associated with X and Y destabilize the anti orientation and stabilize the gauche orientation.

2. The gauche orientation maximizes the stabilizing interaction between the non-bonding electron density of X and the vacant σ^* C–Y antibonding orbital.

A detailed overview of the anomeric effect may be found in Reference [72]. Reference [132] is a collection of more recent research in this area, including attempts to identify the primary factor(s) responsible for the anomeric effect.

In the case of dimethoxymethane, both RX and Y are methoxy groups, so in light of the above discussion one might expect gauche orientations about each of the CH_2–O bonds to be favoured. This was found to be the case by Kubo [133] well before the anomeric effect had itself been recognized. From a consideration of the experimental dipole moment of dimethoxymethane, Kubo concluded that the two methyl groups were located on opposite sides of the O–C–O plane. An electron diffraction study [134] confirmed that dimethoxymethane exists in the gas phase predominantly in the gauche-gauche (gg) conformation (Figure 5.1). The temperature dependence of the gas phase dipole moment [135] and ^{13}C–^{1}H NMR vicinal coupling constants [136] as well as vibrational spectroscopy studies [137] of dimethoxymethane indicate that the gauche-anti (ga) conformer is also present in small amounts. Estimates of the gas-phase energy difference between these two conformers, $\Delta G_{\mathrm{ga-gg}}$, based upon these experimental results range from 5.9 to 10.5 kJ/mol [135–138].

Much of the theoretical work involving dimethoxymethane has focused on the geometries and relative energies of the various conformations. Both *ab initio* and DFT calculations have been shown to reproduce successfully the anomeric effect [139–142]. In addition to the global energy minimum gg conformation and the next most stable ga conformation mentioned above, two other energy minima have been identified [142]: the g^+g^- conformation in which

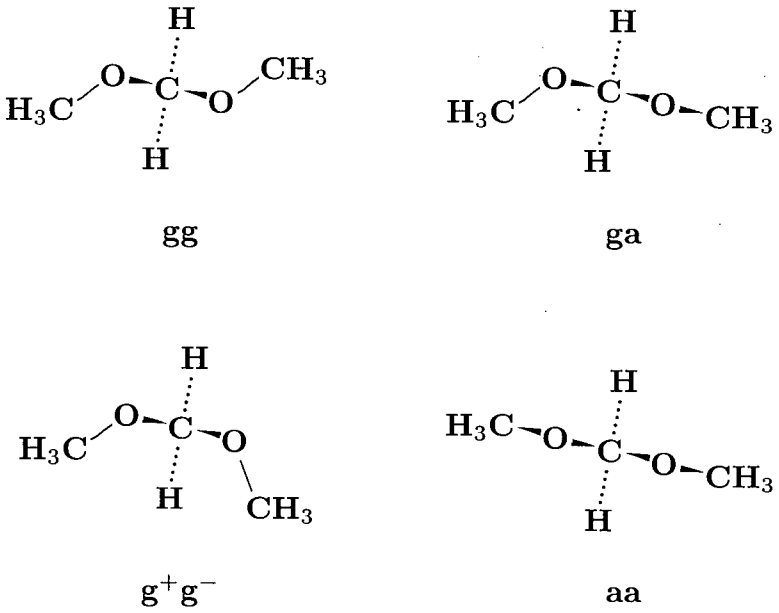

Figure 5.1: Conformations of dimethoxymethane

the orientations about each CH_2–O bond are gauche but, in contrast to the gg conformer, both methyl groups are on the same side of the O–C–O plane, and the aa conformation in which all carbon and oxygen atoms are in approximately the same plane. These four energy-minimum conformations are shown in Figure 5.1. The computational studies of Wiberg and Murcko [140] and Smith et al. [141] indicate that increasing basis set size by the addition of diffuse and polarization functions lowers the energies of the less stable conformers relative to that of the gg conformer. The inclusion of electron correlation was found to have the opposite effect on the relative conformer energies. However, Smith et al. [141] concluded that electron correlation effects were not significant in obtaining optimized geometries. In contrast, Kneisler and Allinger found that electron correlation did have a significant effect on the C–O–C–O dihedral angles and concluded that it should be included in geometry optimizations [142]. They also found that B3LYP-DFT and MP2 calculations resulted in optimized geometries in good agreement with each other and with experiment.

In the present work, a comprehensive investigation of the momentum space valence orbital electron densities of dimethoxymethane has been performed. Experimental data obtained using EMS have been compared with theoretical results obtained from HF, CI and DFT calculations in order to assess the importance of electron correlation effects and basis set size and composition to the accurate description of the valence orbital electron densities of dimethoxymethane. The need to account for conformations other than the most stable gg when interpreting the experimental results and the relationship between molecular conformation and orbital electron density are also investigated.

5.2 Experimental details

Three sets of binding energy spectra of dimethoxymethane have been recorded: long binding energy range spectra (LR-BES) from 4.5–58.7 eV at out-of-plane azimuthal angles of 0° and 9°; outer-valence spectra (OV-BES) from 5.3–23.6 eV at 16 azimuthal angles from 0° to 30°; and inner valence spectra (IV-BES) from 17.9–44.0 eV at 14 azimuthal angles between 0° and 30°. The BES were recorded in the binning data collection mode (Section 3.4.2) at a total energy of 1200 eV. Many scans were accumulated over an appreciable measuring time ($\approx$ 640 hours) in order to improve the signal to noise ratio. The experimental energy resolution function (1.5 eV fwhm) and momentum resolution ($\approx$ 0.1 au fwhm) of the spectrometer were determined from measurements of the helium $(1s)^{-1}$ ionization peak and the argon 3p momentum profile, respectively. The liquid dimethoxymethane sample was obtained from Aldrich Chemical Company, Inc. and had a stated purity of 99%. Dissolved gaseous impurities were removed by repeated freeze-pump-thaw cycles. The sample gas pressure was maintained at 1×10^{-5} torr. Temperature related pressure fluctuations were minimized by immersing the glass sample tube in a constant temperature water bath.

5.3 Computational details

Theoretical momentum profiles of the valence orbitals of dimethoxymethane have been obtained using either the target Hartree–Fock approximation (Equation (2.11)) or the target Kohn–Sham approximation (Equation (2.14)) and the results of single-point HF or DFT calculations, respectively. A range of basis sets of increasing complexity have been used. They are described in Section 2.3.4, with the exception of the 229-CGF basis set described below.

The dependence of the Kohn–Sham DFT results on the exchange–correlation potential energy functional has been investigated by performing DFT calculations using three different functionals. The Vosko, Wilk and Nusair functional [99] was used to perform local spin-density approximation (LSDA) calculations. In addition, two non-local functionals were used: the BP86 functional including the Perdew correlation [106] and Becke exchange [105] gradient corrections and the B3LYP functional, a modification of the hybrid functional proposed by Becke [108] and incorporating the exact exchange energy, with the Lee, Yang and Parr [107] gradient corrections to the correlation potential replacing those of Perdew and Wang [109].

The majority of the calculations have been performed using geometries optimized at the MP2(full) level with the 6-31+G* basis set. Additional geometry optimizations have been performed at the B3LYP/6-31+G* and B3LYP/6-311++G** levels. The optimized geometries are discussed in Section 5.8. GAUSSIAN92 [102] and GAUSSIAN94 [103] were used to perform all of the above mentioned calculations.

To investigate further the effects of electron correlation and relaxation, TMPs corresponding to the two lowest energy ionization processes $((10b)^{-1}$ and $(11a)^{-1})$ of the gg conformer of dimethoxymethane have been calculated by E. R. Davidson within the plane

wave impulse approximation using the results of MRSD-CI calculations of the initial neutral and respective final ion states of dimethoxymethane in the ion-neutral overlap expression of Equation (2.10). The configuration spaces for the multi-reference singles and doubles configuration interaction calculations of both the molecular target and ion wavefunctions were chosen from the results of respective single-reference singles and doubles configuration interaction perturbation calculations. For the CI calculations of both the ion and the neutral, the molecular orbitals of the neutral HF wavefunction were used; the HF virtual orbitals were first converted to K-orbitals [143–145] in order to improve the energy convergence. The CI calculations used frozen core electrons. A 229-CGF basis set has been used for the CI calculations and the HF calculation upon which they are based. This basis set is based on the highly converged atomic basis sets of Partridge [146,147] with the addition of Dunning's "double d" polarization functions [114] for carbon and oxygen and a single p polarization function (exponent 1.30) for hydrogen [148]. An (18s13p2d)/[6s7p1d] contraction has been used for carbon and oxygen and a (10s1p)/[5s1p] contraction for hydrogen. All six components of the Cartesian d functions were kept. This 229-CGF basis set for dimethoxymethane is the same as the 204-CGF acetone basis set described in Chapter 4 and Reference [54][1], with the exception that the two d polarization functions for carbon and oxygen have been contracted to a single two-term d function.

5.4 Valence binding energy spectra

Dimethoxymethane is a 42 electron molecule having, within an independent particle model, 16 valence orbitals and 5 core orbitals. The predominant gg conformer has C_2 symmetry, with three core orbitals of a symmetry and two of b symmetry. According to HF calculations,

[1] In Reference [54], this basis set was referred to incorrectly as 196-GTO and the hydrogen s function contraction was incorrectly stated to be (10s)/[7s] rather than the correct (10s)/[5s].

the valence orbitals alternate in symmetry between a and b, from the inner-valence 4a orbital to the 10b HOMO. From symmetry arguments, ionization from orbitals of b symmetry will result in p-type momentum profiles, or conversely all s-type momentum profiles must be the result of ionization from orbitals having a symmetry.

Binding energy spectra of dimethoxymethane from 4.5 to 58.7 eV at out-of-plane azimuthal angles of $\phi = 0°$ and 9° are shown in Figure 5.2 on a common intensity scale. The close energy spacing of the ionization peaks, their Franck–Condon widths and the EMS instrumental energy resolution of 1.5 eV fwhm allow only partial resolution of the ionization peaks. In order to obtain XMPs of the valence shell of dimethoxymethane, Gaussian functions representing the various valence ionization processes have been fitted to the BES. The individual fitted peaks are represented in Figure 5.2 by the dashed lines and the sums of the fitted peaks by solid lines. For the peaks occurring at binding energies less than 20 eV, the relative energy spacings and Franck–Condon widths were determined from the high resolution He (I) PES measurements of Jørgensen [149], shown in the upper panel of Figure 5.2. Small adjustments to the energy spacings of the peaks were made to account for asymmetries in the Franck–Condon envelopes. The peak widths used to fit the EMS data are a convolution of the Franck–Condon widths estimated from the PES data [149] and the EMS instrumental energy resolution function (1.5 eV fwhm). As a consequence of the close energy spacing of many of the ionization peaks, it was necessary in some instances to fit a function at a single binding energy to represent multiple ionization processes. This has been done for ionizations from MOs 10b and 11a, MOs 9a, 7b and 8a, and MOs 6b, 7a and 5b. In the case of the $(10b)^{-1}$ and $(11a)^{-1}$ ionizations, only a slight splitting was observed using PES [149] and, in the latter two cases, individual ionization peaks were not resolvable (see Figure 5.2), even with the considerably better PES energy resolution of 0.03 eV fwhm [149, 150]. The absolute energy scale of the EMS BES was fixed by setting the position of the first peak,

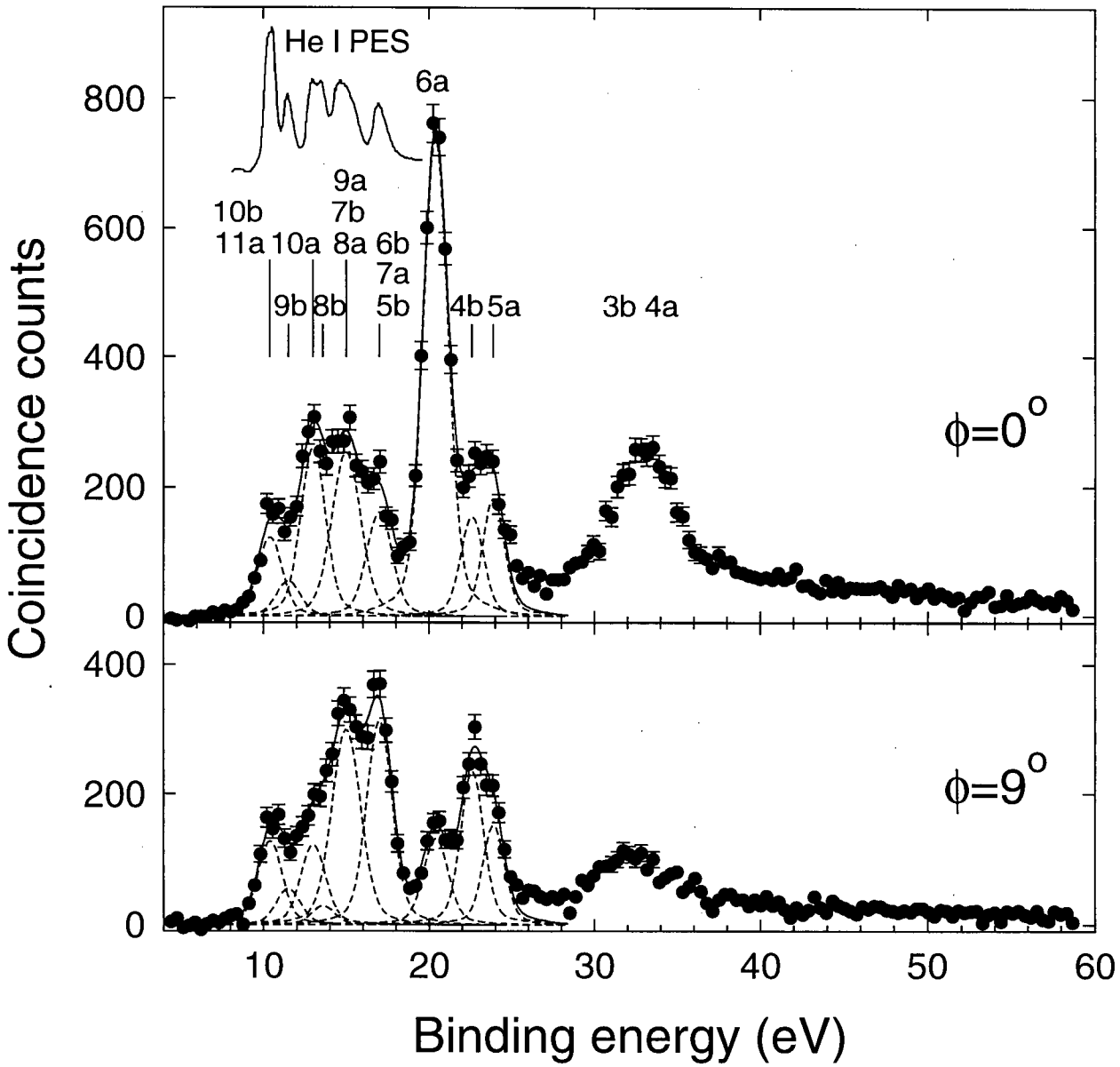

Figure 5.2: Binding energy spectra of dimethoxymethane from 4.5–58.7 eV. The BES (•) at $\phi = 0°$ and 9°, obtained at a total energy of 1200 eV, are shown in the upper and lower panels, respectively. The dashed lines indicate the result of a least-squares fit of Gaussian functions to the ionization peaks and the solid curves are the summed fits. The peak positions and assignments are indicated by the vertical lines. The high resolution (0.03 eV fwhm) He (I) PES of dimethoxymethane, reproduced from Reference [149], is shown in the upper panel on the same energy scale as the EMS data.

Table 5.1: Measured ionization potentials and calculated orbital energies of the valence shell of dimethoxymethane. Orbital energies are HF/aug-cc-pVTZ values for the MP2/6-31+G* optimized gg and ga conformers. All energies are in eV.

Orbital	PES		EMS[b]	−Orbital energy	
origin[a]	[149]	[151]	this work	gg	ga
10b	10.29	10.42	10.41	12.055	11.674
11a	10.53			12.059	12.011
9b	11.44	11.48	11.5	12.696	13.375
10a	12.98	12.92	13.0	14.268	13.692
8b	13.42	13.45	13.6	14.409	14.589
9a				15.532	15.833
7b	14.8	14.60	15.0	16.281	15.993
8a				16.598	16.774
6b				18.244	18.342
7a	17.0		17.0	18.742	18.572
5b				18.795	18.908
6a			20.4	22.843	23.128
4b			22.6	25.343	25.174
5a			23.9	26.598	26.575
3b				36.501	36.569
4a				38.391	38.439

[a]Orbital symmetry labels are those of the C_2 symmetry gg conformer.
[b]Estimated uncertainty ±0.1 eV. The EMS absolute energy scale was determined by setting the first ionization energy to 10.41 eV.

resulting from ionization from the 10b and 11a orbitals, to 10.41 eV, the average of the corresponding high resolution PES ionization potentials [149]. Ionization processes requiring energies greater than $\approx$ 20 eV are not observable by He (I) PES. Consequently, the positions and widths of the fitted peaks representing the $(6a)^{-1}$, $(4b)^{-1}$ and $(5a)^{-1}$ ionization processes have been determined by a fit to the 17.9–44.0 eV inner-valence BES (IV-BES) collected at 14 out-of-plane azimuthal angles ranging from $\phi = 0°$ to 30°. The ionization potentials used in the present work are compared in Table 5.1 with the published He (I) PES values of Jørgensen [149] and Zverev et al. [151] and calculated HF/aug-cc-pVTZ orbital energies of the MP2/6-31+G* optimized gg and ga conformers.

In the outer-valence region (below 20 eV) of the $\phi = 0°$ and 9° experimental BES, several

features are evident. Peaks resulting from ionizations from orbitals 10b and 11a at 10.41 eV, 10a at 13.0 eV, 9a, 7b and 8a at 15.0 eV and from orbitals 6b, 7a and 5b at 17.0 eV have a spacing which is consistent with the results of PES [149, 151], as indicated in Table 5.1 and Figure 5.2. The largest discrepancy is for the $(9a)^{-1} + (7b)^{-1} + (8a)^{-1}$ peak located at 15.0 eV in the current work. In the case of the PES work of Zverev et al. [151], only the leading edge of this peak is contained within the energy range reported, precluding an accurate determination of the position and not surprisingly resulting in a low value. In contrast, Jørgensen reports PES data of dimethoxymethane up to approximately 19.5 eV [149] (Figure 5.2), a range which fully contains the ionization band in question. This broad band, resulting from ionization from three different orbitals, extends from 14.0 to 16.2 eV in the PES data and lacks sufficient structure to allow the determination of individual vertical IPs. The asymmetric nature of the PES band results in a small shift to higher energy in the EMS data relative to the PES data as a consequence of the poorer EMS energy resolution. The $(9a)^{-1} + (7b)^{-1} + (8a)^{-1}$ peak at 15.0 eV and the $(6b)^{-1} + (7a)^{-1} + (5b)^{-1}$ peak at 17.0 eV each exhibit characteristic p-type behaviour, with greater intensity at $\phi = 9°$ than at $\phi = 0°$. In contrast, the $(10a)^{-1}$ peak at 13.0 eV is strongly s-type and the $(10b)^{-1} + (11a)^{-1}$ peak at 10.41 eV has similar intensity at the two azimuthal angles. The positions and intensities of the $(9b)^{-1}$ and $(8b)^{-1}$ ionizations do not allow resolution of these individual peaks in the BES. However, their inclusion in the fitting procedure, using physically realistic positions and widths determined from the PES data [149], is necessary to obtain a reasonable fit to the experimental EMS data. The origins of the 15.0 and 17.0 eV bands, not discussed in the PES studies [149, 151], have been assigned as indicated in Figure 5.2 and Table 5.1 and discussed above based upon an examination of the corresponding experimental momentum profiles of these peaks (see Section 5.5.1, below) and the calculated HF orbital energies shown in Table 5.1.

Three bands are evident in the inner-valence region (above 20 eV) of the binding energy spectra in Figure 5.2. The strong s-type peak at 20.4 eV can be readily assigned to the $(6a)^{-1}$ ionization on the basis of the calculated orbital energies (Table 5.1). The band between 22 and 25 eV appears to consist of two ionizations of differing symmetry, as indicated by the differences in the shape of the peak at $\phi = 0°$ and $\phi = 9°$. The low energy side of the peak displays p-type character, evidenced by the increased intensity in the $\phi = 9°$ spectrum, while the high energy side is of greater intensity at $\phi = 0°$. This observation, in combination with the calculated orbital energies in Table 5.1, supports an assignment of this band to $(4b)^{-1}$ and $(5a)^{-1}$ ionizations at 22.6 and 23.9 eV, respectively. The assignments of these ionization peaks are confirmed by an examination of the respective XMPs in Section 5.5.2 below.

The third ionization band in the inner-valence region is a broad s-type feature between approximately 28 and 37 eV. This is the region in which the parent $(3b)^{-1}$ and $(4a)^{-1}$ ionization processes are expected. However, no attempt has been made in the present work to fit peaks representing $(3b)^{-1}$ and $(4a)^{-1}$ ionizations because of the lack of structure in this BES band, the likelihood that there are many 'satellite' states in this energy range of the BES, and the lack of many-body calculations and synchrotron radiation or X-ray PES studies of dimethoxymethane to serve as a guide for the fitting procedure. Although there are no clear features in the BES above 37 eV, considerable intensity is still observed, particularly at $\phi = 0°$, indicating the presence of predominantly s-type many-body ionization processes (satellite states) in this region.

5.5 Experimental and theoretical momentum profiles

Experimental momentum profiles of the main peaks in the outer- and inner-valence regions of the dimethoxymethane BES have been obtained by performing least-squares fits of the LR-

BES (4.5–58.7 eV), OV-BES (5.3–23.6 eV) and IV-BES (17.9–44.0 eV) data sets described in Section 5.2. Gaussian functions were fixed at those binding energies and widths used to fit the LR-BES (Figure 5.2) and only the peak amplitudes were allowed to vary. For each fitted peak, the distribution of peak areas as a function of momentum, converted from ϕ using Equation (2.5), yields the corresponding experimental momentum profile, as discussed in Section 3.4.4. The three sets of BES data have been placed on the same intensity scale by normalizing the long range and inner-valence spectra to the outer-valence spectra using the respective data collected at $\phi = 0°$ and $\phi = 9°$ over the corresponding overlapping energy ranges of the data sets (i.e., 5.3–23.6 eV for the normalization of the LR-BES to the OV-BES and 17.9–23.6 eV for the normalization of the IV-BES to the OV-BES). Following these two normalizations, all XMPs share a common relative intensity scale. The resulting momentum profiles are shown in Figures 5.3 and 5.5 to 5.11, with data obtained from the OV-BES shown as filled circles (•), data from the IV-BES shown as open circles (○) and data from the LR-BES shown as open squares (□). The error bars are based upon the quality of the fits. Also shown in Figures 5.3–5.11 are theoretical momentum profiles of the corresponding orbitals or sums of orbitals, calculated using the MP2/6-31+G* optimized gg conformer of dimethoxymethane and a number of theoretical methods, as outlined in Section 5.3. The key to the TMP labels in Figures 5.3–5.11 is given in Table 5.2, along with selected calculated properties. TMPs of the gg conformer alone have been used for this comparison with the experimental data because, considering the calculated energy differences between the gg and ga conformers listed in Table 5.2 and the experimental temperature of 298 K, the sample is expected to consist overwhelmingly of dimethoxymethane in the gg conformation. The significance of contributions from other conformers is investigated in Section 5.7. The experimental and theoretical results have been placed on a common intensity scale by normalization of the 10b + 11a (10.41 eV) XMP to the corresponding B3LYP/6-311++G** TMP (Figure 5.3

Table 5.2: Calculated properties of the gauche-gauche (gg) and gauche-anti (ga) conformers of dimethoxymethane and key to the theoretical momentum profiles shown in Figures 5.3–5.11. The calculations were performed using the MP2/6-31+G* optimized geometries.

Key	Calculation	Total energy gg (hartree)	ΔE_0 ga − gg (kJ/mol)	Dipole moment gg (debye)	ga
hf-st	HF/STO-3G	-264.55318	10.23	0.135	1.787
hf-6g	HF/6-31G	-267.82738	16.64	0.342	2.855
	HF/6-31+G*	-267.95876	9.70	0.294	2.325
hf-6p	HF/6-311++G**	-268.03074	8.68	0.277	2.307
hf-229	HF/229-CGF	-268.06916		0.256	
	MP2(full)/6-31+G*	-268.73856	14.17		
ci-229	CI/229-CGF	-268.71508		0.263	
ld-6p	DFT LSDA[a]/6-311++G**	-267.43708	11.85	0.324	1.950
bp-6p	DFT BP86[b]/6-311++G**	-269.63211	10.62	0.312	1.882
b3-6p	DFT B3LYP[c]/6-311++G**	-269.63910	10.10	0.301	2.028

[a]The Vosko, Wilk and Nusair [99] local exchange–correlation functional was used.

[b]The Becke exchange [105] and Perdew correlation [106] functionals were used.

[c]The B3LYP functional is a modification of the hybrid functional proposed by Becke [108] and incorporating the exact exchange energy, with the Lee, Yang and Parr [107] correlation potential replacing that of Perdew and Wang [109].

below). This theoretical momentum profile was chosen for the normalization since it agrees most closely in shape with the XMP.

5.5.1 Outer-valence momentum profiles

The 10b + 11a experimental and theoretical momentum profiles are shown in Figure 5.3. These two orbitals are, to a first approximation, non-bonding orbitals predominantly centred on the two oxygen atoms and represent antisymmetric and symmetric combinations of the oxygen n_π orbitals[2], respectively. There is reasonable agreement between the three DFT calculations (ld-6p, bp-6p and b3-6p) and the experimental profile. In contrast, none of the HF calculations predict the rise in intensity observed experimentally below 0.5 au. In all cases, the theoretical calculations predict greater intensity at high momentum (> 1 au) than is observed experimentally. To investigate the possibility that this discrepancy between the HF and DFT results is a consequence of the neglect of electron correlation effects in the case of the HF calculations, MRSD-CI calculations of the neutral target and two final ion states have been performed by E. R. Davidson and a theoretical momentum profile has been calculated using the CI wavefunctions and the target-ion overlap expression (Equation (2.10)). The resulting TMP (ci-229, dashed line in Figure 5.3) is fairly similar to the HF results and certainly does not reproduce the low p behaviour of either the DFT calculations or the experimental profile.

To understand better the shapes of the 10b + 11a momentum profiles and the differences between the computational methods, it is useful to consider the individual 10b and 11a TMPs, shown in Figure 5.4. Note that the HF/6-31G calculation (hf-6g) reverses the energetic ordering of the (very closely spaced in energy) 10b and 11a orbitals with respect to

[2] n_π refers to non-bonding oxygen orbitals having the majority of the electron density perpendicular to the COC planes; n_σ refers to those having the majority of the electron density in the COC planes.

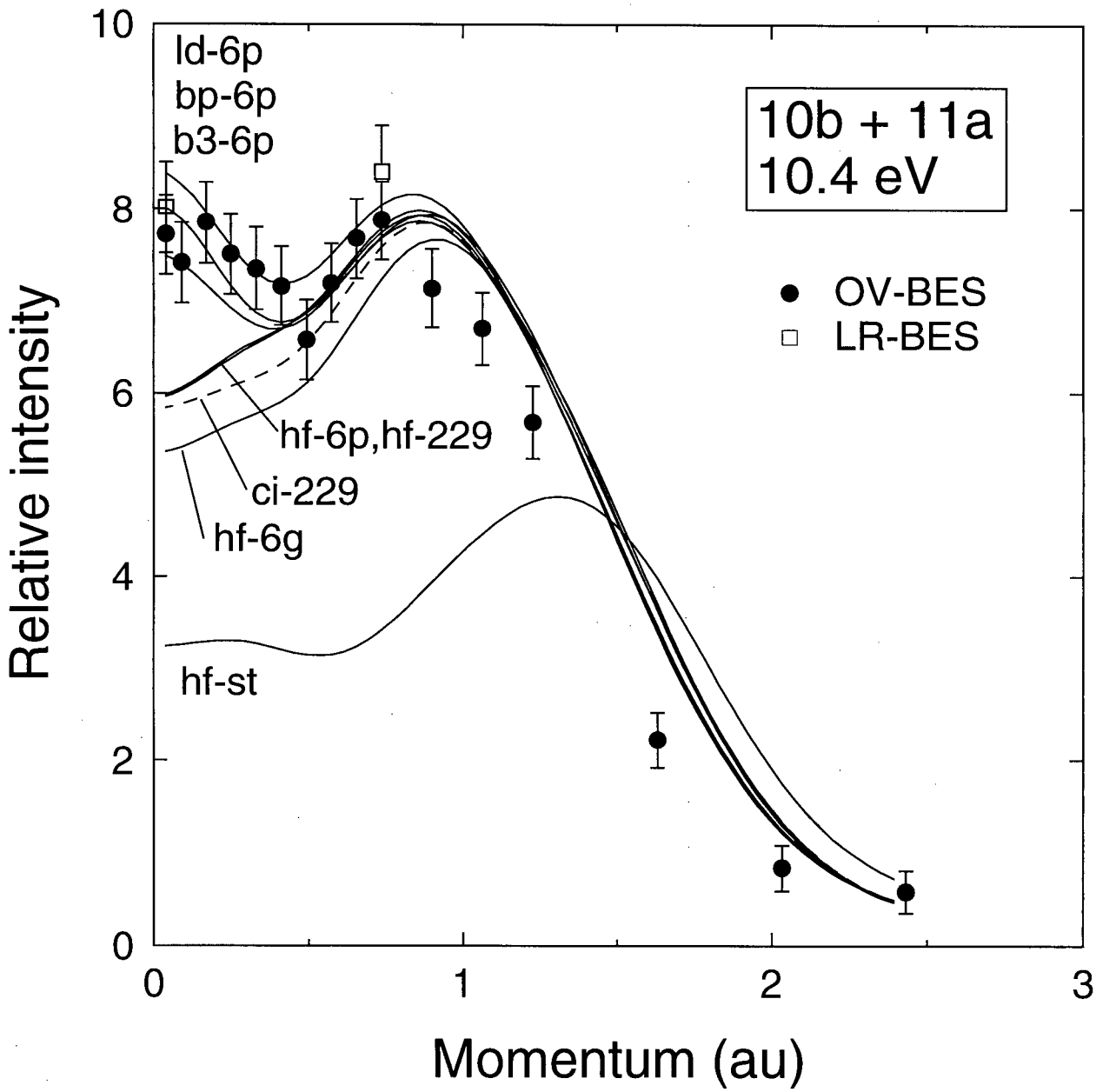

Figure 5.3: Experimental and theoretical 10b + 11a momentum profiles of dimethoxymethane. The XMPs are of the peak fitted at 10.4 eV to the OV-BES (•) and LR-BES (□) data sets. The TMPs have been calculated at the MP2/6-31+G* optimized gauche-gauche geometry. The key to the TMP labels is given in Table 5.2. The experimental angular resolution has been accounted for in the theoretical profiles using the GW-PG method [48].

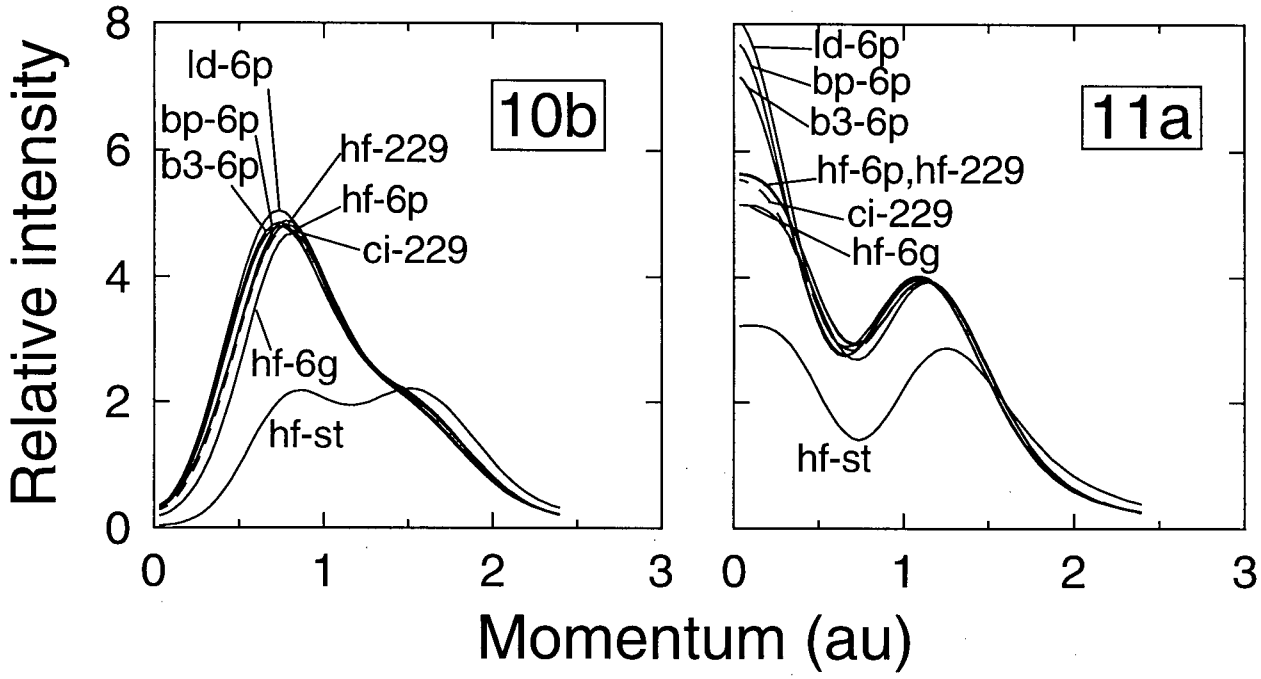

Figure 5.4: Theoretical 10b (left panel) and 11a (right panel) momentum profiles of dimethoxymethane. The profiles have been calculated using the MP2/6-31+G* optimized gauche-gauche geometry. The key to the TMP labels is given in Table 5.2. The experimental angular resolution has been accounted for in the theoretical profiles using the GW-PG method [48].

all of the other calculations considered here. It is clear from Figure 5.4 that the intensity in the 10b + 11a profile near $p = 0$ au is almost entirely due to orbital 11a, while the 10b + 11a profile maximum near 0.8 au contains significant contributions from both orbitals. The differences between the HF and DFT results come almost entirely from the 11a TMPs. All of the calculations of the 10b TMPs, with the exception of the small basis set HF calculations hf-st and to a lesser extent hf-6g, are in reasonable agreement. There is, however, a small but definite shift in the maximum of the 10b profile (p_{MAX}) towards lower momentum in comparing the DFT profiles to the HF profiles. In the case of the 11a TMPs, the calculations shown all predict a momentum profile of the same qualitative shape, with maxima at 0 and ≈ 1.2 au and a minimum near 0.7 au. However, the DFT calculations predict substantially

greater intensity at 0 au than do the CI and HF calculations. The similarity between the respective 10b and 11a HF and CI TMPs seems to suggest that electron correlation effects for these momentum profiles are not sufficiently great to account for the differences between the HF profiles and the DFT and experimental profiles. In view of the disagreement between the 11a DFT and CI TMPs, the reason for the agreement of the 10b + 11a XMP with the corresponding DFT TMPs, but not with the HF and CI TMPs, is not clear.

Previous EMS studies [20, 71, 152, 153] of other molecules have noted a tendency for the DFT TMPs to have greater intensity at low momentum than is the case for HF and CI TMPs, particularly in the case of LSDA DFT calculations. This has been attributed [20] to the underbinding of the large-r electron density in the DFT calculations, resulting in position space orbitals that are too diffuse and, consequently, momentum space profiles with too much intensity at low momentum. This deficiency of the LSDA has been addressed as part of the development of gradient-corrected functionals (Section 2.3.3) and consequently should be less of a problem for DFT TMPs calculated using gradient-corrected functionals. Although an excess of intensity at low momentum can explain the large differences between the HF and CI and the DFT 11a TMPs, it does not explain the good agreement obtained between the experimental data and the DFT profiles. An alternative explanation is that, in order to make these very large CI calculations tractable, too few electron configurations were included, yielding a result that neglects a significant fraction of the electron correlation effects. Additional CI calculations, including a greater number of configurations, are necessary to verify this hypothesis. The computational challenges in performing such calculations on a molecule of the size of dimethoxymethane highlight the appeal of DFT.

Ionization from MO 9b at 11.5 eV results in the experimental momentum profile shown in Figure 5.5. MO 9b may be described as the antisymmetric combination of two O n_σ orbitals. However, the MO calculations performed in the current work also predict some

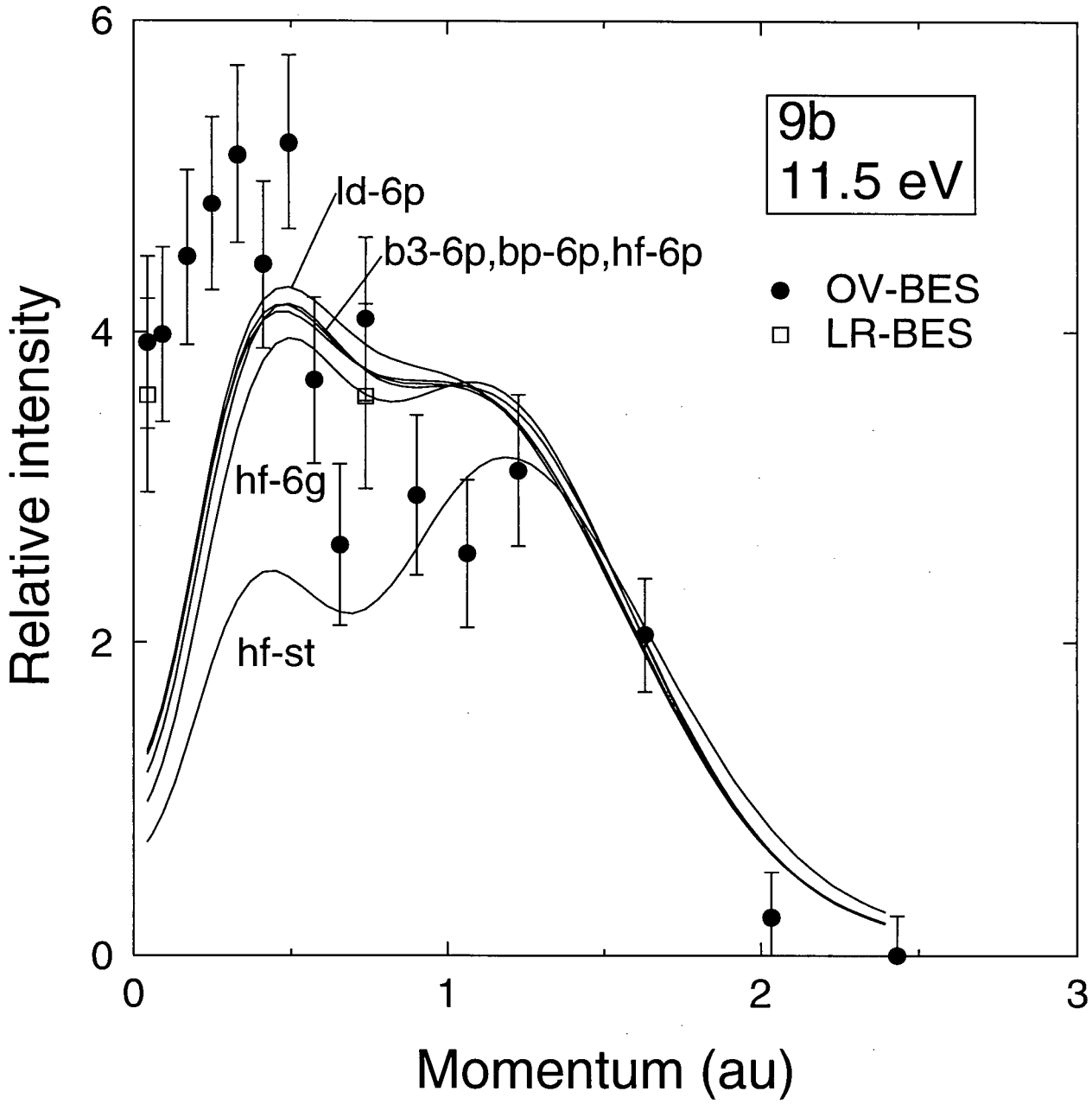

Figure 5.5: Experimental and theoretical 9b momentum profiles of dimethoxymethane. The XMPs are of the peak fitted at 11.5 eV to the OV-BES (•) and LR-BES (□) data sets. The TMPs have been calculated using the MP2/6-31+G* optimized gauche-gauche geometry. The key to the TMP labels is given in Table 5.2. The experimental angular resolution has been accounted for in the theoretical profiles using the GW-PG method [48].

methylene C–H and CH_2–O bonding character for this orbital. The relatively large error bars and the scatter of the experimental data reflect the difficulties in obtaining an accurate experimental momentum profile of an ionization process separated by only ≈ 1 eV from the nearest neighboring ionization ($(11a)^{-1}$). It is clear that all of the theoretical profiles are in poor agreement with the XMP, particularly for $p < 0.5$ au. In contrast, there are only small differences between the TMPs shown in Figure 5.5, with the notable exception of the minimal basis set HF/STO-3G TMP. The HF and DFT B3LYP and BP86 TMPs calculated using the 6-311++G** basis set are very similar to one another. When the HF calculation is performed with the substantially less flexible 6-31G basis set, the resulting TMP has slightly less intensity at low momentum and slightly more at high momentum. This trend continues when the STO-3G minimal basis set is used. The 9b TMP derived from the DFT LSDA calculation has somewhat greater intensity in the vicinity of p_{MAX} than do the other calculations using the 6-311++G** basis set. Although the discrepancies between the 9b XMP and TMPs could be the result of inadequacies in the theoretical calculations, it is more likely that these differences are at least partly the result of limitations in the fitting procedure used to obtain the 9b XMP. The small energy separations from the $(10b)^{-1} + (11a)^{-1}$ peak at 10.41 eV and in particular the very intense s-type $(10a)^{-1}$ peak at 13.0 eV likely result in some contamination of the 9b experimental momentum profile with intensity from these adjacent ionization processes. Alternative theoretical explanations for this discrepancy between experiment and theory are investigated in Sections 5.6–5.8.

Experimental and theoretical momentum profiles for orbitals 10a + 8b are shown in Figure 5.6. Although separate Gaussian functions at 13.0 and 13.6 eV have been used for these ionization processes when fitting the BES (Section 5.4 and Figure 5.2), the resulting XMPs show considerable cross-contamination as a consequence of the small energy spacing between the $(10a)^{-1}$ and $(8b)^{-1}$ ionization processes. Therefore, these two XMPs have been summed

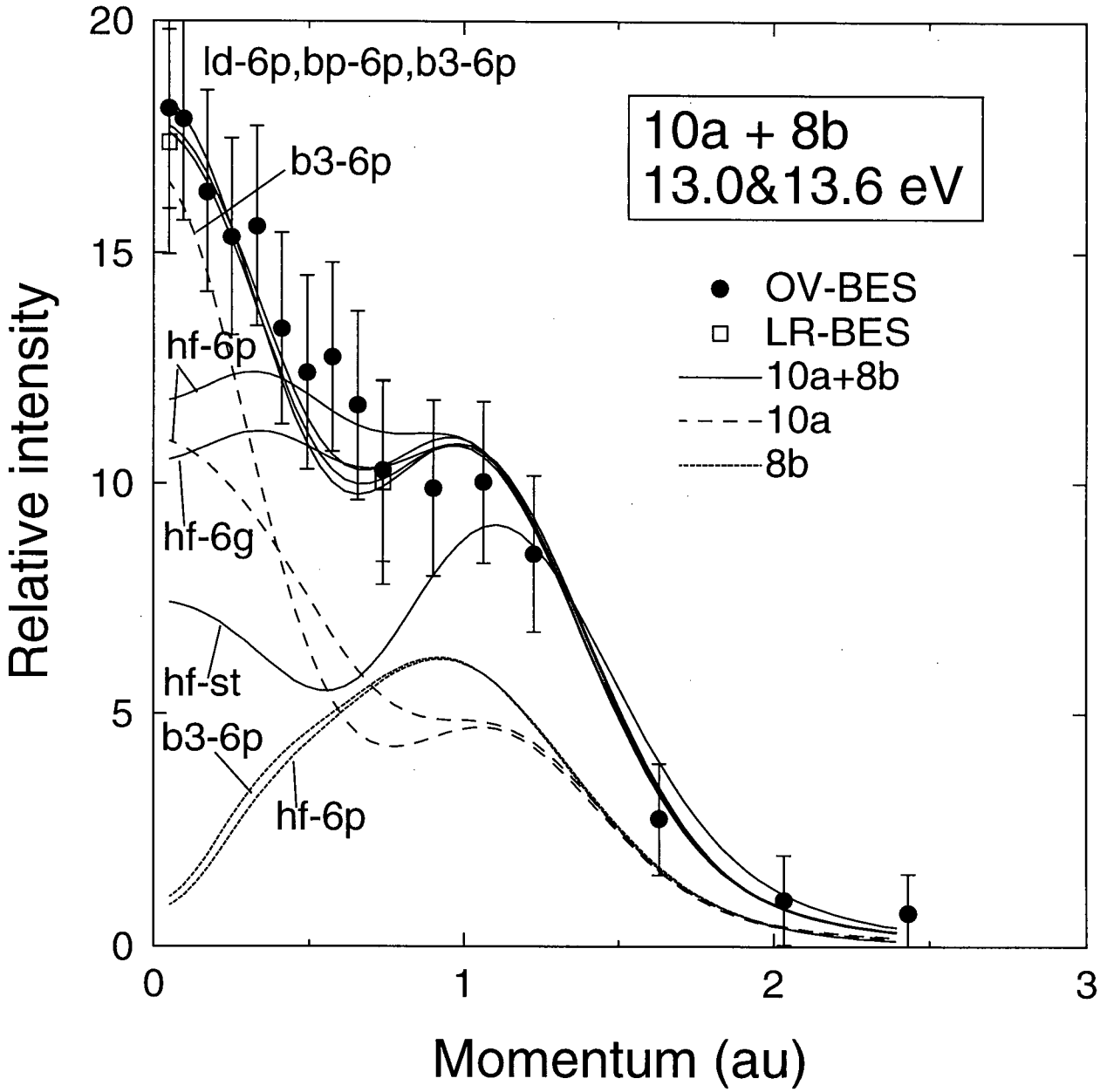

Figure 5.6: Experimental and theoretical 10a + 8b momentum profiles of dimethoxymethane. The XMPs are of the sum of the peaks fitted at 13.0 and 13.6 eV to the OV-BES (•) and LR-BES (□) data sets. The TMPs are sums of the 10a and 8b TMPs calculated using the MP2/6-31+G* optimized gauche-gauche geometry. The individual hf-6p and b3-6p 10a and 8b TMPs are also shown. The key to the TMP labels is given in Table 5.2. The experimental angular resolution has been accounted for in the theoretical profiles using the GW-PG method [48].

together prior to further analysis and comparison with the theoretical results. The considerable intensity near zero momentum is almost entirely attributable to the s-type 10a profile. Both the p-type 8b profile and the 10a profile contribute to the intensity observed near $p = 1$ au. The 10a MO consists primarily of the symmetric combination of O n_σ orbitals plus methyl C–H bonding character. In contrast, MO 8b of the gg conformer of dimethoxymethane is highly delocalized throughout the molecule, with significant C–O and C–H σ-bonding character. The three DFT theoretical profiles are very similar and are in excellent agreement with the experimental data. The HF profiles differ considerably from the XMP, particularly at low momentum, and also exhibit considerable basis set dependence. As was the case for the 10b + 11a profiles, almost all of the differences between the HF and DFT results arise from differences in the a symmetry profiles (10a in this case), with the 8b TMPs showing little variation with theoretical method.

The XMP obtained from the peak fitted to the BES at 15.0 eV is shown in Figure 5.7 and compared with sums of the 9a, 7b and 8a theoretical profiles. The general agreement in terms of both shape and intensity between the XMP and the three DFT TMPs supports the assignment in Section 5.4 of the 15.0 eV peak to the $(9a)^{-1} + (7b)^{-1} + (8a)^{-1}$ ionization processes. The B3LYP/6-311++G** TMP (b3-6p) best matches the shape of the experimental profile. The remaining DFT TMPs have the correct qualitative shape, but predict too much intensity at p_{MAX} and too narrow a peak about p_{MAX}. None of the HF TMPs shown in Figure 5.7 are in good agreement with the experimental data. The HF/6-31G TMP has the shape most similar to the XMP, but is considerably lower in intensity at $p < 1$ au. The HF/6-311++G** TMP, obtained using the same basis set as was used for the DFT TMPs in Figure 5.7, has a very different shape, predicting a maximum near $p = 0$. An examination of the individual TMPs of orbitals 9a, 7b and 8a indicates that the discrepancy between the HF/6-311++G** TMP and the DFT TMPs near zero momentum is primarily a consequence

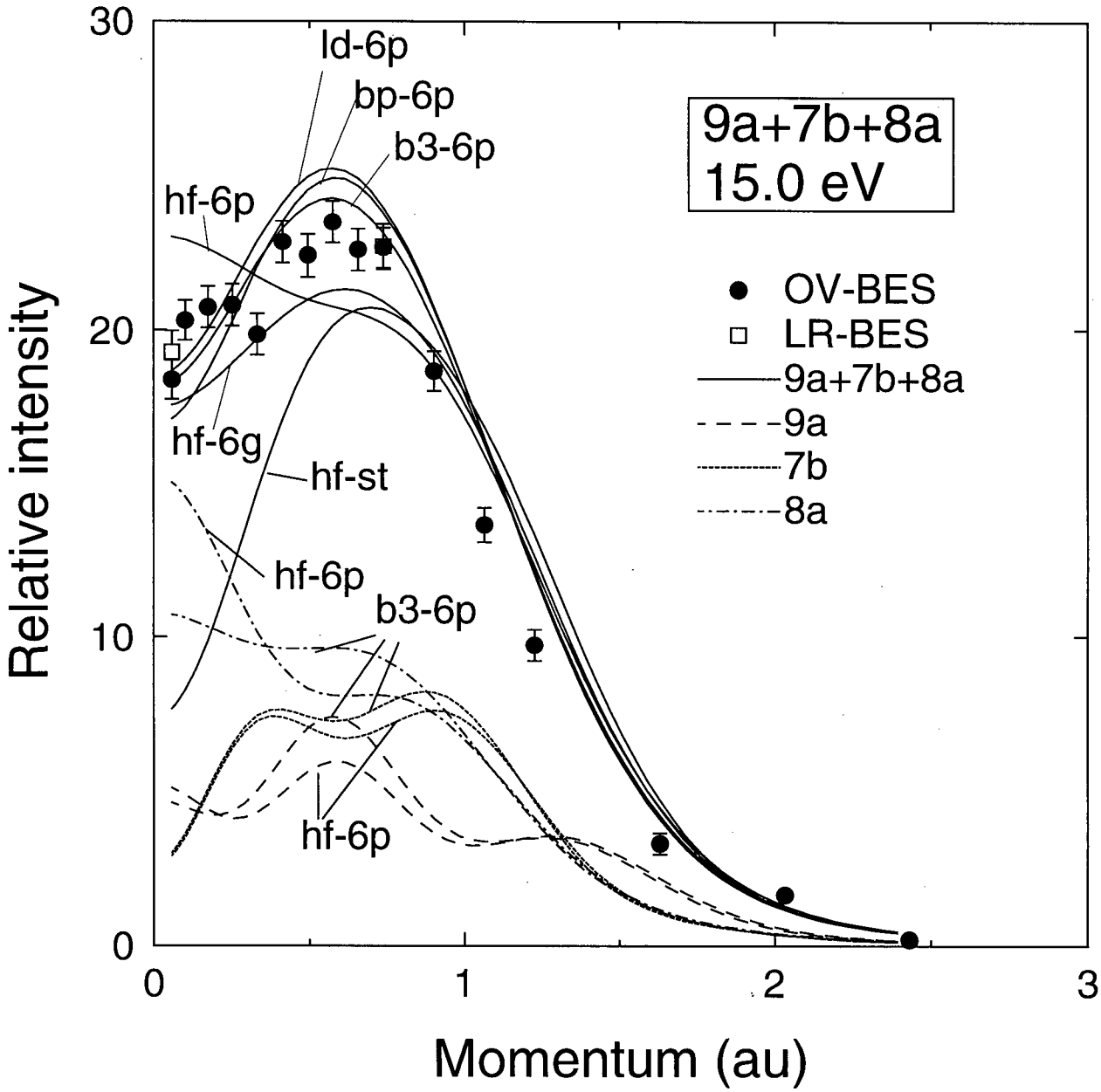

Figure 5.7: Experimental and theoretical 9a + 7b + 8a momentum profiles of dimethoxymethane. The XMPs are of the peak fitted at 15.0 eV to the OV-BES (•) and LR-BES (□) data sets. The TMPs are sums of the 9a, 7b and 8a TMPs calculated using the MP2/6-31+G* optimized gauche-gauche geometry. The individual hf-6p and b3-6p 9a, 7b and 8a TMPs are also shown. The key to the TMP labels is given in Table 5.2. The experimental angular resolution has been accounted for in the theoretical profiles using the GW-PG method [48].

of differences between the HF and DFT 8a profiles. The DFT profiles of both orbitals 9a and 8a have greater intensity than the corresponding HF profiles between ≈ 0.5 and 1.0 au, giving rise to the differences in this momentum region evident in Figure 5.7. The HF/6-311++G** TMP of orbital 7b and the corresponding DFT TMPs differ only slightly. The considerable shape difference between the HF/6-311++G** and HF/6-31G TMPs of orbitals 9a + 7b + 8a is predominantly a result of the considerably greater intensity near $p = 0$ of the 8a TMP obtained from the larger basis set calculation. Although the agreement between the experimental data and the B3LYP/6-311++G** TMP in Figure 5.7 is reasonably good, the experimental data do consistently fall below the theoretical profile for p between ≈ 0.5 and 1.5 au. This could be the result of many-body effects in ionization from one or more of these orbitals, resulting in reduced spectroscopic factors (Section 2.2.3). If this is the case, the missing intensity will be contained in one or more ionization poles at other energies. The other likely explanation for this intensity difference is small errors in the fitting procedure used to obtain the XMP arising from the approximation of using a single peak to fit three separate (albeit closely spaced) ionization processes.

The shape of the XMP obtained at 17.0 eV, shown in Figure 5.8, is qualitatively reproduced by all of the theoretical momentum profiles shown. The considerable difference in intensity between the experimental results and the TMPs can be attributed to a breakdown of the single particle model of ionization, an effect which tends to become more significant at higher ionization energies (see Section 2.2.3 and Reference [154]). The B3LYP/6-311++G** TMP scaled by a factor of 0.82 provides good agreement with the XMP in terms of both shape and intensity, whereas the HF/6-311++G** TMP predicts a somewhat greater p_{MAX} than is observed experimentally. The scaled TMPs do underestimate the observed intensity at low p. This is likely a result of the rather crude approximation of scaling the 6b, 7a and 5b TMPs equally, even though it is highly unlikely that the spectroscopic factors for

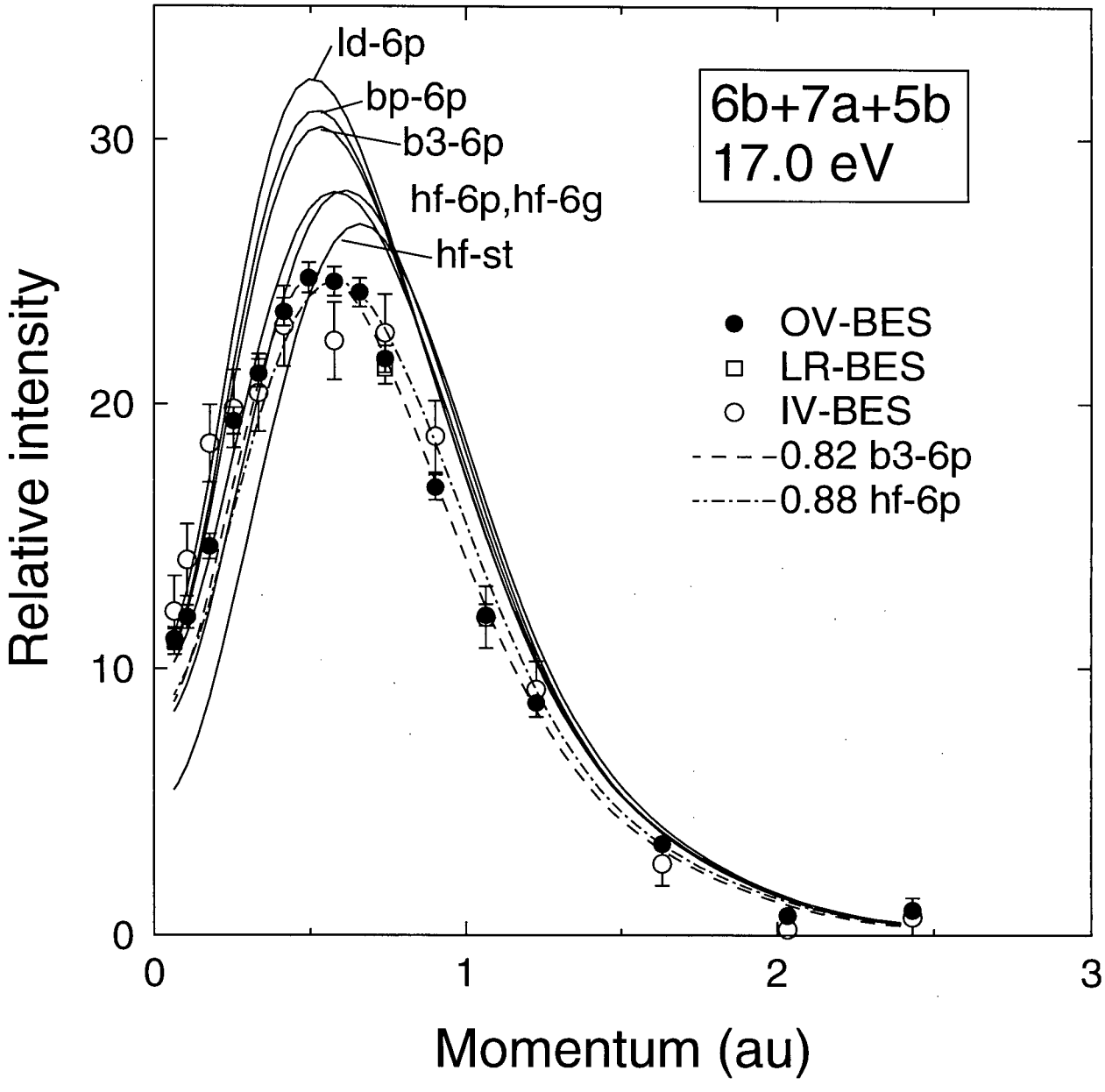

Figure 5.8: Experimental and theoretical 6b + 7a + 5b momentum profiles of dimethoxymethane. The XMPs are of the peak fitted at 17.0 eV to the OV-BES (•), LR-BES (□) and IV-BES (○) data sets. The TMPs are sums of the 6b, 7a and 5b TMPs, calculated using the MP2/6-31+G* optimized gauche-gauche geometry. The key to the TMP labels is given in Table 5.2.

these three ionizations are identical. In comparing the HF results to the experimental data, agreement improves with increasing basis set size as the location of p_{MAX} shifts to lower momentum. The location of p_{MAX} shifts even further towards low momentum in the case of the DFT calculations, with the B3LYP/6-311++G** result giving the best agreement with the experimentally observed p_{MAX}.

5.5.2 Inner-valence momentum profiles

The five inner-valence molecular orbitals of dimethoxymethane (6a, 4b, 5a, 3b and 4a) can all be described as consisting primarily of combinations of the carbon and oxygen 2s atomic orbitals. The momentum profiles of these orbitals are all characterized by spectroscopic factors of significantly less than unity as a result of many-body effects with ionization from these orbitals, as is common with inner-valence ionization [154].

The strongly s-type $(6a)^{-1}$ ionization peak at 20.4 eV in Figure 5.2 corresponds to the XMP shown in Figure 5.9. MO 6a consists of significant 2s electron density on all carbon and oxygen atoms, alternating in phase from methyl C to O to methylene C. The largest fraction of the electron density for this MO is located on the central (methylene) carbon atom. All of the theoretical momentum profiles shown in Figure 5.9 for orbital 6a predict essentially the same shape for this profile and are in good agreement with the experimental results. The theoretical results do differ, however, in the predicted intensity at low momentum, with the DFT and the minimal basis set HF calculations predicting considerably more intensity near $p = 0$ than is the case for the larger basis set HF calculations. It is apparent from the differences in intensity between the experimental and theoretical results that the spectroscopic factor for this ionization process is less than one. When the B3LYP/6-311++G** and HF/6-311++G** TMPs are scaled by 0.80 and 0.85 respectively, a more accurate assessment of the shapes of the theoretical profiles can be made. Both of the scaled profiles match the

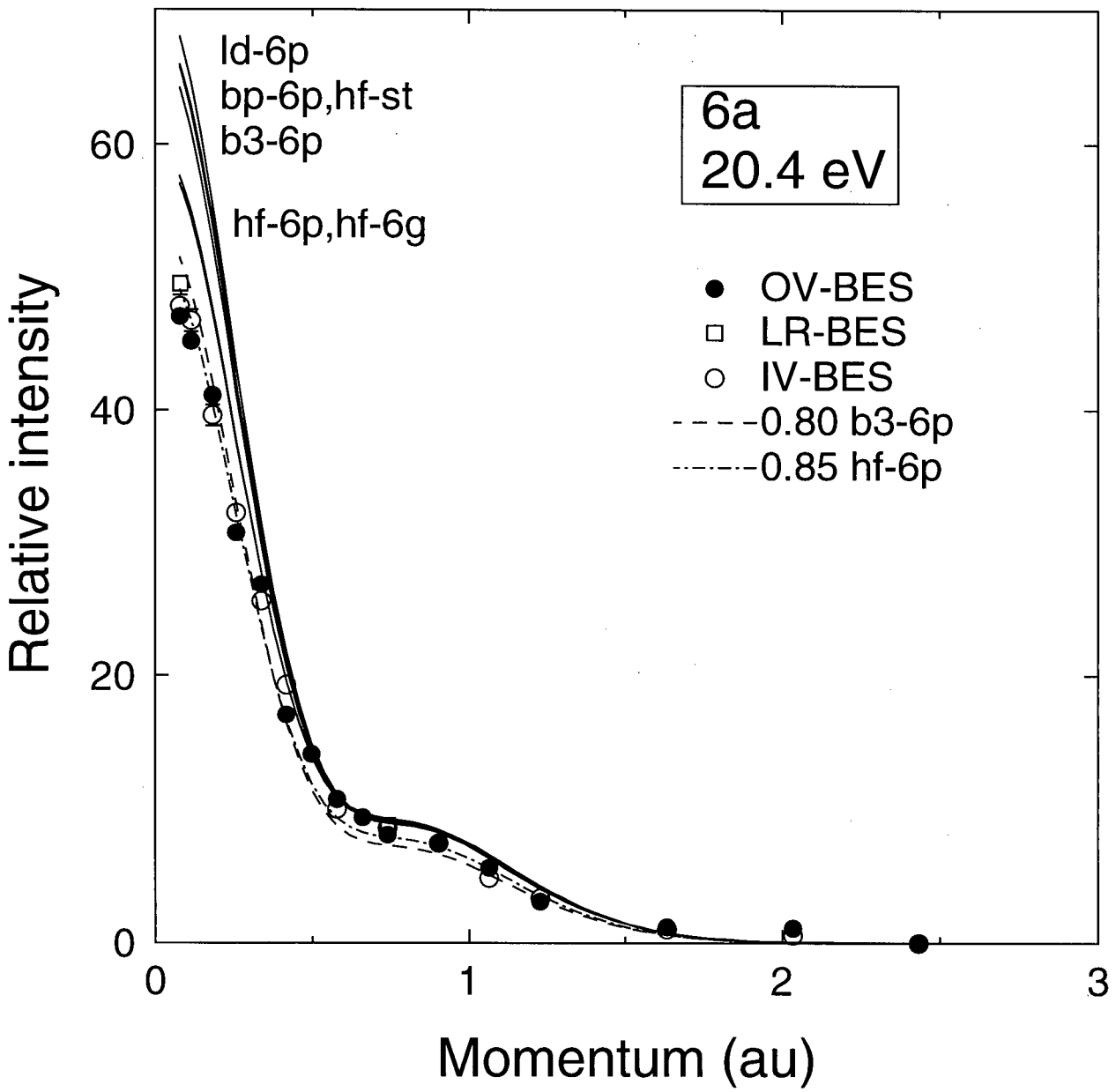

Figure 5.9: Experimental and theoretical 6a momentum profiles of dimethoxymethane. The XMPs are of the peak fitted at 20.4 eV to the OV-BES (•), LR-BES (□) and IV-BES (○) data sets. The TMPs have been calculated using the MP2/6-31+G* optimized gauche-gauche geometry. The key to the TMP labels is given in Table 5.2. The experimental angular resolution has been accounted for in the theoretical profiles using the GW-PG method [48].

XMP fairly well. The DFT TMP slightly overestimates the ratio between the intensity near zero momentum and the intensity at the 'plateau' in the profile between 0.5 and 1.0 au.

The 4b experimental momentum profile, obtained at a binding energy of 22.6 eV, and the corresponding theoretical profiles, are shown in Figure 5.10. The majority of the electron density for this orbital is located on the two methyl carbon nuclei. The opposite phase of the MO on these two nuclei results in the intensity minimum near zero momentum. All of the theoretical calculations correctly predict the p-type nature of this momentum profile and are in good agreement with the shape of the XMP. In contrast to the outer-valence p-type momentum profiles discussed above, there is little variation with calculation of p_{MAX} of the 4b TMPs. A scale factor of ≈ 0.9 is necessary to bring the B3LYP and HF/6-311++G** TMPs into intensity agreement with the experimental data. Using the slightly different scale factors indicated in Figure 5.10, the high degree of consistency between the shapes of the HF and B3LYP momentum profiles is evident. There is some indication of a slight disagreement between theory and experiment at very low momentum, with the experimental results somewhat higher than the theoretical profiles. This could be due to small contributions from the neighboring $(6a)^{-1}$ ionization. Although the energy separation between the two ionization processes is greater than 2 eV, the 6a profile is so intense near $p = 0$ that some intensity from this ionization process may be 'leaking' into the 4b fit at low momentum. Another possibility is that there are one or more low intensity s-type poles in the same binding energy region as the $(4b)^{-1}$ ionization at 22.6 eV.

The 5a experimental and theoretical momentum profiles are shown in Figure 5.11. This MO consists primarily of C 2s character, with the greatest contribution coming from the central carbon atom. The theoretical profiles are very similar in shape but differ somewhat in intensity. As was the case for the 6a and 4b TMPs, the 5a TMPs appear to be less sensitive to the basis set used for the calculation than was the case for the outer-valence

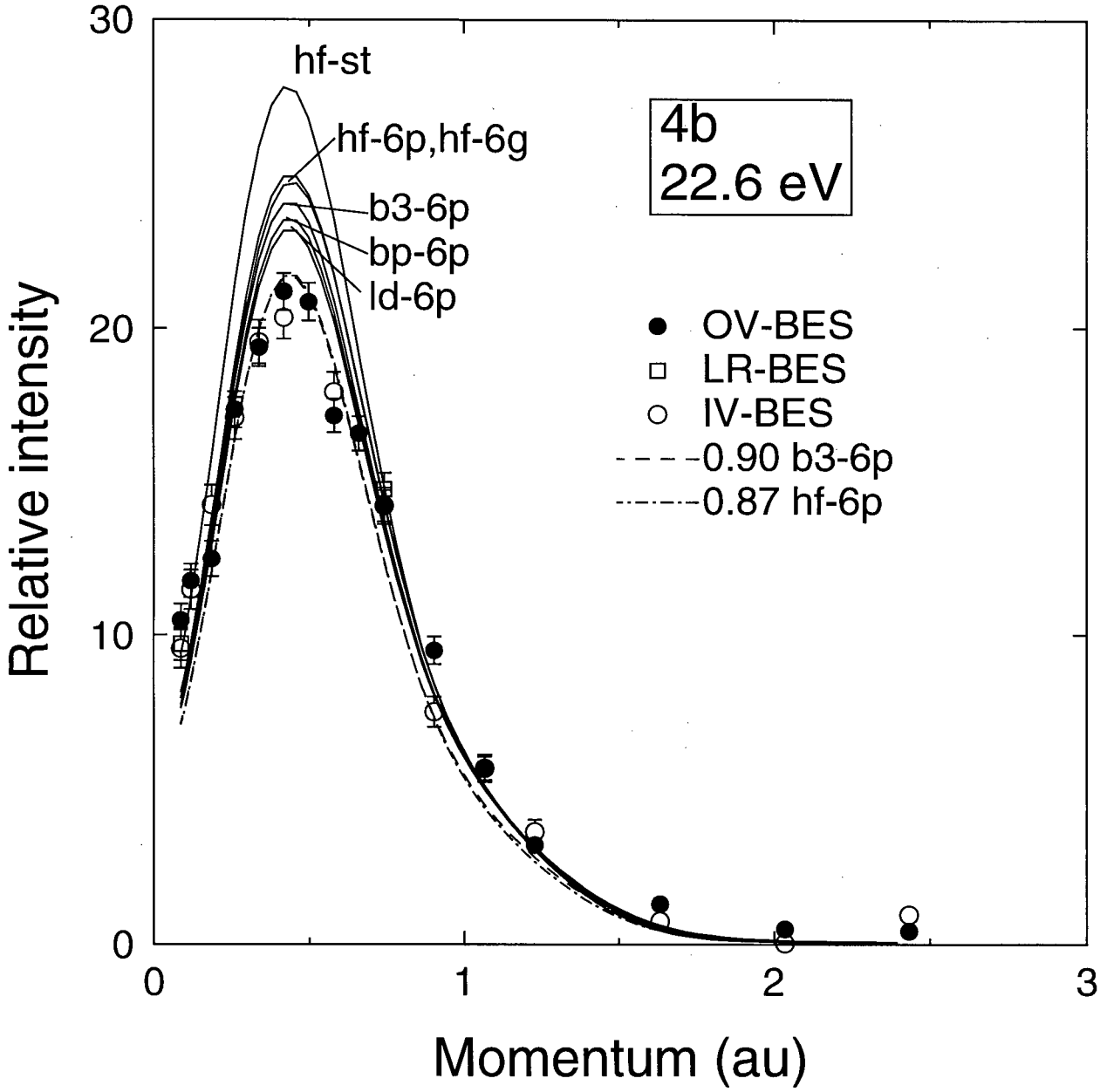

Figure 5.10: Experimental and theoretical 4b momentum profiles of dimethoxymethane. The XMPs are of the peak fitted at 22.6 eV to the OV-BES (•), LR-BES (□) and IV-BES (○) data sets. The TMPs have been calculated using the MP2/6-31+G* optimized gauche-gauche geometry. The key to the TMP labels is given in Table 5.2. The experimental angular resolution has been accounted for in the theoretical profiles using the GW-PG method [48].

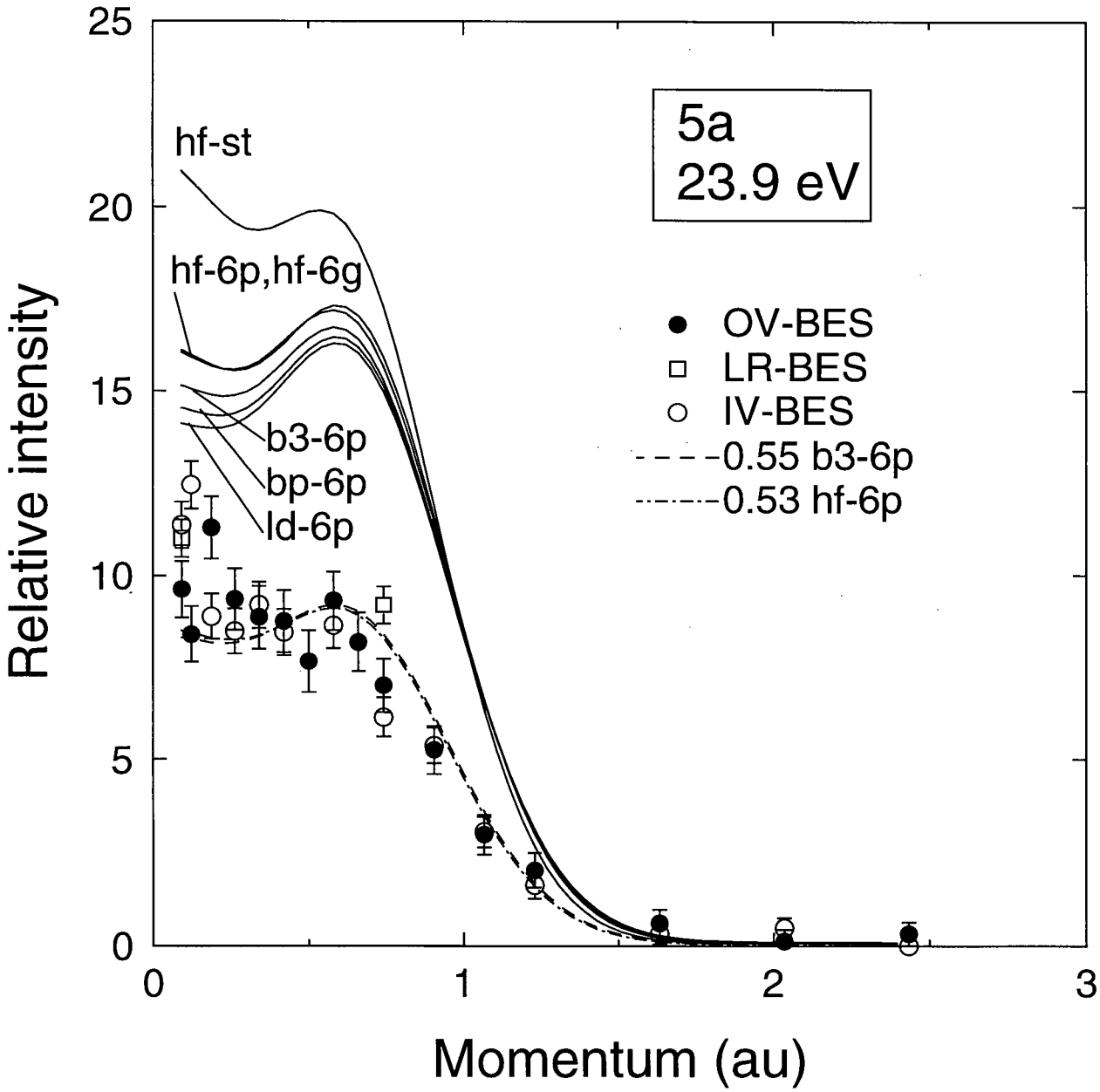

Figure 5.11: Experimental and theoretical 5a momentum profiles of dimethoxymethane. The XMPs are of the peak fitted at 23.9 eV to the OV-BES (•), LR-BES (□) and IV-BES (○) data sets. The TMPs have been calculated using the MP2/6-31+G* optimized gauche-gauche geometry. The key to the TMP labels is given in Table 5.2. The experimental angular resolution has been accounted for using the GW-PG method [48].

TMPs of dimethoxymethane, as illustrated by the similarity between the HF/6-31G and HF/6-311++G** TMPs. It is not surprising that the use of diffuse and polarization functions becomes less important for the inner-valence orbitals, which tend to be more spatially localized and atomic-like than the outer-valence orbitals. The B3LYP and HF 6-311++G** TMPs, when scaled by 0.55 and 0.53 respectively, can be seen to have nearly the same shape and are generally consistent with the XMP, with the exception of a few points near $p = 0$. An examination of the BES in Figure 5.2 reveals that there is significant intensity on the high energy side of the $(5a)^{-1}$ peak, indicating the likely presence of one or more satellite ionization processes in this energy region. Consequently, the 'extra' intensity observed in the 5a experimental momentum profile near $p = 0$ can be reasonably attributed to s-type satellite ionization processes in this binding energy region.

HF orbital energies (Table 5.1) indicate that the parent $(3b)^{-1}$ and $(4a)^{-1}$ ionization peaks should be located within the broad peak evident in the BES (Figure 5.2) between 28 and 37 eV. However, as discussed above (Section 5.4), the relatively structureless nature of the BES in this region and the lack of many-body theoretical calculations or higher energy resolution experimental studies to serve as a guide preclude the determination of XMPs for the $(3b)^{-1}$ and $(4a)^{-1}$ ionizations by fitting of the BES. It is possible, however, to obtain an experimental profile for the entire region simply by summing the BES data over the appropriate energy range. This has been done for the 25–44 eV binding energy range, with the results indicated by the circles (○) and filled squares (■) in Figure 5.12. The data are shown on an angle rather than momentum scale because of the binding energy dependence of the ϕ to p conversion (Equation (2.5)). The experimental angle profile is clearly s-type, as expected from an examination of the 0° and 9° BES (Figure 5.2). The experimental data are compared in Figure 5.12 with B3LYP and HF 6-311++G** theoretical profiles obtained by summing the individual 3b and 4a profiles. As was observed for the other inner-valence

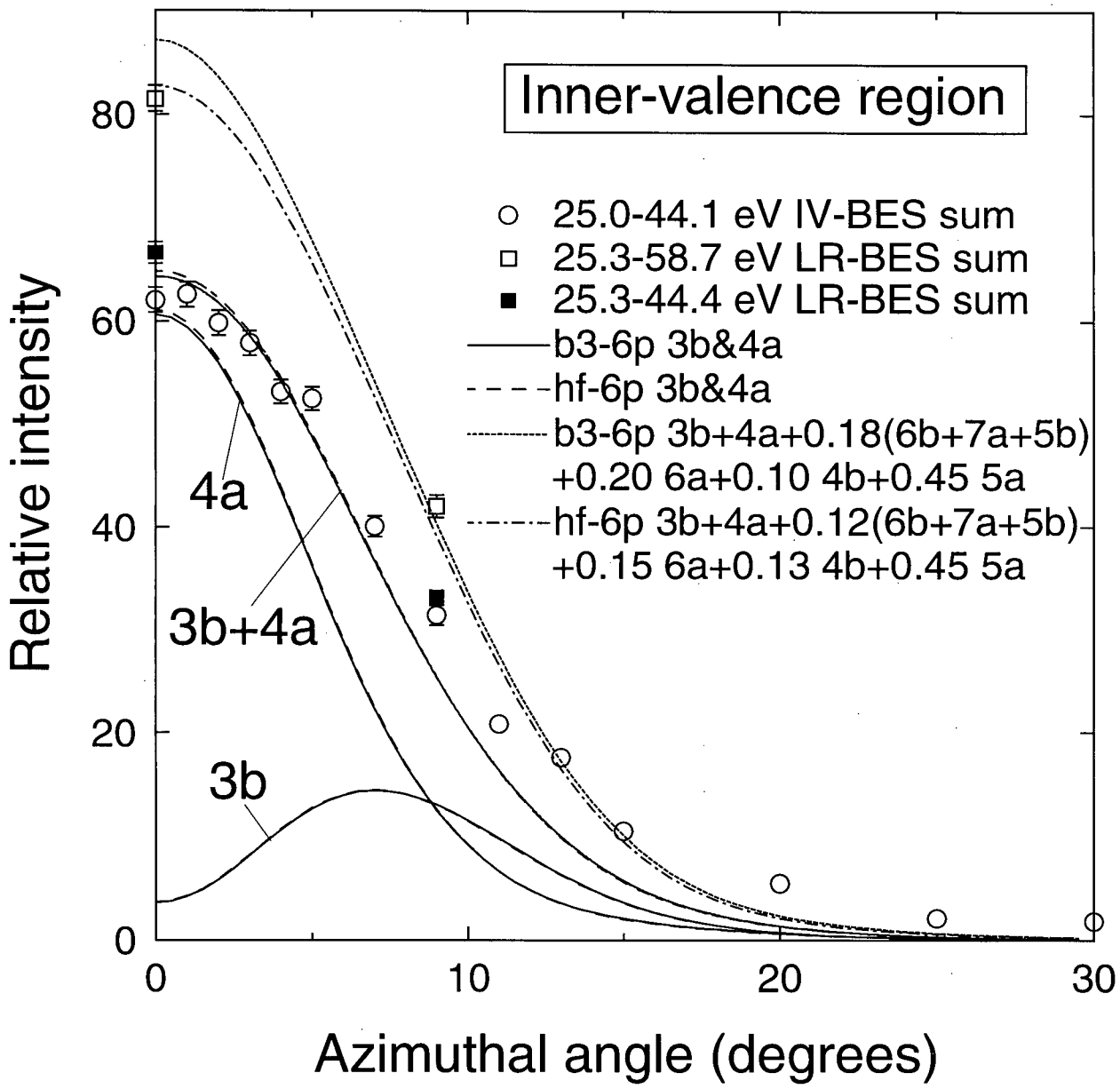

Figure 5.12: Experimental angle profile of the 25–44 eV binding energy range of dimethoxymethane and the individual and summed 3b and 4a theoretical profiles. The XAPs have been obtained by summing the IV-BES (○) and LR-BES (■) binding energy data from 25–44 eV and by summing the LR-BES data from 25–59 eV (□). The theoretical profiles have been calculated using the MP2/6-31+G* optimized gauche-gauche geometry. The key to the TMP labels is given in Table 5.2. The experimental angular resolution has been accounted for in the theoretical profiles using the GW-PG method [48]. Binding energies of 31.1 and 33.1 eV have been used to resolution fold the 3b and 4a TAPs, respectively.

ionization processes, ionization intensity from these orbitals is expected to be spread over multiple poles. It is also likely that satellite peaks due to ionization from valence orbitals other than 3b and 4a are present in the 25–44 eV energy range. Consequently, the intensity agreement evident in Figure 5.12 between the experimental and 3b + 4a theoretical profiles at low azimuthal angles is likely coincidental. The disagreement between the experimental and theoretical profiles at higher azimuthal angles suggests the presence in this energy range of satellite poles resulting from ionizations from other valence orbitals. Alternatively, the greater experimental intensity at high momentum could be the result of distortion effects, which are more likely to occur with inner-valence ionization. The two open squares in Figure 5.12, obtained by summing LR-BES data from 25.3 to 58.7 eV, indicate the significant amount of additional intensity present above 44 eV. If all of the 'missing intensity' from orbitals 6b, 7a, 5b, 6a, 4b and 5a is added to the the 3b and 4a theoretical profiles, the upper curves in Figure 5.12 are obtained. The HF/6-311++G** curve matches well with the two experimental data points, while the B3LYP/6-311++G** curve is somewhat higher at $\phi = 0°$. The discrepancy between the experimental data and the DFT calculation is perhaps not surprising considering the 'extra' experimental intensity observed near zero momentum in the 9b, 6b + 7a + 5b, 4b and 5a XMPs (Figures 5.5, 5.8, 5.10 and 5.11, respectively). Alternatively, this discrepancy could be due to additional s-type valence orbital ionization intensity at binding energies greater than 58.7 eV, the limit of the current study. This is supported by the BES shown in Figure 5.2, which indicate the presence of ionization intensity up to the limit of the monitored binding energy range. The good intensity agreement between the experimental data and the HF calculation could then be partly fortuitous, since had the normalization between theory and experiment been done using the HF/6-311++G** results rather than the B3LYP/6-311++G** (beginning of Section 5.5 above), the experimental data would be lower relative to the theoretical results.

Despite the featureless nature of the broad peak in the BES between 25 and 44 eV, an attempt has been made to further investigate the nature of the ionization processes in this energy range. This has been done by dividing the 25–44 eV binding energy data into 11 energy ranges and considering the experimental angle profiles of each energy range, as shown in Figure 5.13. As can be seen, the experimental profiles for all 11 energy ranges are s-type, although the widths of the profiles differ. Each profile has been fitted using the 3b (p-type) and 4a (s-type) B3LYP/6-311++G** theoretical profiles, with the resulting scale factors and the fitted function shown in each panel of Figure 5.13. The reasoning behind this analysis is that the bulk of the ionization intensity in this binding energy range is likely from the $(3b)^{-1}$ and $(4a)^{-1}$ ionization manifolds, and that even if this is not the case, some indication of the general distribution of s-type and p-type ionization poles in this region might be obtained. Although all profiles are s-type, none of them are narrow enough to be fitted by the s-type 4a profile alone. This suggests that all of these energy ranges contain intensity from multiple many-body ionization poles. In Figure 5.14, the fitted scale factors have been plotted as a function of the central binding energy of each range. The binding energy error bars in Figure 5.14 indicate the widths of the energy ranges and the scale factor error bars are the calculated uncertainties from the least-squares fit. The data shown in Figure 5.14 suggest that p-type ionization poles are concentrated at lower binding energy than are s-type poles, but with significant ionization intensity of both symmetries spread throughout this binding energy range. It is interesting to note that the HF/aug-cc-pVTZ 3b and 4a orbital energies reported in Table 5.1 are in the same order and are separated by a similar energy as the maxima of the plots of the 3b and 4a scale factors shown in Figure 5.14.

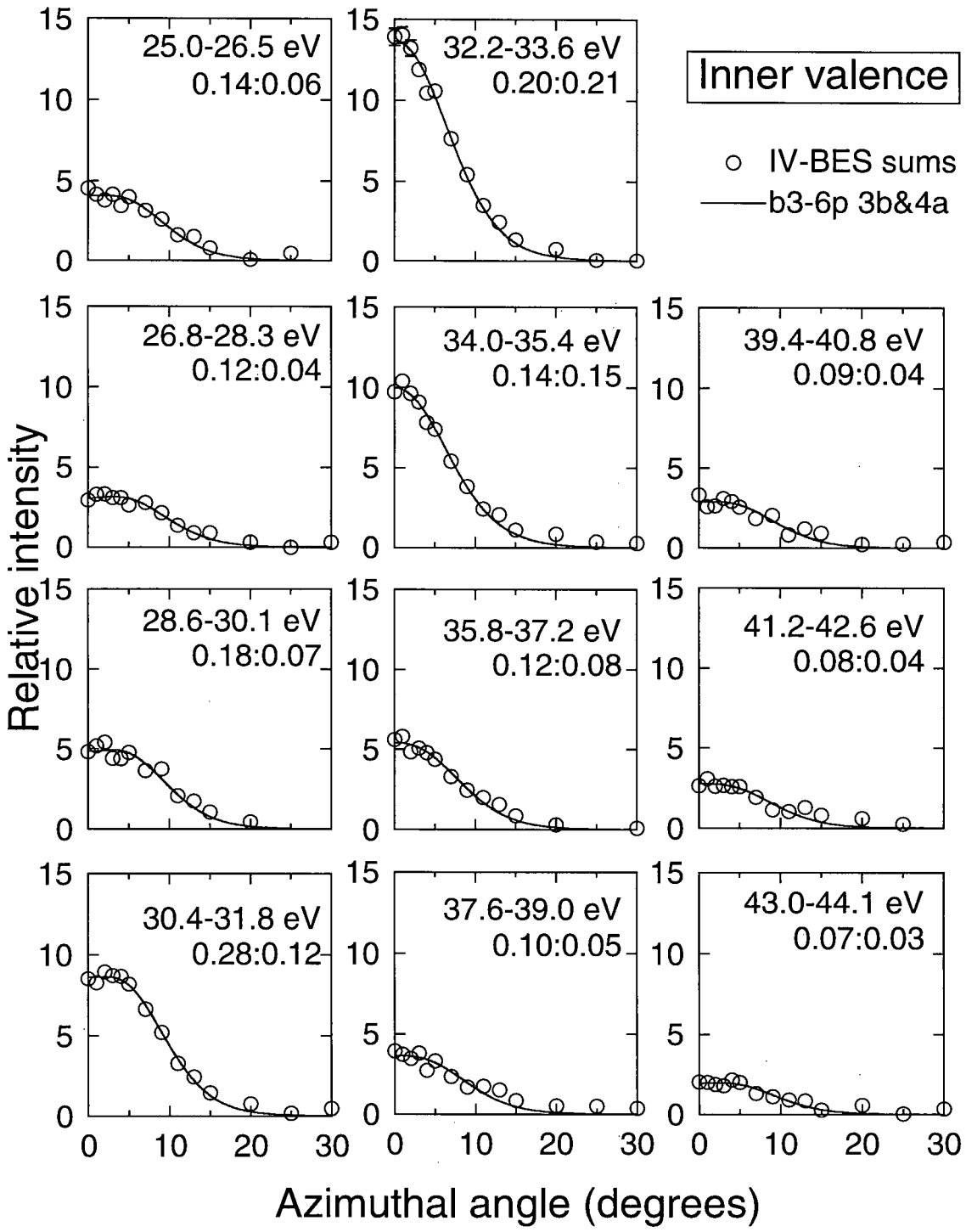

Figure 5.13: Experimental angle profiles (○) of a series of binding energy intervals in the 25–44 eV binding energy range of dimethoxymethane. The results of least-squares fits of the 3b and 4a B3LYP/6-311++G** theoretical profiles (—) to each of the experimental angle profiles are also shown. The binding energy range used for each profile and the fitted scale factors (3b:4a) are indicated in each panel.

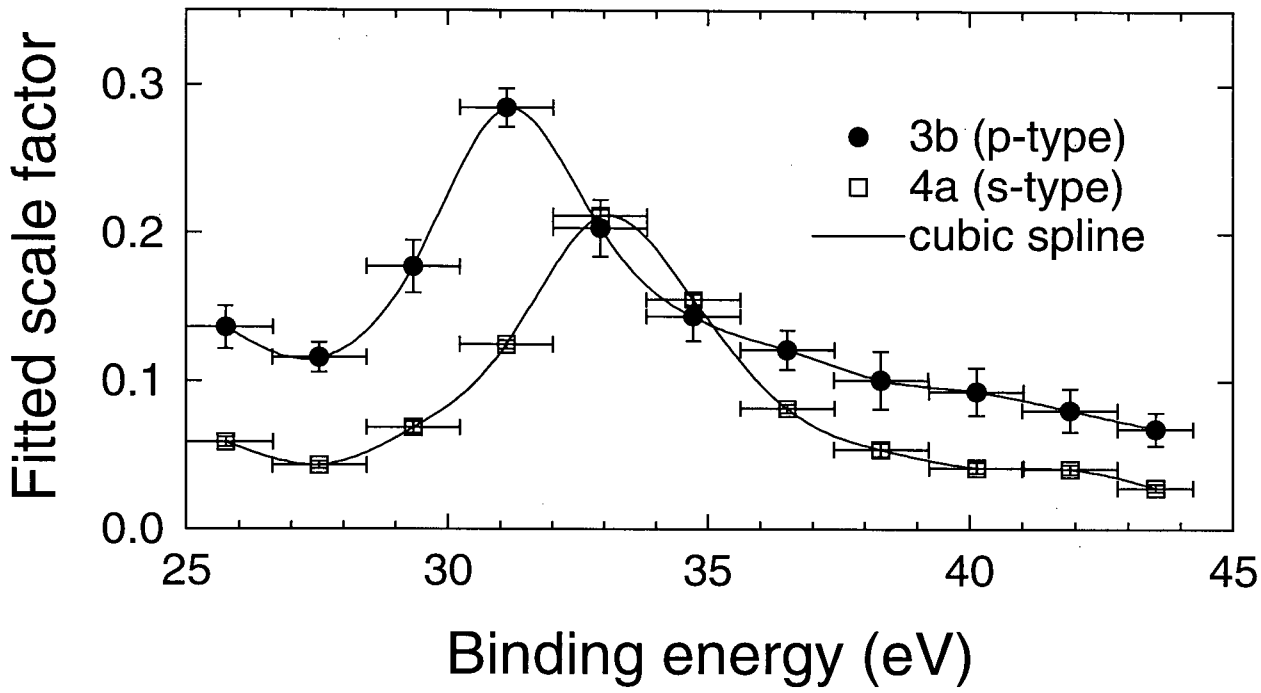

Figure 5.14: Variation of the fitted 3b and 4a scale factors of Figure 5.13 with binding energy. The scale factors were obtained by a least-squares fit of the 3b and 4a B3LYP/6-311++G** theoretical angle profiles to experimental angle profiles obtained by summing data over selected energy ranges of the experimental BES. Each data point is located at the average energy of the binding energy range used for that fit, with the binding energy error bars indicating the width of each binding energy range and the scale factor error bars indicating the calculated uncertainties of the fits. The solid lines are a cubic spline fit to the data.

5.6 Computational method and basis set effects

The theoretical momentum profiles in Figures 5.3–5.11 and the other calculated properties reported in Table 5.2 indicate a dependence upon the calculation by which they have been obtained. Effects resulting from both changes in the basis set and theoretical method used are evident. Comparing the HF and DFT (LSDA, BP86 and B3LYP) TMPs calculated using the 6-311++G** basis set and shown in Figures 5.3–5.11, several general observations can be made. For the outer-valence orbital momentum profiles (10b–5b), the DFT calculations predict more intensity at low momentum than do the HF calculations. This results in much

higher maxima at $p = 0$ for the s-type momentum profiles and a shift in the position of the profile maxima towards low p combined with an increase in the profile maxima for the p-type TMPs. In contrast, this behaviour is reversed for the inner-valence 4b and 5a orbital momentum profiles and there are only very slight differences between the 6-311++G** HF and B3LYP TMPs of the most tightly bound 3b and 4a orbitals. The differences between the HF and DFT TMPs are greatest for the LSDA calculations and least for the DFT calculations using the B3LYP functional. Keeping in mind the approximately inverse weighting of p and r space resulting from the Fourier transform relating the two (Equation (1.1)), two separate effects can be used to explain the observed behaviour:

1. As discussed by Duffy et al. [20], in the local spin-density approximation (LSDA), the incorrect asymptotic form of the exchange–correlational functional results in large-r electrons that are less bound than they should be, causing the orbitals to be more diffuse and consequently yielding momentum profiles that are too high at low momentum. The improved asymptotic form of Becke's gradient corrected exchange functional [105] used in the BP86 calculations lessens the under-binding of the large-r electrons and therefore lowers the TMPs near $p = 0$. The inclusion of the HF exchange term in Becke's three parameter exchange functional [108] (B3LYP) further improves the description of the large-r electron density and hence further decreases the low p intensity of the calculated momentum profiles. This effect may be expected to become less significant for the inner-valence orbitals because of their more contracted (localized) electron density when compared with the outer-valence orbitals.

2. Initial state correlation, not accounted for in the HF calculations but included in the DFT calculations, may result in an r-space contraction of the core orbitals as a result of the ability of the electrons to avoid each other [20]. If this also occurs for the

4b and 5a inner-valence orbitals, this would explain the decreased intensity at low momentum of the 4b and 5a DFT TMPs in comparison to the HF TMPs. In addition, this contraction of the core and possibly inner-valence orbitals would result in more effective screening of the nuclear charge and lead to more diffuse outer-valence orbitals and consequently outer-valence TMPs with greater intensity at low momentum. In previous EMS studies of NH_3, H_2O and HF [20, 45, 47, 155], the effect of electron correlation on the outer-valence TMPs, accounted for either by extremely large MRSD-CI calculations or density functional methods, has been similar to that observed here for dimethoxymethane, resulting in increased intensity at low momentum.

Overall, the DFT calculations provide better agreement with the experimental momentum profiles than do the HF calculations, suggesting that target electron correlation is an important factor in the momentum profiles of dimethoxymethane. As was discussed in Section 5.5.1, the differences between the DFT and CI 11a TMPs, illustrated in Figure 5.4, do not contradict this conclusion if they are the result of an insufficiently large MRSD-CI calculation.

The energies reported in Table 5.2 also display a sensitivity to theoretical method. Although it is not meaningful to directly compare the total energies calculated by the HF and post-HF methods with those from the DFT calculations, the relative electronic energies of the gg and ga conformers ($\Delta E_{0,\mathrm{ga-gg}}$) are comparable. As noted in References [140] and [141], the inclusion of electron correlation effects results in an increase in the calculated energy difference between the gg and ga conformers. This may be seen in Table 5.2 by comparing $\Delta E_{0,\mathrm{ga-gg}}$ from the HF/6-31+G* and MP2/6-31+G* calculations and from the HF/6-311++G** and the various DFT/6-311++G** calculations. The comparatively large value of $\Delta E_{0,\mathrm{ga-gg}}$ obtained by the MP2/6-31+G* calculations is likely too large as a result of the rather modest basis set used and the incomplete accounting of electron correlation.

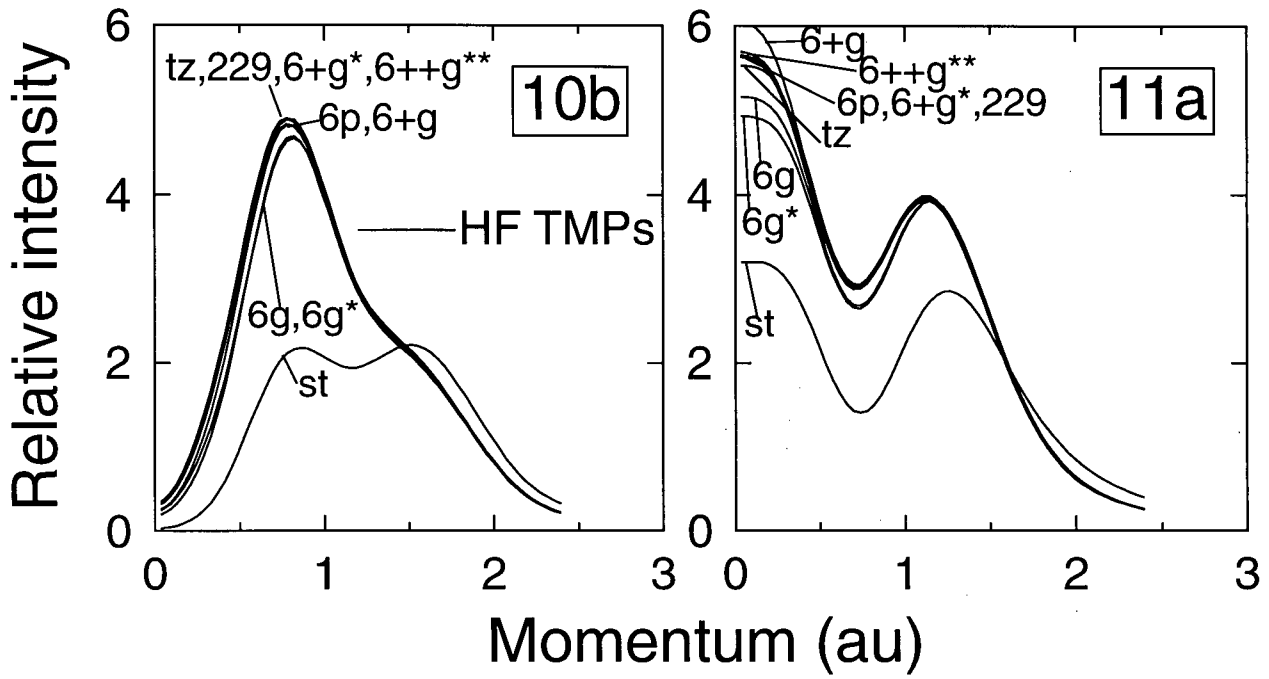

Figure 5.15: Basis set dependence of the 10b (left panel) and 11a (right panel) Hartree–Fock theoretical momentum profiles of dimethoxymethane. The TMPs were calculated using the MP2/6-31+G* optimized gauche-gauche geometry. TMPs shown are the results of HF calculations using the following basis sets: STO-3G (st), 6-31G (6g), 6-31+G (6+g), 6-31G* (6g*), 6-31+G* (6+g*), 6-31++G** (6++g**), 6-311++G** (6p), aug-cc-pVTZ (tz) and the 229-CGF basis set (229) described in Section 5.3. The experimental angular resolution has been accounted for using the GW-PG method [48].

This is supported by the observation by Wiberg and Murcko [140] that increasing the size of the basis set results in a decrease in $\Delta E_{0,\mathrm{ga-gg}}$ (this trend is also evident from the HF results in Table 5.2) and the fact that the MP2/6-31+G* total energy for the gg conformer is 0.02 hartree lower than that obtained from the CI/229-CGF calculation, which may be expected to be more accurate.

To further assess the dependence of the calculated results upon basis set, additional HF and DFT-B3LYP calculations have been performed. 10b and 11a theoretical momentum profiles of the MP2/6-31+G* optimized gg conformer of dimethoxymethane, calculated using a range of basis sets, are shown in Figure 5.15 obtained using the HF method and in Figure

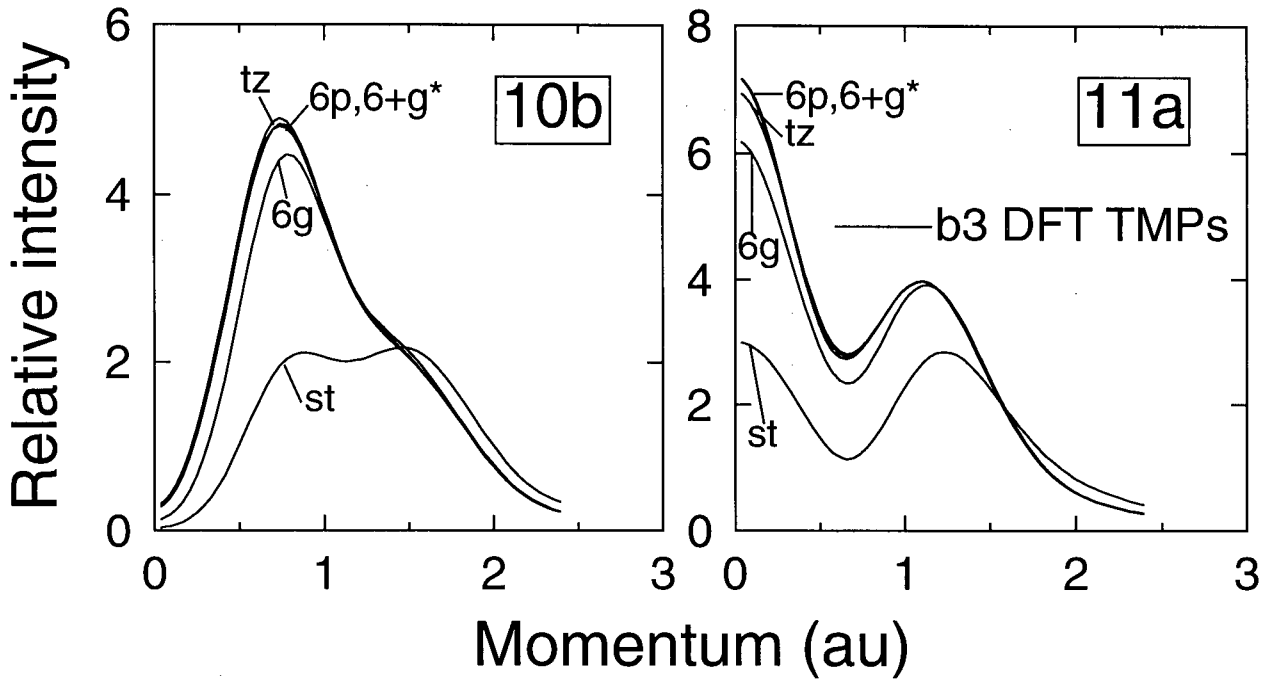

Figure 5.16: Basis set dependence of the 10b (left panel) and 11a (right panel) B3LYP-DFT theoretical momentum profiles of dimethoxymethane. The TMPs were calculated using the MP2/6-31+G* optimized gauche-gauche geometry. TMPs shown are the results of DFT calculations using the B3LYP exchange–correlation functional and the following basis sets: STO-3G (st), 6-31G (6g), 6-31+G* (6+g*), 6-311++G** (6p) and aug-cc-pVTZ (tz). The experimental angular resolution has been accounted for using the GW-PG method [48].

5.16 obtained using DFT with the B3LYP functional. Several variations of the 6-31G basis set involving augmentation with diffuse and polarization functions (Section 2.3.4) have been used. In addition, the TMPs obtained using the minimal STO-3G basis set and the 6-311++G**, 229-CGF and aug-cc-pVTZ basis sets are shown. The 10b and 11a TMPs have been selected for this comparison because the results in Figures 5.3 to 5.11 indicate that the outer-valence orbital TMPs are the most sensitive to variations in the computational method and because the outer-valence orbitals are of greatest significance to chemical behaviour. The corresponding total energies and dipole moments from these calculations are shown in Table 5.3, along with the momentum values corresponding to the maxima of the 10b TMPs (p_{MAX}) and the maximum intensities of the 11a TMPs.

Table 5.3: Basis set and computational method dependence of calculated properties of the gauche-gauche (gg) conformer of dimethoxymethane. The calculations were performed using the MP2/6-31+G* optimized geometry.

Calculation	Total energy (hartree)	Dipole moment (debye)	10b p_{MAX} (au)	11a max (arb. units)
HF/STO-3G	-264.55318	0.135	1.510	3.211
HF/6-31G	-267.82738	0.342	0.809	5.163
HF/6-31+G	-267.83452	0.314	0.793	6.051
HF/6-31G*	-267.95148	0.301	0.816	4.934
HF/6-31+G*	-267.95876	0.294	0.794	5.624
HF/6-31++G**	-267.97126	0.289	0.791	5.683
HF/6-311++G**	-268.03074	0.277	0.787	5.648
HF/aug-cc-pVTZ	-268.06017	0.241	0.780	5.526
HF/229-CGF	-268.06916	0.256	0.780	5.631
CI/229-CGF	-268.71508	0.263	0.779	5.548
LSDA/6-311++G**	-267.43708	0.324	0.735	8.028
BP86/6-311++G**	-269.63211	0.312	0.736	7.664
B3LYP/STO-3G	-266.03937	0.153	1.457	2.986
B3LYP/6-31G	-269.46239	0.361	0.789	6.176
B3LYP/6-31+G*	-269.56528	0.333	0.752	7.150
B3LYP/6-311++G**	-269.63910	0.301	0.743	7.155
B3LYP/aug-cc-pVTZ	-269.66590	0.261	0.739	6.926

Considering the HF calculations, it is clear that the STO-3G basis set is inadequate for describing the valence orbital momentum densities of dimethoxymethane. Calculations using this basis set tend to seriously underestimate the intensity at low momentum, reflecting inadequacies in modeling the outer spatial regions of electron density, which approximately correspond to low momentum because of the Fourier-transform relationship between p and r space. In addition, the total energy and dipole moment from the HF/STO-3G calculation (Table 5.3) differ considerably from those calculated using larger basis sets. The use of the 6-31G basis set results in a considerable improvement in the calculated energy for the gg conformer as well as a large increase in the predicted low p intensity for the 10b and 11a TMPs. This behaviour is typical of that observed for the other valence orbitals of dimethoxymethane shown in Figures 5.5–5.11. In general, the HF/6-31G calculations are in much better agreement with experiment than are the HF/STO-3G TMPs. However, even for those momentum profiles where the HF calculations are in reasonable agreement with the experimental data (Figures 5.8–5.11), the HF/6-31G TMPs tend to underestimate the intensity at low momentum. The addition of diffuse functions to the heavy atoms (6-31+G) improves the description of the low momentum region, resulting in a shift in the location of the maximum of the p-type 10b profile (p_{MAX}) towards lower momentum and a considerable increase in the maximum of the 11a TMP (Figure 5.15 and Table 5.3). The calculated dipole moment also changes significantly from the HF/6-31G value. Note, however, that only a small improvement in the total energy results. These effects are reasonable since the addition of diffuse functions will improve the description of the outer spatial regions of the electron density and consequently the low p region of the momentum density but will have little effect on the energy, to which the outer regions of electron density contribute little. In the case of the 11a TMP, the HF/6-31+G calculation predicts more intensity near zero momentum than do any of the other HF calculations considered here, including those using

substantially more complete basis sets, suggesting that in this case, the under-emphasis of the diffuse electron density has been over-corrected. In contrast, the addition of heavy-atom polarization functions to the 6-31G basis set, giving the 6-31G* basis set, results in only a small change in the TMPs, particularly for the 10b orbital, but a considerable (> 0.1 hartree) improvement in the total energy and a somewhat greater change in the dipole moment than was obtained by adding the diffuse functions. The dependence of the dipole moment on the intermediate regions of electron density results in the observed significant changes in the calculated values for this property using both the 6-31+G and 6-31G* basis sets. The HF/6-31G* TMPs actually have slightly less intensity at low p than do the HF/6-31G TMPs, suggesting that the addition of polarization functions to the basis set improves the description of the small and medium r electron density at some expense to the description of the large r density. The inclusion of both heavy-atom diffuse and polarization functions has the expected effect, resulting (in comparison to the HF/6-31G* results) in only a slight improvement in the total energy but markedly increasing the predicted low p intensity in the 10b and 11a TMPs. The further addition of diffuse and polarization functions to the hydrogen atoms (the 6-31++G** basis set) results in little change in the 10b and 11a TMPs. This is not unexpected, since these two outer-valence orbitals consist of electron density centred predominantly on the oxygen atoms, with some electron density on the carbons but little on the hydrogens. Interestingly, a comparison of the remaining HF/6-31+G* and HF/6-31++G** valence TMPs of dimethoxymethane (not shown) indicates that the addition of diffuse and polarization functions to the hydrogen atoms also has little effect on the TMPs of orbitals with significant C–H bonding character. Slight changes in the total energy and dipole moment of the gg conformer of dimethoxymethane do result with the inclusion of hydrogen diffuse and polarization functions. The use of even larger basis sets for the HF calculations (i.e., 6-311++G**, 229-CGF and aug-cc-pVTZ)

results in little further change in the TMPs, indicating that the valence momentum profiles of dimethoxymethane are reasonably converged at the HF level using the 6-31+G* basis set. In the case of the inner-valence 6a, 4b and 5a momentum profiles (Figures 5.9–5.11), the HF/6-31G and HF/6-311++G** TMPs are nearly the same, indicating that the inclusion of diffuse and polarization functions is less important for describing the inner-valence orbitals, which are more atomic-like than the outer-valence orbitals.

In the case of the DFT calculations using the B3LYP functional, a comparison similar to the one just discussed for the HF method (but using a smaller number of basis sets) indicates essentially the same basis set dependence as was observed for the HF calculations (Figure 5.16 and Table 5.3). These results indicate the importance of considering basis set effects and electron density emphasis when performing quantum mechanical calculations. If only a single property is being calculated, it is essential to choose a basis set that will accurately model the appropriate region of the electron density. For example, a basis set that is well suited to calculating total energies may give very poor results for properties primarily dependent upon the large r regions of electron density. When several molecular properties are off interest, the basis set must be sufficiently flexible—containing both polarization and diffuse functions—to reasonably model all regions of electron density [45, 46].

5.7 Consideration of other conformers

In the analysis of the experimental momentum profiles of dimethoxymethane in Section 5.5, it was assumed that the experimental results are dominated by the gauche-gauche conformer; consequently, contributions from other conformers of dimethoxymethane were ignored. The MP2/6-31+G* electronic energy difference between the gg and ga conformers ($\Delta E_{0,\mathrm{ga-gg}}$) is 14.17 kJ/mol (Table 5.2), suggesting that at the experimental temperature of 25°C it is

Table 5.4: Relative thermodynamic quantities of the conformers of dimethoxymethane. The values are based upon B3LYP/6-31+G* geometry optimization and frequency calculations. Reported values are relative to those of the gg conformer at the experimental temperature of 298 K.

Conf.	ΔE_0 (kJ/mol)	ΔE_{zpv} (kJ/mol)	$\Delta(\Delta H(298))$ (kJ/mol)	ΔS_{298} (J/mol·K)	ΔG_{298} (kJ/mol)	g	Abund. (%)
gg	0.0	0.0	0.0	0.0	0.0	2	89.87
ga	10.618	−0.894	0.142	7.106	7.748	4	7.90
g^+g^-	15.878	−0.739	0.418	21.409	9.173	2	2.22
aa	24.535	−2.179	0.594	6.321	21.066	1	0.01

reasonable to consider only the gg conformer. However, the values for $\Delta E_{0,\text{ga}-\text{gg}}$ obtained by the other calculations shown in Table 5.2 are, with the exception of the HF/6-31G value, less than the MP2/6-31+G* value. In addition, published estimates of the energy difference between these conformers determined using various experimental techniques range from 5.9 to 10.5 kJ/mol [135–138]. In view of this considerable uncertainty in $\Delta E_{0,\text{ga}-\text{gg}}$ and the discrepancies between the XMPs and the gg TMPs for some momentum profiles (particularly 9b), an investigation of the effect of including contributions from other conformers of dimethoxymethane when analyzing the EMS data has been performed.

The relative Gibbs free energies (ΔG_{298}) of the gg, ga, g^+g^- and aa conformers of dimethoxymethane have been determined using the procedures described in Section 2.4.2. The calculations are based upon optimized geometries and vibrational frequencies obtained using DFT with the B3LYP functional and the 6-31+G* basis set. This level of theory was used rather than the MP2/6-31+G* level because of the considerable gain in efficiency realized by the DFT calculations over MP2 calculations using the same basis set. The results of these free energy calculations are shown in Table 5.4. The B3LYP and MP2 optimized geometries are discussed in Section 5.8 below. In the absence of a specific recommendation for a scale factor for use with B3LYP/6-31+G* vibrational frequencies, all vibrational frequencies were scaled by a factor of 0.963 (recommended by Rauhut and Pulay [156] for use

with B3LYP/6-31G* vibrational frequencies) prior to the calculation of the thermodynamic quantities shown in Table 5.4. The relative free energy of each conformer has been calculated using Equation (2.38) at the experimental temperature $T = 298$ K. All values are relative to those of the gg conformer. The relative populations of the conformers have been calculated using Equation (2.37).

The consideration of vibrational and rotational contributions to the relative conformer free energies (Table 5.4) results in a considerable decrease in the energies of all other conformers relative to that of the most stable gg conformer. The predicted population of the aa conformer remains negligible at the experimental temperature, so contributions from this conformer may reasonably be neglected when analyzing the experimental data. A population of $\approx 8\%$ for the ga conformer, however, is sufficiently large that it could potentially have a discernible impact on the momentum profiles. Theoretical momentum profiles of the weighted conformer sum have been obtained by summing the individual gg, ga and g^+g^- conformer TMPs, weighted by the calculated conformer populations at 298 K, for each orbital or sum of orbitals corresponding to the experimental momentum profiles. The results for orbitals 21+20, 19, 18+17 and 16+15+14 are indicated by the dashed lines in Figure 5.17 and are compared with the respective gg conformer TMPs (solid lines). MO numbers rather than symmetry labels have been used because of the different symmetries of the conformers. In obtaining these conformer sum TMPs, the variation of the ionization potentials with conformer has been neglected. This assumes that the ionizations from a particular orbital for all conformers will be contained within the corresponding peaks fitted to the binding energy spectra. An examination of the HF/aug-cc-pVTZ//MP2/6-31+G* orbital energies for the gg and ga conformers (Table 5.1) suggests that this is a good assumption for the inner-valence orbitals but is less reasonable for the outermost valence orbitals.

It is apparent from Figure 5.17 that contributions from conformers other than gg do

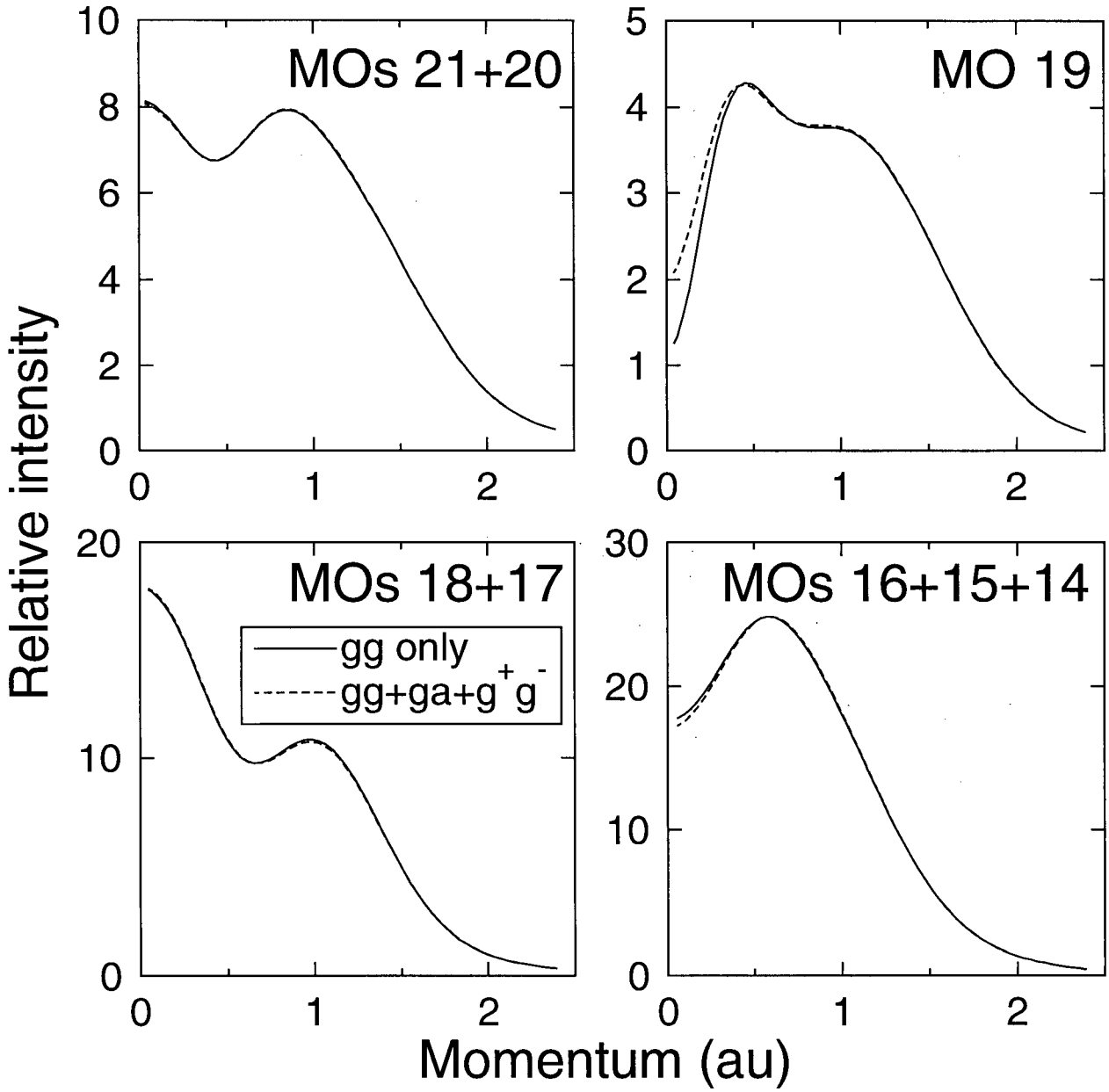

Figure 5.17: Comparison of dimethoxymethane outer-valence theoretical momentum profiles of the gauche-gauche (gg) conformer (solid lines) and of a conformer sum (dashed lines) weighted using calculated conformer abundances at 298 K. The TMPs were obtained from B3LYP/6-31+G*//B3LYP/6-31+G* calculations of each conformer. The experimental angular resolution has been accounted for using the GW-PG method [48].

not dramatically affect the momentum profiles of dimethoxymethane at the experimental temperature of 298 K. Of the profiles shown in Figure 5.17, only that for MO 19 shows any significant change when the ga and g^+g^- conformers are included. In this case, the individual ga and g^+g^- TMPs are both s-type, leading to the observed increase in intensity at low momentum. This results in slightly improved agreement between theory and experiment for MO 19 (9b in the case of the gg conformer, Figure 5.5). However, the bulk of the discrepancy between theory and experiment for the 9b momentum profile is not accounted for by the inclusion of contributions from other conformers of dimethoxymethane. This change in the shape of the MO 19 TMP upon inclusion of other conformers does suggest an alternative explanation for the observed disagreement between the 9b XMP and the TMPs (Figure 5.5)—namely vibrational effects. The low calculated vibrational frequency corresponding to torsions about the O–CH_2 bonds (the B3LYP/6-31+G* value is 98.2 cm^{-1}) indicates that there is appreciable excitation of this vibrational mode at the experimental temperature. Consequently, the approximation of using the equilibrium geometry in performing the TMP calculations (Section 2.2.2) may be inaccurate. Testing of this hypothesis requires the calculation of vibrationally averaged TMPs of dimethoxymethane (as was done recently for the $1b_{3u}$ TMP of ethylene [71]), a considerable computational task for a molecule of the size of dimethoxymethane. In general, the profiles shown in Figure 5.17 suggest that the population of the gg conformer is sufficiently great at 298 K to allow the EMS data to be interpreted on the basis of the presence of the gg conformer alone, as was assumed in Section 5.5.

5.8 Optimized geometries

The calculated theoretical momentum profiles discussed in Sections 5.5 and 5.6 above have been obtained using MP2/6-31+G* optimized geometries, while those in Section 5.7 were

calculated using B3LYP/6-31+G* optimized geometries. In comparing the experimental and theoretical momentum profiles and interpreting any differences, the sensitivity of the conformer geometries to the theoretical method used for the geometry optimizations as well as the sensitivity of the TMPs to small changes in the conformer geometries should be considered. To this end, additional geometry optimizations of the gg and ga conformers of dimethoxymethane have been performed using density functional theory with the B3LYP functional and the 6-311++G** basis set. Optimized parameters of the gg conformer from this work are compared in Table 5.5 with experimental values obtained by electron diffraction [134] and with the results of MP2/6-31G**, MP2/6-311++G** and B3LYP/6-31G** geometry optimizations recently reported by Kneisler and Allinger [142]. As noted by Kneisler and Allinger, the calculated bond lengths show little variation between calculations. In the case of the CH_2–O bonds, the calculated equilibrium values exceed the experimental average value by approximately 0.02 Å. Kneisler and Allinger [142] recommend a value of −0.0079 Å for conversion from average bond lengths to equilibrium values. The calculated bond angles are smaller than the experimental values (with the exception of the B3LYP/6-31G** OCO angle), with the B3LYP results in somewhat closer agreement with experiment than the MP2 results. The dihedral angle *d*COCO is the parameter most sensitive to the computational method. All of the calculated values of *d*COCO are greater than the experimental value of 63.3°, by about 2–3° in the case of the MP2 calculations and about 5° in the case of the density functional theory results.

A comparison of the calculated parameters of the ga conformer (Table 5.6) results in similar observations. The MP2 and B3LYP CO bond lengths calculated using the three basis sets differ by no more than 0.010 Å and generally by much less. As was noted for the gg conformer, the DFT bond angles are greater than the corresponding MP2 values. In the case of the dihedral angles, there is little disagreement between MP2 and DFT for the one

Table 5.5: Theoretical and experimental geometrical parameters of the gauche-gauche conformer of dimethoxymethane. Bond distances (r), angles (a) and dihedral angles (d) are shown. Distances are in angstroms and angles in degrees. rCO refers to the central CH_2–O bonds and rOC to the terminal O–CH_3 bonds.

	MP2			B3LYP			Experiment[a]
	6-31+G*[b]	6-31G**[c]	6-311++G**[c]	6-31+G*[b]	6-31G**[c]	6-311++G**[b]	
rCO	1.408	1.405	1.402	1.406	1.404	1.405	1.382
rOC	1.429	1.425	1.422	1.425	1.422	1.425	1.432
aCOC	112.47	111.76	112.02	113.97	113.40	113.88	114.6
aOCO	113.45	113.59	113.65	114.16	114.40	113.93	114.3
dCOCO	65.67	64.5	66.56	68.03	64.5	68.87	63.3

[a]Electron diffraction data from Reference [134].

[b]This work.

[c]From Reference [142].

Table 5.6: Optimized geometrical parameters of the gauche-anti conformer of dimethoxymethane. Bond distances (r), angles (a) and dihedral angles (d) are shown. Distances are in angstroms and angles in degrees. rCO refers to the central CH_2–O bonds and rOC to the terminal O–CH_3 bonds. Values preceding the slashes refer to the gauche methoxy group and those following the slashes refer to the anti methoxy group. The calculated energy differences in kJ/mol between the gg and ga conformers are also shown.

	MP2			B3LYP		
	6-31+G*[a]	6-31G**[b]	6-311++G**[b]	6-31+G*[a]	6-31G**[b]	6-311++G**[a]
rCO	1.389/1.418	1.387/1.414	1.383/1.412	1.386/1.417	1.385/1.414	1.384/1.416
rOC	1.430/1.422	1.425/1.417	1.422/1.414	1.428/1.416	1.428/1.412	1.425/1.415
aCOC	112.81/111.40	112.14/111.21	112.24/110.81	114.37/112.81	113.61/112.69	114.26/112.77
aOCO	109.54	109.59	109.84	110.10	110.02	110.00
dCOCO	64.91/178.40	64.82/175.14	65.31/178.71	67.24/178.42	64.82/175.14	67.20/178.14
$\Delta E_{0,\mathrm{ga-gg}}$	14.17	14.54	11.31	10.62	11.19	10.31

[a]This work.

[b]From Reference [142].

which is anti. In the case of the gauche dihedral angle, the DFT values are approximately 2° greater than the MP2 results. The generalized anomeric effect is evident in comparing the two CH_2–O (rCO) bond lengths of the ga conformer of dimethoxymethane. The length of the CH_2–O bond about which the dihedral angle is approximately 65° is about 0.03 Å less than that corresponding to the near 180° dihedral angle. Averaging these two bond lengths results in values very similar to (0.004 Å less than) the calculated CH_2–O bond lengths for the gg conformer. This is reasonable in light of the $n_\pi \rightarrow \sigma^*$ explanation of the anomeric effect; in the case of the ga conformer, the CH_2–O bond on the gauche side of the molecule is shortened because of increased C–O bonding character and the one on the anti side is lengthened as a consequence of increased C–O antibonding character. For the gg conformer, each CH_2–O bond will be affected by both of these effects, resulting in a bond length approximately the average of the two for the ga conformer. In the case of the O–CH_3 bond lengths for the ga conformer, the ones for the gauche methoxy group are essentially the same as the corresponding gg conformer values, while those for the anti methoxy group agree with the corresponding aa conformer values reported in Reference [142].

The good agreement between B3LYP/6-31G** and MP2/6-311++G** relative energies (Table 5.6), bond lengths and bond angles noted by Kneissler and Allinger [142] does not appear to be fortuitous upon consideration of the additional B3LYP calculations performed in the current work. The DFT results vary less with changes in basis set than do the MP2 results. Consequently, the B3LYP/6-311++G** results are in good agreement with both the B3LYP/6-31G** and MP2/6-311++G** results. In summary, the optimized MP2 and B3LYP geometries are reasonably consistent with one another, with the most significant differences occuring for the calculated dihedral angles.

Single point HF and B3LYP DFT calculations using the 6-311++G** basis set have been performed using the three optimized gg conformer geometries calculated in the present work.

Selected calculated properties are compared in Table 5.7. The same trends are evident with both the HF and DFT calculations. The total energy improves from the MP2/6-31+G* geometry to the B3LYP/6-31+G* and B3LYP/6-311++G** geometries. The calculated dipole moment and location of p_{MAX} of the 10b TMP decrease in the same order as do the total energies and the intensity of the 11a TMP at zero momentum follows the reverse trend. Smaller differences are obtained between the calculations using the two B3LYP geometries than between the MP2 and B3LYP geometries. The changes in these properties track the changes in the dihedral angle *d*COCO reported in Table 5.5. The significance of the variations of the TMPs calculated using different optimized geometries has been assessed by comparing valence orbital B3LYP/6-311++G** TMPs calculated using the MP2/6-31+G*, B3LYP/6-31+G* and B3LYP/6-311++G** optimized geometries of the gg conformer. The results for the 10b, 11a and 9a TMPs are shown in Figure 5.18. For all of the valence orbitals of the gg conformer, TMPs calculated using the B3LYP/6-31+G* and B3LYP/6-311++G** optimized geometries are essentially indistinguishable. For about half of the valence orbitals, TMPs calculated using the MP2 and DFT geometries are also essentially identical. All but two of the remaining orbitals show very small variations of a magnitude similar to that seen for the 10b TMPs in Figure 5.18. The 11a and 9a TMPs are the only ones that display significant changes with geometry. In view of these observations, it may be concluded that small differences in the geometries used to calculate TMPs of dimethoxymethane do not, for the most part, result in significant changes in the resulting momentum profiles. However, the possibility of the choice of an inaccurate conformer geometry for the calculation of TMPs cannot be ruled out as a factor contributing to differences between theoretical and experimental results for a small number of the dimethoxymethane momentum profiles.

Table 5.7: Calculated properties of the gauche-gauche (gg) conformer of dimethoxymethane at three levels of geometry optimization.

Calculation	Total energy (hartree)	Dipole moment (D)	10b p_{MAX} (au)	11a max (arb. units)
HF/6-311++G**//MP2/6-31+G*	-268.03074	0.277	0.787	5.648
HF/6-311++G**//B3LYP/6-31+G*	-268.03123	0.217	0.767	6.210
HF/6-311++G**//B3LYP/6-311++G**	-268.03168	0.185	0.764	6.270
B3LYP/6-311++G**//MP2/6-31+G*	-269.63910	0.301	0.743	7.155
B3LYP/6-311++G**//B3LYP/6-31+G*	-269.63939	0.248	0.726	7.936
B3LYP/6-311++G**//B3LYP/6-311++G**	-269.63943	0.220	0.723	7.936

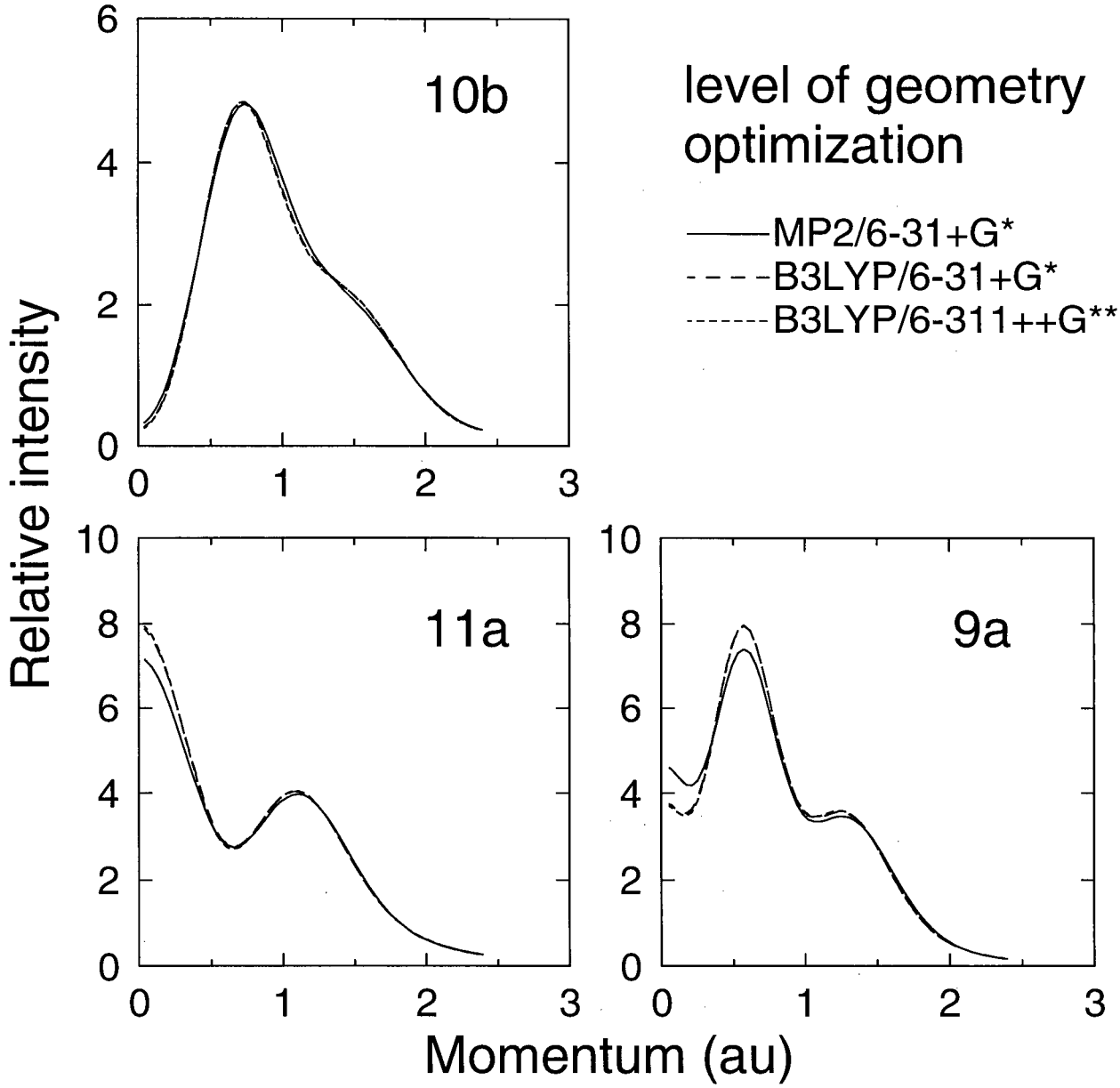

Figure 5.18: Variation with geometry of the 10b (upper left panel), 11a (lower left panel) and 9a (lower right panel) theoretical momentum profiles of dimethoxymethane. The TMPs have been obtained from single-point B3LYP/6-311++G** calculations using gauche-gauche conformer geometries optimized at the MP2/6-31+G* (solid lines), B3LYP/6-31+G* (long dashed lines) and B3LYP/6-311++G** (short dashed lines) levels. The experimental angular resolution has been accounted for in the theoretical profiles using the GW-PG method [48].

Chapter 6

Glycine

6.1 Introduction

An understanding of the electronic structure and electron density distribution of amino acids is of considerable importance because of their role as the basic structural units of proteins. Information concerning the electron density distributions of proteins is relevant to areas of protein biochemistry concerned with conformation, molecular recognition and reactivity. However, the large size and structural complexity of proteins considerably limits the range of experimental and theoretical methods that can be applied to the study of these fundamental biochemical molecules. Consequently, studies of simpler systems are necessary both to gain experimental information that can possibly be applied to larger molecules and to evaluate theoretical methods prior to their application to larger systems. As the simplest amino acid, glycine (NH_2CH_2COOH) is an important model compound in biochemistry. Glycine is small enough that a broad range of theoretical methods can be employed and experimental data are attainable for comparison with theory, making this molecule an obvious test case for the evaluation of approximate theoretical methods being considered for use with larger molecules.

Despite being the smallest amino acid, glycine has proven to be a challenging system for theoretical study. The neutral glycine molecule, the form found in the gas phase, has considerable conformational flexibility as a result of the three bond axes about which torsions can occur—namely the N–C, C–C and C–O(hydroxyl) bonds. This conformational flexibility, in combination with several intramolecular hydrogen bonding possibilities, results in numerous stable conformers and thus considerably increases the challenge of accurate theoretical modeling. Much of the theoretical work on glycine to date has focussed on determining the geometries and relative energies of these stable conformers. It is apparent from this quantum mechanical work that the results for glycine are very sensitive to the theoretical method employed and to the nature of the basis set used. In particular, it has been found that the results from semiempirical and HF calculations vary considerably [79]. Conclusions based on HF calculations regarding the geometries and relative energies of the glycine conformers that are energy minima on the glycine potential energy surface are strongly basis set dependent [79, 80, 82]. The use of flexible basis sets containing both diffuse and polarization functions appears necessary in order to perform meaningful geometry optimization calculations on glycine. This has been attributed to the presence of several non-bonding electron pairs and intramolecular hydrogen bonds [82]. Electron correlation effects have also been shown to play a significant role in glycine, with their inclusion, whether through Møller–Plesset (MP) perturbation theory [81,82,157], CI [83] or DFT [84,85], having a particularly significant effect on the relative conformer energies. With respect to determining geometries, there is some disagreement as to the necessity of employing theoretical methods that take account of electron correlation effects in glycine [157–159]. Regardless, recent high level calculations using large basis sets and MP2 [81], CI [83] and DFT with hybrid functionals [84, 85] are in fairly close agreement not only for the conformer geometries but also for their relative energies.

The need to perform relatively large calculations in order to obtain dependable results for the geometries and relative energies of the glycine conformers raises the question as to the sensitivity of other calculated properties of glycine to basis set size and composition and to electron correlation effects. Because of the importance of the outer valence orbitals—and in particular the HOMO electron density—to chemical reactivity [3, 4], it is of particular interest to investigate the importance of the considerations mentioned above to the valence orbital electron density distributions of glycine. As mentioned in Section 1.1.2, EMS measurements and associated calculations have clearly shown that electron correlation effects are a determining factor in the long range (low momentum) parts of the outer-valence orbital electron density distributions in NH_3 [9, 47] and the methylamines [160]. Therefore, since for most conformers of glycine the HOMO electron density is predominantly located on the nitrogen atom, it is of interest to see if similar electron correlation effects are also a determining factor in the valence orbital electron density distributions of glycine.

In this chapter, the first detailed and comprehensive EMS study of the outer-valence momentum profiles of glycine is presented. The improved sensitivity provided by the multichannel electron momentum spectrometer described in Chapter 3 and the development of the heated sample probe shown in Figure 3.2 have been key to making these experimental measurements feasible. The roles of basis set size and composition and also electron correlation effects in modeling the outer-valence electron densities of glycine have been studied by comparing the experimental measurements to HF and DFT calculations using a range of basis sets. In view of the success of DFT, via the TKSA, in describing electron correlation effects in the valence momentum profiles of small molecules [20, 21, 71], this study of glycine is of particular interest to further evaluate the effectiveness of the TKSA for describing the valence electron densities of larger molecules.

Several other previously published studies are pertinent to the current work. The outer-

valence photoelectron spectrum of glycine has been reported by Debies and Rabalais [161] in 1974 and by Cannington and Ham [162] in 1983 using He(I) and He(II) resonance radiation respectively. Both studies found three peaks in the low binding energy region, at 10.0, 11.1 and 12.1 eV, assigned as ionizations from non-bonding nitrogen (HOMO), carbonyl oxygen and hydroxyl oxygen orbitals, respectively. The two studies made the same assignments for the symmetry of the second and third orbitals (a′ and a″, respectively) but differed on the symmetry of the HOMO, with Debies and Rabalais predicting an out of plane (a″) orbital and Cannington and Ham predicting an in plane (a′) orbital. Recently, Hu, Chong and Casida [163] have calculated the IPs of the two most stable conformers of glycine using a parametrized second-order Green function times screened interaction (pGW2) method. Their calculated IPs of the global-minimum conformer (**Ip**, see below) are in very good agreement with the experimental values reported by Cannington and Ham [162]. As to the assignment of the photoelectron spectrum, the calculations of Hu et al. [163] support the assignment by Cannington and Ham [162] for the HOMO (i.e., a′), but indicate that the previous assignments [162] of the ninth and tenth IPs (i.e., ionizations from MOs 12 and 11) were reversed and should be a′ and a″, respectively.

As stated above, there are several stable conformers of glycine present in the gas phase. In fact, theoretical studies have found as many as eight conformers [79–84], which are illustrated in Figure 6.1. The conformer labels are those used by Császár [81], where **p** and **n** denote planar (C_s symmetry) and non-planar (C_1) heavy-atom frameworks, respectively. Only a few of these conformers have been observed experimentally. Both conformers **Ip** and **IIp** have been identified by microwave spectroscopy [73–77]. In the recent study by Godfrey and Brown [77], the non-observance of conformers other than **Ip** and **IIp**, in combination with a consideration of their instrumental sensitivity and estimated absorption coefficients for conformers **IIp** and **IIIp**, initially lead to the prediction of an upper limit of 0.2 for

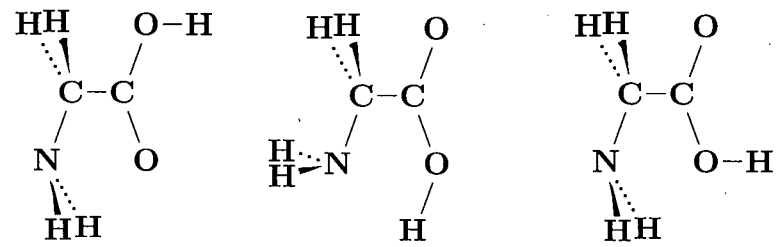

Ip
52.6%

IIp
9.0%

IIIp
29.6%

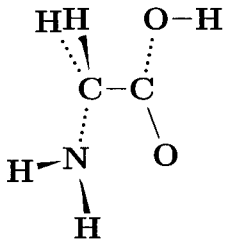

IVn
6.8%

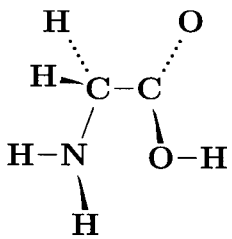

Vn
1.6%

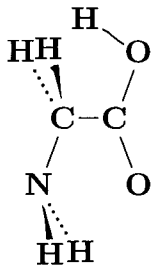

VIp
0.3%

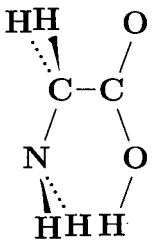

VIIp
0.1%

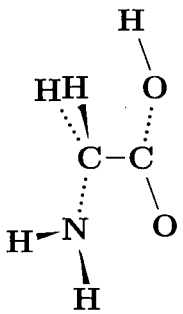

VIIIn
0.0%

Figure 6.1: Conformers of glycine. Following the labeling scheme used in Reference [81], **p** denotes a C_s symmetry conformer and **n** a C_1 symmetry conformer. The calculated abundance of each conformer based on the relative free energies (see Section 6.3 and Table 6.2) at the experimental temperature of 165°C is also indicated.

the abundance of **IIIp** relative to that of **IIp** at the experimental temperature of 235°C. In contrast, the most elaborate theoretical studies [81, 83, 84] predict that conformer **IIIp** should be present in a proportion considerably larger than this. In this regard, Godfrey and Brown [77] point out that their limited observations (only **Ip** and **IIp**) could be due to relaxation of the other conformers to **Ip** in the expanding gas jet. A recently published theoretical study [164] of the barriers to interconversion between glycine conformers indicates that this explanation is likely correct. This is further supported by recently reported evidence for a third conformer, obtained by an infrared spectroscopy study of glycine trapped in inert gas matrices [78].

The results of the microwave studies [76,77] are in agreement with an electron diffraction study [165] and the various theoretical calculations that predict that the most stable conformer is **Ip**. In the case of conformer **II**, the microwave data indicates that this conformer has C_s symmetry with a planar heavy-atom framework (i.e. **IIp**). At the highest levels of theory employed thus far [81, 83, 84], the geometry-optimized structure is a C_1 symmetry conformer (**IIn**) resulting from a slight out-of-plane twist of the planar heavy-atom skeleton. These calculations also indicate that structure **IIp** is a saddle-point between two equivalent **IIn** structures [79, 81–83]. However, the energy difference between the **IIp** and **IIn** forms is calculated to be quite small and is less than the calculated zero-point vibrational energy. Therefore, while the equilibrium geometry may correspond to **IIn**, the average geometry is expected [77, 79–81, 83] to be **IIp**, in agreement with the microwave studies. In the case of the third conformer, the calculated energy minimum is either the C_s symmetry **IIIp** or the C_1 symmetry **IIIn** form, depending upon the theoretical method and basis set used. However, the highest level post-HF and DFT calculations [81, 83–85] all predict **IIIp** to be the true energy minimum, although the energy difference from **IIIn** is very small ($\approx$ 0.03 kJ/mol). Of the remaining predicted energy minima, three (**IVn**, **Vn** and **VIIIn**) are of C_1

symmetry and two (**VIp** and **VIIp**) are of C_s symmetry. These C_1 symmetry conformers (**IVn**, **Vn** and **VIIIn**) differ considerably from their C_s symmetry analogs both in terms of geometry and energy, in contrast to the situation for **IIn** and **IIIn** described above.

6.2 Experimental details

Binding energy spectra of gaseous glycine over the energy range of 6–27 eV were recorded sequentially at relative azimuthal angles of 0°, 1°, 2°, 3°, 4°, 6°, 8°, 11°, 14°, 17°, 20°, 25° and 30° using the binning data collection mode at a total energy of 1200 eV. Many scans were accumulated over an appreciable measuring time ($\approx$ 1100 hours) in order to improve the signal to noise ratio of the data. The heated sample probe described in Chapter 3 and shown in Figure 3.2 was used to admit gaseous glycine into the experimental interaction region by sublimation of the solid sample (from MCB Chemicals) at 165°C. This temperature was chosen so that the singles and coincidence count rates were similar to those typically obtained for gaseous samples (see Section 3.3). Earlier experiments have shown that when glycine is sublimated in this temperature range using glass sample holders, sample decomposition does not occur [166, 167].

The experimental energy resolution function (1.5 eV fwhm) and the momentum resolution ($\approx$ 0.1 au fwhm) of the spectrometer were determined from measurements of the helium $(1s)^{-1}$ binding energy peak and the argon 3p momentum profile, respectively. Helium gas was admitted into the collision chamber during the data acquisition for glycine to serve as an internal standard for energy calibration and to aid in the monitoring of the experimental conditions. In particular, it was necessary to ensure that no charging effects occurred because of condensed glycine deposits which built up on the spectrometer during the experiment. No change in the width or position of the sharp He $(1s)^{-1}$ peak was detected during the long

data accumulation period. Furthermore, the He 1s XMP, obtained by a least-squares fit of Gaussian functions to the EMS BES (see Figure 6.4 below) is in excellent agreement with the TMP calculated from the highly-correlated He wavefunction of Davidson [168], as shown in Figure 6.2.

6.3 Computational Details

In the present work, HF and DFT calculations were performed for each of the eight MP2/6-311++G** geometry optimized conformers shown in Figure 6.1 and predicted by Császár [81] to be energy-minima on the glycine conformational potential energy surface. Calculations were carried out for the C_s symmetry conformers **Ip**, **IIp**, **IIIp**, **VIp** and **VIIp** (having a planar heavy-atom skeleton) and the C_1 symmetry conformers **IVn**, **Vn** and **VIIIn**. The **IIp** and **IIIp** geometries were used for this study even though they are saddle points rather than energy minima on the MP2/6-311++G** potential energy surface because, as discussed in Section 6.1, in both cases the effective ground state structures are expected to be the C_s symmetry conformers. The HF calculations for each of these eight conformers were performed using a series of basis sets of increasing complexity, ranging from the STO-3G (st) minimal basis set with 30 contracted Gaussian functions (CGFs) to the 345-CGF near-Hartree–Fock limit aug-cc-pVTZ (tz) basis set of Dunning and co-workers [114, 115]. Theoretical momentum profiles for the valence orbitals of each of the conformers were obtained using the THFA (Equation (2.11)) with each of the HF wavefunctions. Momentum profiles were also calculated using the TKSA (Equation (2.14)) from the Kohn-Sham orbitals obtained from DFT calculations. The KS-DFT calculations were performed with a variant of the aug-cc-pVTZ basis set, referred to in the present work as the trun-pVTZ (tt) basis set, from which the heavy-atom f polarization functions and hydrogen d polar-

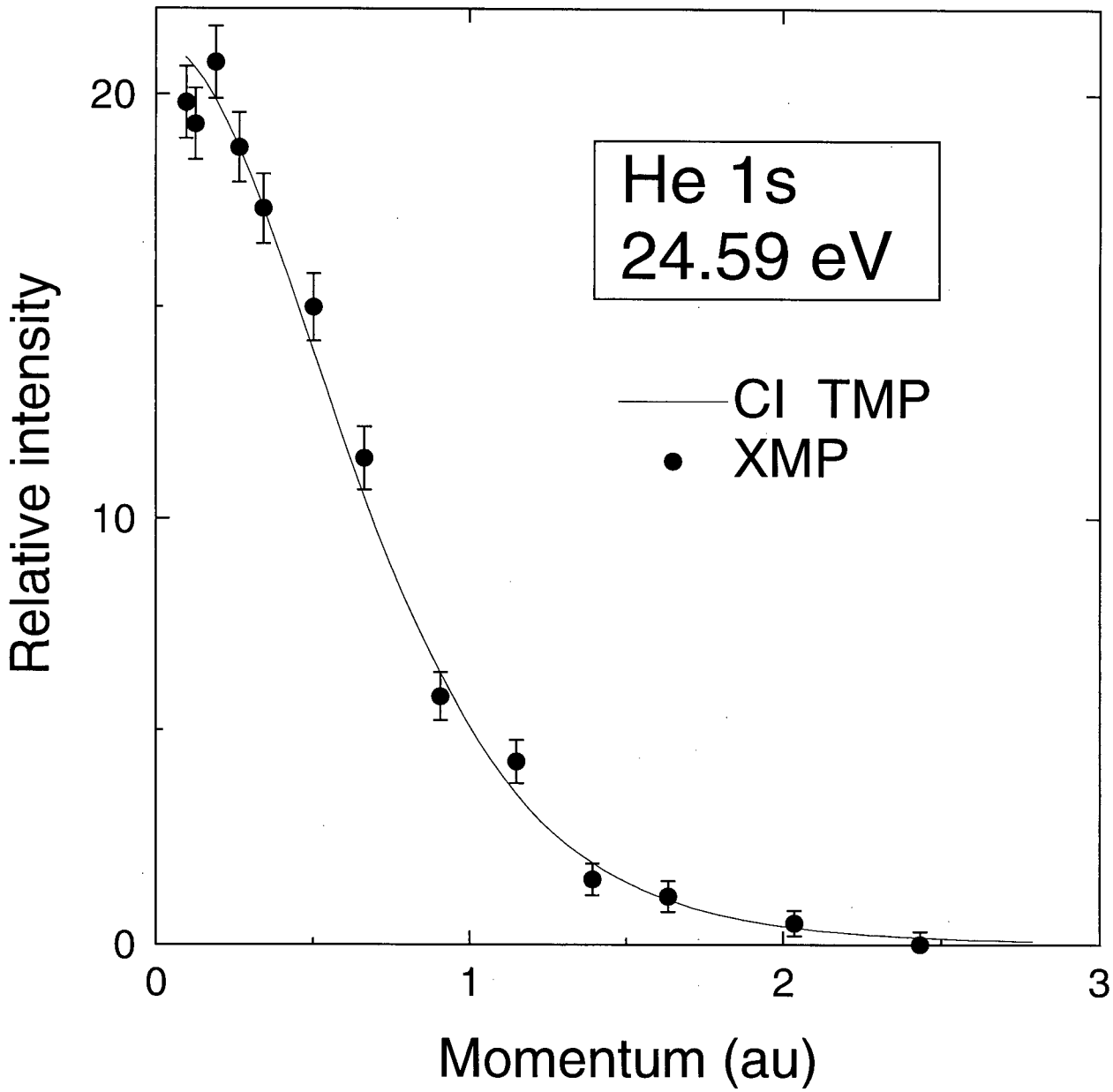

Figure 6.2: Experimental and theoretical He 1s momentum profiles. The experimental profile (•) is that of the He $(1s)^{-1}$ ionization peak (see Figure 6.4) and was monitored during the glycine data collection to ensure correct spectrometer operation. The theoretical profile (—) was obtained using Davidson's highly-correlated He wavefunction [168].

ization functions have been removed. The resulting 240-CGF basis set still contains d and p polarization functions on the heavy atoms and hydrogens, respectively. This truncation was necessary because the version of the *deMon* program [100, 101] used to perform some of the DFT calculations cannot process f functions. The DFT calculations were performed within the local spin-density approximation using the Vosko, Wilk and Nusair [99] functional (LSDA) and also using two gradient-corrected functionals: the first (BP86) consisting of the Perdew 1986 correlation [106] and Becke 1988 exchange [105] functionals and the second (B3LYP) being the hybrid functional proposed by Becke [108] and incorporating the exact exchange energy, but with the Lee, Yang and Parr [107] correlation functional replacing that of Perdew and Wang [109]. A summary of the calculations performed and selected calculated properties are shown in Table 6.1. The basis sets (with the exception of the trun-pVTZ basis set described above) and exchange–correlation functionals used are discussed in greater detail in Sections 2.3.4 and 2.3.3, respectively. All HF calculations were performed using GAUSSIAN92 [102]. DFT calculations with the LSDA and BP86 functionals were performed using the *deMon* [100, 101] density functional program with an "extrafine nonrandom" grid and the B3LYP DFT calculations were performed using GAUSSIAN92 with the "Int=FineGrid" option. The effects on the TMPs of the finite spectrometer acceptance angles (i.e., the momentum resolution) have been folded into the calculated profiles using the GW-PG method [48].

For comparison with the experimental momentum profiles, the TMPs for the five lowest energy conformers (**Ip**, **IIp**, **IIIp**, **IVn** and **Vn**) were Boltzmann weighted using Equation (2.37) according to the experimental temperature of 165°C and their calculated Gibbs free energies at that temperature relative to the free energy of the most stable conformer (**Ip**), and summed together. The remaining three conformers (**VIp**, **VIIp** and **VIIIn**) were not included in this sum since the free energy calculations (see below) indicate that they will

Table 6.1: Summary of calculations performed and calculated properties of glycine. All calculations were performed using the MP2/6-311++G** optimized geometries reported in Reference [81].

Key	Method	Basis Set	Total energy (hartree)	Dipole moment[a] (debye)	
			Ip	**Ip**	**IIp**
st	HF	STO-3G	-279.114538	1.185	4.638
4g	HF	4-31G	-282.403960	1.271	6.936
6g	HF	6-311G	-282.768248	1.258	6.914
6p	HF	6-311++G**	-282.921717	1.286	6.302
tt	HF	trun-pVTZ[f]	-282.942077	1.275	6.098
tz	HF	aug-cc-pVTZ	-282.951366	1.276	6.097
ld	DFT LSDA[b]	trun-pVTZ[f]	-282.326642	1.210	5.715
bp	DFT BP86[c]	trun-pVTZ[f]	-284.572595	1.182	5.591
b3	DFT B3LYP[d]	trun-pVTZ[f]	-284.548905	1.199	5.689
	DFT BP86[e]	cc-pVQZ		1.213	5.583
	experiment			1.0–1.4[g]	4.5–4.6[h]

[a]Theoretical values are for a non-rotating, non-vibrating molecule.

[b]The Vosko, Wilk and Nusair [99] local exchange–correlation functional was used.

[c]The Becke exchange [105] and Perdew correlation [106] functionals were used.

[d]The B3LYP functional is a modification of the hybrid functional proposed by Becke [108] and incorporating the exact exchange energy, with the Lee, Yang and Parr [107] correlation potential replacing that of Perdew and Wang [109].

[e]Calculated by Chong [169] using the CCSD/DZP geometries of Hu et al. [83]. Also reported in Reference [169] and from the same calculations are: $\mu_a = 1.001$ D and $\mu_b = 0.685$ D for conformer **Ip** and $\mu_a = 5.514$ D and $\mu_b = 0.873$ D for conformer **IIp**.

[f]The trun-pVTZ basis set is the aug-cc-pVTZ basis set with the f functions on the heavy atoms and the d functions on the hydrogens removed.

[g]Suenram and Lovas [76] determined μ_a of conformer **Ip** to be 1.0 ± 0.15 D and $\mu_b \neq 0, \mu_a > \mu_b$.

[h]Brown et al. [74] found μ_a of conformer **IIp** to be 4.5 D and $\mu_b < 1$ D.

Table 6.2: Relative thermodynamic quantities and abundances (Abund.) of the conformers of glycine. All values are relative to those of conformer **Ip** and were calculated at the experimental temperature of 438 K. Vibrational frequencies (scaled by 0.97) and rotational constants from Reference [81] were used to calculate the relative entropies (ΔS), zero-point vibrational energies (ΔE_{zpv}) and thermal energies ($\Delta(\Delta H)$) of all conformers except **IIIp**, for which the vibrational frequencies from Reference [83] were used.

Conf.	ΔE_0[a] (kJ/mol)	ΔE_{zpv} (kJ/mol)	$\Delta(\Delta H(438))$ (kJ/mol)	ΔS_{438} (J/mol·K)	ΔG_{438} (kJ/mol)	Abund. (%)
Ip	0.0	0.0	0.0	0.0	0.0	52.61
IIn	2.058	1.613	−1.305	−9.321	6.449	8.96
IIIp	6.663	0.072	0.081	10.764	2.100	29.56
IVn	5.156	0.203	−0.402	−5.720	7.463	6.78
Vn	10.503	0.482	−0.456	−4.852	12.655	1.63
VIp	19.750	−1.102	−0.499	1.498	18.491	0.33
VIIp	24.081	−1.369	0.351	0.136	23.004	0.10
VIIIn	25.265	−0.662	−0.049	−4.420	26.491	0.04

[a]Best MP estimates from Reference [81].

account for only $\approx 0.5\%$ of the sample at the experimental temperature. The use of free energies for the TMP weighting is a more physically realistic treatment than the use of electronic energies alone, as was done in a preliminary analysis of the glycine HOMO electron density [152]. The calculated thermodynamic quantities are summarized in Table 6.2. The relative free energies at 165°C differ significantly from the relative electronic energies of the glycine conformers. Free energies were calculated with the harmonic oscillator–rigid rotor approximation using the standard statistical-mechanical formulae discussed in Section 2.4.2. The final predictions of Császár [81] for the relative conformer energies were used for the relative electronic energies ΔE_0. The rotational constants and vibrational frequencies (scaled by 0.97 as recommend in Reference [81]) reported by Császár [81] for the MP2/6-311++G** geometry optimized conformers were then used to calculate the relative zero-point vibrational energies ΔE_{zpv}, thermal energies $\Delta(\Delta H(T))$ and entropies ΔS_T of the conformers. The vibrational frequencies of conformer **IIIp** were not reported by Császár, so the relative thermodynamic properties for this conformer were calculated using the vibrational frequen-

cies reported by Schaefer et al. [83] and calculated at the HF/DZP level. Relative Gibbs free energies at 438 K were then calculated using Equation (2.38) of Section 2.4.2.

The energy of conformer **IIp** relative to that of conformer **Ip** has been determined to be 5.4–6.7 kJ/mol by infrared spectroscopy of glycine isolated in an inert gas matrix [78], and 5.9 ± 1.8 kJ/mol by microwave spectroscopy [76]. Both of these experimental results are in agreement with the calculated relative Gibbs free energy of **IIp** reported in Table 6.2. In contrast, the calculated relative energy of **IIIp** is less than the single reported experimental value of 3.8–6.3 kJ/mol, obtained in the same infrared spectroscopy study mentioned above [78]. The disagreement between the calculated and experimental values for **IIIp** could be a result of the use of HF [83] rather than MP2 [81] vibrational frequencies to calculate the free energy of this conformer or uncertainties in the experimental value, determined in a challenging experiment involving infrared spectroscopy of glycine trapped in an inert gas matrix [78]. In this regard, in a recent density functional study of glycine [85], Hagler et al. found that the use of vibrational frequencies calculated using the MP2 or B3LYP-DFT methods, rather than the HF method, resulted in a significantly greater relative free energy for conformer **IIIp**. This difference was primarily attributed to a very low value for the first vibrational frequency of this conformer when calculated at the HF level of theory. The impact this has on the Boltzmann weighted conformer sum TMPs discussed in the following sections has been investigated by setting the relative free energy of conformer **IIIp** to 12.02 kJ/mol, the value reported by Hagler et al. [85] for the temperature of 473 kelvin and obtained using vibrational frequencies calculated at the MP2/DZP level of theory. Using this new value for the free energy of **IIIp**, the relative populations of conformers **Ip**–**VIIIn** become 72.68, 12.38, 2.68, 9.37, 2.25, 0.45, 0.13 and 0.05%, respectively. Comparing these values with those in Table 6.2 indicates that this change in the free energy of **IIIp** has a rather large effect on the estimated conformer abundances, particularly for conformers **Ip**

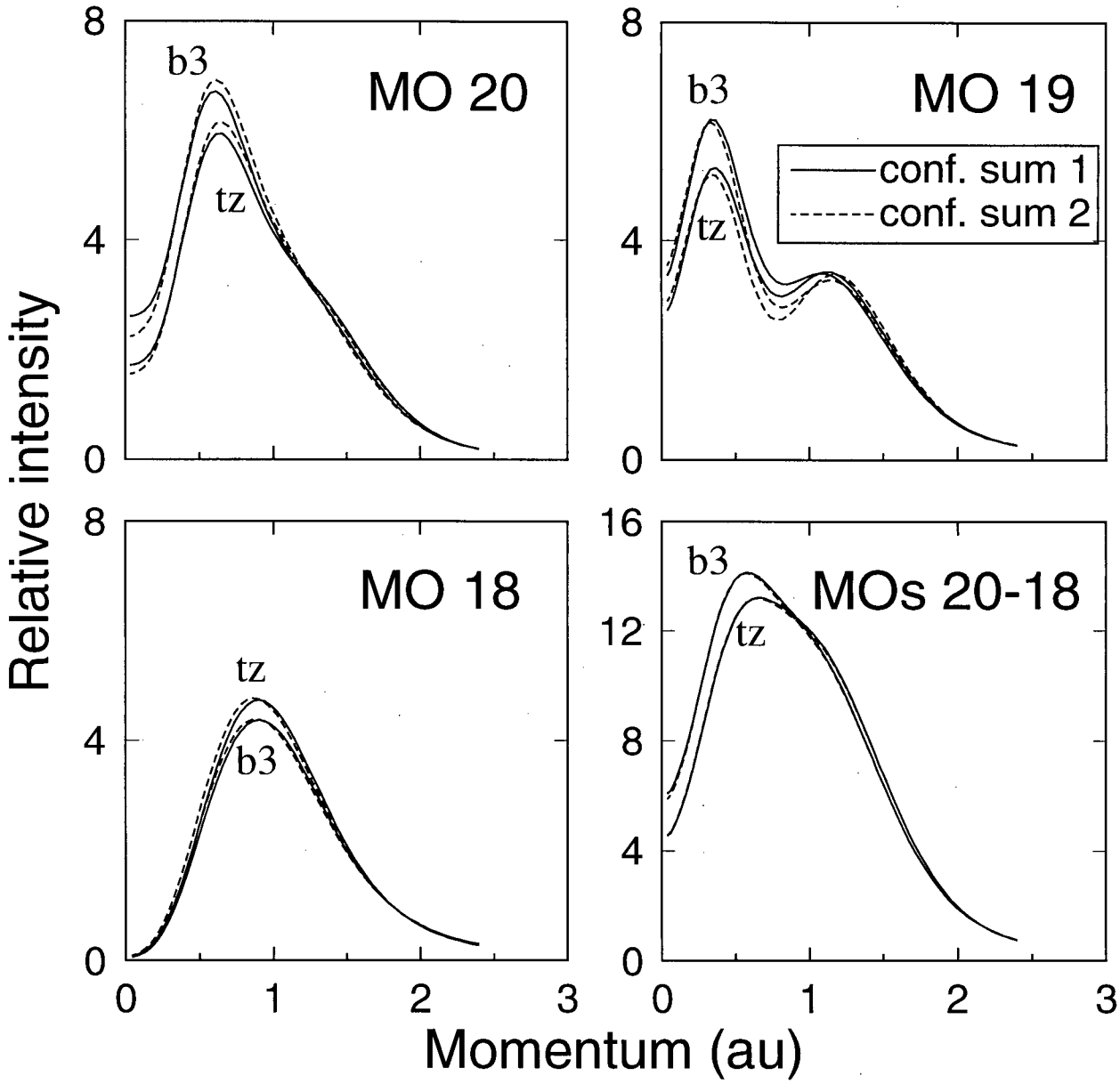

Figure 6.3: Effect of conformer abundances on the conformer sum theoretical momentum profiles of glycine. Boltzmann weighted conformer sum TMPs of MOs 20–18 obtained using the conformer abundances reported in Table 6.2 (conf. sum 1, solid lines) and the abundances obtained if the free energy of **IIIp** is set to 12.02 kJ/mol (conf. sum 2, dashed lines) are compared. Refer to the text for further details. The key to the TMP labels is given in Table 6.1.

and **IIIp**. In Figure 6.3, conformer sum TMPs of MOs 20–18 of glycine obtained using these abundances (conf. sum 2, the dashed lines) are compared with the corresponding TMPs obtained using the abundances reported in Table 6.2 (conf. sum 1, the solid lines). Despite the considerable differences in conformer abundances, the changes in the conformer sum TMPs of glycine are minor and do not alter the discussion in the remainder of this chapter, which is based upon the abundances reported in Table 6.2.

6.4 Valence binding energy spectra

Glycine is a 40 electron molecule, with 15 valence orbitals. The PES study of Cannington and Ham [162], as well as the HF calculations performed in the present study, indicate that ionizations from the 12 highest energy valence orbitals should be observable in the energy range studied in the current work. In the case of the C_s symmetry conformers, eight of these orbitals have a′ symmetry and four have a″ symmetry. The remaining three valence and five core orbitals outside of the energy range of this study are all of a′ symmetry. Ionizations from the a″ symmetry orbitals of C_s symmetry conformers will result in p-type momentum profiles. As a consequence of the nodal plane in these orbitals, the corresponding momentum profiles will have no intensity at zero momentum except for the small contribution from instrumental momentum resolution effects. Ionizations from a′ symmetry orbitals of the C_s symmetry conformers and from the orbitals of the C_1 symmetry conformers may give rise to either s-type or p-type momentum profiles, depending upon the nature of the orbital in question. For example, molecular orbitals that strongly resemble atomic p orbitals will have p-type momentum profiles, although because of the lack of a nodal plane in these molecular orbitals, greater intensity at zero momentum may be observed than in the case of the a″ momentum profiles. In the following discussion of the EMS experimental results for glycine,

the molecular orbitals are referred to by number rather than by symmetry label because of the expected presence in the experimental sample of multiple conformers of different symmetries.

The glycine binding energy spectra obtained at relative azimuthal angles of 0° and 8° are shown in Figure 6.4, with the fitted Gaussian peaks used to obtain the experimental momentum profiles (using the procedure described in Section 3.4.4) shown as dashed lines. The high resolution PES spectrum, digitized from figure 1 of Reference [162], from which the vertical ionization peak positions and Franck–Condon widths used for the fitting procedure were determined, is shown in the bottom panel of Figure 6.4. The reported ionization potentials and fitted Gaussian functions are indicated by vertical bars and dashed lines, respectively. The absolute energy scale of the BES was established using the He $(1s)^{-1}$ ionization peak at 24.58 eV. The peak positions used to fit the BES data and the experimental PES [162] and theoretical pGW2 [163] valence IPs of glycine are shown in Table 6.3.

As a result of the close energy spacing of the glycine valence orbitals, it is not possible for the most part to identify individual ionization peaks in the EMS BES. However, examination of the $\phi = 0°$ and 8° BES shown in Figure 6.4 reveals five distinct regions. The lowest energy region, between approximately 9 and 12 eV, contains peaks due to ionization from the three outermost orbitals of glycine (MOs 20, 19 and 18). The observed intensity in this energy region is greater at $\phi = 8°$, indicating that these orbitals are predominantly p-type. This is as expected since these orbitals, centred predominantly on the nitrogen and two oxygen atoms, are largely "lone-pair" in character. The second region, from approximately 12 to 16 eV, is of greater overall intensity than the first one, particularly in the case of the $\phi = 0°$ spectrum. This is because of the presence of ionizations from four orbitals (MOs 17–14, with IPs of 13.6, 14.4, 15.0 and 15.6 eV, from PES [162]) in this energy range and also because the overall symmetry of these bands is s-type, as a consequence of the predominantly σ-bonding

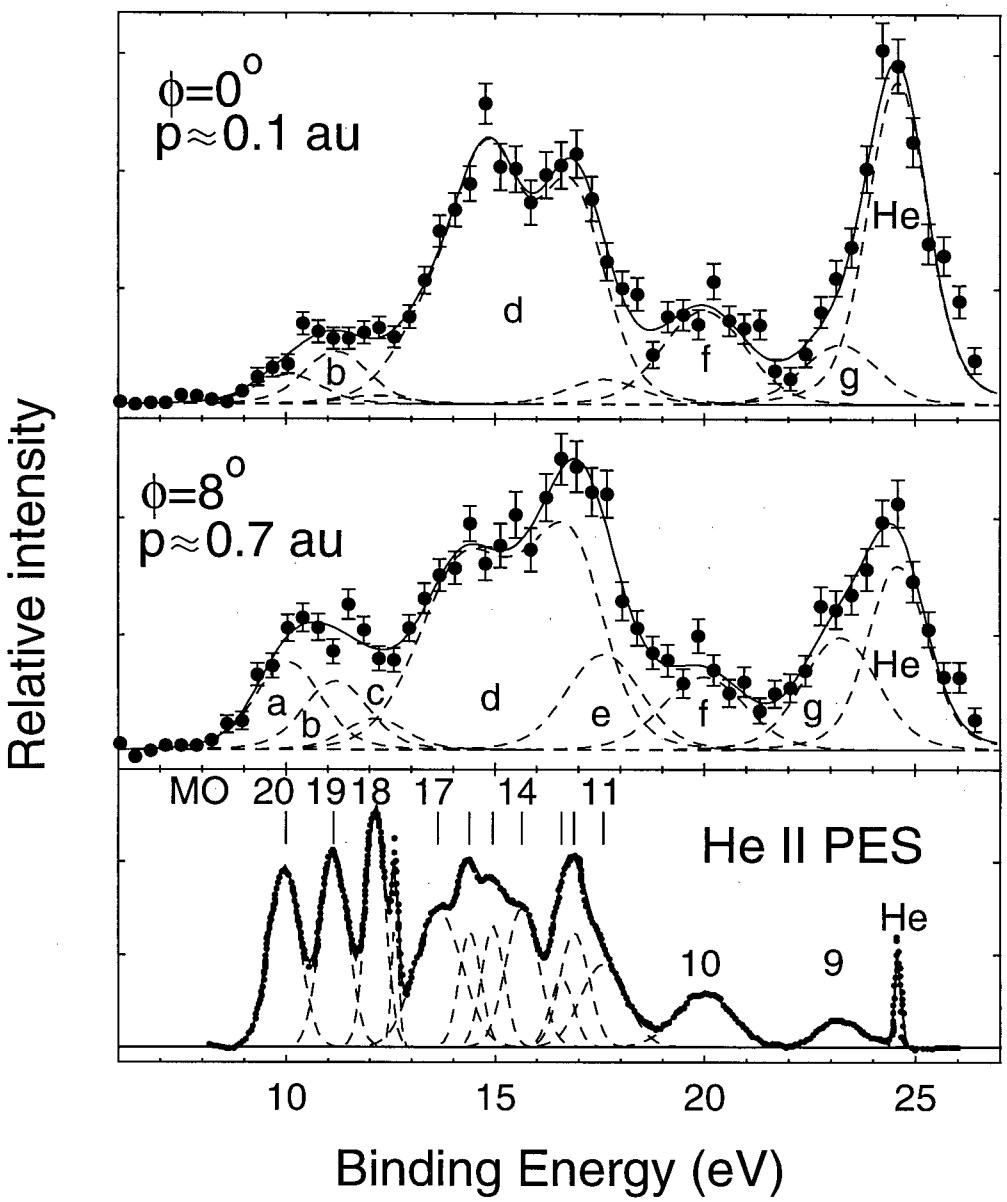

Figure 6.4: Binding energy spectra of glycine. The top two panels show the EMS BES from this work for the binding energy range of 6 to 27 eV at out-of-plane azimuthal angles of $\phi = 0°$ and 8°, obtained at a total energy of 1200 eV. The approximate corresponding electron momenta, calculated using Equation (2.5), are also indicated. The dashed lines represent the results of a least-squares fit of Gaussian functions to the ionization peaks and the solid curves are the summed fits. The areas indicated by a–g, plotted as a function of momentum or angle, give the experimental profiles shown in Figures 6.5, 6.6 and 6.8–6.14. The lower panel shows the He(II) PES spectrum reported by Cannington and Ham [162]. The vertical ionization energies are indicated by vertical lines. The fitted Gaussian functions used to estimate the Franck–Condon widths of the ionization processes are indicated by dashed lines. The sharp peak in the PES at 12.7 eV has been attributed by Debies and Rabalais [161] to HCl.

Table 6.3: Measured and calculated valence ionization potentials of glycine. All energies are in eV.

MO origin	EMS[a]	PES[b]	pGW2[c]	
			Ip	**IIp**
20	10.1	10.0	9.94	9.81
19	11.2	11.1	10.64	11.10
18	12.1	12.2	11.87	11.22
17	13.6	13.6	13.65	13.28
16	14.4	14.4	14.62	13.86
15	15.0	15.0	14.70	15.01
14	15.6	15.6	15.34	15.30
13	16.6	16.6	16.84	16.39
12	16.9	16.9	16.88	17.81
11	17.6	17.6	17.58	18.34
10	20.0	20.2		
9	23.2	23.2		

[a]Ionization peak energies used to fit the EMS binding energy spectra.
[b]From Reference [162].
[c]Parametrized second-order Green function times screened interaction method from Reference [163].

nature of these orbitals. The third region, of comparable intensity to the second, runs from 16 to $\approx$ 18.5 eV and is due to ionization from MOs 13, 12 and 11 (IPs 16.6, 16.9 and 17.6 eV) [162]. The overall symmetry in this region is p-type. The fourth "region," located at 20 eV, arises from ionization from MO 10 and is s-type, although the intensity at 8° is comparable to that at 0°. The final region in the BES shown in Figure 6.4 is dominated by the He $(1s)^{-1}$ calibration peak at 24.6 eV. However, a p-type lower energy shoulder is evident at $\approx$ 23 eV due to ionization from MO 9 of glycine.

6.5 Momentum profiles

The experimental momentum profiles (XMPs) of the valence orbitals of glycine are shown in Figures 6.5, 6.6 and 6.8 to 6.14 (see below). The Franck–Condon widths and close energy

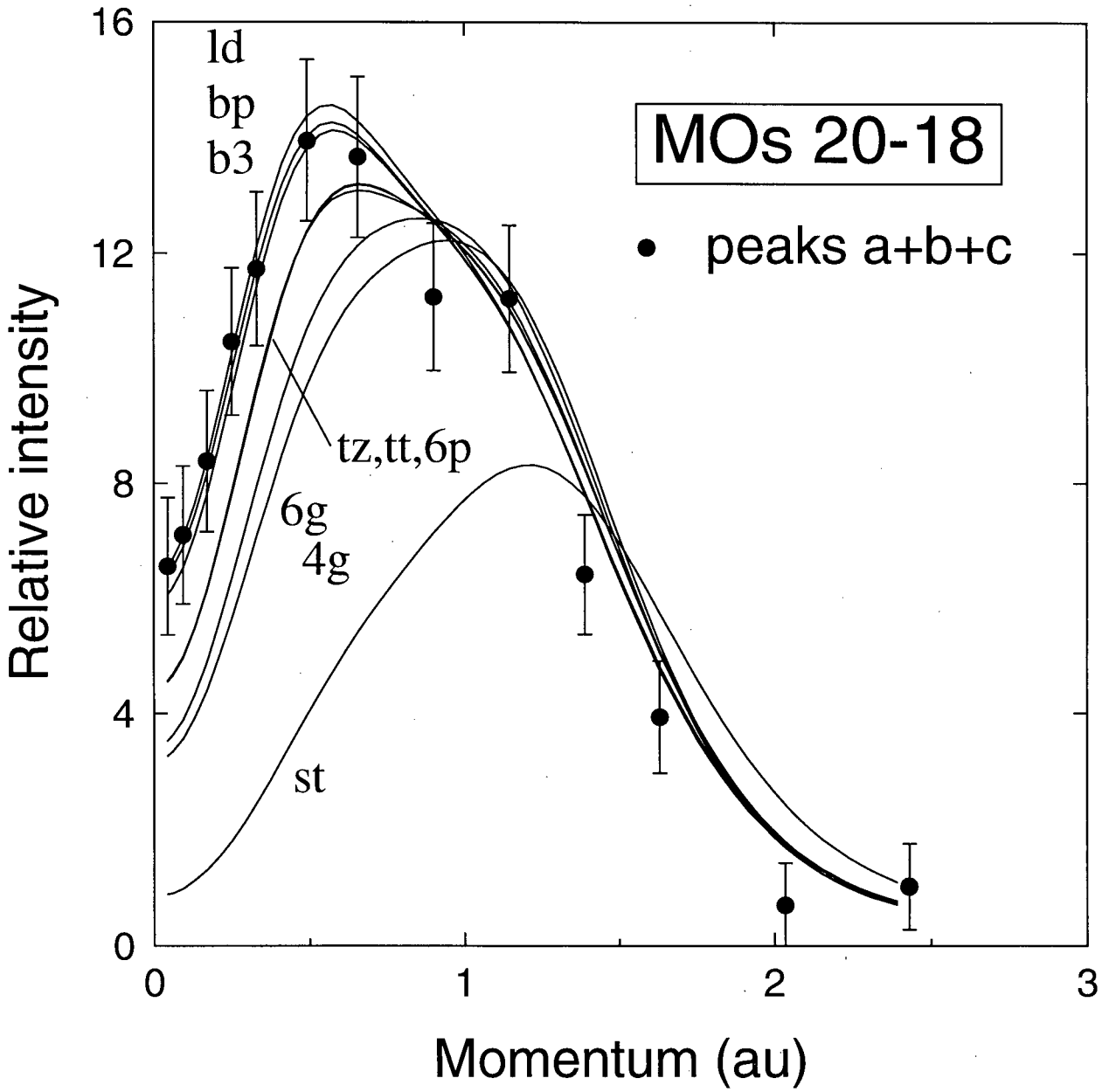

Figure 6.5: Experimental and theoretical summed outer-valence momentum profiles of glycine. The experimental profile (•) is the sum of the profiles of fitted peaks a, b and c (IPs 10.1, 11.2 and 12.1 eV, see Figure 6.4) and the corresponding theoretical profiles (—) are the sum of the TMPs of MOs 20–18. The key to the TMP labels is given in Table 6.1. The XMP has been normalized to the b3 TMP.

spacing of the ionization peaks necessitated the use of a fitting procedure to obtain the individual XMPs. As shown in Figure 6.4 for the $\phi = 0°$ and $\phi = 8°$ BES, the set of thirteen BES were fitted using Gaussian peaks for each ionization process located at the PES vertical ionization energies [162]. The widths of the fitted peaks were fixed at values obtained by convoluting the EMS instrumental energy resolution function (fwhm=1.5 eV) with the Franck–Condon widths of the ionization peaks estimated by fitting Gaussian functions to the high resolution PES spectrum reported by Cannington and Ham [162] and shown in the lower panel of Figure 6.4. The distribution of fitted peak areas for an individual ionization process as a function of momentum is the desired XMP. Also shown on Figures 6.5, 6.6 and 6.8 to 6.14 are the calculated TMPs produced from the calculations discussed in Section 6.3 and summarized in Table 6.1. The TMPs used for comparison with the experimental data are the sums of the TMPs of the five conformers (**Ip**, **IIp**, **IIIp**, **IVn** and **Vn**) predicted to be the most prevalent in the sample mixture (> 99.5%), Boltzmann weighted according to their relative Gibbs free energies and the experimental temperature of 165°C, as explained in Section 6.3. Also shown on Figures 6.6, 6.8, 6.9 and 6.12 are the individual TMPs for these five most stable conformers. Although the XMPs as measured are on a common relative intensity scale, the data are not absolute. Therefore, a single normalization between theory and experiment is necessary before the calculations and measurements can be compared. This has been done by comparing the XMP obtained by summing fitted peaks a, b and c (IPs 10.1, 11.2, 12.1 eV) with the corresponding summed TMPs of MOs 20–18, as shown in Figure 6.5. A least-squares fit of the XMP to the B3LYP DFT TMP (b3) was then performed because this theoretical distribution provides the best overall agreement for shape with the experimental data. All experimental profiles for glycine were then scaled using the factor resulting from this fit, with all HF and DFT theoretical profiles kept on a common intensity scale.

The momentum profile for the sum of the three outermost valence orbitals of glycine (Figure 6.5) exhibits p-type symmetry, as expected from the examination of the BES in Section 6.4. The atomic p orbital-like nature of MOs 20, 19 and 18 results in the minimum at zero momentum. Although all of the theoretical profiles correctly predict the general shape of the experimental profile, only the DFT results (ld, bp and b3) are in good quantitative agreement with the experimental data. The HF calculations predict the profile maximum to occur at a higher momentum than is observed experimentally for these orbitals and also underestimate the intensity in the low momentum region. Not surprisingly, the discrepancy between the HF TMPs and the XMP is greatest for the 30-CGF minimal basis set calculation (st) and decreases as the basis set size increases. However, there are no significant differences between the 145-CGF 6-311++G** (6p) TMP and the 345-CGF aug-cc-pVTZ (tz) TMP, suggesting that no further improvement in the agreement between the HF TMPs and experiment would be obtained by using a yet larger basis set. Although the calculated momentum profile, which emphasizes the small p (predominantly large r) region of electron density, appears converged at the HF level using the 6-311++G** basis set, further improvements in the total energy and dipole moments (see Table 6.1), which emphasize small and medium r, respectively, are obtained using the larger trun-pVTZ (tt) and aug-cc-pVTZ (tz) basis sets. This demonstrates the importance of considering a number of properties emphasizing different regions of electron density when evaluating the accuracy of a wavefunction.

The highest occupied molecular orbital of glycine, MO 20, has a binding energy of 10.1 eV as determined by EMS and a p-type momentum profile (Figure 6.6). The theoretical calculations indicate that this orbital is predominantly centred on the nitrogen atom and, in the case of the C_s symmetry conformers, is symmetric with respect to reflection through the plane of the heavy-atom framework (i.e., of a′ symmetry). This agrees with the PES assignment of Cannington and Ham [162] and the pGW2 calculations of Hu et al. [163],

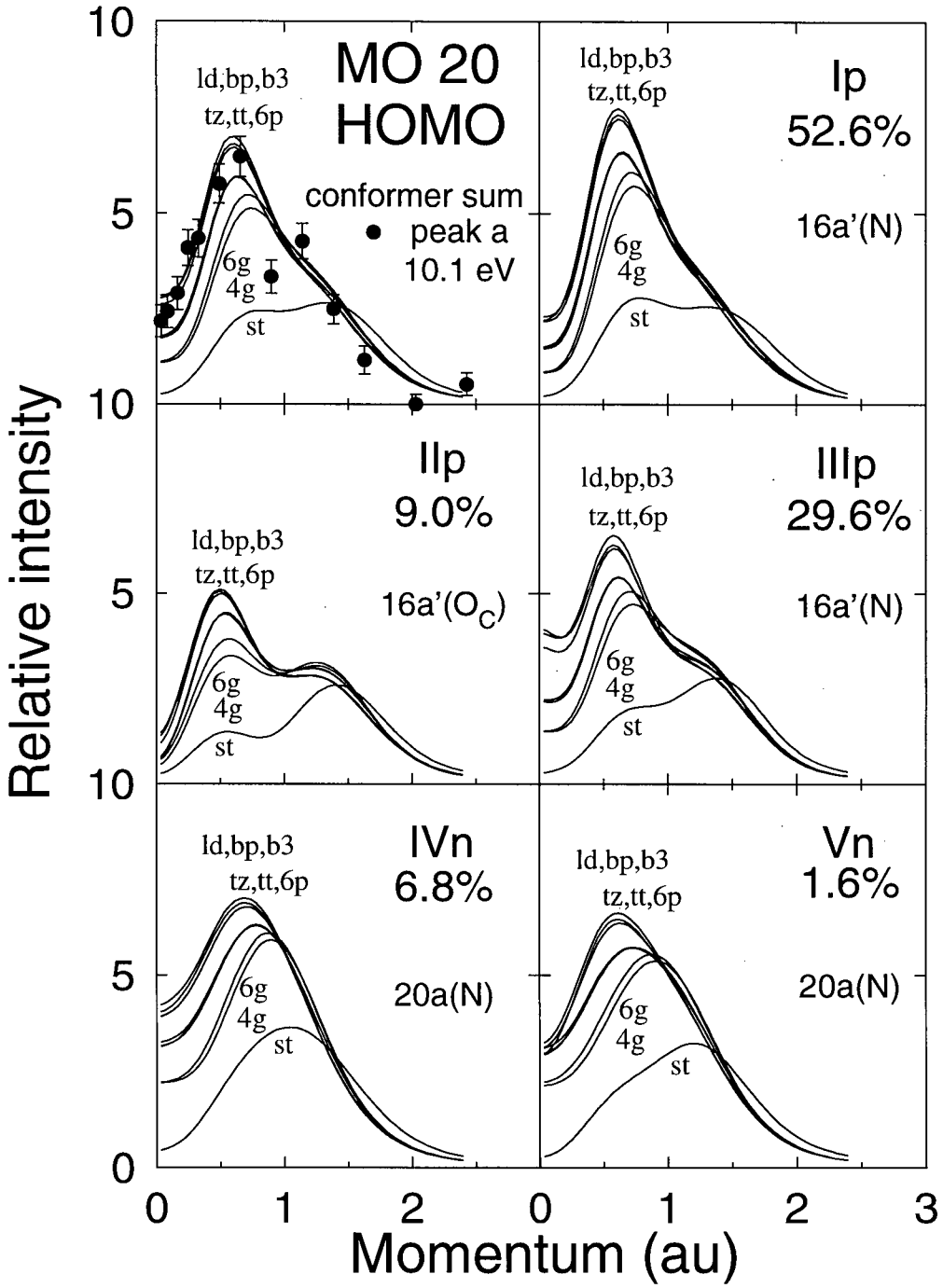

Figure 6.6: Experimental and theoretical momentum profiles for the HOMO (MO 20, IP 10.1 eV) of glycine. The XMP (•) and the TMPs (—) for the conformer sum are shown in the top-left panel. The remaining panels contain profiles for each of the five most abundant conformers, as indicated. The corresponding MO symmetry labels are indicated in each panel, along with the atom on which the greatest proportion of the electron density for that MO is centred. The key to the TMP labels is given in Table 6.1.

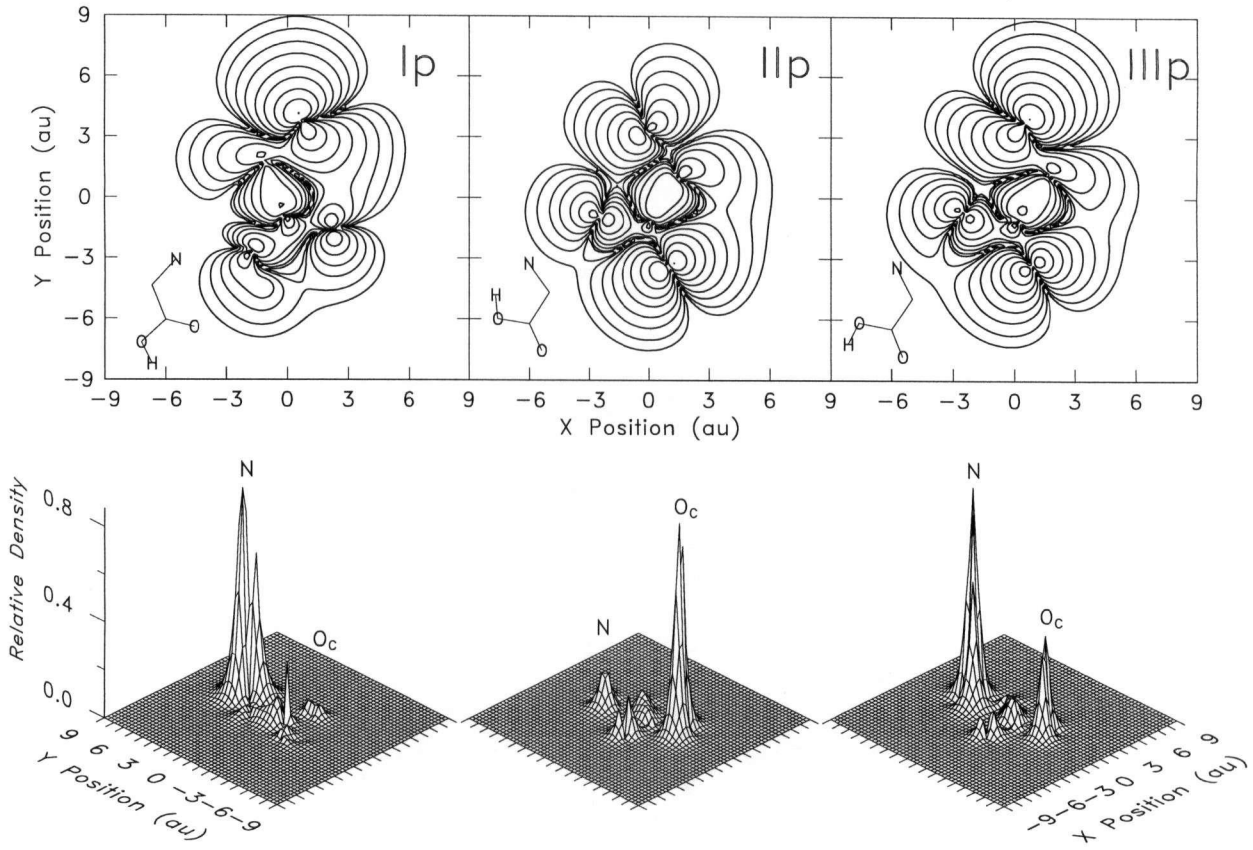

Figure 6.7: Position space electron density maps for the HOMOs of the three lowest energy conformers of glycine. The maps were calculated using the results of the B3LYP DFT calculation. The electron density in the symmetry plane of the molecule (i.e., the plane containing the heavy-atom nuclei) is shown. The contour lines in the upper panels represent 0.01, 0.03, 0.1, 0.3, 1.0, 3.0, 10.0, 30.0 and 99.0% of the maximum density.

but not the earlier assignment by Debies and Rabalais [161]. The exception is the **IIp** conformer, for which the HOMO electron density is predominantly located on the carbonyl oxygen (indicated by O_C on Figure 6.6). This is illustrated by the position-space electron density maps for this orbital for conformers **Ip**, **IIp** and **IIIp**, shown in Figure 6.7. This difference in the nature of the HOMO is most likely a result of conformer **IIp** being the only one of the five most stable glycine conformers containing an intramolecular hydrogen bond to the nitrogen atom (see Figure 6.1). This will stabilize the nitrogen "lone pair" electron density and consequently increase the binding energy of the electrons in this orbital.

Concurrently, the carbonyl oxygen non-bonding orbital of conformer **IIp** is destabilized by the unfavorable anti orientation of the acid group. The minimum in the experimental profile at zero momentum results from the nodal surface between the two lobes of electron density in this largely atomic p-like orbital. The intensity that is observed at zero momentum results from the small contributions to this orbital from electron density at other parts of the molecule, such as the σ-bonding character between the two carbon atoms evident from the electron density maps in Figure 6.7. The multiple nodal surfaces in this orbital result in two-lobed MO 20 momentum profiles for many of the conformers, as shown in Figure 6.6. The three DFT TMPs (ld, bp and b3) provide the best agreement with the experimental data. The higher level HF TMPs (tz,tt and 6p) are essentially indistinguishable from one another and in fair agreement with the XMP, correctly predicting the position of the profile maximum (p_{MAX}), but underestimating the intensity at low momentum. The smaller basis set HF calculations, in contrast, differ markedly from the experimental data. The 6g and 4g calculations correctly predict the qualitative shape of the momentum profile but place p_{MAX} at too great a momentum. The minimal basis set st profile fails to predict correctly even the qualitative features of the momentum profile. Because of this poor agreement, the 4g and st TMPs have not been included for comparison with the other XMPs of glycine in the present work. Note that the use in the present work of free energies for the Boltzmann weighting of the TMPs together with the determination of the XMP by fitting the BES has resulted in further improved agreement between the HOMO XMP and the DFT TMPs compared with the earlier preliminary analysis [152]. In this earlier analysis, the XMP was obtained by summing the experimental data over a range of binding energies and electronic energies (rather than free energies) were used for the Boltzmann weighting of the TMPs.

Molecular orbitals 19 and 18 (Figures 6.8 and 6.9) have binding energies of 11.2 and 12.1 eV, respectively. While both may generally be described as p-type profiles, the MO

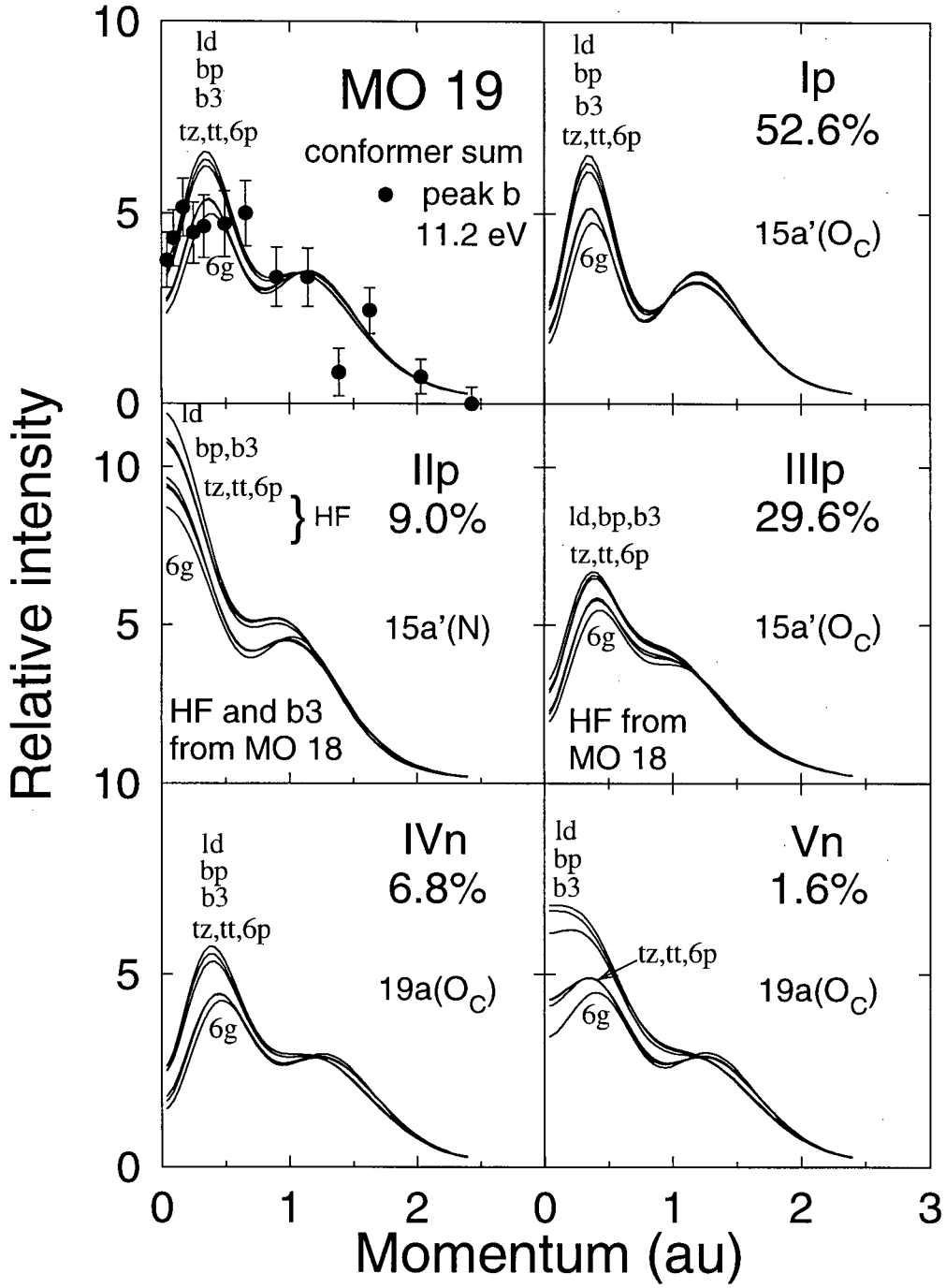

Figure 6.8: Experimental and theoretical momentum profiles for MO 19 (IP 11.2 eV) of glycine. The XMP (•) and the TMPs (—) for the conformer sum are shown in the top-left panel. The remaining panels contain profiles for each of the five most abundant conformers, as indicated. The corresponding MO symmetry labels are indicated in each panel, along with the atom on which the greatest proportion of the electron density for that MO is centred. The key to the TMP labels is given in Table 6.1.

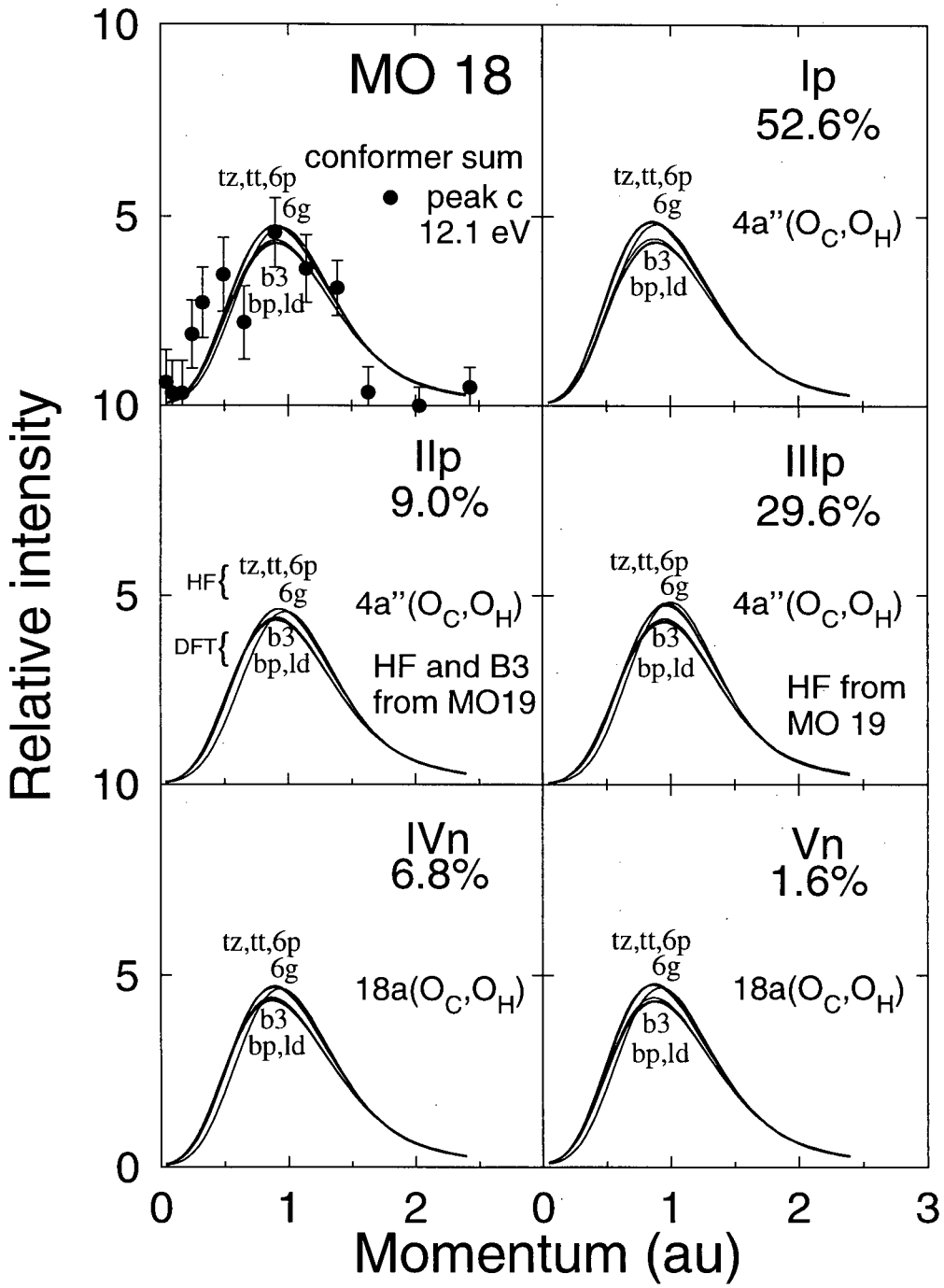

Figure 6.9: Experimental and theoretical momentum profiles for MO 18 (IP 12.1 eV) of glycine. The XMP (•) and the TMPs (—) for the conformer sum are shown in the top-left panel. The remaining panels contain profiles for each of the five most abundant conformers, as indicated. The corresponding MO symmetry labels are indicated in each panel, along with the atoms on which the greatest proportion of the electron density for that MO is centred. The key to the TMP labels is given in Table 6.1.

19 profile has considerably more intensity at zero momentum than does the profile for MO 18. There is some disagreement amongst the theoretical calculations as to the symmetries of these orbitals. In the case of conformers **Ip**, **IVn** and **Vn**, all calculations performed predict MOs 19 and 18 to be predominantly oxygen "lone-pair" orbitals centred on the carbonyl oxygen (O_C), and on both the carbonyl and hydroxyl oxygens (O_C,O_H), respectively. In the case of conformer **IIIp**, the DFT calculations predict MO 19 to be predominantly centred on the carbonyl oxygen and of a′ symmetry and MO 18 to be centred on both oxygen atoms and of a″ symmetry, with the situation reversed for the HF calculations. For conformer **IIp**, the ld and bp DFT results predict the electron density of MO 19 to be predominantly located on the nitrogen atom and of a′ symmetry and that of MO 18 to be concentrated on the two oxygen atoms and of a″ symmetry. The reverse is true for the HF and b3 DFT calculations. A comparison of the two XMPs and the various TMPs helps to clarify the situation. The XMP obtained at 11.2 eV (MO 19) has significant intensity at zero momentum while the 12.1 eV XMP (MO 18) essentially drops to zero near zero momentum. This drop to zero is consistent with the a″ symmetry momentum profiles, which have no intensity at zero momentum because of the nodal plane in these orbitals. In contrast, the a′ symmetry profiles for conformers **IIp** and **IIIp** have some intensity at zero momentum. Therefore, for conformers **IIp** and **IIIp**, MO 19 is assigned as an a′ symmetry orbital and MO 18 as an a″ symmetry orbital. This symmetry assignment is consistent with that of Cannington and Ham from a consideration of the PES of glycine and related molecules [162]. In Figures 6.8 and 6.9, the inverse ordering of orbitals 19 and 18 for conformers **IIp** and **IIIp** has been corrected as indicated to allow a more meaningful comparison of the theoretical and experimental momentum profiles. Reasonable overall shape agreement between the XMP and TMPs for each of MOs 19 and 18 is obtained. However, a comparison of the XMPs for these orbitals reveals a correspondence between some experimental data points which

are lower than the theoretical profiles in the one case and higher in the other (consider in particular the points between 0.3 and 0.7 au). This is most likely a result of limitations in the energy resolution (1.5 eV fwhm) and the resulting uncertainties in the deconvolution procedure used to obtain experimental momentum profiles for these energetically closely spaced orbitals. In addition to the challenge of separating two momentum profiles differing in binding energy by only 0.9 eV, the situation for glycine is complicated by the fact that the energies for particular molecular orbitals vary to at least some degree with changes in molecular conformation. The HF/aug-cc-pVTZ calculations conducted in the present study indicate variations in orbital energy between conformers **Ip** through **Vn** of approximately 0.5 eV for each of MOs 19 and 18 and, in the case of some conformers, an energy spacing between MOs 19 and 18 of considerably less than 0.9 eV. However, a sufficient gap is predicted between the highest energy MO 20 and the lowest energy MO 19 and likewise between MOs 18 and 17 to provide reasonable confidence that a sum of fitted peaks b and c will account for all intensity resulting from ionization from MOs 19 and 18 without introducing intensity resulting from ionization from MO 20 or 17. In Figure 6.10, the XMP obtained by summing these two experimental profiles is compared with the corresponding TMPs for the sum of MOs 19 and 18. The resulting XMP is in good quantitative shape agreement with the three DFT TMPs. In contrast, the HF TMPs give a poor representation of the experimental data in the low momentum region below $p = 0.7$ au.

In the case of molecular orbitals 17 through 12 (binding energy range $\approx$ 13–17 eV), the energy separation between orbitals is quite small and prevents the determination of meaningful momentum profiles for individual orbitals. For this reason, a sum of fitted peaks has been considered in this region and is compared in Figure 6.11 with the summed theoretical profiles of MOs 17–11. MO 11 has also been included in the sum to avoid complications resulting from differing predictions of orbital ordering by the HF and DFT

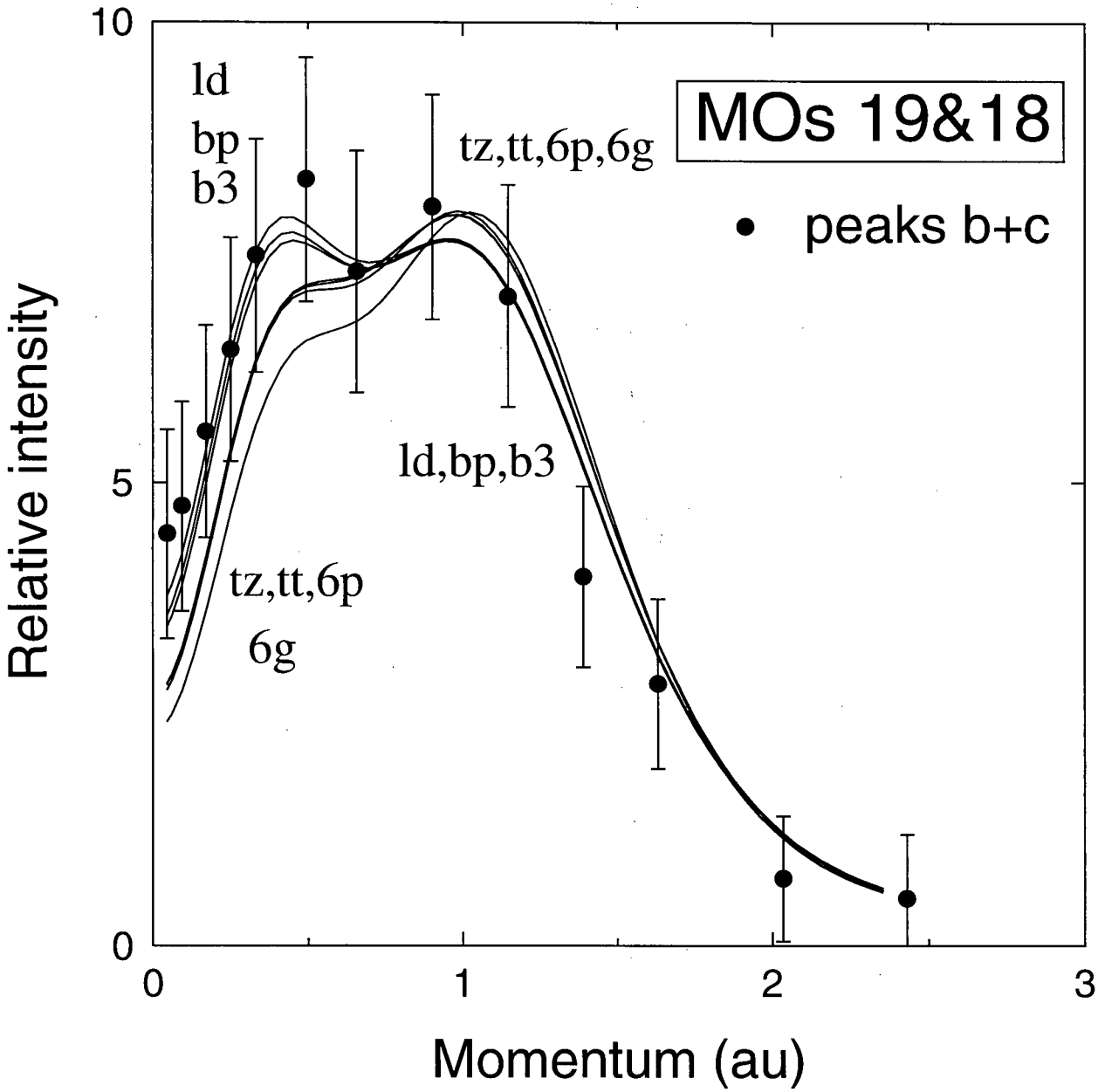

Figure 6.10: Experimental (•) and theoretical (—) momentum profiles for the sum of MOs 19 and 18 of glycine. The key to the TMP labels is given in Table 6.1.

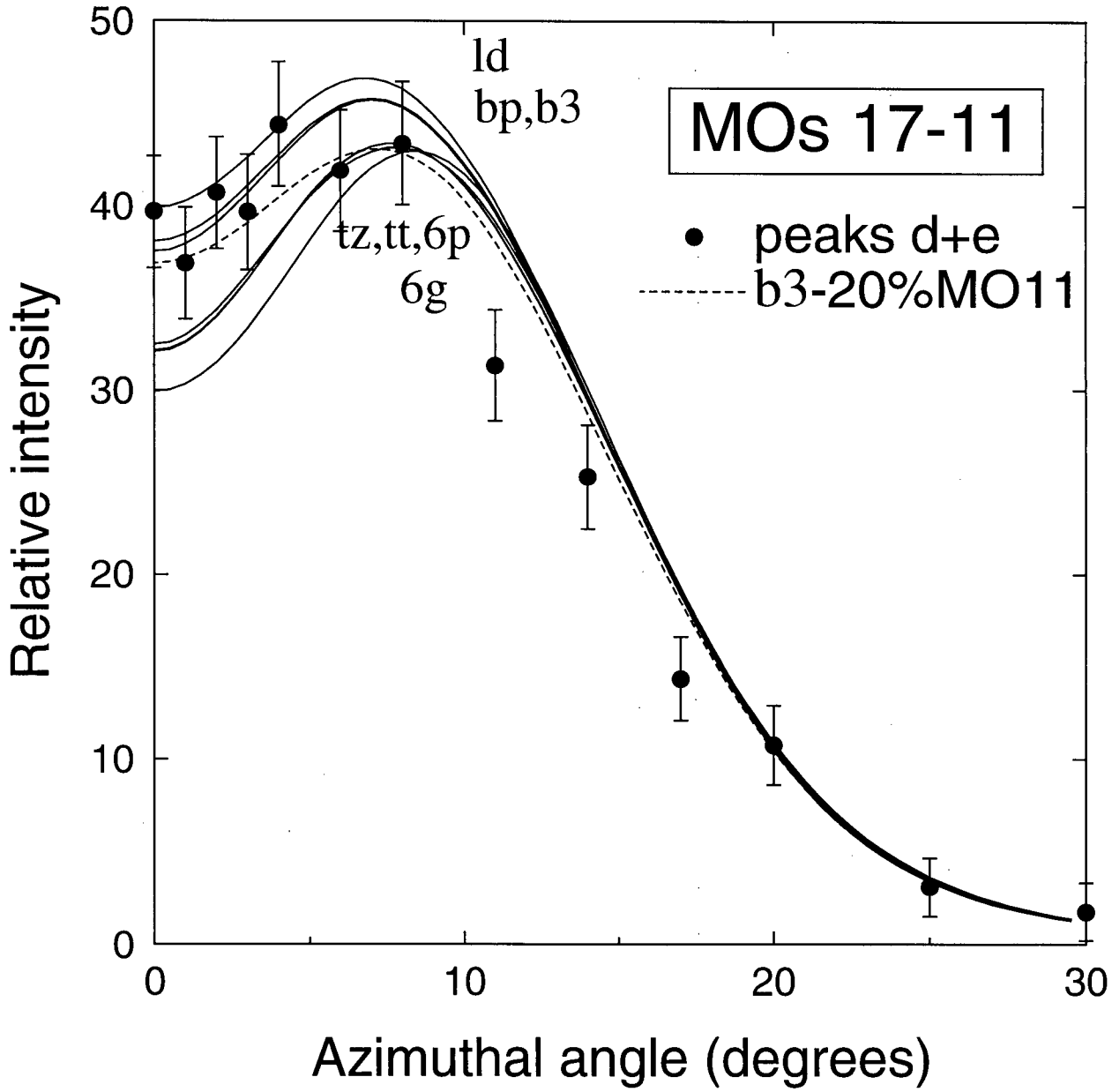

Figure 6.11: Experimental (•) and theoretical (—) angle profiles for the sum of MOs 17–11 of glycine. The key to the TMP labels is given in Table 6.1. The dashed line represents the b3 DFT TMP sum for MOs 17–11 minus 20% of the b3 profile of MO11 (see text for details).

calculations. This issue is addressed further below for MO 11. The data are plotted using an out-of-plane azimuthal angle (ϕ) rather than momentum scale because of the variation of momentum with electron binding energy for a given azimuthal angle (Equation (2.5)). These orbitals are responsible for the bulk of the molecular bonding in glycine and the σ-bonding nature of several of them results in the considerable intensity observed in the profiles at low values of ϕ. Only qualitative agreement is obtained between the shapes of the experimental profile and all of the theoretical profiles. The DFT profiles are consistent with the experimental data at small and large values of ϕ, but are higher than the experimental results for intermediate angles. The HF calculations, in contrast, fall below the experimental data at low ϕ and agree at intermediate and high values. In view of the good agreement between the DFT TMPs and the experimental data for MOs 20–18, a likely explanation for the behaviour observed for MOs 17–11 is that one or more of the p-type ionization processes occurring in this region have spectroscopic factors of less than one (see Equation (2.11)). If 20% of the pole strength for MO 11 is removed from the b3 DFT TMP sum for MOs 17–11, the resulting dotted line (Figure 6.11) shows somewhat improved agreement with experiment (see the following paragraph and Figure 6.12 below, where the remaining 80% of the MO 11 b3 DFT TMP fits the XMP for MO 11 quite well). As discussed in Sections 1.1.2 and 2.2.3, inner-valence ionization processes frequently show a range of energy poles as a consequence of final ion state electron correlation effects [154].

Experimental and theoretical momentum profiles for the ionization process at 17.6 eV, arising from ionization from MO 11, are shown in Figure 6.12. There is disagreement between the HF and DFT calculations as to the symmetry of this orbital. However, a comparison of the shape of the XMP with those of the various TMPs clearly indicates that, in the case of the C_s symmetry conformers, this is an a″ orbital, in agreement with the DFT predictions and the pGW2 calculations of Hu et al. [163]. An examination of the MO calculations indicates

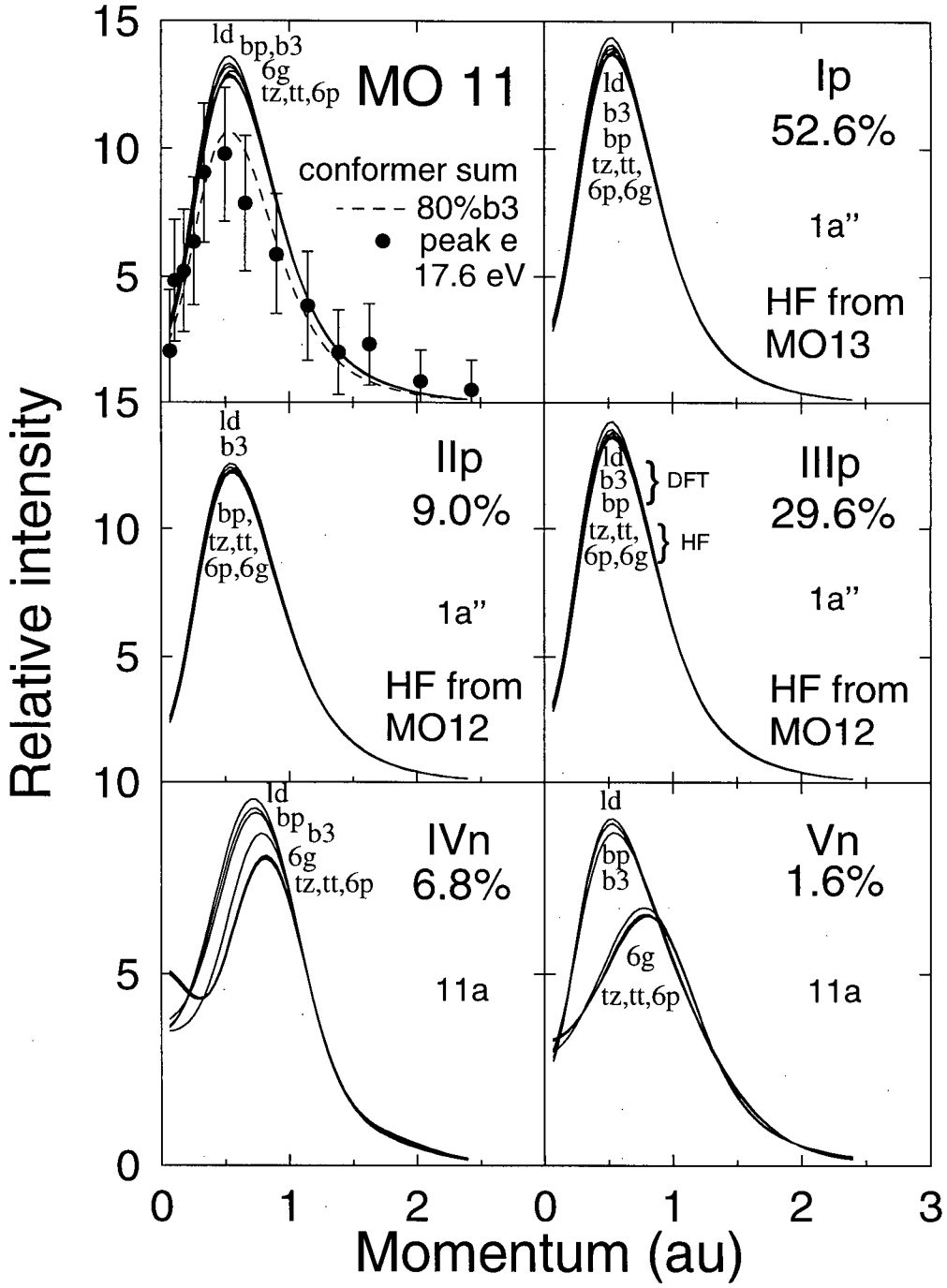

Figure 6.12: Experimental and theoretical momentum profiles for MO 11 (IP 17.6 eV) of glycine. The XMP (•) and the TMPs (—) for the conformer sum are shown in the top-left panel. The remaining panels contain profiles for each of the five most abundant conformers indicated. The corresponding MO symmetry labels are indicated in each panel. The key to the TMP labels is given in Table 6.1. The dashed line represents the b3 DFT TMP scaled by 80% (see text for details).

that this orbital may be primarily thought of as a pseudo-π orbital responsible for NH_2 σ-bonding, but with significant contributions to CH_2 bonding as well. For comparison between theory and experiment, the TMPs for the HF orbitals having the appropriate a″ symmetry have been shown in Figure 6.12 (i.e., MO 13 for **Ip** and MO 12 for **IIp** and **IIIp**). Although there are also clear differences between the HF and DFT TMPs for the C_1 conformers **IVn** and **Vn**, the lack of symmetry in these conformers makes it difficult to determine the correct MOs to use for comparison with the XMP. Consequently, the predicted MO 11 TMPs have been used. Because of the small relative populations of conformers **IVn** and **Vn**, this will not significantly affect the Boltzmann-weighted conformer sum TMPs that are compared with experiment in the upper-left panel of Figure 6.12. It is evident from Figure 6.12 that there are only slight differences between calculations for this orbital and that all TMPs shown are consistent with the shape of the XMP. There is, however, a considerable discrepancy in terms of intensity between theory and experiment. The b3 TMP must be scaled by 80% to bring it into agreement with the XMP. This represents a break-down of the single particle model of ionization due to final state correlation and relaxation effects. The remaining intensity would be expected to be observed as satellite peaks at other binding energies, possibly outside of the energy range examined in the current study. This "missing intensity" at least partly explains the disagreement between theory and experiment seen for the sum of MOs 17–11 in Figure 6.11 at intermediate out-of-plane azimuthal angles (see the discussion in the preceding paragraph). The shape of the MO 11 momentum profile would result in a significant drop in experimental intensity for the MO 17–11 sum at intermediate angles, but very little change at lower or higher angles if the spectroscopic factor for this ionization process at 17.6 eV is lower than unity.

In the case of MO 10 (Figure 6.13, electron binding energy 20.0 eV), all theoretical momentum profiles are in reasonably close agreement, differing, however, in the relative

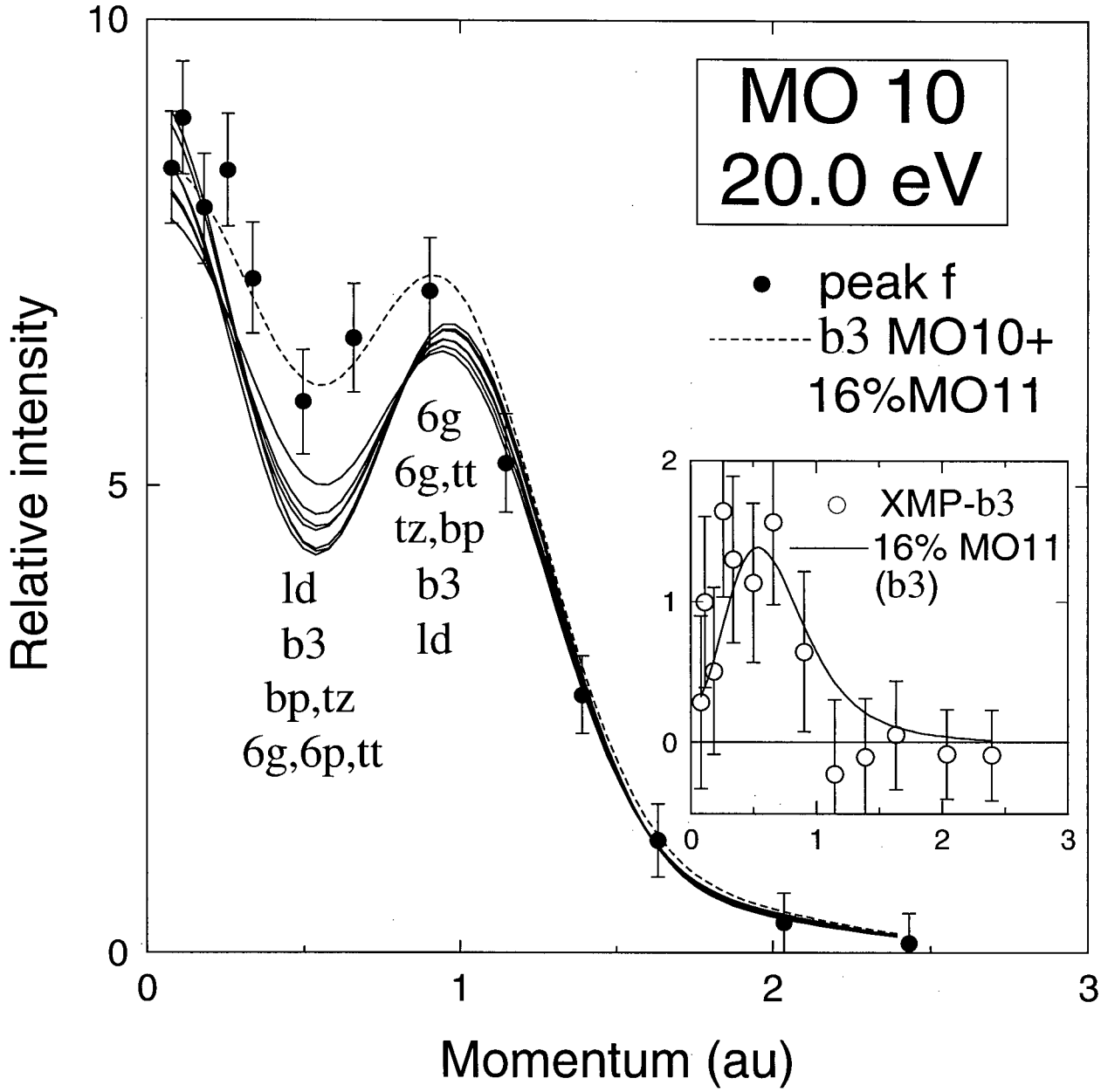

Figure 6.13: Experimental (•) and theoretical (—) momentum profiles for MO 10 (IP 20.0 eV) of glycine. The key to the TMP labels is given in Table 6.1. The dashed line represents the b3 DFT TMP sum (MO 10 + 16% MO 11). The inset shows the (XMP - b3 TMP) difference (○) compared with 16% of the b3 TMP for MO 11.

magnitudes of the maximum at zero au and the minimum near 0.5 au. All HF and DFT calculations indicate that MO 10 consists primarily of carbon 2s electron density. However, there is also a significant σ-bonding component, particularly between the hydroxyl oxygen and hydrogen. The XMP is consistent with the general features of the theoretical profiles, although there is a significant difference in intensity for the region between approximately 0.2 and 1.0 au. One possible explanation for this additional experimentally observed intensity is the presence in this binding energy region of satellite peaks from the MO 11 ionization process (see discussion in previous paragraph and Figure 6.12). An examination of the momentum profile obtained by subtracting the b3 TMP of MO 10 from the 20.0 eV XMP (see inset of Figure 6.13) supports this explanation. The resulting profile is consistent with the b3 MO 11 TMP scaled by 16%. Including this additional intensity in the b3 TMP (dashed line, Figure 6.13) eliminates the discrepancy between theory and experiment.

Molecular orbital calculations indicate that MO 9, like MO 10, is comprised, to a considerable degree, of carbon 2s electron density. However, the two orbitals differ in that MO 9 also contains significant nitrogen 2s density and no appreciable bonding character. Upon examining the XMP for this inner-valence orbital (Figure 6.14), it is apparent that the spectroscopic factor for this ionization process is significantly less than one. In addition to this intensity difference between theory and experiment, the XMP (solid circles) is higher than all of the TMPs near zero momentum and appears to peak at a slightly lower momentum than do the TMPs. These last two observations could be a result of contamination of this XMP with signal from the adjacent and considerably more intense s-type He $(1s)^{-1}$ ionization calibration peak (see Figure 6.4). This seems likely since, as shown in Figure 6.14, the XMP ($\bullet$) minus the scaled He 1s TMP [168] gives a momentum profile ($\circ$) which agrees well for shape with the b3 DFT TMP.

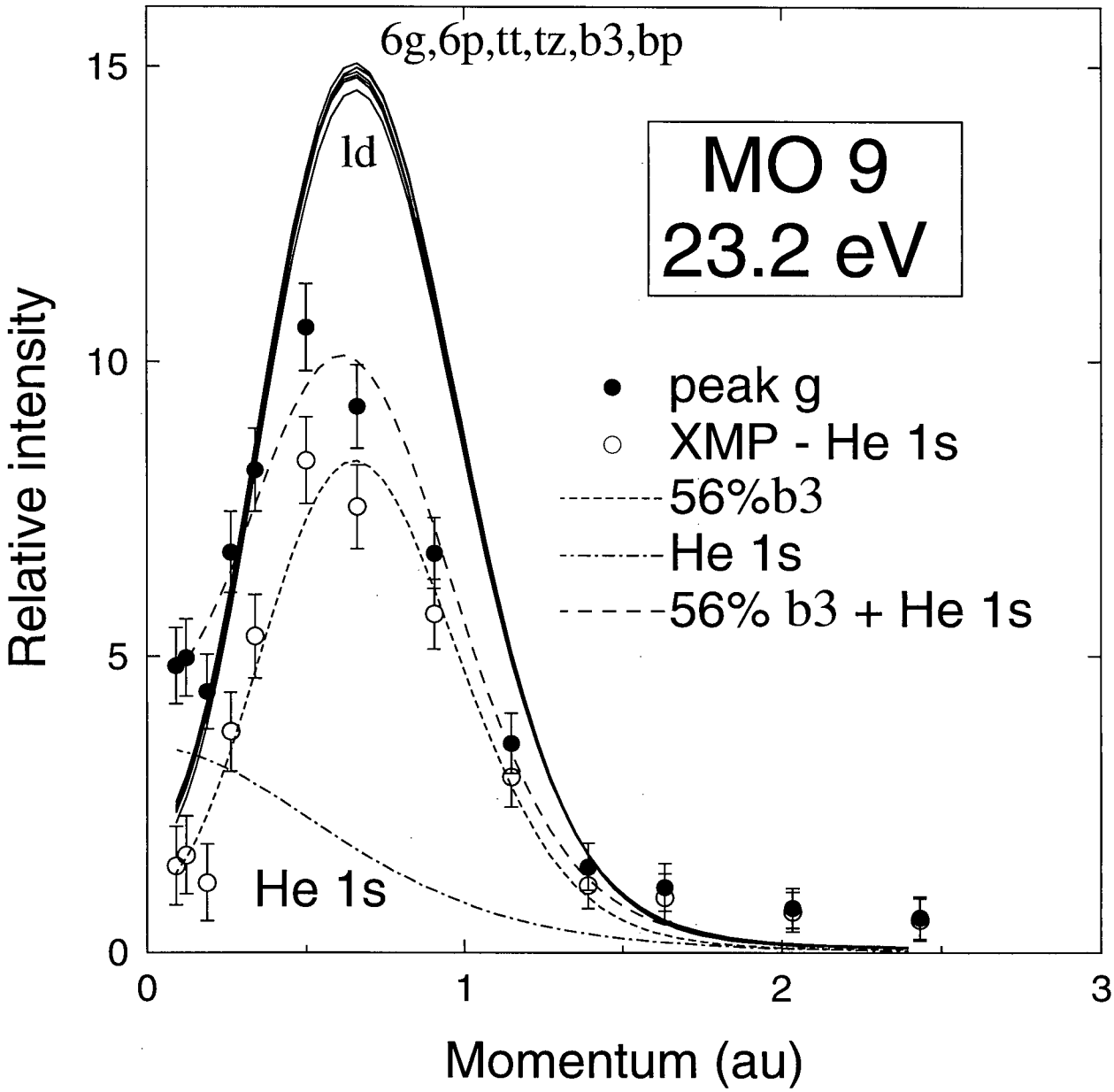

Figure 6.14: Experimental (•) and theoretical (—) momentum profiles for MO 9 (IP 23.2 eV) of glycine. The key to the TMP labels is given in Table 6.1. The dot-dashed line corresponds to the shape of the He 1s TMP obtained using the highly correlated He wavefunction reported by Davidson [168]. The short dashed line represents 56% of the b3 DFT TMP of MO 9. The long dashed line is the sum of the dot-dashed and short dashed lines. The open circles are the result of subtracting the He 1s TMP (dot-dashed line) from the measured XMP.

6.5.1 General observations

In comparing the various glycine theoretical momentum profiles with the experimental data, it can be seen that the profiles for the chemically important outer-valence orbitals (MOs 20–18) are most sensitive to changes in the basis set or theoretical method used and those for MOs 11–9 are relatively insensitive to changes in the computational method. There is a steady improvement in the agreement between the HF TMPs and the XMPs with increasing basis set size. The minimal basis set STO-3G HF calculations (st on Figures 6.5 and 6.6) produce TMPs that differ dramatically from the experimental profiles. This basis set clearly does not have the necessary flexibility to accurately describe the outer-valence molecular orbitals of glycine. Some improvement occurs in going to the 4-31G (4g) and 6-311G (6g) split-valence basis sets. However, the outer-valence TMPs calculated using these basis sets still tend to agree poorly with the XMPs, particularly at low momentum. The addition of diffuse and polarization functions to the 6-311G basis set (the 6-311++G** (6p) calculations) results in improved agreement between theory and experiment for many of the profiles. This is typified by an increase in the predicted intensity at low momentum and a shift of the maxima of the momentum profiles (p_{MAX}) towards zero momentum in the case of p-type profiles. This is a consequence of the improved description of the spatially diffuse regions of the electron density when using the 6-311++G** basis set. Because of the Fourier transform relationship between position and momentum space, these outer regions of electron density roughly correspond to the low momentum regions in momentum space. Further increases in basis set size from the 145-CGF 6-311++G** basis set to the 240-CGF trun-pVTZ (tt) and 345-CGF aug-cc-pVTZ (tz) basis sets result in no further appreciable change in the momentum profiles. It would therefore appear unnecessary to employ such large basis sets for Hartree–Fock calculations of momentum profiles and perhaps other properties of glycine that are predominantly dependent on the large-r regions of the electron density. It is important

to note, however, that further improvements in both total energy and dipole moment are obtained by using the two larger basis sets (see Table 6.1).

The apparent near convergence of the HF results for momentum profile, total energy and dipole moment suggests that the HF limit has been closely approached. However, a discrepancy still remains between these theoretical profiles and the experimental data, particularly in the region of low momentum where the HF results tend to underestimate the intensity. This discrepancy is essentially removed when the KS-DFT profiles are considered. The DFT calculations predict a further shift towards low momentum in the maxima of the p-type momentum profiles from those predicted by the HF calculations. The orbital ordering predicted by the DFT calculations also appears to be more consistent with the experimental data than that predicted by the HF calculations. The improved agreement between theory and experiment, particularly at lower momentum (< 1 au), can be attributed to the inclusion of electron correlation effects via the exchange–correlation functional in DFT. Although there are small differences in the momentum profiles obtained from the DFT calculations using different functionals, it is not evident that one calculation provides markedly better agreement with experiment. However, it is important to note that a recent theoretical study [84] of the geometries and relative energies of the conformers of glycine determined using DFT found that, amongst the functionals considered, only the hybrid B3LYP functional reproduced the energetic ordering of the glycine conformers predicted in studies using post-HF methods.

Chapter 7

Conclusions

In this work, EMS measurements of the valence binding energy spectra and momentum profiles of acetone, dimethoxymethane and glycine have been presented. This is the first EMS study of dimethoxymethane and glycine and the first complete valence study of acetone. These EMS measurements, of what are fairly large molecules in comparison with most previous EMS studies, were possible because of the construction of the energy-dispersive multichannel spectrometer described in Chapter 3. The increased sensitivity of this multichannel spectrometer was necessary for the collection of the considerable data required for complete valence shell studies with reasonable statistical precision and in a practical period of time. The three molecules studied have also allowed the assessment of the target Kohn–Sham approximation (TKSA) for larger molecules than have been considered previously [20, 21].

The study of acetone (Chapter 4) confirms the disagreement between experiment and theory for the $5b_2$ momentum profile suggested by the previous single-channel EMS study [54]. None of the theoretical methods considered in the present work (i.e., HF, MRSD-CI and DFT) adequately describes the $5b_2$ XMP of acetone. The similarity of the CI and DFT TMPs to the HF TMPs suggests that this discrepancy is not the result of electron correlation effects. A possible explanation is that distortion of the incoming and outgoing electrons is

occurring in the (e, 2e) reaction, particularly for $p > 1$ au. Investigation of this possibility must await the development of DWIA methods for molecules (Section 2.2.1) and/or EMS spectrometers with much higher impact energies.

For the remaining outer-valence momentum profiles of acetone, agreement between the XMPs and HF TMPs is fair. DFT TMPs calculated using the TKSA and the 6-311++G** basis set are in somewhat better agreement with the XMPs. There is little difference between the inner-valence HF and DFT TMPs, both of which reproduce the shapes of the corresponding experimental profiles.

Of the three molecules studied, the greatest differences between the HF and DFT TMPs are observed for dimethoxymethane (Chapter 5). These differences are most significant for the low momentum regions of the outer-valence s-type momentum profiles (i.e., 11a, 10a and 8a). The DFT TMPs are generally in good agreement with the XMPs of dimethoxymethane. This is not the case for the HF outer-valence TMPs, which tend to underestimate the intensity observed experimentally at low momentum. MRSD-CI calculations of the 10b and 11a TMPs of dimethoxymethane yielded momentum profiles similar to the ones obtained from large-basis set HF calculations and in disagreement with both the DFT TMPs and the experimental 10b + 11a momentum profile, perhaps indicating that an insufficient number of electron configurations were included in the MRSD-CI calculations. These results underscore the considerable challenge in performing accurate post-HF calculations of a molecule of the size of dimethoxymethane and illustrate the appeal of the considerably less costly density functional methods. The present study of dimethoxymethane also provided the first experimental determination of the inner-valence $(6a)^{-1}$, $(4b)^{-1}$ and $(5a)^{-1}$ IPs.

The study of glycine (Chapter 6) has demonstrated the feasibility of obtaining gas-phase experimental momentum profiles of low vapour pressure solids and shown that useful results may be obtained even when the molecule is present in a number of conformations. A joint

consideration of the experimental and theoretical results has allowed for the determination of the nature and ordering of many of the valence ionizations of glycine. As was observed in the study of dimethoxymethane, the HF TMPs of glycine tend to underestimate the low momentum intensity observed in the outer-valence experimental profiles. Agreement between experiment and theory is improved significantly when the DFT momentum profiles are considered.

In each of the three molecules studied, the single-particle model of ionization breaks down for binding energies of 16 or 17 eV and higher. This is evidenced by XMPs that are of significantly less intensity than the corresponding theoretical profiles, indicating spectroscopic factors (pole strengths) of less than unity. Furthermore, in the cases of acetone and dimethoxymethane, for which measurements were performed up to $\approx$ 60 eV, ionization intensity is spread over the entire energy range from 25–60 eV, with little structure evident in this region of the binding energy spectra and with indications that the ionization intensity extends to higher binding energies. This is indicative of the presence of many low-intensity ionization poles throughout this energy range. The respective experimental angular profiles in this binding energy range indicate that most of this ionization intensity can be attributed to the $(5a_1)^{-1}$ and $(4a_1)^{-1}$ ionization manifolds in the case of acetone and the $(3b)^{-1}$ and $(4a)^{-1}$ ionization manifolds in the case of dimethoxymethane. However, for both molecules, the experimental results indicate that other ionization manifolds also contribute to the observed intensity at binding energies greater than 25 eV. Further many-body theoretical studies of inner-valence ionization of acetone and dimethoxymethane would allow a more detailed analysis of the present experimental results.

Assessments of the effects of the basis set on the calculated TMPs results in similar conclusions for acetone, glycine and dimethoxymethane. In all three molecules, use of a minimal basis set (e.g., STO-3G) or a split-valence basis set (e.g., 4-31G, 6-31G, 6-311G)

without diffuse and polarization functions results in TMPs in poor agreement with experiment. This was found to be the case for both HF and DFT calculations. Basis set effects are most significant for the outer-valence momentum profiles, where use of any of the small basis sets mentioned above tends to result in TMPs that underestimate the low momentum intensity. The addition of diffuse and polarization functions to the basis sets generally results in improved agreement between experiment and theory, typified by shifts of the p_{MAX} of p-type TMPs towards lower momentum and increases in the intensity of the $p = 0$ maximum of s-type profiles. Considering the Fourier transform relationship between position and momentum space (Equation (1.1)), this demonstrates the importance of utilizing diffuse and polarization functions when describing the large r (small p) outer-valence electron density of acetone, glycine and dimethoxymethane. Basis set effects have been found to be of considerably less importance for the inner-valence TMPs of all three molecules. Further increasing basis set size beyond that of the 6-311++G** basis set does not result in appreciable changes to the TMPs of these molecules. Consequently, it is recommended that the 6-311++G** basis set be used for the calculation of valence momentum profiles and other large-r properties of these and similar molecules. It should be noted, however, that the results for dimethoxymethane (Section 5.6) indicate that the valence TMPs of this molecule are essentially converged using the 6-31+G* basis set, suggesting that this basis set may be a more efficient choice for the calculation of TMPs of larger molecules. If other molecular properties (e.g., the total energy) that are more dependent upon the small-r electron density are also of interest, however, then use of a larger basis set should be considered.

The present study involving larger molecules further supports the validity of the TKSA for the application of DFT to EMS, initially evaluated by Duffy et al. [20, 21] using atoms and small molecules. Only small variations of the DFT TMPs are observed with changes in the exchange–correlation functional. In general, the LSDA TMPs tend to have the greatest

intensity at low momentum, most likely as a result of overestimation of the large-r electron density when using this functional. The use of gradient-corrected functionals tends to decrease the theoretical intensity at low momentum. Unfortunately, the statistical precision of the present data is insufficient to comment on the relative accuracy of the various functionals for calculating theoretical momentum profiles.

The discrepancies between even the large basis set HF calculations and the experimental momentum profiles of acetone, dimethoxymethane and glycine indicate the inadequacy of non-correlated methods for calculating the outer spatial regions of the valence electron distributions of these molecules. This finding is consistent with the observation that some accounting of electron correlation is necessary for the accurate calculation of other properties (e.g., relative conformer energies and/or geometries) of glycine [157] and dimethoxymethane [142]. The good agreement between the DFT momentum profiles and the experimental data for these molecules suggests that DFT is an effective choice for accounting for these electron correlation effects and modeling the longer range electron density. This is particularly encouraging considering the relative efficiency of DFT as compared with post-HF methods for the inclusion of electron correlation.

While the present work would not have been possible without the construction of the energy-dispersive multichannel spectrometer, the experimental results also demonstrate the limitations of this instrument. Determination of individual XMPs corresponding to energetically close ionization processes was, in many cases, very difficult or impossible. In order to obtain more accurate experimental results for acetone, glycine and dimethoxymethane or to perform EMS studies of yet larger molecules, further improvements in instrumentation are necessary. In this regard, a new electron momentum spectrometer, multichannel both in energy and in angle and with high energy resolution (predicted to be 0.05 eV fwhm), is currently being developed in this research group [131]. When completed, this spectrom-

eter will be capable of detecting outgoing electrons in a full circle (i.e., all values of the out-of-plane azimuthal angle) above the interaction region simultaneously, in contrast to the energy-dispersive instrument used in the present work or the angle-dispersive instrument of Todd et al. [55], which detect outgoing electrons at only a single azimuthal angle or a comparatively small range of azimuthal angles, respectively. This will result in an increase in sensitivity of at least four orders of magnitude over that of the energy-dispersive instrument described in Chapter 3 and will greatly expand the range of potential targets for EMS experiments.

Bibliography

[1] P. Coppens and E. D. Stevens. *Adv. Quantum Chem.* **10** (1977) 1–35.

[2] D. A. Kohl and L. S. Bartell. *J. Chem. Phys.* **51** (1969) 2891–2904.

[3] K. Fukui. In *Applied Quantum Chemistry, Proceedings of the Nobel Laureate Symposium on Applied Quantum Chemistry*, edited by V. H. Smith, Jr., H. F. Schaefer III and K. Morokuma, pages 1–25. D. Reidel Publishing Company, Boston, 1986.

[4] K. Fukui, T. Yonezawa and H. J. Shingu. *J. Chem. Phys.* **20** (1952) 722–725.

[5] I. E. McCarthy and E. Weigold. *Phys. Reports* **27** (1976) 275–371.

[6] E. Weigold and I. E. McCarthy. *Adv. At. Mol. Phys.* **14** (1978) 127–179.

[7] I. McCarthy and E. Weigold. *Rep. Prog. Phys.* **91** (1991) 789–879.

[8] C. E. Brion. *Int. J. Quantum Chem.* **29** (1986) 1397–1428.

[9] C. E. Brion. In *The Physics of Electronic and Atomic Collisions*, edited by T. Andersen, B. Fastrup, F. Folkmann, H. Knudsen and N. Andersen, volume 295 of *AIP Conference Proceedings*, pages 350–359. American Institute of Physics, New York, 1993.

[10] C. A. Coulson and W. E. Duncanson. *Proc. Camb. Philos. Soc.* **37** (1941) 55–66, 67–73, 74–81, 397–405, 406–421.

[11] C. A. Coulson and W. E. Duncanson. *Proc. Camb. Philos. Soc.* **38** (1942) 100–108.

[12] W. E. Duncanson. *Proc. Camb. Philos. Soc.* **39** (1943) 180–188.

[13] P. T. Measures, K. A. Mort, N. L. Allen and D. L. Cooper. *J. Comput. Aided Mol. Des.* **9** (1995) 331–340.

[14] N. L. Allan and D. L. Cooper. *Topics in Current Chemistry* **173** (1995) 85–111.

[15] D. L. Cooper, K. A. Mort, N. L. Allan, D. Kinchington and C. McGuigan. *J. Am. Chem. Soc.* **115** (1993) 12615–12616.

[16] E. Weigold, Y. Zheng and W. von Niessen. *Chem. Phys.* **150** (1991) 405–427.

[17] Y. Zheng. *Electron Momentum Spectroscopy of Laser-Excited Atoms and Molecules.* Ph.D. thesis, The Flinders University of South Australia, 1989.

[18] J. P. D. Cook, I. E. McCarthy, A. T. Stelbovics and E. Weigold. *J. Phys. B: At. Mol. Phys.* **17** (1984) 2339–2352.

[19] K. T. Leung and C. E. Brion. *Chem. Phys.* **82** (1983) 87–111.

[20] P. Duffy, D. P. Chong, M. E. Casida and D. R. Salahub. *Phys. Rev. A* **50** (1994) 4707–4728.

[21] P. Duffy. *A Combined Experimental and Theoretical Study of the Electronic Structure of Molecules by Electron Momentum Spectroscopy and Density Functional Theory.* Ph.D. thesis, The University of British Columbia, 1995.

[22] J. George A. Baker, I. E. McCarthy and C. E. Porter. *Phys. Rev.* **120** (1960) 254–264.

[23] Y. F. Smirnov and V. G. Neudachin. *JETP Lett.* **3** (1966) 192–193.

[24] V. G. Neudachin, G. A. Novoskol'tseva and Y. F. Smirnov. *JETP* **28** (1969) 540–543.

[25] A. E. Glassgold and G. Ialongo. *Phys. Rev.* **175** (1968) 151–159.

[26] H. Ehrhardt, M. Schulz, T. Tekaat and K. Willmann. *Phys. Rev. Lett.* **22** (1969) 89–92.

[27] J. U. Amaldi, A. Egidi, R. Marconero and G. Pizzella. *Rev. Sci. Instrum.* **40** (1969) 1001–1004.

[28] R. Camilloni, A. Giardini Guidoni, R. Tiribelli and G. Stefani. *Phys. Rev. Lett.* **29** (1972) 618–621.

[29] E. Weigold, S. T. Hood and P. J. O. Teubner. *Phys. Rev. Lett.* **30** (1973) 475–478.

[30] S. T. Hood, E. Weigold, I. E. McCarthy and P. J. O. Teubner. *Nature Phys. Sci.* **245** (1973) 65–68.

[31] V. G. Levin. *Phys. Lett.* **39A** (1972) 125–126.

[32] S. T. Hood, A. Hamnett and C. E. Brion. *Chem. Phys. Lett.* **41** (1976) 428–430.

[33] M. A. Coplan, J. H. Moore and J. A. Tossell. *J. Chem. Phys.* **68** (1978) 329–330.

[34] M. P. Banjavcic, B. H. Watt, T. D. Pope, T. A. Daniels, R. P. Hammond and K. T. Leung. *Chem. Phys. Lett.* **160** (1989) 371–376.

[35] C. E. Brion. In *Correlations and Polarization in Electronic and Atomic Collisions and (e,2e) Reactions*, edited by P. J. O. Turner and E. Weigold, volume 122 of *Inst. Phys. Conf. Series*, pages 171–179. Institute of Physics, Bristol, 1992.

[36] K. T. Leung. In *Theoretical Models of Chemical Bonding. Part 3. Molecular Spectroscopy, Electronic Structure and Intramolecular Interactions*, edited by Z. B. Maksic, pages 339–386. Springer-Verlag, New York, 1991.

[37] M. A. Coplan, J. H. Moore and J. P. Doering. *Rev. Mod. Phys.* **66** (1994) 985–1014.

[38] K. T. Leung and C. E. Brion. *J. Electron Spectrosc. Relat. Phenom.* **35** (1985) 327–352.

[39] A. O. Bawagan, C. E. Brion, E. R. Davidson, C. Boyle and R. F. Frey. *Chem. Phys.* **128** (1988) 439–455.

[40] L. S. Cederbaum, W. Domcke, J. Schirmer and W. von Niessen. *Adv. Chem. Phys.* **65** (1986) 115–159.

[41] I. E. McCarthy. *J. Electron Spectrosc. Relat. Phenom.* **36** (1985) 37–58.

[42] C. L. French, C. E. Brion and E. R. Davidson. *Chem. Phys.* **122** (1988) 247–269.

[43] C. L. French, C. E. Brion, A. O. Bawagan, P. S. Bagus and E. R. Davidson. *Chem. Phys.* **121** (1988) 315–333.

[44] Y. Zheng, C. E. Brion, M. J. Brunger, K. Zhao, A. M. Grisogono, S. Braidwood, E. Weigold, S. J. Chakravorty, E. R. Davidson, A. Sgamellotti and W. von Niessen. *Chem. Phys.* **212** (1996) 269–300.

[45] A. O. Bawagan, C. E. Brion, E. R. Davidson and D. Feller. *Chem. Phys.* **113** (1987) 19–42.

[46] D. Feller, C. M. Boyle and E. R. Davidson. *J. Chem. Phys.* **86** (1987) 3424–3440.

[47] A. O. Bawagan, R. Müller-Fiedler, C. E. Brion, E. R. Davidson and C. Boyle. *Chem. Phys.* **120** (1988) 335–337.

[48] P. Duffy, M. E. Casida, C. E. Brion and D. P. Chong. *Chem. Phys.* **159** (1992) 347–363.

[49] A. O. Bawagan and C. E. Brion. *Chem. Phys. Lett.* **137** (1987) 573–577.

[50] A. O. Bawagan and C. E. Brion. *Chem. Phys.* **123** (1988) 51–63.

[51] A. Minchinton, C. E. Brion and E. Weigold. *Chem. Phys.* **62** (1981) 369–375.

[52] Y. Zheng, E. Weigold and C. E. Brion. *J. Electron Spectrosc. Relat. Phenom.* **53** (1990) 153–175.

[53] S. A. C. Clark, A. O. Bawagan and C. E. Brion. *Chem. Phys.* **137** (1989) 407–426.

[54] B. P. Hollebone, P. Duffy, C. E. Brion, Y. Wang and E. R. Davidson. *Chem. Phys.* **178** (1993) 25–38.

[55] B. R. Todd, N. Lermer and C. E. Brion. *Rev. Sci. Instrum.* **65** (1994) 349–358.

[56] P. Storer, R. S. Caprari, S. A. C. Clark, M. Vos and E. Weigold. *Rev. Sci. Instrum.* **65** (1994) 2214–2226.

[57] Y. Zheng, I. E. McCarthy, E. Weigold and D. Zhang. *Phys. Rev. Lett.* **64** (1990) 1358–1360.

[58] N. Lermer, B. R. Todd, N. M. Cann, C. E. Brion, Y. Zheng, S. Chakravorty and E. R. Davidson. *Can. J. Phys.* **74** (1996) 748–756.

[59] N. Lermer. *Development and Application of a Momentum Dispersive Multichannel Electron Momentum Spectrometer.* Ph.D. thesis, The University of British Columbia, 1995.

[60] N. Lermer, B. R. Todd, N. M. Cann, Y. Zheng, C. E. Brion, Z. Yang and E. R. Davidson. *Phys. Rev. A* (1997). Submitted for publication.

[61] I. E. McCarthy, A. Ugbabe, E. Weigold and P. J. O. Teubner. *Phys. Rev. Lett.* **33** (1974) 459–462.

[62] A. J. Dixon, I. E. McCarthy and E. Weigold. *J. Phys. B: At. Mol. Phys.* **9** (1976) L195–L198.

[63] A. D. Smith, M. A. Coplan, D. J. Chornay, J. H. Moore, J. A. Tossell, J. Mrozek, V. H. Smith, Jr. and N. S. Chant. *J. Phys. B: At. Mol. Phys.* **19** (1986) 969–980.

[64] A. Lahmam-Bennani, A. Duguet, C. Dupré and C. Dal Cappello. *J. Electron Spectrosc. Relat. Phenom.* **58** (1992) 17–22.

[65] E. Weigold, I. E. McCarthy, A. J. Dixon and S. Dey. *Chem. Phys. Lett.* **47** (1977) 209–212.

[66] R. G. Parr and W. Yang. *Density Functional Theory of Atoms and Molecules.* Oxford University Press, New York, 1989.

[67] J. K. Labanowski and J. W. Andzelm, editors. *Density Functional Methods in Chemistry.* Springer-Verlag, New York, 1991.

[68] W. Kohn, A. D. Becke and R. G. Parr. *J. Phys. Chem.* **100** (1996) 12974–12980.

[69] J. Rolke, Y. Zheng, C. E. Brion, S. J. Chakravorty, E. R. Davidson and I. E. McCarthy. *Chem. Phys.* **215** (1997) 191.

[70] K. Kimura, S. Katsumata, Y. Achiba, T. Yamazaki and S. Iwata. *Handbook of HeI photoelectron sectra of fundamental organic molecules.* Halsted Press, New York, 1981.

[71] B. P. Hollebone, J. J. Neville, Y. Zheng, C. E. Brion, Y. Wang and E. R. Davidson. *Chem. Phys.* **196** (1995) 13–35.

[72] A. J. Kirby. *The Anomeric Effect and Related Stereoelectronic Effects at Oxygen.* Springer-Verlag, Berlin, 1983.

[73] R. D. Suenram and F. J. Lovas. *J. Mol. Spectrosc.* **72** (1978) 372–382.

[74] R. D. Brown, P. D. Godfrey, J. W. V. Storey and M.-P. Bassez. *J. Chem. Soc., Chem. Commun.* (1978) 547–548.

[75] L. Schäfer, H. L. Sellers, F. J. Lovas and R. D. Suenram. *J. Am. Chem. Soc.* **102** (1980) 6566–6568.

[76] R. D. Suenram and F. J. Lovas. *J. Am. Chem. Soc.* **102** (1980) 7180–7184.

[77] P. D. Godfrey and R. D. Brown. *J. Am. Chem. Soc.* **117** (1995) 2019–2023.

[78] I. D. Reva, A. M. Plokhotnichenko, S. G. Stepanian, A. Y. Ivanov, E. D. Radchenko, G. G. Sheina and Y. P. Blagoi. *Chem. Phys. Lett.* **232** (1995) 141–148. Erratum *Chem. Phys. Lett.* **235** (1995) 617.

[79] J. H. Jensen and M. S. Gordon. *J. Am. Chem. Soc.* **113** (1991) 7917–7924.

[80] M. Ramek, V. K. W. Cheng, R. F. Frey, S. Q. Newton and L. Schäfer. *J. Mol. Struct.* **235** (1991) 1–10.

[81] A. G. Császár. *J. Am. Chem. Soc.* **114** (1992) 9568–9575.

[82] D. Yu, D. A. Armstrong and A. Rauk. *Can. J. Chem.* **70** (1992) 1762–1772.

[83] C.-H. Hu, M. Shen and H. F. Schaefer III. *J. Am. Chem. Soc.* **115** (1993) 2923–2929.

[84] V. Barone, C. Adamo and F. Lelj. *J. Chem. Phys.* **102** (1995) 364–370.

[85] D. T. Nguyen, A. C. Scheiner, J. W. Andzelm, S. Sirois, D. R. Salahub and A. T. Hagler (1997). To be published.

[86] F. P. Larkins. *J. Phys. B: At. Mol. Phys.* **14** (1981) 1477–1484.

[87] S. Dey, I. E. McCarthy, P. J. O. Teubner and E. Weigold. *Phys. Rev. Lett.* **34** (1975) 782–785.

[88] A. O. Bawagan, L. Y. Lee, K. T. Leung and C. E. Brion. *Chem. Phys.* **99** (1985) 367–382.

[89] A. O. Bawagan and C. E. Brion. *Chem. Phys.* **144** (1990) 167–178.

[90] M. E. Casida. *Phys. Rev. A* **51** (1995) 2005–2013.

[91] J. Rolke and C. E. Brion. *Chem. Phys.* **207** (1996) 173–192.

[92] J. Rolke, N. Cann, Y. Zheng, B. P. Hollebone, C. E. Brion, Y. A. Wang and E. R. Davidson. *Chem. Phys.* **201** (1995) 1–21.

[93] I. N. Levine. *Quantum Chemistry.* Allyn and Bacon, Inc., Boston, third edition, 1983.

[94] W. J. Hehre, L. Radom, P. v.R. Schleyer and J. A. Pople. Ab Initio *Molecular Orbital Theory.* John Wiley & Sons, New York, 1986.

[95] K. Raghavachari and J. B. Anderson. *J. Phys. Chem.* **100** (1996) 12960–12973.

[96] C. Møller and M. S. Plesset. *Phys. Reports* **46** (1934) 618.

[97] P. Hohenberg and W. Kohn. *Phys. Rev.* **136** (1964) B864–B871.

[98] W. Kohn and L. J. Sham. *Phys. Rev.* **140** (1965) A1133–A1138.

[99] S. H. Vosko, L. Wilk and M. Nusair. *Can. J. Phys.* **58** (1980) 1200–1211.

[100] A. St-Amant and D. R. Salahub. *Chem. Phys. Lett.* **169** (1990) 387–392.

[101] D. R. Salahub, R. Fournier, P. Mlanarski, I. Papai, A. St-Amant and J. Ushio. In *Density Functional Methods in Chemistry*, edited by J. Labanowski and J. Andzelm, pages 77–100. Springer-Verlag, New York, 1991.

[102] M. J. Frisch, G. W. Trucks, H. B. Schlegel, P. M. W. Gill, B. G. Johnson, M. W. Wong, J. B. Foresman, M. A. Robb, M. Head-Gordon, E. S. Replogle, R. Gomperts, J. L. Andres, K. Raghavachari, J. S. Binkley, C. Gonzalez, R. L. Martin, D. J. Fox, D. J. Defrees, J. Baker, J. J. P. Stewart and J. A. Pople. *Gaussian 92/DFT, Revision F.4.* Gaussian, Inc., Pittsburgh PA, 1993.

[103] M. J. Frisch, G. W. Trucks, H. B. Schlegel, P. M. W. Gill, B. G. Johnson, M. A. Robb, J. R. Cheeseman, T. Keith, G. A. Petersson, J. A. Montgomery, K. Raghavachari, M. A. Al-Laham, V. G. Zakrzewski, J. V. Ortiz, J. B. Foresman, C. Y. Peng, P. Y. Ayala, W. Chen, M. W. Wong, J. L. Andres, E. S. Replogle, R. Gomperts, R. L. Martin, D. J. Fox, J. S. Binkley, D. J. Defrees, J. Baker, J. P. Stewart, M. Head-Gordon, C. Gonzalez and J. A. Pople. *Gaussian 94, Revision B.3.* Gaussian, Inc., Pittsburgh PA, 1995.

[104] P. A. M. Dirac. *Proc. Camb. Phil. Soc.* **26** (1930) 376–385.

[105] A. D. Becke. *Phys. Rev. A* **38** (1988) 3098–3100.

[106] J. P. Perdew. *Phys. Rev. B* **33** (1986) 8822–8824.

[107] C. Lee, W. Yang and R. G. Parr. *Phys. Rev. B* **37** (1988) 785–789.

[108] A. D. Becke. *J. Chem. Phys.* **98** (1993) 5648–5652.

[109] J. P. Perdew and Y. Wang. *Phys. Rev. B* **45** (1992) 13244–13249.

[110] W. J. Hehre, R. F. Stewart and J. A. Pople. *J. Chem. Phys.* **51** (1969) 2657–2664.

[111] W. J. Hehre, R. Ditchfield and J. A. Pople. *J. Chem. Phys.* **56** (1972) 2257–2261.

[112] P. C. Hariharan and J. A. Pople. *Theor. Chim. Acta* **28** (1973) 213–222.

[113] R. Krishan, J. S. Binkley, R. Seeger and J. A. Pople. *J. Chem. Phys.* **72** (1980) 650–654.

[114] T. H. Dunning, Jr. *J. Chem. Phys.* **90** (1989) 1007–1023.

[115] R. A. Kendall, T. H. Dunning, Jr. and R. J. Harrison. *J. Chem. Phys.* **96** (1992) 6796–6806.

[116] M. J. Frisch, J. A. Pople and J. S. Binkley. *J. Chem. Phys.* **80** (1984) 3265–3269.

[117] T. Clark, J. Chandrasekhar, G. W. Spitznagel and P. v. R. Schleyer. *J. Comp. Chem.* **4** (1983) 294.

[118] D. A. McQuarrie. *Statistical Mechanics.* Harper & Row, New York, 1976.

[119] J. E. Mayer. *Equilibrium Statistical Mechanics.* The International Encyclopedia of Physical Chemistry and Chemical Physics. Pergamon Press, Oxford, 1968.

[120] J. A. Simpson. *Rev. Sci. Instrum.* **35** (1964) 1698–1704.

[121] S. D. Kevan. *Rev. Sci. Instrum.* **54** (1983) 1441–1445.

[122] J. L. Wizu. *Nucl. Instr. and Meth.* **162** (1979) 587–601.

[123] C. W. Gear. In *Proceedings of the Skytop Conference on Computer Systems in Experimental Nuclear Physics*, page 552. USAEC, 1969.

[124] S. J. Chakravorty and E. R. Davidson. Private communication.

[125] G. Bieri, L. Åsbrink and W. von Niessen. *J. Electron Spectrosc. Relat. Phenom.* **27** (1982) 129–178.

[126] Y. Zheng, J. J. Neville, C. E. Brion, Y. Wang and E. R. Davidson. *Chem. Phys.* **188** (1994) 109–129.

[127] T. Iijima. *Bull. Chem. Soc. Japan* **45** (1972) 3526–3530.

[128] J. D. Swalen and C. C. Costain. *J. Chem. Phys.* **31** (1959) 1562–1574.

[129] H. Partridge. *J. Chem. Phys.* **90** (1989) 1043–1047.

[130] H. Partridge. *J. Chem. Phys.* **87** (1987) 6643–6647.

[131] C. E. Brion. Private communication.

[132] G. R. J. Thatcher, editor. *The Anomeric Effect and Associated Stereoelectronic Effects*, volume 539 of *ACS Symposium Series*, Washington, DC, 1993. American Chemical Society.

[133] M. Kubo. *Sci. Papers Inst. Phys. Chem. Res. (Tokyo)* **29** (1936) 179–187.

[134] E. E. Astrup. *Acta Chem. Scand.* **27** (1973) 3271–3276.

[135] T. Uchida, Y. Kurita and M. Kubo. *J. of Polymer Sc.* **19** (1956) 365–372.

[136] A. Abe, K. Inomata, E. Tanisawa and I. Ando. *J. Mol. Struct.* **238** (1990) 315–323.

[137] M. Sakakibara, Y. Yonemura, H. Matsuura and H. Murata. *J. Mol. Struct.* **66** (1980) 333–337.

[138] A. Abe and J. E. Mark. *J. Am. Chem. Soc.* **98** (1976) 6468–6476.

[139] G. A. Jeffrey, J. A. Pople, J. S. Binkley and S. Vishveshwara. *J. Am. Chem. Soc.* (1978) 373–379.

[140] K. B. Wiberg and M. A. Murcko. *J. Am. Chem. Soc.* **111** (1989) 4821–4828.

[141] G. D. Smith, R. L. Jaffe and D. Y. Yoon. *J. Phys. Chem.* **98** (1994) 9072–9077.

[142] J. R. Kneisler and N. L. Allinger. *J. Comp. Chem.* **17** (1996) 757–766.

[143] D. Feller and E. R. Davidson. *J. Chem. Phys.* **74** (1981) 3977–3979.

[144] I. L. Cooper and C. N. M. Pounder. *J. Chem. Phys.* **77** (1982) 5045–5052.

[145] P. Fantucci, V. Bonačić-Koutecký and J. Koutecký. *J. Comp. Chem.* **6** (1985) 462.

[146] H. Partridge. *Near Hartree-Fock quality GTO basis sets for the second-row atoms.* NASA Technical Memorandum 89449, 1987.

[147] H. Partridge. *Near Hartree-Fock quality GTO basis sets for the first- and third-row atoms.* NASA Technical Memorandum 101044, 1989.

[148] C. J. Maxwell, F. B. C. Machado and E. R. Davidson. *J. Am. Chem. Soc.* **114** (1992) 6496–6504.

[149] F. S. Jørgensen. *J. Chem. Research (S)* (1981) 212–213.

[150] F. S. Jørgensen and J. P. Snyder. *J. Org. Chem.* **45** (1980) 1015–1020.

[151] V. V. Zverev, Y. Y. Villem, N. V. Villem, E. N. Klimovitskii and B. A. Arbuzov. *Zh. Obshch. Khim.* **52** (1982) 1888–1893.

[152] Y. Zheng, J. J. Neville and C. E. Brion. *Science* **270** (1995) 786–788.

[153] J. J. Neville, Y. Zheng and C. E. Brion. *J. Am. Chem. Soc.* **118** (1996) 10533–10544.

[154] W. von Niessen, J. Schirmer and L. S. Cederbaum. *Comp. Phys. Reports* **1** (1984) 57–126.

[155] E. R. Davidson, D. Feller, C. M. Boyle, L. Adamowicz, S. A. C. Clark and C. E. Brion. *Chem. Phys.* **147** (1990) 45–50.

[156] G. Rauhut and P. Pulay. *J. Phys. Chem.* **99** (1995) 3093–3100.

[157] R. F. Frey, J. Coffin, S. Q. Newton, M. Ramek, V. K. W. Cheng, F. A. Momany and L. Schäfer. *J. Am. Chem. Soc.* **114** (1992) 5369–5377.

[158] A. G. Császár. *J. Mol. Struct.* **346** (1995) 141–152.

[159] M. Ramek, F. A. Momany, D. M. Miller and L. Schäfer. *J. Mol. Struct.* **375** (1996) 189–191.

[160] B. P. Hollebone and C. E. Brion. Unpublished work.

[161] T. P. Debies and J. W. Rabalais. *J. Electron Spectrosc. Relat. Phenom.* **3** (1974) 315–322.

[162] P. H. Cannington and N. S. Ham. *J. Electron Spectrosc. Relat. Phenom.* **32** (1983) 139–151.

[163] C.-H. Hu, D. P. Chong and M. E. Casida. *J. Electron Spectrosc. Relat. Phenom.* (1997). In press.

[164] P. D. Godfrey, R. D. Brown and F. M. Rodgers. *J. Mol. Struct.* **376** (1996) 65–81.

[165] K. Iijima, K. Tanaka and S. Onuma. *J. Mol. Struct.* **246** (1991) 257–266.

[166] D. Gross and G. Grodsky. *J. Am. Chem. Soc.* **77** (1955) 1678–1680.

[167] G. Junk and H. Svec. *J. Am. Chem. Soc.* **85** (1963) 839–845.

[168] E. R. Davidson. *Int. J. Quantum Chem.* **37** (1990) 811–819.

[169] D. P. Chong. *Can. J. Chem.* **74** (1996) 1005–1007.